Measured and Calculated Dose Distributions in the "Claws" – a Specially Designed Gold Applicator Loaded with I-125 Seeds

Christoph Jan Trauernicht

Thesis presented in fulfillment of the requirements for the degree of

Doctor of Philosophy

in the Department of Radiation Medicine (Division of Medical Physics)

at the University of Cape Town

in the subject of

Medical Physics

Supervisor: Prof. E.R. Hering

Division of Medical Physics

Department of Radiation Medicine

University of Cape Town

Co-supervisor: Dr. F.C.P. du Plessis

Department of Medical Physics

University of the Free State

Date: 10 November 2019

DECLARATION

I, Christoph Jan Trauernicht, hereby declare that the work contained in this thesis is my own work (except where acknowledgements indicate otherwise) and that I have not previously in its entirety or in part submitted it at any university for a degree. I empower the university to reproduce for the purpose of research either the whole or any portion of the contents in any manner whatsoever.

Signature: Signed by candidate

Date: 10 November 2019

THESIS STRUCTURE AND OVERVIEW

The objective of this study was to investigate the “Claws”, a unique gold applicator used at Groote Schuur Hospital for the treatment of retinoblastoma.

CHAPTER 1 of this thesis gives some background on the intraocular brachytherapy programme at Groote Schuur Hospital, where the “Claws” were designed. The aims of the thesis are briefly described: these include the characterization of the OncoSeed 6711 I-125 seed and the characterization of the “Claws”, using measurements, calculations and Monte Carlo simulations.

CHAPTER 2 is dedicated to setting the scene of this work: it describes the classification and treatment of retinoblastoma, different types of I-125 seeds, including the OncoSeed 6711, different types of intraocular brachytherapy plaques that are in use around the world and a brief introduction to various radiation interactions.
This is followed by a description of the TG-43 dosimetry protocol and published dosimetry data on the OncoSeed 6711. The literature review continues with a description of radiochromic/gafchromic film dosimetry, as well as thermoluminescent dosimetry in brachytherapy. Monte Carlo methods are introduced in this section, an overview of EGSnrc is given, which is followed by an overview of egs_brachy.

CHAPTER 3 describes the equipment used and methods applied in this thesis. It describes the detectors used for the spectral measurements of the seed, the phantoms that were manufactured, the CAD drawing that was put together, the manufacture of the PVC “Claws” and attempts at micro-CT scanning the “Claws” model. The chapter ends with a description of the egs_brachy Monte Carlo parameters used in this study.

CHAPTER 4 contains the results. These include the dosimetric description of the OncoSeed 6711 I-125 seed, as well as the results of the spectral measurements. A section describes some of the issues that arise when doing gafchromic film dosimetry. Measured and planned dose distributions in the “Claws” are presented. Monte Carlo simulation results of a final simulation with 64.000.000.000 histories are shown. This is followed by an analysis of the results of the various dose distributions and contains the relative doses to critical structures in and around the “Claws”. This was not possible to this extent until now, because the treatment planning systems in use have not been able to take the gold shielding of the “Claws” into account.

CHAPTER 5 is dedicated to discussions and conclusions.

A list of references then follows to complete the thesis.

ABSTRACT

Introduction:

The "Claws" is a unique gold applicator for whole-eye radiotherapy that was designed at Groote Schuur Hospital. It is used to treat retinoblastoma. Under general anaesthesia, a pericorneal ring is attached to the four extraocular muscles, and four legs, each loaded with I-125 seeds, are inserted beneath the conjunctiva in-between each pair of muscles and attached anteriorly to the ring. The four legs that are now sutured onto the ring give it a claw-like appearance, hence the name for the applicator. The applicator was designed in such a way that the dose is directed towards the middle of the eye, while sparing surrounding tissues. The dose to the organs at risk could never be determined accurately, because the treatment planning system (TPS) is not able to take into account the gold shielding. Additionally, the TPS approximates each seed as a point source and not as a line source, therefore not taking any anisotropy into account.

Aims:

The first aim of this project was to accurately determine various dosimetric and physical characteristics of a single I-125 seed and to then compare these to published data.
Spectral measurements of the OncoSeed 6711 using various detectors were also done.
The next aim was to formalize the model of the "Claws" so that the applicator can potentially also be manufactured elsewhere.

The next aim was to describe the "Claws" dosimetrically. This was done

- Using thermoluminescent dosimeters in a solid water phantom
- Using gafchromic film in a solid water phantom
- Using treatment planning systems TheraPlan Plus and BrachyVision
- Using Monte Carlo simulations – egs_brachy

The final aim of the thesis was the comparison of measured and calculated data. The Monte Carlo simulations take into account the seed anisotropy as well as the gold shielding; therefore the relative dose to critical structures can be estimated more reliably.

Method and Materials:

Gafchromic film and thermoluminescent dosimeters (TLDs) were used for measurements in various specially designed phantoms to determine the seed parameters, as well as dose distributions in the eye. Dose distributions were calculated on two treatment planning systems. A CAD drawing of the “Claws” was created and used to create the input file for Monte Carlo simulations using egs_brachy. The final Monte Carlo calculation simulated 64.000.000.000 particle histories at voxel sizes of 0.1 mm x 0.1 mm x 0.1 mm.

Results:

Measured seed data matched published seed data.

Significant dose distribution changes were found when comparing measured and Monte Carlo data to planned data, especially near the periphery of the eye between adjacent legs.

The Monte Carlo calculated dose to the optic nerve is 64.8 % of the central dose in the eye, while the planned dose is 93.7 %. The Monte Carlo lens dose varies from 72.0 % - 86.1 %, while the planned dose varies from 73.0 % - 84.3 %. Monte Carlo calculated dose to the bony orbit is 11.3 %, while the planned dose is 54.7 %.

Conclusion:

Measured seed data matched published seed data.

The “Claws” were formalized with CAD drawings.

Measured and Monte Carlo simulated dose distributions matched well, while planned dose distributions showed discrepancies in certain regions of the eye and outside of the eye.

This clearly indicates that the gold shielding of the applicator walls must be taken into account during dose calculations. It can be concluded that the “Claws” were extensively described and characterized in this work.

ACKNOWLEDGEMENTS

I am grateful to a large number of people:

To my supervisor Egbert Hering, thank you for you guidance, for the time spent together, your wisdom and for making me a better medical physicist.

To my co-supervisor Freek du Plessis, thank you for the hours you spent helping me getting the Monte Carlo code installed, getting me up and running and for the discussions we had.

To Gerrie, your LDR knowledge, your encouragement and your gentle nature made it a pleasure to work with you!

Dr Karen Lecuona, the work you do in the opthalmic theatre is phenomenal! Clare and Julie, thank you for doing what you do!

Thank you Susan and Marilyn for your mould room experience and willingness to help load and unload “Claws”. Robin, thank you for your help with the manufacture of the phantoms.

Along the way I had questions for a number of people who were experts at draughting (Clarence, Kobus, JD Marx from Esteq), and who all had ideas to help solve issues I encountered with the “Claws” drawings, but without Richard these drawings would not have been as good as they are now.

Dete, your Monte Carlo help and access to the Bloemfontein HPC cluster proved invaluable. I am grateful for your expert advice!

Hannes and Ute, thank you for your open house when I was in Bloemfontein.

Anton and Stephan, your micro-CT scanner is really cool, as is the software that comes with it! Thanks for your help!

Paul Papka, thank you for allowing me to use your detector and granting me access to the LEPS at iThemba LABS. Peane Maleka, thank you for allowing me to use the Germanium detector.

Thank you to Craig Saas at SAAO, who allowed me to use their milling maching to make a model of the “Claws”. Thank you also to Ulrike and Janus for a crash course in macro-photography, and to Alistair for letting me use his microscope.

Thank you Wayne, for lending me the PTW SourceCheck 4π chamber.

Thank you to the medical physics team at Groote Schuur Hospital, who have all had PhD conversations with me along the way.

Thank you to the medical physics team at Tygerberg Hospital (Monique, Tumelo, Hlaps, Thokozani, Ricus, Didi, Ruan, Cheryl, Lelanie) for allowing me to finish this work and for stepping up while I was busy with the thesis.
Thanks for your support, Hannah and Richard! Thank you to Tygerberg Hospital and Stellenbosch University management for giving me four months to finally complete this project.
Thank you to the postgraduate office at UCT, particularly Adri (the oracle), as well as Diane and Lorraine, for always encouraging me and helping with all the administrative issues that come with a PhD.
Thank you to the team from the UCT research office and from the STARS programme: Mignonne, Gudrun, Mathilde, Lyn, Gaëlle, Judith and Charles, you'll be glad to hear I handed in!
Graeme and Michelle, thank you for encouraging me to finish.

To my parents, who have been behind me all the way!

To my awesome wife Sonja, thank you for your patience and for always having my back, I love you!

And finally a thank you to my Creator, for giving me the ability to do this work and for blessing me with the right people along the way.

This research project was partially funded in terms of the MRC's Flagship Awards Project SAMRC-RFA-UFSP-01-2013/HARD.
I would also like to thank UCT for offering me a research development grant to buy a good PC and get some micro-CT scanning done.

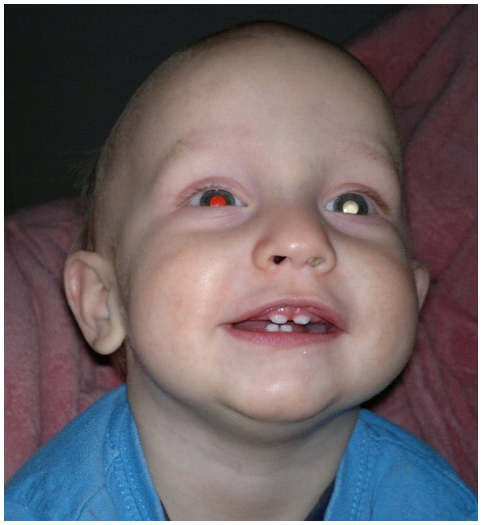

For my nephew Ralf, retinoblastoma survivor.

CONTENTS

CHAPTER 1 Introduction 18

1.1 Introduction 18

1.2 Intraocular Brachytherapy at Groote Schuur Hospital 20
1.2.1 The Manufacturing Process 20
1.2.2 The "Claws" 26
1.2.3 Other Unusual Plaques from Groote Schuur Hospital 29

1.3 Aims of the Thesis 33

CHAPTER 2 Literature Review 35

2.1 Retinoblastoma 35
2.1.1 Classification of Retinoblastoma used at Groote Schuur Hospital 35
2.1.2 Treatment of Retinoblastoma 36

2.2 Various Types of I-125 Seeds 37

2.3 The OncoSeed 6711 Seed 39

2.4 Various Types of I-125 Plaques 43

2.5 Radiation Interactions 49
2.5.1 Photon Interactions 49
2.5.1.1 Coherent Scatter 49
2.5.1.2 Photoelectric Effect 50
2.5.1.3 Compton Scatter 51
2.5.1.4 Pair Production & Photonuclear Interactions 52
2.5.1.5 Relative Importance of Photon Interactions 53
2.5.2 Electron Interactions with Matter 55
2.5.2.1 Collision Interactions 55
2.5.2.2 Radiative Interactions (Bremsstrahlung) 56

2.6 Calculation of the Treatment Time 57

2.7 The TG-43 Protocol 60
2.7.1 Air Kerma Strength - S_K 63
2.7.2 Dose Rate Constant – Λ 64
2.7.3 Geometry Function – G 64
2.7.4 Radial Dose Function – g 65
2.7.5 Anisotropy Function - F 67

2.8 The Dosimetry of the OncoSeed 6711 68

2.9 Dosimetry 72
2.9.1 Radiochromic Film Dosimetry 72
2.9.1.1 Gafchromic EBT and EBT 2 Film 72
2.9.1.2 Gafchromic EBT 3 Film 76
2.9.2 Thermoluminescent Dosimetry 77
2.9.3 Other Dosimetry 78

2.10 Monte Carlo Methods 79
2.10.1 EGSnrc 84
2.10.2 egs_brachy 86
2.10.3 MCSHOW 87

CHAPTER 3 Equipment and Methods 88

3.1 The PTW Sourcecheck 4π Chamber 91

3.2 The Medium Voltage Unit 92

3.3 The Cobalt Teletherapy Unit 94

3.4 Gafchromic Film Calibration 94

3.5 Thermoluminescent Dosimeter Calibration 96

3.6 Detectors used for Measurements of the I-125 Spectrum 97

3.6.1 NaI(Tl) Scintillation Detector 97

3.6.2 HPGe Detector 98

3.6.3 The Low-Energy Photon Spectrometer 99

3.6.4 The Silicon Drift Detector 100

3.7 Measurements of the OncoSeed 6711 I-125 Seed Dosimetric Parameters 102

3.7.1 Measurement of the Seed Anisotropy using Film 103

3.7.2 Measurement of the Seed Anisotropy using TLDs 105

3.7.3 Measurement of the Radial Dose Function 105

3.7.4 Dose Rate Constant 106

3.8 The "Claws" 109

3.9 Measurement of the Dose Distribution in the "Claws" 110

3.9.1 Thermoluminescent Dosimetry (TLD) and Gafchromic Film 111

3.10 The CAD Model of the "Claws" 113

3.11 Manufacture of PVC "Claws" 114

3.12 Attempts at Micro-CT Imaging of the "Claws" 117

3.13 Conversion of the CAD Model to a Phantom File 120

3.14 Description of Monte Carlo Parameters Used (egs_brachy parameters) 122

3.15 egs_brachy 126

CHAPTER 4 RESULTS 127

4.1 The OncoSeed 6711 I-125 Seed 127

4.1.1 The Geometry Function for the OncoSeed 6711 131

4.1.2 Measured Spectra in Air 134

4.1.2.1 NaI(Th) Scintillation Detector 134

4.1.2.2 HPGe Detector 135

4.1.2.3 The Low-Energy Photon Spectrometer 136

4.1.2.4 The Silicon Drift Detector 137

4.1.2.5 Determination of the Average Energy of the OncoSeed 6711 139

4.1.3 Anisotropy in Air 141

4.1.4 Apparent Activity Measurements with the Sourcecheck 4π Chamber 143

4.1.5 Dose Rate Constant 144

4.2 Differences in Gafchromic Film with Time and Scanner 147

4.3 Measured Anisotropy and Radial Dose Function in Solid Water 151

4.3.1 Anisotropy 151

4.3.2 Radial Dose Function 156

4.4 Measured Doses in the "Claws" 157

4.4.1 TLD Measurements 157

4.4.2 Gafchromic Film Measurements 159

4.5 Planned Doses in the "Claws" 162

4.5.1 TheraPlan Plus 162

4.5.2 BrachyVision 166

4.6 Monte Carlo Dose Distributions 172

4.7 Comparison of Dose Profiles in the "Claws" 178

4.8 Doses to Critical Structures 181

4.8.1 Nerve 181
4.8.2 Bony Orbit 181
4.8.3 Lens of the Eye 183

4.9 Qualitative Comparison of TPP Planned Dose Distribution and egs_brachy Results ……. 185

CHAPTER 5 Discussion and Conclusion 188

5.1 The OncoSeed 6711 I-125 Seed 188

5.2 The "Claws" 190

5.3 Future Work 193

CHAPTER 6 References 195

LIST OF FIGURES

Figure 1: The Brass Eyeball with the Shape of a Tumour *21*
Figure 2: A Selection of Brass Eyeballs in use at Groote Schuur Hospital *21*
Figure 3: The Flat Gold Plate is Shaped in a Lead Mould to the Correct Curvature *22*
Figure 4: (L) Lead Glass Shield (R) Loading of a Plaque with I-125 Seeds *23*
Figure 5: Structure of the Acrylic Polymer Repeating Unit *23*
Figure 6: Filling up the Plaque with Acrylic *24*
Figure 7: Insertion of a Plaque in Theatre *24*
Figure 8: A Selection of Custom Gold Plaques with the Original Gold Sheet *25*
Figure 9: Custom Plaques with a Cantilever to Allow for Placement near the Lens *25*
Figure 10: Plaques with a Notch for Placement around the Optic Nerve *25*
Figure 11: The Claws *26*
Figure 12: Positioning of the Pericorneal Ring *27*
Figure 13: Insertion of one of the Legs *Figure 14: Nearing the End of Surgery* *27*
Figure 15: X-rays of the "Claws" in-situ *28*
Figure 16: Plaque Designed to Treat the Lacrimal Gland *29*
Figure 17: Applicator Designed to Irradiate Blood Vessels Growing into the Cornea *29*
Figure 18: The Conjunctiva Plaque *30*
Figure 19: Convex Plaque to Treat the Superior Orbital Wall *30*
Figure 20: Patient Treated with an Orbital Implant in one Eye and the "Claws" in the other Eye to Help Preserve some Vision in that Eye. *31*
Figure 21: Seed Dimensions as Provided by the Supplier *40*
Figure 22: Seed Dimensions According to (Dolan et al., 2006) *41*
Figure 23: Various COMS Standard and Notched Eye Plaques (Images used from www.eyephysics.com, used with permission) *44*
Figure 24: The ROPES Plaques (Images from www.eyephysics.com, used with permission) *46*
Figure 25: A Number of Eye Physics Plaques (Image from www.eyephysics.com, used with permission) *47*
Figure 26: The Photoelectric Effect – An Incoming Photon Results in the Ejection of a Photoelectron. Characteristic Radiation or Auger Electrons are Emitted. *51*
Figure 27: Compton Scatter *52*
Figure 28: Relative Importance of Photon Attenuation Processes *53*
Figure 29: Relative Importance of Photon Interactions in Water (Left) and Gold (Right) *54*
Figure 30: Illustration of the Bremsstrahlung Process *56*
Figure 31: Plot of Doserate vs. Time *58*
Figure 32: The Seed Geometry Used in the TG-43 Report *62*
Figure 33: Configuration of the GAFCHROMIC EBT2 Film *75*
Figure 34: Configuration of the Gafchromic EBT3 Film *76*
Figure 35: Photon Transport Logic *83*
Figure 36: Simplified Schematic Diagram for egs_brachy Input *87*
Figure 37: Flowchart for Measurements and Results of the I-125 Seed *89*
Figure 38: Flowchart for Measurements and Results of the "Claws" *90*
Figure 39: (a) Diagram of the 4π Chamber (b) Diagram of the I-125 Seed Measurement Insert *92*
Figure 40: The Medium Voltage Unit at Groote Schuur Hospital *92*
Figure 41: Tube Voltage Selection Options with Filters *93*
Figure 42: Comparison of Absorbed Dose Distributions in Lineal Energy Measured for the 6711 Seed and an X-Ray Field Generated by an Accelerating Potential of 70 kVp with 1.25 mm Al Filtration *93*
Figure 43: Theratron 780c Co-60 Teletherapy Unit *94*
Figure 44: Sample Calibration for an EBT2 Film *95*
Figure 45: Sample Calibration Glow Curve *96*
Figure 46: The Thin-Window NaI Detector Coupled to a PMT *97*
Figure 47: The HPGe Detector: Model GC4530 ..... *98*
Figure 48: The LEPS Detector at iThemba LABS *99*
Figure 49: Design of the Amptek Silicon Drift Detector as Shown in the Pamphlet (Amptek, 2015) *100*
Figure 50: The X-123 Silicon Drift Detector *101*
Figure 51: Solid Water Phantom with Slots for TLD Anisotropy Measurements for Different Angles at Distances of 2, 3 and 5 cm *102*
Figure 52: Solid Water Phantom with Slots for TLD Radial Dose Function Measurements *102*

Figure 53: Perspex Jig for In-Air Measurements of the Seed Spectrum *103*
Figure 54: Anisotropy Image in Gafchromic EBT2 Film (Size Reduced for Display Purposes) (left) and EBT3 Film (Cropped for Display Purposes) (right) *103*
Figure 55: Solid Water Eye Phantom for TLD Measurements in the "Claws" *110*
Figure 56: Solid Water Phantom for Gafchromic Film Measurements in the "Claws" *110*
Figure 57: Seven TLDs in the Phantom *111*
Figure 58: "Leg-to-Leg" Measurement on the Central Plane *112*
Figure 59: "Anterior-to-Posterior" Measurement *112*
Figure 60: Sup/Inf or Lateral Measurement (Cylindrical Symmetry) *112*
Figure 61: Images of the "Claws" Model *114*
Figure 62: The Ballnose Cutters used during the Manufacture of the PVC "Claws" *115*
Figure 63: Images showing the Manufacture of the PVC Legs of the "Claws" *115*
Figure 64: Images Showing the Manufacture of the PVC Ring of the "Claws" *116*
Figure 65: The Original PVC Block, the Woods Metal Insert Added for Stabilization and the Ring *116*
Figure 66: The Woods Metal Insert Used for Stabilization During the Manufacture of the Legs *116*
Figure 67: (a) PVC Legs and Ring (b) PVC "Claws" Glued Together and Loaded with Seeds *116*
Figure 68: The micro-CT scanner at Stellenbosch University: (a) the Cabinet (b) the Two X-Ray Tubes inside the Cabinet *117*
Figure 69: Various Micro-CT Projection Angles *117*
Figure 70: Image Reconstruction at 20 µm Resolution *118*
Figure 71: Severe Image Artifacts *118*
Figure 72: Sagittal View of the "Claws" at (a) 17 µm (b) 100 µm and (c) 200 µm *119*
Figure 73: 100 µm Slices of the "Claws" Shown Every 1 mm *120*
Figure 74: Image of the Monte Carlo "Claws" Model. One seed is included, but not yet in the right position or orientation. *121*
Figure 75: NCRP Report No. 58 Spectrum for I-125 ..... *123*
Figure 76: The Ends of 11 Seeds Magnified 100 Times under a Microscope *128*
Figure 77 a, b, c: Macro Photographs of the Silver Rod *128*
Figure 78: The Titanium Casing *129*
Figure 79: The OncoSeed 6711 ..... *130*
Figure 80: Trigonometry Ratios that are Positive in the Four Quadrants *133*
Figure 81: Seed Spectrum Measured with a NaI(Th) Scintillation Detector *134*
Figure 82: Seed Spectrum Measured with a HPGe Detector *135*
Figure 83: Seed Spectrum Measured with the Low-Energy Photon Spectrometer *136*
Figure 84: Seed Spectrum Measured with the Silicon Drift Detector *137*
Figure 85: The Gold Backing of the "Claws" Introduces Gold Characteristic X-Rays *138*
Figure 86: Spectral Changes at 10 mm for $\theta = 0°$ (red) vs $\theta = 90°$ (blue) *139*
Figure 87: Anisotropy in Air at r = 0.5 cm *142*
Figure 88: Anisotropy in Air at r = 1 cm *142*
Figure 89: Anisotropy in Air at r = 3 cm *142*
Figure 90: Film Density Comparison for Two Different Scanners *147*
Figure 91: Optical Density vs. Dose when Scanning in Landscape vs Portrait Orientation *148*
Figure 92: EBT2 Film Response Changes after 1 Day *148*
Figure 93: Relative Gafchromic Film Response Over Time *149*
Figure 94: Anisotropy at 0.5 cm *151*
Figure 95: Anisotropy at 1 cm *152*
Figure 96: Anisotropy at 2 cm *152*
Figure 97: Anisotropy at 3 cm *153*
Figure 98: Anisotropy at 5 cm *153*
Figure 99: Anisotropy Measured with TLDs at 2 cm *154*
Figure 100: Anisotropy Measured with TLDs at 3 cm *154*
Figure 101: Anisotropy Measured with TLDs at 5 cm *155*
Figure 102: Radial Dose Function Measured with Film (green) and TLDs (blue) *156*
Figure 103: "Leg-to-Leg" Measured Doses on the Central Plane *158*
Figure 104: Sup/Inf or Lateral Measurement on the Central Plane *158*
Figure 105: Inverted Red Channel Image and Measuring Plane of the Film *159*
Figure 106: Measurements from Leg-to-Leg on Central Plane *160*
Figure 107: Inverted Red Channel Image on the Central Plane of the "Claws" *160*
Figure 108: Measured Sup/Inf or Lateral Doses on Central Plane *161*
Figure 109: Measured Doses from Lens towards the Posterior of the Eye at 3 mm Intervals *161*

Figure 110: Dose Distribution (Anterior View) on the Central Plane at z = 0. ..... *162*
Figure 111: Dose Distribution (Anterior Views) at z = 0.5 cm, -0.5 cm, 1 cm, -1 cm (Clockwise from Top Left) *163*
Figure 112: Dose Distribution (Lateral View) on the x = 0 cm and x = 0.5 cm Planes *163*
Figure 113: Calculated Dose from Leg-to-Leg on the Central Plane *164*
Figure 114: Calculated Dose from Lens to Posterior, Normalized to 100 % at the Center *165*
Figure 115: Dose on Central Plane *165*
Figure 116: Anterior View: Dose Calculated with Point Source Model of 6711 Seed *166*
Figure 117: Transverse View: Dose Calculated with Point Source Model of 6711 Seed *166*
Figure 118: Calculated Dose from Leg-to-Leg on the Central Plane *167*
Figure 119: Calculated Dose from Lens to Posterior *167*
Figure 120: Dose Profile on Central Plane for Sup/Inf or Lateral View *168*
Figure 121: Display of the Line Sources in the BrachyVision Treatment Planning System *169*
Figure 122: Anterior View: Dose Calculated with Line Source Model of 6711 Seed *169*
Figure 123: Transverse View: Dose Calculated with Line Source Model of 6711 Seed *170*
Figure 124: Calculated Dose from Leg-to-Leg on the Central Plane *170*
Figure 125: Calculated Dose from Lens to Posterior *171*
Figure 126: Dose on Central Plane for Sup/Inf or Lateral Views *171*
Figure 127: Anterior View on the Central Plane (z=0) *172*
Figure 128: Lateral View *173*
Figure 129: "Leg-to-Leg" Doses – Monte Carlo Simulated Results *174*
Figure 130: Egs_brachy Calculated Profile from Leg-to-Leg *175*
Figure 131: Egs_brachy Calculated Profile from Lens to Posterior *175*
Figure 132: Egs_brachy Calculated Profile for Sup/Inf or Lateral Views *175*
Figure 133: Anterior View on the z = 0 Plane *176*
Figure 134: Lateral View on the X = 0 Plane *177*
Figure 135: Comparison of "Leg-to-Leg" Profiles *178*
Figure 136: Comparison of Lens-to-Posterior Doses *179*
Figure 137: Sup/Inf or Lateral Profile Comparison *179*
Figure 138: Cross-Section Through the "Claws", Showing the Recessed Seeds in the Legs *180*
Figure 139: Dose Point for the Bony Orbit Dose *182*
Figure 140: Chart for Estimating Lengths in Millimetres in an Emmetropic (Normal) Eye *183*
Figure 141: Simplified Diagram of an Eye Used at Groote Schuur Hospital *183*
Figure 142: Dose Gradient from Center of Eye to Cornea towards the Cornea on Central Axis *184*
Figure 143: TPP Planned Dose Distribution *186*
Figure 144: Egs_brachy Calculated Dose Distribution *186*

LIST OF EQUATIONS

Equation 1 a, b, c: Compton Kinematics *52*
Equation 2: Scenario 1 ..... *58*
Equation 3: Scenario 2 ..... *58*
Equation 4 ..... *58*
Equation 5: Equivalent Time *59*
Equation 6: Equivalent Time *59*
Equation 7: Determination of Treatment Time *59*
Equation 8: TG-43 Formalism *62*
Equation 9: Air Kerma Strength *63*
Equation 10: The Dose Rate Constant *64*
Equation 11: Point Source Approximation *64*
Equation 12: Line Source Approximation *64*
Equation 13: The Radial Dose Function *65*
Equation 14: Modified Sigmoid Function *65*
Equation 15: Double Exponential Function *66*
Equation 16: Fifth-Order Polynomial Fit *66*
Equation 17: Modified Fit *66*
Equation 18: The Anisotropy Function *67*
Equation 19: Temperature and Pressure Correction *91*
Equation 20: Source Strength Calculation *91*
Equation 21: Determination of Co-ordinates *104*
Equation 22: Formula for Calculating the Dose Rate Constant *107*
Equation 23: Polynomial Fit for a Monoenergetic Dose Rate Constant *107*
Equation 24: Proposed Fitting Function to Mass-Energy Absorption Coefficient of Air *108*
Equation 25: Determination of θ_1 and θ_2 ..... *131*
Equation 26: Determination of β *132*
Equation 27: Determination of the Average Energy *139*

LIST OF TABLES

Table 1: Characteristic X-Rays of Tellurium-52 ..... *41*
Table 2: Characteristic X-Rays of Silver-47 ..... *42*
Table 3: Characteristic X-Rays of Titanium-22 ..... *42*
Table 4: Relevant Characteristic X-Rays of Gold-79 ..... *42*
Table 5: I-125 Output Data *68*
Table 6: I-125 Output Data *69*
Table 7: The Radial Dose Function of the OncoSeed 6711 I-125 Seed *70*
Table 8: Anisotropy Function for the 6711 Seed *71*
Table 9: Coefficients for the Polynomial Fit of $\Lambda(E)$ *107*
Table 10: Fitting Parameters for Mass-Energy Absorption Coefficient in Air *108*
Table 11: Seed Positions in the "Claws" *109*
Table 12: Monte Carlo Transport Parameter and Cross Section Options *124*
Table 13: Measured Seed Dimensions *130*
Table 14: The Geometry Function for the OncoSeed 6711 ..... *132*
Table 15: The Normalized Geometry Function for the OncoSeed 6711 (Active Length = 2.85 mm) *133*
Table 16: Relative Intensity of Emissions *140*
Table 17: Measurement Results *143*
Table 18: Measurement Results *144*
Table 19: Dose Rate Constants for the OncoSeed 6711 ..... *146*
Table 20: Scanner Response *150*
Table 21: Comparison of Relative Doses *181*
Table 22: Lens Dose in the "Claws" *184*

CHAPTER 1 INTRODUCTION

1.1 Introduction

Ophthalmic tumors are fairly rare and diverse and their diagnosis and treatment usually requires special expertise and equipment, including patient care by a multidisciplinary team *(Singh et al., 2013).*

Brachytherapy is the placing of radioactive sources into or close to a tumour. Brachytherapy "requires significant involvement and communication among members of the physics, dosimetry and medical staff " *(Nath et al., 1997).*

The earliest paper that was found on using radiation to treat eye disease was from 1910 *(Lawson and Davidson, 1910),* where radium was applied directly to the affected part of the eye or eyelid. One earlier paper *(Manby, 1905)* described the use of 5 mg of radium bromide to treat rodent ulcer near the eye, but not in the eye or eyelid.

Early attempts at treating malignant intra-ocular neoplasms included using radon seeds *(Moore, 1930, Moore et al., 1931),* Ra-226 *(Stallard, 1948)* and Co-60 *(Stallard, 1966, Brady et al., 1982).* Ru-106 plaques were introduced in the 1960's *(Lommatzsch and Vollmar, 1966).* Ta-182 plaques were used at Groote Schuur Hospital for the treatment of retinoblastoma *(Stannard et al., 1979),* but gave high doses to the bony orbit, leading to deformation in later years *(Hering, 2019).* *(Stannard et al., 2013)* stated that the Groote Schuur Hospital oncologist Dr Sealy was the first to use I-125 on ophthalmic tumours *(Sealy et al., 1976).* Groote Schuur Hospital's first I-125 eye applicator used to be exhibited in the museum of the British Radiological Society in London *(Hering, 2019),* but it could not be ascertained whether that applicator is still there or not.

Commonly used radionuclides for intra-ocular brachytherapy include I-125, Pd-103 and Ru-106 *(Singh et al., 2013, Finger et al., 1993, Finger et al., 2002).*

Retinoblastoma is a rare primary intraocular tumour with an incidence of approximately one in 20.000 births (*Singh et al., 2013)* (one in 17.000 live births *(Moll et al., 1997)*). It is a childhood cancer and the median age at diagnosis is < 12 months for the bilateral form or 24 months for the unilateral unifocal form *(Cassoux et al., 2017).* In the United States there are about 350 cases of retinoblastoma annually, and about double that including Europe, Russia and Australia *(Chiu-Tsao et al., 2012).*

Before the beginning of the 20th century, retinoblastoma was, for all intents and purposes, a death sentence. The discovery of X-rays by Wilhelm Conrad Roentgen in 1895, as well as the discovery of radioactivity by Henri Becquerel in 1896, led to an improvement in cancer treatments. By 1949, published survival of retinoblastoma had improved to 74 % *(Reese et al., 1949).* Current 5-year survival rates in industrialized countries lie at 98 % *(Cassoux et al., 2017),* with improvements in local therapy (thermotherapy, laser application, cryotherapy or brachytherapy) and chemotherapy (particularly the use of VEC – Vincristine, Etoposide and Carboplatin, as well as Melphalan) making a huge difference in the survival figures. Unfortunately, survival rates in developing countries remain low *(Singh and Daniels, 2016, Chantada, 2011),* with some countries reporting survival rates as low as 0 – 5 %.

The American Brachytherapy Society consensus guidelines for plaque brachytherapy of uveal melanoma and retinoblastoma *(Simpson et al., 2014)* state that not all retinoblastomas are suitable for plaque brachytherapy, but that it is an effective eye- and vision-sparing method to treat patients with intra-ocular tumours.

1.2 Intraocular Brachytherapy at Groote Schuur Hospital

The low dose-rate brachytherapy programme at Groote Schuur Hospital goes back over 50 years *(Sealy et al., 1964)*; however, intraocular brachytherapy using I-125 was introduced at Groote Schuur Hospital in 1976 by the late Dr R Sealy *(Sealy et al., 1976)*. In his obituary he was described as "a world leader in the role of radiation in treating eye tumours, particularly the use of radioactive isotopes around the eye. Sealy pioneered the use of low-energy isotopes, which enabled sensitive structures to be protected." *(Abratt, 2006)*

Sealy published a number of papers on ophthalmic tumours and low dose-rate brachytherapy, amongst many others *(Sealy et al., 1976, Sealy, 1977, Sealy et al., 1980, Sealy et al., 1987, Sevel and Sealy, 1969, Sevel et al., 1973a, Sealy et al., 1964, Sevel et al., 1973b)*.

Plaque design and insertion techniques changed over the years at the hospital *(Hill et al., 1992)*. Groote Schuur Hospital is the only hospital in South Africa that uses ophthalmic plaques with I-125.

1.2.1 The Manufacturing Process

All plaques at Groote Schuur Hospital are custom made by the mould room technologists. Plaques are made of 24 carat gold (requiring a gold license), which comes in the form of a flat sheet of gold. 24 carat gold is quite soft and thus malleable. It is also non-toxic. The tumour outline is drawn by the oncologist onto a brass eyeball of an appropriate diameter (22 mm for children, 24 mm for adults and in rare cases also 20 mm or 25 mm).

Figure 1: The Brass Eyeball with the Shape of a Tumour

Figure 2: A Selection of Brass Eyeballs in use at Groote Schuur Hospital

The prescription and depth of treatment are given separately.

Proposed seed positions are drawn onto the brass eyeball by a medical physicist and read off in polar co-ordinates, which are inscribed on the brass eyeballs. The gold plaques are manufactured manually. Suture holes are drilled into the plaques for fixation in the eye. A dummy plaque made of high impact acrylic is also manufactured to test the positioning in theatre before the insertion of the radioactive plaque.

Figure 3: The Flat Gold Plate is Shaped in a Lead Mould to the Correct Curvature

Plaques usually have a wall of 1 mm height around all edges of the plaque, but some plaques have one or two of the walls removed if there is tumour involvement.

Treatment planning happens on the TheraPlan Plus Version 3.8 Build 500 (TPP) treatment planning system (TPS). Seed activities are selected by the medical physicist to match the prescription dose. Batches of 25 seeds are delivered every six weeks and it is very common to mix seeds of a number of batches during a treatment. This, of course, requires careful separation of seed activities, which happens in the mould room with a dose calibrator / activity meter. Seed activities are initially confirmed by the medical physicist, as recommended by the AAPM Low Energy Brachytherapy Source Calibration Working Group *(Butler et al., 2008)* or the "Nederlandse Commissie voor Stralingsdosimetrie" Report 20 *(Aalbers et al., 2012)*.

The TPS approximates each seed as a point source. The I-125 seed that was used until 2017 was the OncoSeed 6711 (on which this work is also based), and has since been replaced by the AgX100 seed.

The most common prescription for the treatment of ocular melanomas is 70 Gy given to the apex of the tumour over 5 days.

Seeds are manually glued onto the plaque with superglue behind lead glass.

Figure 4: (L) Lead Glass Shield **(R) Loading of a Plaque with I-125 Seeds**

Acrylic is then used to fill up the plaque. The acrylic is supplied as a two-component kit, namely a one liter bottle of Wright Cottrell "Excel Rapid Repair Liquid" and a 850 g box of "Excel Rapid Repair Material". These are mixed in the appropriate proportions to form the PMMA. The PMMA composition was given as (CH_2=C[CH_3]CO_2H) by the manufacturer *(Robertson, 2014)*. In the same communication the structure of the polymer repeating unit was given as:

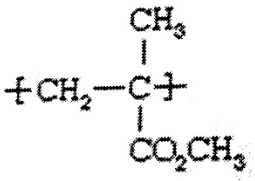

Figure 5: Structure of the Acrylic Polymer Repeating Unit

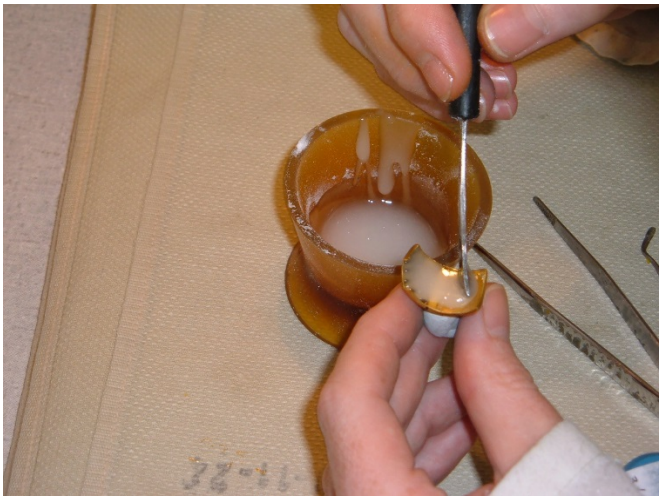

Figure 6: Filling up the Plaque with Acrylic

Once completed, the plaque is sterilized before insertion.

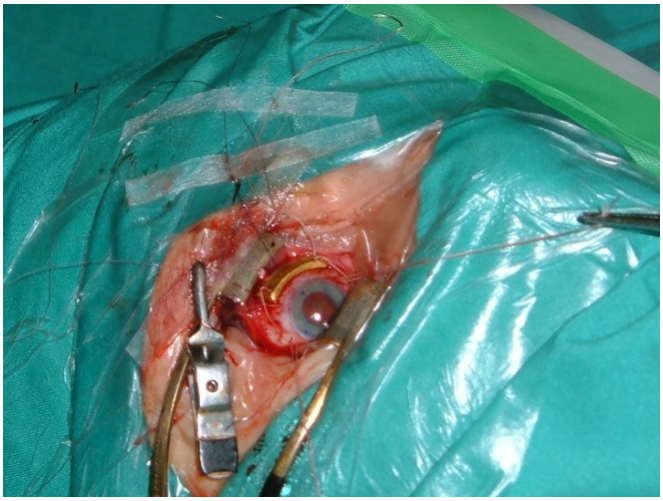

Figure 7: Insertion of a Plaque in Theatre

A removal notice is issued for the removal of the plaque.

After the removal of the plaque it is soaked in chloroform, which dissolves the acrylic and allows the seeds to be extracted and sorted. Large gold plaques can potentially be re-moulded into smaller plaques for use on other patients.

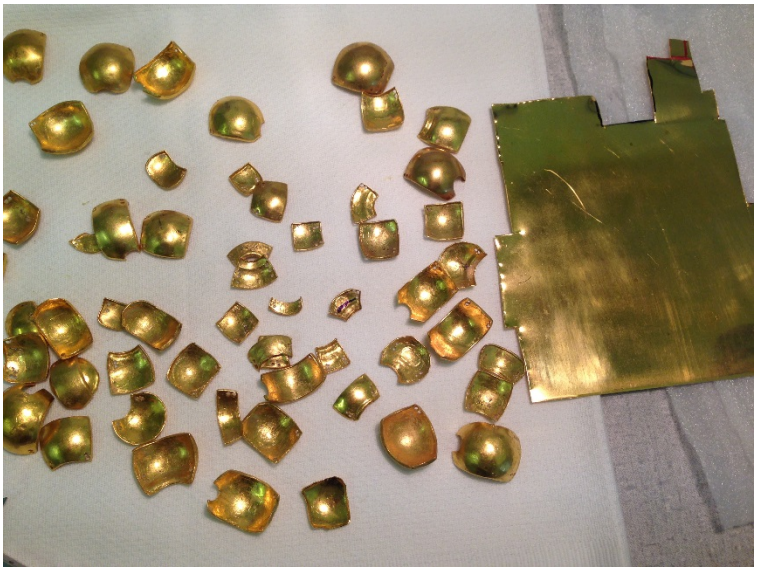

Figure 8: A Selection of Custom Gold Plaques with the Original Gold Sheet

Figure 9: Custom Plaques with a Cantilever to Allow for Placement near the Lens

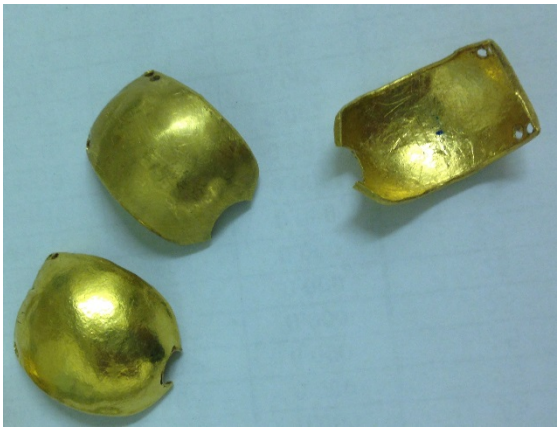

Figure 10: Plaques with a Notch for Placement around the Optic Nerve

1.2.2 The “Claws”

The “Claws” is a unique gold applicator that was designed at Groote Schuur Hospital. This is the applicator described in this thesis. It was originally built by a jeweller based on the description of Dr Sealy. It is used to treat children with retinoblastoma, who require whole eye radiotherapy. Under general anaesthesia, a pericorneal ring is attached to the four extraocular muscles, and four appendages/legs, each loaded with ^{125}I seeds, are inserted beneath the conjunctiva in-between each pair of muscles and attached anteriorly to the ring. The four legs that are now sutured onto the ring give it a claw-like appearance, hence the name for the applicator.

Figure 11: The Claws

Figure 11 (a) (b) (c)

(a) The pericorneal ring and four attachments

(b) The “Claws” with a few I-125 seeds

(c) The “Claws” loaded on a brass model of an eyeball

The “Claws” were designed in such a way that all the components of the “Claws” rest on the eyeball during treatment. The ring of the “Claws” is attached to the four extra-ocular muscles, which are situated at 12:00, 3:00, 6:00 and 9:00 o’clock. The legs are sutured onto the ring of the “Claws” in-between these muscles under the Tenon’s fascia. This is a thin membrane around the eyeball, separating it from the orbital fat. The

tenon's fascia and conjunctiva are closed over the legs, adding further stability to the implant. If the extra-ocular muscles move the eye, the "Claws" remain in position on the eyeball and will move with the eye *(Mustak, 2019, Maree, 2019)*.

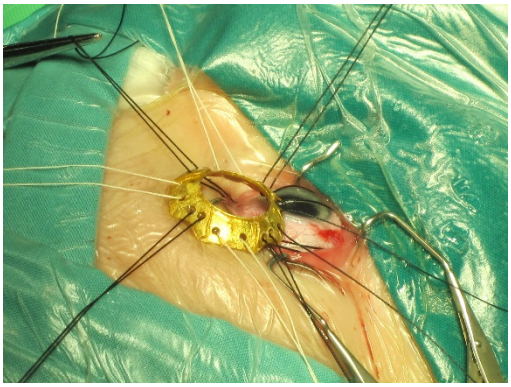

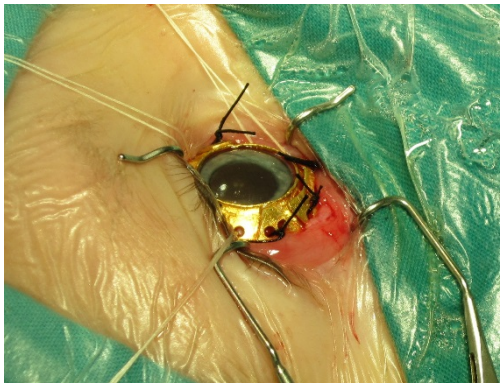

Figure 12: Positioning of the Pericorneal Ring

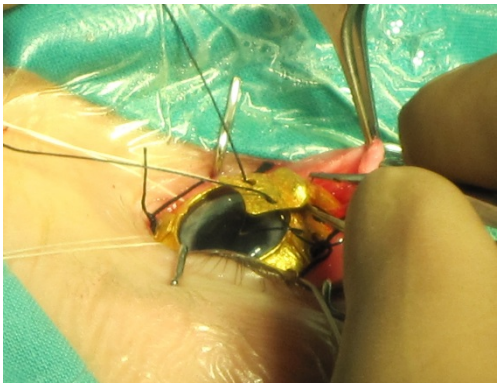

Figure 13: Insertion of one of the Legs

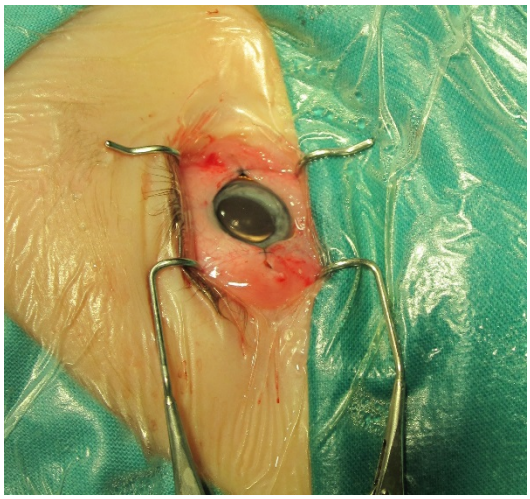

Figure 14: Nearing the End of Surgery

At the end of surgery the "Claws" are barely visible (see Figure 14).

A typical prescription for the "Claws" is 40 Gy given to the center of the eye over four days.

The applicator was designed in such a way that the dose is directed towards the middle of the eye, while sparing surrounding tissues. The tissue sparing could never be determined, because TPP cannot take any shielding into account during dose

calculations. The calculated dose for the surrounding tissues thus represents the maximum unshielded dose.

Certain seeds may be omitted to reduce the dose to an unaffected part of the eye.

General anaesthesia is also required for the removal of the applicator. The “Claws” and the I-125 seeds can be reused after sterilization. In the original “Claws” all seeds had the same activity.

The radioactive loading and implant procedures of the “Claws” are similar to those of plaques.

An X-ray of the “Claws” in-situ used to be taken for record-keeping, but this is no longer done.

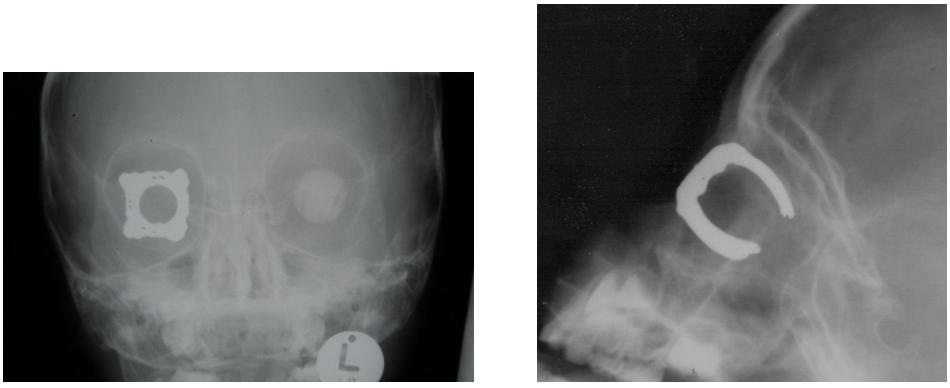

Figure 15: X-rays of the “Claws” in-situ

The eye is often left unpadded after surgery, particularly if it is the only seeing eye *(Stannard et al., 2001)*. The “Claws” are used to treat Stage 0 retinoblastoma, when the cancer is still contained in the eye (see Chapter 2.1.1 for staging).

1.2.3 Other Unusual Plaques from Groote Schuur Hospital

Other uncommon LDR brachytherapy procedures using plaques include the treatment of the lacrimal gland, where the seeds are glued to the convex side of the lacrimal gland plaque.

Figure 16: Plaque Designed to Treat the Lacrimal Gland

On the left hand side of Figure 16 is the actual gold plaque without seeds, on the right a dummy plaque that was used for dose calculations.

At one point an I-125 applicator was designed to irradiate blood vessels growing into the cornea of the eye *(Hering et al., 1989)*.

Figure 17: Applicator Designed to Irradiate Blood Vessels Growing into the Cornea

A stainless steel conjunctiva plaque was also in use for a few years, as described by *(Sealy et al., 1980)*.

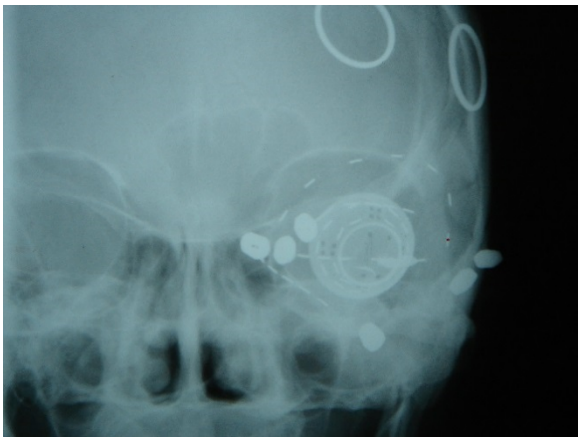

Figure 18: The Conjunctiva Plaque

Figure 19: Convex Plaque to Treat the Superior Orbital Wall

Figure 19 shows a convex plaque where the seeds were glued onto the outside of the gold to treat the superior orbital wall, when residual tumour was discovered after surgery.

Other LDR procedures using I-125 include the treatment of keloid scars, various implants in and around the eye (either with or without a prosthetic eye in situ), floor of mouth or tongue, including the use of custom applicators *(Stannard et al., 2014, Stannard et al., 2011, Stannard et al., 2004, Stannard et al., 2000, Stannard et al., 1987, Hering et al., 1977).*

One case of perianal synovial sarcoma was also treated with LDR brachytherapy at the hospital *(Tovey et al., 2017).* Implants, being flexible, require post-operative planning to determine the optimal removal time of the implant. Orbital implants are used to treat residual tumour in the eye socket after enucleation.

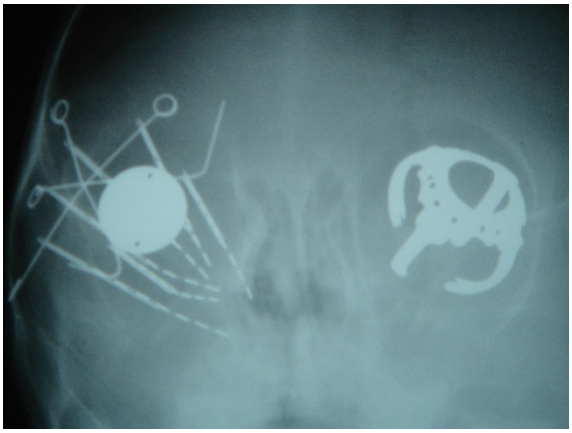

Figure 20: Patient Treated with an Orbital Implant in one Eye and the "Claws" in the other Eye to Help Preserve some Vision in that Eye.

Theraplan Plus (TPP), the current treatment planning system, can only approximate each radioactive source as a point source. This means that any anisotropic dose distribution around a radioactive seed is disregarded. As mentioned, the shielding of the gold is not taken into account at all, meaning that the dose to the critical structures in and around the eye is not determined accurately, but rather represents the maximum unshielded dose to that region. In order to address these limitations, this project was started.

As an interesting side-note, at some point the Relative Biological Effectiveness (RBE) of I-125 was investigated. Initial studies by *(Kim and Hilaris, 1975)* suggested that the RBE of I-125 "would be slightly higher than 1 and less than 1.5".

(Zeitz et al., 1977) predicted an RBE of 1.4 for I-125. Studies done at Groote Schuur Hospital suggested a value of 1.7 relative to Ta-182 by *(Hering et al., 1978),* obtained by irradiating broad bean (*Vicia faba)* roots for dose rates of about 6 cGy/hr at an

irradiation distance of 2.3 cm. A value of 1.5 was determined for I-125 using the same plant, when compared to Ir-192 *(Hering, 1980)*. A value of 1.5 was used for purposes of dose calculation at the time *(Sealy et al., 1980)*. Later on the RBE of I-125 relative to Ir-192 was determined to be 1.8 ± 0.03 at low dose rates of 40 – 80 cGy/hr *(Hering et al., 1987)*.

The use of an RBE of 1.5 and the associated reduction in physical dose was eventually discontinued, because of clinical recurrences of the cancer *(Stannard et al., 2001)*.

However, literature suggests that there may still be some work to be done in this field: *(Marchese et al., 1984)* proposed an RBE for I-125 of 1.2 relative to Cs-137 when irradiating mouse embryo cells, which did not vary with dose rate over the range 10 – 76 cGy/hr. *(Scalliet and Wambersie, 1987)* noted that RBE values of 1.15 – 1.20 are observed for high doses and high dose rates. *(Ling et al., 1995)* suggested an RBE of 1.4 for I-125 relative to Co-60 at dose rates of about 0.07 Gy/hr. *(Brenner et al., 1999)*'s work suggests an RBE for I-125 of 1.23 relative to Ir-192 and 1.37 relative to Co-60, and *(Wuu and Zaider, 1998)* predict an RBE of 1.5 relative to Co-60.

(Nath et al., 2005) wrote that "a profound dose-rate effect is observed over the dose-rate range of 6 to 20 cGy/hr" for I-125 when irradiating Chinese hamster lung cells. *(Nikjoo and Lindborg, 2010)* wrote a topical review on the RBE of low energy electrons and photons, they list an RBE of 1.16 for double strand breaks for I-125.

While an RBE of 1 is still used at Groote Schuur Hospital at this point, it may be that the question surrounding the RBE of I-125 still requires some input from the fields of micro- and nano-dosimetry *(Bug et al., 2017, Rabus, 2019)*.

1.3 Aims of the Thesis

It was always considered a weakness that the dose to critical structures could not be worked out reliably at Groote Schuur Hospital when gold plaques and “Claws” were used. This meant that the oncologists had to work with incomplete data, which is far from ideal. The project was originally proposed to determine the dose to critical structures in and around the eye during treatment with the “Claws”. It was then expanded with the following aims:

The first aim of this project was to accurately determine various dosimetric and physical characteristics of a single I-125 seed and to then compare these to published data.

Spectral measurements of the OncoSeed 6711 using various detectors were also done.

The next aim was to formalize the model of the “Claws” so that the applicator can potentially also be manufactured elsewhere.

The next aim was to describe the “Claws” dosimetrically. This was done

- Using thermoluminescent dosimeters in a solid water phantom
- Using gafchromic film in a solid water phantom
- Using treatment planning systems TheraPlan Plus and BrachyVision
- Using Monte Carlo simulations – egs_brachy

The final aim of the thesis was the comparison of measured and calculated data. The Monte Carlo simulations take into account the seed anisotropy as well as the gold shielding, therefore the relative dose to critical structures can be estimated more reliably.

In terms of hypothesis testing, these aims can be written as:

Hypothesis 1: Measured I-125 spectra will vary depending on the detector. A detector with a better energy resolution will show more detail.

Hypothesis 2: Measured dosimetric and physical characteristics of the I-125 seeds match published data

Hypothesis 3: Dose distributions inside the eye will be similar for measured data, planned data and Monte Carlo simulated data.

Hypothesis 4: Simulated doses to critical organs will be less than planned doses, because of the gold shielding of the applicator

Hypotheses 1 & 2 are specific to the OncoSeed 6711, while hypotheses 3 & 4 refer to the “Claws”.

CHAPTER 2 LITERATURE REVIEW

2.1 Retinoblastoma

Retinoblastoma is a rare retinal tumour. It is an infancy and childhood cancer and can appear unilaterally or bilaterally *(Cassady and Abramson, 1993)*. Approximately one-third of cases carry a hereditary genetic defect associated with retinoblastoma. These carriers are at an increased risk for second malignancies and about 25 % of hereditary retinoblastoma survivors die of a second cancer by age 50 *(Singh et al., 2013)*.

2.1.1 Classification of Retinoblastoma used at Groote Schuur Hospital

The initial Reese-Ellsworth group classification for retinoblastoma was first published in 1963 *(Reese and Ellsworth, 1963)*, with several recommendations for revisions since *(Ellsworth, 1969, De Sutter et al., 1987a, De Sutter et al., 1987b, Rosengren et al., 1989, Grabowski and Abramson, 1987, Pratt et al., 1997)*.

The intraocular group classification of Stage 0 retinoblastoma that is used at Groote Schuur Hospital is based on a paper by *(Murphree, 2005)*.

In the paper five groups are proposed, based on risk:

“Group A - Very low risk: Eyes with small discrete tumors away from critical structures. All tumors are 3 mm or smaller, confined to the retina, and located at least 3 mm from the foveola and 1.5 mm from the optic nerve. No vitreous or subretinal seeding is allowed.

Group B – Low risk: Eyes with no vitreous or subretinal seeding and discrete retinal tumor of any size or location. Retinal tumors may be of any size or location not in Group A. No vitreous or subretinal seeding allowed. A small cuff of subretinal fluid extending no more than 5 mm form the base of the tumor is allowed.

Group C – Moderate risk: Eyes with only focal vitreous or subretinal seeding and discrete retinal tumors of any size and location. Any seeding must be local, fine, and limited so as to be theoretically treatable with a radioactive plaque. Retinal tumors are discrete and of any size and location. Up to one quadrant of subretinal fluid may be present.

Group D – High risk: Eyes with diffuse vitreous or subretinal seeding and/or massive, nondiscrete endophytic or exophytic disease. Eyes with more extensive seeding than Group C. Massive and/or diffuse intraocular disseminated disease may consist of fine or „greasy" vitreous seeding or avascular masses. Subretinal seeding may be plaque-like. Includes exophytic disease and more than one quadrant of retinal detachment.

Group E – Very high risk with any one or more of the following: Eyes that have been destroyed anatomically or functionally by the tumor. Eyes with one or more of the following: irreversible neovascular glaucoma, massive intraocular hemorrhage, aseptic orbital cellulitis, tumor anterior to anterior vitreous face, tumor touching the lens, diffuse infiltrating retinoblastoma, phthisis or pre-phthisis."

2.1.2 Treatment of Retinoblastoma

(Stannard et al., 2013) describe various treatment options for retinoblastomas, ranging from transpupillary thermotherapy or cryotherapy with or without chemotherapy for group A and B eyes, to treatment with I-125 or Ru-106 plaques for group C eyes. Radiotherapy to the whole eye may be needed for some group C eyes and most group D eyes, if other methods fail (systemic, intraarterial or intravitreal chemotherapy).

External beam radiotherapy using photons, electrons or protons can be used for whole-eye radiotherapy. *(Buchgeister et al., 2007)* developed a fixation aid for aligning the eye for external beam radiotherapy, which was used on 50 patients in Germany between

2003 and 2006. External beam radiotherapy continues to play an important role in the treatment of extrascleral and intraneural extension of retinoblastoma *(Finger, 2009).*

Despite the relatively low mortality rate from retinoblastoma in industrialized countries (98 % according to *(Cassoux et al., 2017)*), approximately a quarter of hereditary retinoblastoma survivors die of a second cancer by age 50 years *(Yu et al., 2009).* As such, radiotherapy has to a large degree been replaced by upfront chemotherapy in patients with early stage disease. However, radiotherapy remains important in cases of advanced disease *(Singh et al., 2013).*

The "Claws", the applicator described in this work, is another approach for radiotherapy, with local control and retention of vision in 85 % of 13 group A-C eyes and a local control rate of 58 % in 38 group D eyes with eye retention in 39 % (see Chapter 2.1.1 for classification description). The "Claws" result in good long-term cosmesis and there is no recorded incidence of a second non-ocular malignancy *(Stannard et al., 2013).*

2.2 Various Types of I-125 Seeds

I-125 is commonly used in the treatment of ophthalmic tumours. A number of manufacturers supply these seeds, which vary somewhat in design.

The I-125 seeds with selected references include:

Amersham, EchoSeed, 6733 *(Sowards and Meigooni, 2002b, Meigooni et al., 2002a)*

Amersham, OncoSeed, 6702 *(Williamson and Quintero, 1988, Williamson, 1988, Williamson, 1991)*

Amersham, OncoSeed, 6711 – discussed in more detail in Chapter 2.3, as this is the seed used in the "Claws"

Amersham, ThinSeed, 9011 *(Kennedy et al., 2010)*

BEBIG GmbH (Eckert & Ziegler), IsoSeed, I25.S17 *(Lymperopoulou et al., 2005, Pantelis et al., 2006, Moutsatsos et al., 2014)*

BEBIG GmbH (Eckert & Ziegler), IsoSeed, I25.S06 *(Hedtjärn et al., 2000, Patel et al., 2001)*

Bacon Co., Argentina, Braquibac™ *(Pirchio et al., 2007)*

Best Industries, Best I-125, 2301 *(Sowards and Meigooni, 2002a, Meigooni et al., 2000, Nath and Yue, 2002, Heintz et al., 2001)*

DraxImage Inc./Cytogen, BrachySeed, LS-1 *(Williamson, 2002, Wang and Sloboda, 2002, Chan and Prestwich, 2002, Nath and Yue, 2001)*

IBt, InterSource, 1251L *(Meigooni et al., 2002c, Reniers et al., 2001)*

Ibt-Bebig, SmartSeed *(Abboud et al., 2010)*

Imagyn, IsoStar, IS-12501 *(Gearheart et al., 2000, Nath and Yue, 2000, Ibbott and Nath, 2001, Ibbott et al., 2002)*

Implant Sciences, I-Plant, 3500 *(Duggan and Johnson, 2001, Rivard, 2002, Duggan, 2004, Wallace, 2002)*

IsoAid, Advantage, IA1-125A *(Meigooni et al., 2002b) (Solberg et al., 2002)*

Core Oncology Inc. (formerly: Mills Bio. Pharm.), ProstaSeed, 125SL/SH *(Wallace, 2000, Li, 2002)*

Brachytherapy Services, Prospara, Med3631 *(Wallace and Fan, 1998, Rivard, 2001, Li et al., 2000, Wallace and Fan, 1999)*

Nucletron/Elekta, SelectSeed, 130.002 *(Karaiskos et al., 2001, Anagnostopoulos et al., 2002, Papagiannis et al., 2006)*

Source Tech Medical Model STM1251 *(Kirov and Williamson, 2001, Li and Williamson, 2002)*, also under Bard Urological Division

Syncor, PharmaSeed, BT-125 *(Popescu et al., 2000, Solberg et al., 2002)*

Theragenics, AgX100 *(Chen et al., 2012, Mourtada et al., 2012)*

The Carleton Laboratory for Radiotherapy Physics (CLRP) houses a database of brachytherapy seed dosimetry parameters.

(http://www.physics.carleton.ca/clrp/seed_database).

Another invaluable source of information on brachytherapy seeds is housed at http://rpc.mdanderson.org/rpc/brachyseeds/source_registry.htm, which is the joint AAPM/IROC Houston registry of brachytherapy sources.

The Universitat de València also houses a database of dosimetry parameters for source models used in brachytherapy at https://www.uv.es/braphyqs/ .

2.3 The OncoSeed 6711 Seed

The OncoSeed 6711 seeds were the seeds of choice for many years at Groote Schuur Hospital. The silver marker shows up on X-rays and can be used to help identify seeds in implants. The apparent activity of the seeds when they are delivered every six weeks is around 5 mCi, which, based on personal experience, is already on the "hot" side for many plaques and implants if those activity seeds were to be used exclusively; therefore, seeds from different batches are commonly used when designing a plaque or implant. It should be pointed out here that the use of "apparent activity" is generally considered obsolete *(Williamson et al., 1999)* and is not recommended, but seems to be a quantity that is preferred at Groote Schuur Hospital for historic reasons. However, the conversion to and from air-kerma strength is given by a single factor. An apparent activity of 5.20 mCi for the OncoSeed 6711 corresponds to air kerma strength of 6.60 μGym^2h^{-1} .

The package insert of the OncoSeed IMC6711 seed *(OncoSeed™, 2005)* describes the seed as follows: “Iodine-125 is adsorbed onto a silver rod and encapsulated in a welded titanium capsule. The silver rod acts as an X-ray marker.”

The dimensions of the silver rod are given as 3.0 mm long with a diameter of 0.5 mm, housed in a titanium capsule with a 0.8 mm diameter and a length of 4.5 mm, see Figure 21 below:

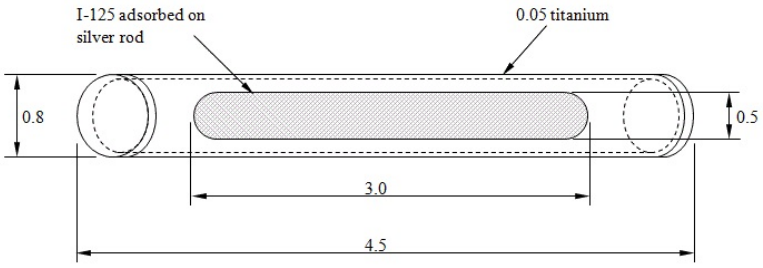

Figure 21: Seed Dimensions as Provided by the Supplier

The seed was originally introduced in 1983 *(Dolan et al., 2006)* and has been described extensively in literature *(Kubo, 1985b, Kubo, 1985a, Ling et al., 1985, Williamson, 1988, Williamson and Quintero, 1988, Weaver et al., 1989, Chiu-Tsao et al., 1990, Sloboda and Menon, 2000, Weaver, 1998, Nath et al., 1990, Nath et al., 1997, Luxton et al., 1990, Rivard et al., 2004, Dolan et al., 2006, Williamson, 1991).*

(Dolan et al., 2006) carefully examined a number of seeds and came to the following conclusions:

“The source consists of a beveled right circular cylinder of silver coated with a radioactive layer and encased inside a cylindrically symmetric titanium shell.” The radioactive layer is a 2.5:1 molecular ratio mixture of AgBr and AgI and was estimated to be between 1 – 3 µm thick. Seed dimensions were slightly adjusted from those of the package insert and are given in Figure 22.

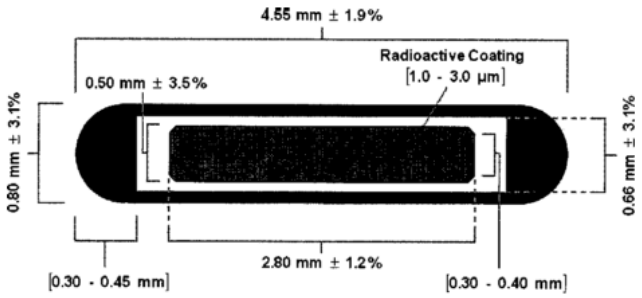

Figure 22: Seed Dimensions According to *(Dolan et al., 2006)*

Interestingly, the source wire shows bevelling, which until 2006 had been ignored. *(Dolan et al., 2006)* observed the beveling angle to be 45 ° ± 10 %.

I-125 has a half-life of 59.43 days and decays by electron capture via the excited level of 35.5 keV of Te-125 into the ground state of Te-125. A number of characteristic X-rays and Auger electrons are emitted. The iodine in the seed is adsorbed onto a silver rod and encapsulated in a welded titanium capsule. The electrons are absorbed by the titanium wall of the I-125 seed.

Relevant characteristic X-ray energies in the OncoSeed 6711 are given in the following tables:

Tellurium - 52	Energy [keV]	Relative Probability
$K\alpha_2$	27.202	54
$K\alpha_1$	27.472	100
$K\beta_3$	30.944	28.6
$K\beta_1$	30.996	
$K\beta_5$	31.236	
$K\beta_2$	31.700	6.2
$K\beta_4$	31.774	
$KO_{2,3}$	31.812	

Table 1: Characteristic X-Rays of Tellurium-52

Silver - 47	Energy [keV]	Relative Probability
$K\alpha_2$	21.990	53
$K\alpha_1$	22.163	100
$K\beta_3$	24.912	27.7
$K\beta_1$	24.942	
$K\beta_5$	25.145	
$K\beta_2$	25.456	4.8
$K\beta_4$	25.512	

Table 2: Characteristic X-Rays of Silver-47

Titanium – 22	Energy [keV]	Relative Probability
$K\alpha_1$	4.511	100
$K\alpha_2$	4.504	50
$K\beta_{1,3}$	4.932	15

Table 3: Characteristic X-Rays of Titanium-22

Additionally, since the seeds are glued onto a gold backing, the following energies correspond to the gold L-shell characteristic X-rays:

Gold – 79	Energy [keV]	Relative Probability
$L\alpha_1$	9.713	100
$L\alpha_2$	9.628	11
$L\beta_1$	11.442	67
$L\beta_2$	11.585	23
$L\gamma_1$	13.382	13

Table 4: Relevant Characteristic X-Rays of Gold-79

The I-125 decay data was obtained from the website of the Laboratoire National Henri Becquerel (http://www.nucleide.org/DDEP_WG/DDEPdata.htm), last updated on 20 October 2017. Characteristic X-ray wavelengths can also be obtained from *(Bearden, 1967)* or *(Bearden and Burr, 1967)* or online from the Lawrence Berkeley National Laboratory X-ray data booklet at http://xdb.lbl.gov/.

The OncoSeed 6711 was available for purchase through AEC Amersham. The gold material of the "Claws" effectively shields the low-energy gamma ray and X-rays. This is one aspect that will be clearly shown in the Monte Carlo simulations in the "Results" chapter, as opposed to conventional treatment planning system dose calculations, which cannot take into account the gold shielding. Seed dimensions are small and thus the seeds are suitable to be used in various plaques, applicators and implants. The seeds can be used repeatedly, allowing for cost-effective treatment.

2.4 Various Types of I-125 Plaques

Eye sparing treatment with brachytherapy yields excellent local control *(Binder et al., 2016)*. The Collaborative Ocular Melanoma Study (COMS) is the largest and arguably the best known study that compared the efficacy of plaque brachytherapy for moderately large (3 – 8 mm height) tumours versus enucleation.

(https://clinicaltrials.gov/ct2/show/NCT00000124)

The study started in November 1986 and enrollment completed in July 1998 with 1317 patients enrolled. The study was conducted in 43 clinical centers in the United States and Canada and there are numerous publications on this trial *(Diener-West et al., 2001a, John et al., 2001, Earle et al., 1987, COMS, 1993, Wells et al., 1996, Hawkins and Melia, 1997, Grossniklaus et al., 1997, COMS, 1997, Albert et al., 1998, Moy and Melia, 1999, Melia et al., 2001, Willson et al., 2001, Moy et al., 2001, Diener-West et al., 2001b, Byrne et al., 2002, Margo, 2004, COMS, 2004)*, to name a few. The study showed that for medium sized choroidal melanomas there was no survival benefit between enucleation or brachytherapy and that eye plaque treatment is effective. The plaques that were used in this study became known as COMS plaques. The COMS standard plaques have diameters of 10 mm, 12 mm, 14 mm, 16 mm, 18 mm, 20 mm

and 22 mm respectively. They are circular in design, but could also be notched for treatment in the vicinity of the optic nerve. They are gold plaques with a Silastic seed carrier insert. The plaques have 5, 8, 13, 13, 21, 24 and 21 seed slots respectively.

Figure 23: Various COMS Standard and Notched Eye Plaques (Images used from www.eyephysics.com, used with permission)

COMS adopted the revised dose rate constant for the 6711 seed, based on the TG-43 protocol, but still used the point source approximation for their dose calculation. They

also disregarded the influence of the Silastic insert, the gold backing and any collimation from the lip of the plaque.

When the dosimetry was re-evaluated *(Krintz et al., 2003),* the incorporation of the seed anisotropy, the line source approximation, the Silastic transmission and gold shield attenuation resulted in dose reductions of 7 – 21 % to structures of interest in the eye. *(Astrahan, 2005)* concluded that it was both possible and practical to do treatment planning for COMS eye plaques that takes into account extra-ocular air, gold and the Silastic carrier. The AAPM and ABS formed a task group (Task Group 129) that published a report on the dosimetry of COMS eye plaques in 2012 *(Chiu-Tsao et al., 2012).* They found that a commonly used prescription of 85 Gy at 5 mm depth in a homogeneous medium delivered only about 75 Gy for I-125 when accounting for COMS plaque heterogeneities, which is a difference of more than 10 %.

Traeshel and BEBIG both manufacture these types of plaques. Radiochromic film has been used to study these plaques *(Acar et al., 2013)* and modifications to the plaque design have been published *(Astrahan et al., 2005).*

When the Silastic insert was not in use, it was more difficult to localize the seeds, but a simple solution was proposed by *(Emery and Szechter, 1998).* Seeds were initially affixed to a plaque with a very thin layer of dental acrylic. A magnified photocopy image of the plaque was taken and the Y and Z coordinates of each seed were then measured with a metal ruler or caliper. The X-coordinate could be worked out if the plaque radius of curvature was known. It is not clear how often this technique was used in practice.

The ROPES plaque (Radiation Oncology Physics and Engineering Services, Australia) consists of an acrylic insert with holes to place I-125 seeds, as well as a stainless steel backing *(Granero et al., 2004).*

Figure 24: The ROPES Plaques (Images from www.eyephysics.com, used with permission)

The creator of the Australian ROPES plaques has passed away; it is not known to the author if these plaques are currently available.

Eye Physics, LLC created and updated their own set of Eye Physics plaques *(Astrahan et al., 1997)* and designed the Plaque Simulator *(Astrahan et al., 1990a, Astrahan et al., 1990b)*, a commercially available treatment planning system sold by Bebig at one point. The Eye Physics plaques are thinner than the COMS plaques and thus move the seeds physically closer to the eye. The plaques use a slotted design, with gold collimating

edges absorbing much of the shallow angle dose of each seed. All Eye Physics (EP) plaques intentionally use source dosimetric characteristics to their best advantage. Source anisotropy determines seed locations, groupings and orientations within the plaques and wasted radiation is collimated away because each radiation source is individually collimated into a "fan-beam". The dosimetric difference between Eye Physics and COMS plaques and other home-made plaques is analogous to external beam use of multi-leaf collimators vs simple rectangular fields *(Astrahan, 2019, personal communication).*

The second generation Eye Physics plaques were manually prototyped in wax from 1984 - 2010. The current third generation Eye Physics plaques are prototyped using stereolithography 3D printing in a special direct casting resin. The prototypes are then converted to 18K gold using lost-wax casting *(Astrahan, 2019).*

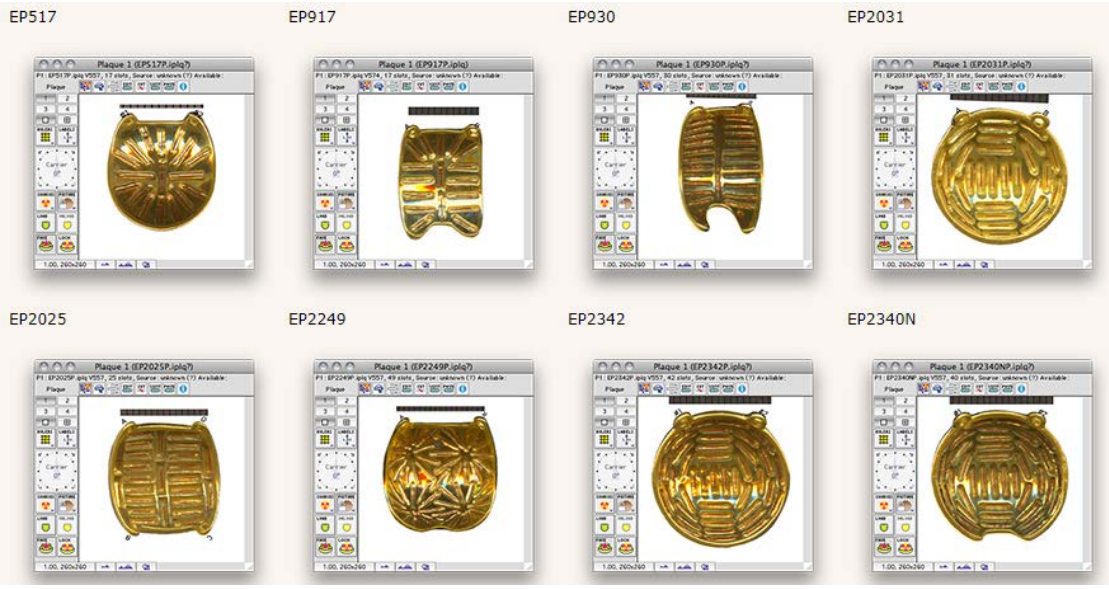

Figure 25: A Number of Eye Physics Plaques (Image from www.eyephysics.com, used with permission)

Finger's slotted eye plaque *(Finger, 2007)* was a plaque with variable length slots to accommodate the optic nerve during treatment of circumpapillary and juxtapapillary intraocular tumours.

The "Nag" eye plaques were 18k gold plaques of 0.6 mm thickness, loaded with I-125 seeds, custom made in various shapes and sizes to encompass the tumour base with an added margin of 1 mm *(Nag et al., 2003).*

The main difference between Groote Schuur Hospital's "Claws" and other plaques is that the "Claws" are used for whole-eye radiotherapy and also treat vitreous seeding in the eye, while other plaques are used for localized treatment within the eye and treat a single tumour only.

2.5 Radiation Interactions

2.5.1 Photon Interactions

In radiation oncology ionizing radiation is used to damage and kill cells.

The overall process of attenuation (the combination of absorption and scatter) results from several different interactions of photons with atoms. The photons that do not interact are transmitted.

2.5.1.1 Coherent Scatter

Coherent scatter refers to interactions where the photon undergoes a change in direction, but not a change in wavelength or energy. No ionization occurs with coherent scattering. There are two types of coherent scattering: Thomson scattering and Rayleigh scattering.

Rayleigh scattering is the elastic scattering of a photon off an entire atom. This mechanism is likely to occur only for very low-energy photons. In Rayleigh scattering, incoming photons are absorbed by the atom's electrons. The electrons are not raised to higher orbits, but vibrate instead. They vibrate with the same frequency and phase as the incoming electromagnetic wave. The excess energy is immediately emitted in the form of photons. The new photons have the same energy and phase as the incoming photons, but are scattered in different directions *(Curry et al., 1990)*.

Thomson scattering is the elastic scattering of a photon by a free charged particle. It is the low-energy limit of Compton scattering, described in Chapter 2.5.1.3.

Coherent scatter is an interaction that needs to be considered at the low energies of the I-125 radioactive decay. Although no energy is lost in coherent scatter (and thus no dose is deposited), it adds to the attenuation coefficient. The photon scattering angle depends on the atomic number of the medium, as well as the initial photon energy.

Lower energies tend to have larger scattering angles *(Attix, 1986)*. It was also taken into account for the Monte Carlo simulations in this work.

2.5.1.2 Photoelectric Effect

In the photoelectric effect, an incoming high-energy photon interacts with a tightly bound inner orbit electron and transfers all its energy to the electron, which is ejected from the atom. The ejected electron is known as a photoelectron and the kinetic energy of the photoelectron is equal to the incident photon energy minus the binding energy of the orbital electron. The atom is left with a positive charge. Immediately an electron from an outer shell fills the hole, bringing the atom closer to its ground state. An L shell electron may fill the K shell, and then an M shell electron may fill the K shell. Ultimately a free electron will neutralize the atom. When these electrons fall to lower orbits, photons are produced. The energy of each photon equals the energy difference between the electron shell levels through which the electrons fall. These energy differences are characteristic for each element and are thus known as characteristic radiation *(Stanton and Stinson, 1996)*.

An electron cascade does not always result in the production of characteristic X-rays. A competing process, particularly for low Z elements, is Auger electron emission. The ejection of an Auger electron can be explained in a two-step process. In the first step, the energy needed to eject the Auger electron comes from the de-excitation of another electron from an outer to an inner orbit. The de-excitation energy is transferred to another electron in the atom. If the energy is greater than the binding energy of this electron, it will be ejected from the atom and is referred to as an Auger electron. Excess energy is transformed into kinetic energy of the Auger electron *(Bushberg et al., 2003)*. The probability of the photoelectric effect depends on both the energy of the incoming photon (E) and the atomic number (Z) of the material.

Probability of photoelectric interaction $\approx \frac{Z^3}{E^3}$

This means that the higher the atomic number of a material the more likely the interaction, but the higher the energy of the incoming photon the less likely the interaction *(Stanton and Stinson, 1996)*. The low-energy photons of I-125 deposit their energy in tissues primarily by the photoelectric effect *(Huang et al., 1990)*.

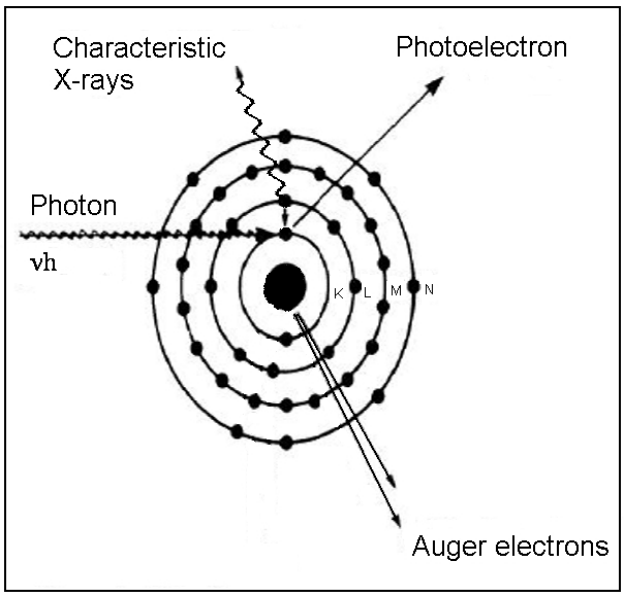

Figure 26: ***The Photoelectric Effect – An Incoming Photon Results in the Ejection of a Photoelectron. Characteristic Radiation or Auger Electrons are Emitted.***

2.5.1.3 Compton Scatter

In Compton scattering, a relatively high-energy photon interacts with a loosely bound electron in an atom's outer shell. Some of the energy of the incoming photon knocks the electron out of the atom, leaving behind a positively charged ion. The remaining energy emerges as a new photon with reduced energy and a change in direction *(Compton, 1923)*.

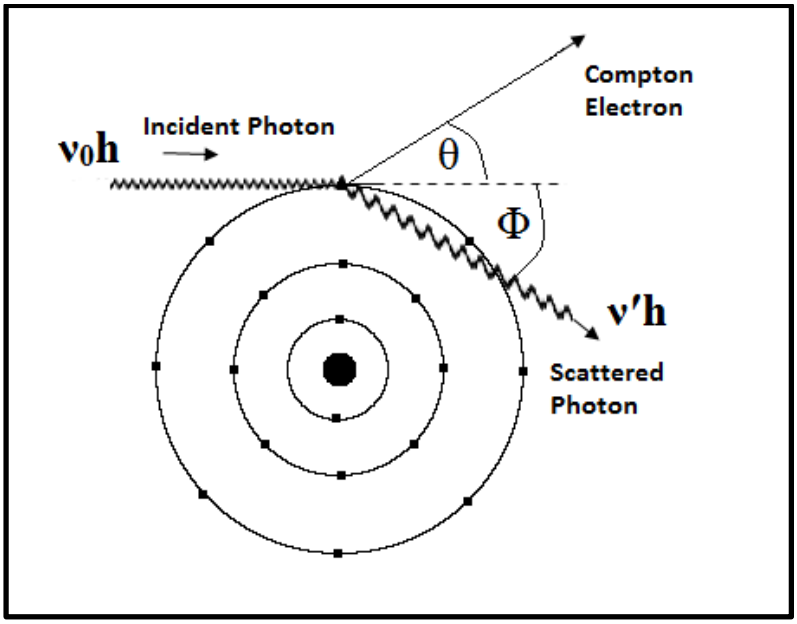

Figure 27: Compton Scatter

By applying the laws of conservation of energy and momentum, the following relationships can be derived *(Marmier and Sheldon, 1969)*:

$$E = h\nu_o \cdot \frac{\alpha \cdot (1-\cos\Phi)}{1+\alpha \cdot (1-\cos\Phi)}; \quad h\nu' = \frac{h\nu_o}{1+\alpha \cdot (1-\cos\Phi)}; \qquad \cot\theta = (1+\alpha)\cdot\tan\frac{\Phi}{2}$$

Equation 1 a, b, c: Compton Kinematics

where $h\nu_o$, $h\nu'$ and E are the energies of the incident photon, scattered photon and electron respectively and θ and Φ are the angles as indicated on Figure 27.

$\alpha = h\nu_o/m_oc^2$ where m_oc^2 is the rest energy of the electron (0.511 MeV)

2.5.1.4 Pair Production & Photonuclear Interactions

Pair production is only possible at energies > 1.022 MeV and photonuclear interactions only become relevant at even higher energies. The gamma energy of the radioactive decay of I-125 is 35.5 keV, therefore these interactions are not relevant for this thesis and will thus not be described.

2.5.1.5 Relative Importance of Photon Interactions

The various processes of photon attenuation can now be considered by examining the effects of photon energy and atomic mass number Z of the absorber on their relative importance. Figure 28 shows the proportion of the various interactions. Data was taken from *(Berger et al., 1998)* and plotted in MS Excel. The lines in the figure indicate the values of the photon energy and Z where the probabilities of occurrence of two major processes are equal.

It can be clearly seen that at energies < 0.1 MeV in water ($Z_{eff}(H_2O)$ = 7.42) *(Jayachandran, 1971)* the photoelectric effect is relatively important, but Compton scatter also needs to be considered.

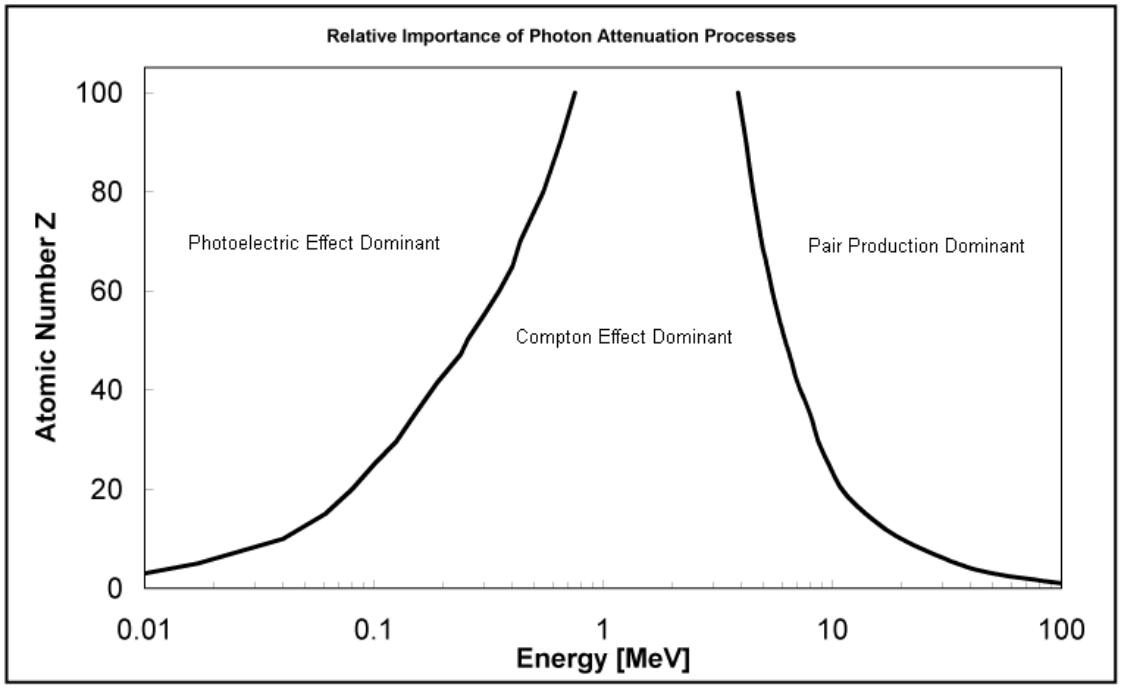

Figure 28: ***Relative Importance of Photon Attenuation Processes***

(Data from XCOM: Photon Cross Sections Database: http://physics.nist.gov/cgi-bin/Xcom/xcom3_1 *(Berger et al., 1998)* - interpolated in MS Excel)

Photon cross-section data can be obtained interactively at an updated website (https://physics.nist.gov/PhysRefData/Xcom/html/xcom1.html), in which materials can

be identified by element, compound or mixture, over the energy range 0.001 MeV – 100000 MeV.

For example, for hydrogen only 6.387 % of photon interactions at 10 keV are coherent scatter, while for carbon this fraction is 6.826 % and for gold the fraction is 4.096 %.

At 20 keV the percentage of coherent scattering interactions drops to 1.810 % for hydrogen, 1.688 % for carbon and 2.845 % for gold.

Figure 29 shows the relative importance of coherent scatter, incoherent scatter and the photoelectric effect for water (H_2O) and gold for an energy range of 1 keV – 30 keV, as obtained from the XCOM database. The photoelectric effect dominates all interactions in this energy range.

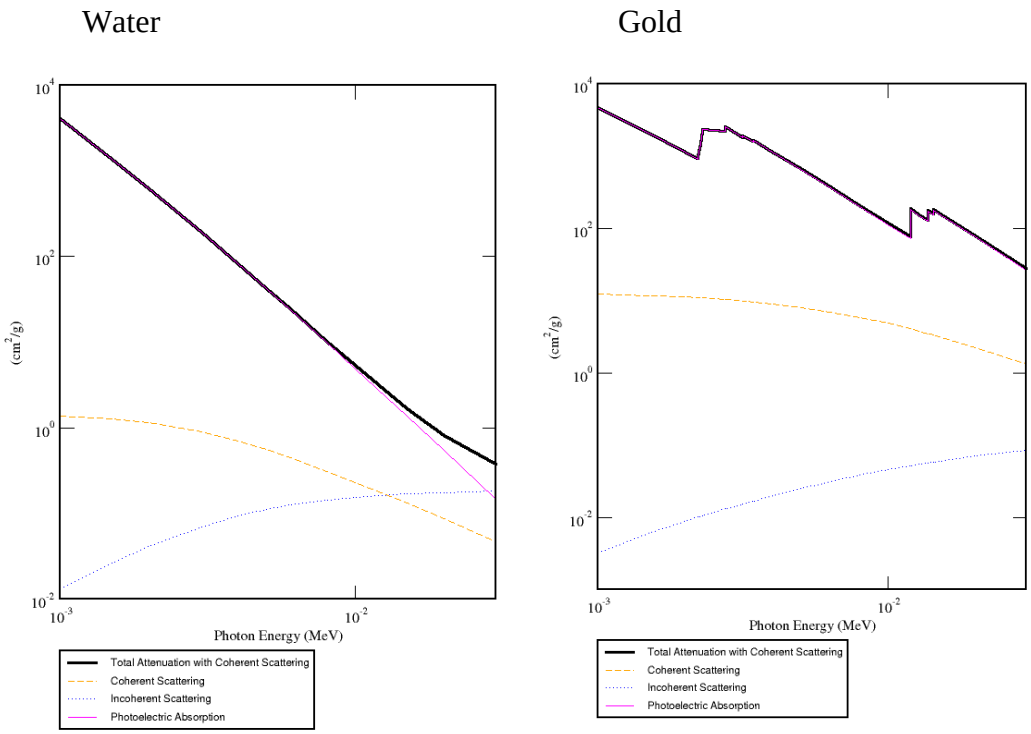

Figure 29: Relative Importance of Photon Interactions in Water (Left) and Gold (Right)

2.5.2 Electron Interactions with Matter

There are two broad classes of these electron interactions – **collision interactions** with subsequent characteristic radiation production and **radiative interactions**, which produce bremsstrahlung radiation *(Klevenhagen, 1985, Stanton and Stinson, 1996)*.

The fundamental difference is that the collisional losses involve the outer atomic electrons while the radiative losses involve the atomic nucleus *(Klevenhagen, 1985)*.

2.5.2.1 Collision Interactions

In collision interactions electrons interact with electrons in the target and transfer energy and momentum like balls on a pool table. These collisions can either be elastic, i.e. energy and momentum are conserved, or inelastic, in which momentum is conserved but kinetic energy is not conserved. Different amounts of energy are exchanged in collisions. Excitation is the transfer of some of the incident particle's energy to electrons in the target material, promoting them to higher energy levels. Ionization occurs if enough energy is given to the electron to remove it from the atom. This can then result in the formation of characteristic X-rays or Auger electrons *(Stanton and Stinson, 1996)*.

Collisional losses can also be described in terms of the ratio of the distance from the nucleus that the electron travels at ("impact parameter") and the classical atomic radius *(Attix, 1986)*. Soft collisional losses occur when this distance is much greater that the atomic radius, and they account for about half of the energy transferred to the absorbing medium *(Attix, 1986)*. Hard collisions occur when the distance of approach of the electron is roughly equal to the atomic radius. It becomes more likely that the incident electron will interact with a single electron, which can be ejected with considerable energy.

2.5.2.2 Radiative Interactions (Bremsstrahlung)

Sometimes an electron interacts with the positive charge (Coulomb field) of an atomic nucleus. This can happen when the distance of approach (impact parameter) is much less than the atomic radius *(Attix, 1986)*. The electron may interact with the electromagnetic field of the atomic nucleus resulting in radiative losses. This process is called bremsstrahlung, which is German for "braking radiation".

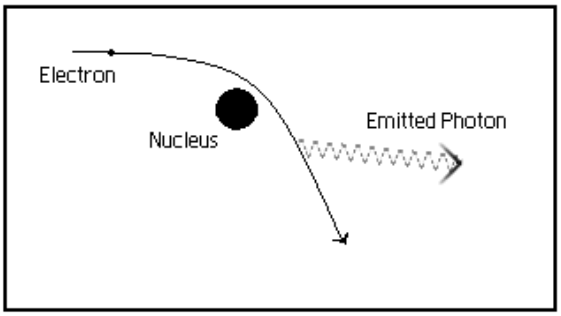

Figure 30: ***Illustration of the Bremsstrahlung Process***

In this case the electric field of the nucleus exerts a force on the incoming electron and causes it to change its direction and velocity. This in turn corresponds to a loss in the kinetic energy of the electron, and by the law of conservation of energy this energy shows up as an X-ray photon with energy equal to the energy loss of the electron *(Stanton and Stinson, 1996)*.

In bremsstrahlung the maximum energy of the X-rays equals the kinetic energy of the incoming electrons. This occurs when all of the incoming electrons' kinetic energy is transformed into the resulting X-ray. Bremsstrahlung production is the dominant energy-loss process at high energies and collisional losses are more significant at low energies. Bremsstrahlung has a differential atomic cross section proportional to Z^2 *(Attix, 1986)*.

The radiation yield, that is the fraction of electron energy converted into bremsstrahlung, was looked up for water and gold at 35 keV in *(Berger and Seltzer,*

1982): for water the radiation yield is 0.0002599 and for gold it is 0.004117, around 15 times higher than for water.

Since the gamma energy of the I-125 decay is at 35.5 keV, the maximum energy of any released electrons cannot be larger than 35.5 keV. As a point of interest, the range of a 35 keV electron was looked up in *(Berger and Seltzer, 1982)*.

The range of electrons released at 35 keV is 0.02 mm in liquid water and 0.003 mm in gold *(Berger and Seltzer, 1982)* and the range decreases with a decrease in energy. The gold of the plaque is 0.5 mm thick, so no electrons will traverse the gold.

With such a short range, any charged particle energy deposition can be assumed to be local, even with voxel sizes of 0.1 mm x 0.1 mm x 0.1 mm, as used in the Monte Carlo simulations in this work.

2.6 Calculation of the Treatment Time

I-125 decays with a halflife of 59.43 days or 1426.32 hours. This means that over the course of a four or five day treatment, the dose rate will decrease.

For example, if the prescription is 40 Gy to the center of the eye over 4 days, this corresponds to a dose rate of 41.67 cGy/hour at that point, if there were no radioactive decay. However, because there is radioactive decay, the initial dose rate will have to be slightly higher for the same treatment over 4 days.

We can work out T_{eq}, the equivalent time, which is the time that the applicator would have to be in-situ at the higher initial dose rate, if there were no radioactive decay.

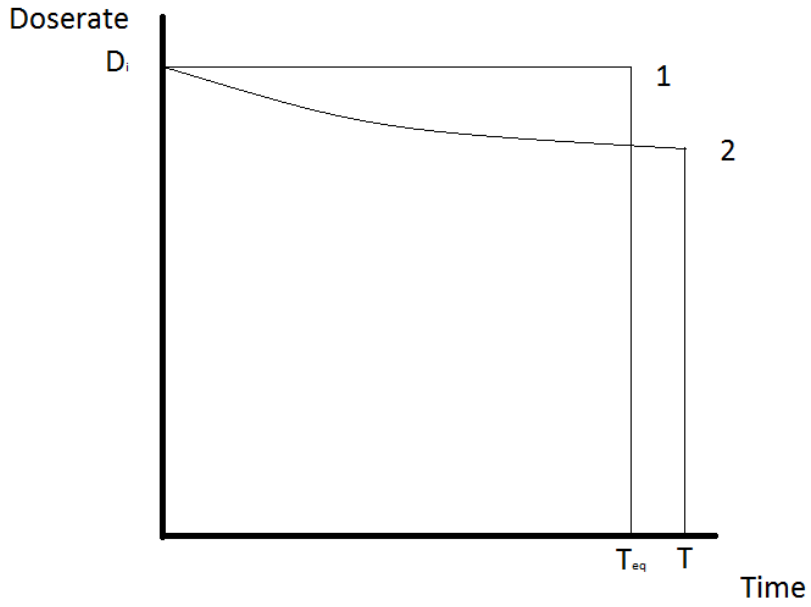

Figure 31: Plot of Doserate vs. Time

Scenario 1 in Figure 31 refers to a constant dose rate (no radioactive decay), in which the total dose is reached after T_{eq}. Scenario 2 refers to the actual scenario, in which there is radioactive decay. For both the initial dose rate is D_i.

The total dose is given by the area under each curve, both scenario 1 and 2 give the same total dose.

Scenario 1: Total dose = $D_i \cdot T_{eq}$

Equation 2: Scenario 1

Scenario 2: Total dose = $\int_0^T \boldsymbol{D_i \cdot e^{-\lambda \cdot t}}$

Equation 3: Scenario 2

where $\lambda = \ln 2 / T_{1/2}$ = decay constant and t = time

The total dose in Equation 2 equals the dose in Equation 3, thus

$D_i \cdot T_{eq} = \int_0^T \boldsymbol{D_i \cdot e^{-\lambda \cdot t}}$

Equation 4

$$T_{eq} = \frac{1}{-\lambda} \cdot e^{-\lambda \cdot t} \Big|_{0}^{T}$$

Equation 5: Equivalent Time

$$T_{eq} = \frac{1}{-\lambda} \left(e^{-\lambda \cdot T} - 1\right)$$

Equation 6: Equivalent Time

For a treatment time of 4 days = 96 hours and a halflife of 1426.32 hours

(and thus $\lambda = 0.000485969$ per hour) , $T_{eq} = 93.80$ hours.

This means that the initial dose rate required for the actual treatment can be calculated as 40 Gy / 93.80 hours = 42.64 cGy/hour. If this were ignored, the error on a four day treatment would be 2.35 %.

If the planned dose rate does not match 42.64 cGy/hour exactly, the treatment time T can be determined by solving for T in terms of T_{eq}.

$$T = \frac{-\ln(1-\lambda \cdot T_{eq})}{\lambda} = \frac{-\ln\left(1-T_{eq}\left(\frac{ln2}{T_{1/2}}\right)\right)}{\frac{ln2}{T_{1/2}}}$$

Equation 7: Determination of Treatment Time

TheraPlan Plus, the treatment planning system used for the LDR brachytherapy dose calculations, cannot take into account radioactive decay. Therefore this calculation needs to be made for each patient.

2.7 The TG-43 Protocol

The American Association of Physicists in Medicine (AAPM) formed Task Group (TG) 43 in 1988 to review the dosimetry of interstitial brachytherapy sources and to recommend a dosimetry protocol *(Nath et al., 1995)*.

The dose calculation protocol that was recommended by TG-43 is based on measured or measurable quantities, either in one or two dimensions. The protocol introduced the anisotropy function, the dose rate constant, the geometry factor, the radial dose function and air kerma strength. Apparent activity was replaced by air kerma strength, the exposure rate constant was replaced by the dose rate constant, the inverse square distance was taken into account by the geometry factor and the radial dose function replaced the tissue attenuation factor. The anisotropy constant was replaced by the anisotropy function.

The protocol works well for two dimensional dose distributions around cylindrically symmetric sources. An updated protocol was published in 2004 (TG-43U1) *(Rivard et al., 2004)*, and an additional supplement in 2007 *(Rivard et al., 2007)*. This was followed by supplement 2 in 2017 *(Rivard et al., 2017)*. Both supplements included data for new brachytherapy sources.

The following definitions are used throughout the formalism and quoted from TG-43U1:

1) "A source is defined as any encapsulated radioactive material that may be used for brachytherapy. There are no restrictions on the size or on its symmetry.
2) A point source is a dosimetric approximation whereby radioactivity is assumed to subtend a dimensionless point with a dose distribution assumed to be spherically symmetric at a given radial distance r. The influence of inverse

square law, for the purpose of interpolating between tabulated transverse-plane dose-rate values, can be calculated using $1/r^2$.

3) The transverse-plane of a cylindrically symmetric source is that plane which is perpendicular to the longitudinal axis of the source and bisects the radioactivity distribution.
4) A line source is a dosimetric approximation whereby radioactivity is assumed to be uniformly distributed along a 1D line-segment with active length L. While not accurately characterizing the radioactivity distribution within an actual source, this approximation is useful in characterizing the influence of inverse square law on a source's dose distribution for the purposes of interpolating between or extrapolating beyond tabulated TG-43 parameter values within clinical brachytherapy treatment planning systems.
5) A seed is defined as a cylindrical brachytherapy source with active length, L, or effective length, L_{eff} (described later in greater detail) less than or equal to 0.5 cm."

The effective length is, for example, used for sources containing multiple radioactive segments and is irrelevant to the OncoSeed 6711 seed.

The geometry assumed in the TG-43 dose calculation formalism is based on the following image (Figure 32):

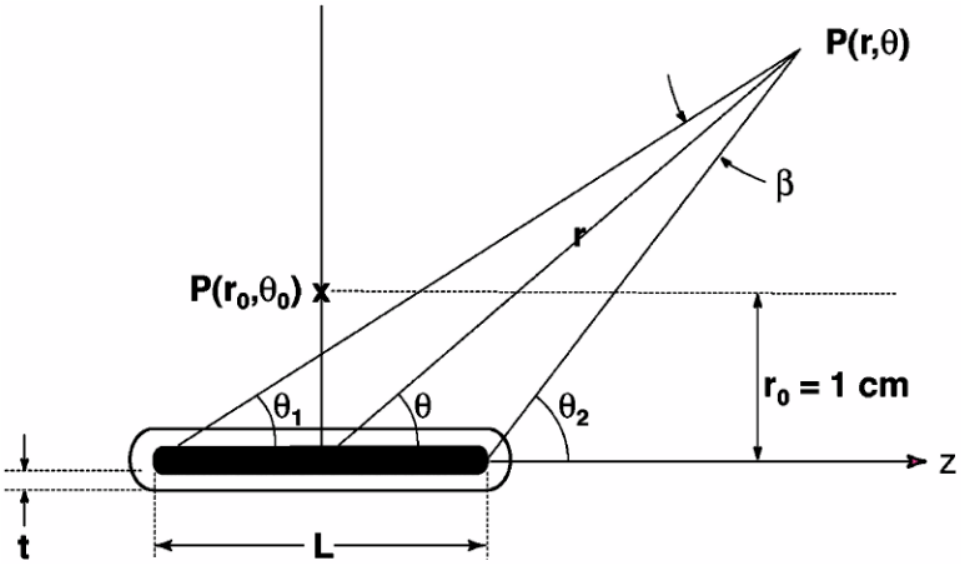

Figure 32: The Seed Geometry Used in the TG-43 Report

The reference point is represented by $P(r_0,\theta_0)$ and lies on the transverse bisector of the source at a distance of 1 cm from the center of the source.

$P(r_0,\theta_0) = P(1cm, \pi/2)$

The general formalism for the two-dimensional case gives the dose rate at point $P(r,\theta)$ as:

$$\dot{D}(r,\theta) = S_K \cdot \Lambda \cdot \frac{G_L(r,\theta)}{G_L(r_0,\theta_0)} \cdot g_L(r) \cdot F(r,\theta)$$

Equation 8: TG-43 Formalism

Where S_K = air kerma strength – see Chapter 2.7.1

Λ = dose rate constant [cGy h^{-1} U^{-1}] – see Chapter 2.7.2

r = distance from the center of the seed to the point of interest [cm]

θ = polar angle identifying the point of interest P(r,θ) relative to the longitudinal axis of the seed

G_L = geometry function – see Chapter 2.7.3

g_L = radial dose function – see Chapter 2.7.4

F = anisotropy function – see Chapter 2.7.5

The subscript L indicates the function is for a line source; it may also be replaced with a P for point source approximations.

2.7.1 Air Kerma Strength - S_K

Kerma is the energy transferred to charged particles as a result of indirectly ionizing radiation. *(Attix, 1986)* defines kerma as "the kerma is the expectation value of the energy transferred to charged particles per unit mass at a point of interest, including radiative-loss energy but excluding energy passed from one charged particle to another".

The air kerma strength is a measure of the strength of the brachytherapy source. The end-user will have to verify that the air kerma strength is accurate, usually in a calibrated well-type ionization chamber ("activity meter" or "dose calibrator").

The TG-43 report introduces the unit U for air kerma strength, with

$1\ U = 1\ \mu Gy\ m^2\ h^{-1} = 1\ cGy\ cm^2\ h^{-1}$

Air kerma strength is specified as the product of the air kerma rate in vacuum, usually measured along the transverse bisector of the source at a calibration distance d, and the square of the distance, i.e.

$$S_K = \dot{K}(d) \cdot d^2$$

Equation 9: Air Kerma Strength

The calibration distance must be large enough that the source can be treated as a point source, i.e. all geometry effects are excluded in the calculation. In *(Rivard et al., 2004)* the subscript δ is added to the air kerma rate, indicating a photon cut-off energy of δ (usually 5 keV for low-energy photon-emitting brachytherapy sources). The contribution to the air kerma rate of photon energies below δ is ignored.

2.7.2 Dose Rate Constant – Λ

The dose rate constant is defined as the ratio of the dose rate at the reference position $P(r_0,\theta_0)$ and S_K. The units are cGy h^{-1} U^{-1}, which ends up being cm^{-2}.

$$\Lambda = \frac{\dot{D}(r_0,\theta_0)}{S_K}$$

Equation 10: The Dose Rate Constant

The value of the dose rate constant is dependent on the radionuclide, the source model and the method used to determine the air kerma strength.

2.7.3 Geometry Function – G

The geometry function $G_L(r,\theta)$ provides an inverse square correction for the dose rate calculation. The geometry function does not take attenuation and scatter into consideration, but provides an inverse square correction based on an approximate model of the activity distribution in the source. The TG-43 formalism recommends the geometry function to be approximated by a point or a line source model, which yields sufficient accuracy.

The geometry function of the point source model is just a simple inverse square correction. The line source model takes into account the source length L, the angle θ at the point of interest $P(r,\theta)$ and the angle subtended by the ends of the source β (see Figure 32) with respect to the point of calculation.

Thus: $G_P(r,\theta) = \frac{1}{r^2}$ (point source approximation)

Equation 11: Point Source Approximation

and $G_L(r,\theta) = \begin{cases} \frac{\beta}{L\, r\, sin\theta} & if\ \theta \neq 0^\circ \\ \left(r^2 - \frac{L^2}{4}\right)^{-1} & if\ \theta = 0^\circ \end{cases}$ (line source approximation)

Equation 12: Line Source Approximation

(Karaiskos et al., 2000) found that the point source approximation is valid for the determination of geometry factors at radial distances larger than twice the active length of the source for an elongated brachytherapy source (within 2 %).

2.7.4 Radial Dose Function – g

The radial dose function takes into account the effects of scatter and absorption in the medium along the transverse axis of the source. It excludes any inverse square type correction, as this is included in the geometry function. It applies only to the transverse axis at $\theta = \theta_0 = \pi/2$.

The source material(s) and filtration can also influence the radial dose function.

The radial dose function is given by:

$$g(r) = \frac{\dot{D}(r,\theta_0)}{\dot{D}(r_0,\theta_0)} \cdot \frac{G(r_0,\theta_0)}{G(r,\theta_0)}$$

Equation 13: The Radial Dose Function

The value of the function is equal to 1 at the reference distance r_0 and $\theta_0 = \pi/2$.

The radial dose function can be used as g_P (for a point source) or as g_L (for a line source).

The relevant geometry function G_P or G_L will need to be inserted into Equation 13.

The TG-43 dosimetry protocol *(Nath et al., 1995)* recommends fitting a fifth-order polynomial to fit radial dose functions.

(Moss, 2000) suggests using a fitting equation to describe this function for the OncoSeed 6711 seed. The modified sigmoid function takes the following shape:

$$g(r) = a5 \cdot \frac{a3 + e^{[a1\cdot(r-a4)]}}{a3 + e^{[a1\cdot(r-a4)]} + e^{[a2\cdot(r-a4)]}}$$

Equation 14: Modified Sigmoid Function

With fitting parameters

$a1 = -9.527\cdot10^{-1}$; $a2 = 3.037 \cdot 10^{-1}$; $a3 = 8.499 \cdot 10^{-1}$; $a4 = 2.545$; $a5 = 1.115$

A double exponential fit was recommended by *(Furhang and Anderson, 1999, Furhang and Wallace, 2000)*:

$$g(r) = a_0 \cdot e^{-a_1 \cdot r} + a_2 \cdot e^{-a_3 \cdot r}$$

Equation 15: Double Exponential Function

with fitting parameters a_0 = 1.964, a_1 = 0.337, a_2 = -0.933 and a_4 = 0.842 for the 6711 seed.

(Meigooni et al., 2003) suggested a modified fifth-order polynomial of the shape:

$$g(r) = (a_0 + a_1 \cdot r + a_2 \cdot r^2 + a_3 \cdot r^3 + a_4 \cdot r^4 + a_5 \cdot r^5) \cdot e^{-a_6 \cdot r}$$

Equation 16: Fifth-Order Polynomial Fit

However, in their publication this was not done for the OncoSeed 6711, but for a Pd-103 seed.

(Taylor and Rogers, 2008b) proposed a modification to *(Meigooni et al., 2003)*'s formula to allow for a more rapid variation of the fitting function at small radii. Their function takes the shape of:

$$g(r) = (a_0 \cdot r^{-2} + a_1 \cdot r^{-1} + a_2 + a_3 \cdot r + a_4 \cdot r^2 + a_5 \cdot r^3) \cdot e^{-a_6 \cdot r}$$

Equation 17: Modified Fit

With fit parameters a_0 = 5.9638 x 10^{-4} cm^2, a_1 = -1.3360 x 10^{-2} cm, a_2 = 1.1634, a_3 = 0.40710 cm^{-1}, a_4 = -5.5487 x 10^{-3} cm^{-2}, a_5 = 1.7421 x 10^{-3} cm^{-3} and a_6 = 0.44080 cm^{-1}.

Fit parameters for a number of different I-125 seeds, not just the OncoSeed 6711, are given in their publication.

2.7.5 Anisotropy Function - F

The anisotropy function accounts for the anisotropic dose distribution around the source. This function gives the angular variation of the dose rate about the source at each distance due to self-absorption, oblique filtration of photons through the seed capsule and scattering and absorption of photons in the medium.

The anisotropy function is given by:

$$F(r, \theta) = \frac{\dot{D}(r,\theta)}{\dot{D}(r,\theta_0)} \cdot \frac{G(r,\theta_0)}{G(r,\theta)}$$

Equation 18: The Anisotropy Function

This two-dimensional anisotropy function uses the line source approximation of the geometry function.

2.8 The Dosimetry of the OncoSeed 6711

(Attix, 1986) describes I-125 as having a half-life of 60.2 days, while *(Nath et al., 1995)* state a half-life of 59.4 days and the package insert *(OncoSeed, 2005)* states a half-life of 59.43 days. It decays via electron capture to the first excited state of Te-125, and de-excites through internal conversion (93 % of the time) or via gamma emission (7 % of the time) *(Nath et al., 1995)*. The radionuclide output data is given by *(Attix, 1986)*:

Radiation	Mean number / disintegration	Mean energy / particle [MeV]
Gamma	0.0666	0.0354
K alpha-1 X-Ray	0.7615	0.0274
K alpha-2 X-Ray	0.3906	0.0272
K-beta-1 X-Ray	0.2056	0.0309
K-beta-2 X-Ray	0.0426	0.0318
L X-Rays	0.2226	0.0037
K Int Con Electron	0.8000	0.0036
L Int Con Electron	0.1142	0.0309
M Int Con Electron	0.0190	0.0346
KLL Auger Electron	0.1416	0.0226
KLX Auger Electron	0.0597	0.0264
KXY Auger Electron	0.0096	0.0301
LMM Auger Electron	1.5442	0.0029
MXY Auger Electron	3.6461	0.0008

Table 5: I-125 Output Data

This data differs subtly from the data that is given in TG-43U1, as shown in Table 6:

I-125 (half-life = 59.40 ± 0.01 days)	
Photon Energy [keV]	Photons per disintegration
27.202	0.406
27.472	0.757
30.98	0.202
31.71	0.0439
35.492	0.0668

Table 6: I-125 Output Data

The weighted mean energy of the I-125 decay is given as 28.37 keV with a total of 1.476 photons per disintegration *(Rivard et al., 2004).*

The iodine in the seed is adsorbed onto a silver rod and the silver produces characteristic X-rays that affect the spectrum as well. The titanium capsule also produces characteristic X-rays at a lower energy.

The recommended dose rate constant in a water medium, according to TG-43, is 0.88 cGy h^{-1} U^{-1}. This was updated to the consensus dose rate constant, which is given in TG-43U1 as $\Lambda = 0.965$ cGy h^{-1} U^{-1}.

The radial dose function and anisotropy function are listed in the next two tables. The consensus g(r) values are obtained from the TG-43U1 report.

r [cm]	Radial Dose Function of 6711 Seed	
	Line Source Approximation L = 3 mm	Point Source Approximation
0.10	1.055	0.696
0.15	1.078	0.853
0.25	1.082	0.982
0.50	1.071	1.048
0.75	1.042	1.036
1.00	1.000	1.000
1.50	0.908	0.912
2.00	0.814	0.819
3.00	0.632	0.636
4.00	0.496	0.499
5.00	0.364	0.367
6.00	0.270	0.272
7.00	0.199	0.200
8.00	0.148	0.149
9.00	0.109	0.110
10.00	0.0803	0.0809

Table 7: The Radial Dose Function of the OncoSeed 6711 I-125 Seed

It should be noted that only the active length of the seed, and not the total length of the titanium capsule, is used in the line source approximation.

The anisotropy function F(r,θ) for the 6711 seed, as given in TG-43U1, is:

θ[°]	r [cm]					
	0.5	1	2	3	4	5
0	0.333	0.370	0.442	0.488	0.520	0.550
5	0.400	0.429	0.497	0.535	0.561	0.587
10	0.519	0.537	0.580	0.609	0.630	0.645
20	0.716	0.705	0.727	0.743	0.752	0.760
30	0.846	0.834	0.842	0.846	0.848	0.852
40	0.926	0.925	0.926	0.926	0.928	0.928
50	0.972	0.972	0.970	0.969	0.969	0.969
60	0.991	0.991	0.987	0.987	0.987	0.987
70	0.996	0.996	0.996	0.995	0.995	0.995
80	1.000	1.000	1.000	0.999	0.999	0.999

Table 8: Anisotropy Function for the 6711 Seed

The brachytherapy source activity distribution is usually assumed to be uniformly distributed, but most brachytherapy sources demonstrate variations of 2 % - 20 % in the intensity of emissions about the long axis *(DeWerd et al., 2011)*.

According to the combined report of the AAPMB TG No. 138 and GEC ESTRO *(DeWerd et al., 2011)*, the dosimetric uncertainty for low-energy photon-emitting brachytherapy sources is approximately 9 % (95 % confidence interval), excluding the uncertainties in dose delivery due to the physical implantation. *(Mitch et al., 2009)* states that “current brachytherapy dose measurement technologies are not satisfactory, barely achieving 10 % measurement accuracy under the best of circumstances”.

(Kutcher et al., 1994) suggest an uncertainty of ± 15 % as a more realistic number for plaque brachytherapy.

2.9 Dosimetry

Gafchromic film dosimetry and thermoluminescent dosimetry were used for this study and are discussed in detail in the following pages.

These devices have been used for I-125 dosimetry in literature and were available for this study. Other dosimetric devices that have been used to study LDR brachytherapy seeds are also mentioned, but not described in detail.

2.9.1 Radiochromic Film Dosimetry

One of the early radiation detectors making use of the change of colour was the human skin; the "erythema dose" was the dose needed to produce visible reddening of the skin *(Mould, 1993, Meyer and Glasser, 1926, Chamberlain and Newell, 1928, Richards, 1955)*. Fortunately this unit was soon discontinued, but the change of colour of certain materials upon irradiation is still a relevant form of measuring dose.

(Soares, 2006) wrote a very useful paper on the practical application of radiochromic film dosimetry. The desirable characteristics of radiochromic film include: sensitivity to ionizing radiation, ease of use, tissue equivalence, no dose-rate dependence, no light dependence, environmentally stable, rugged, of a reasonable size and not too thick, as well as a uniform response to radiation over the whole film. Gafchromic film performs well in high dose gradients *(Devic, 2011)* and was used in this study.

2.9.1.1 Gafchromic EBT and EBT 2 Film

Radiochromic films produce permanent visible colour change when irradiated. The AAPM Task Group No. 55 published recommendations on radiochromic film dosimetry *(Niroomand-Rad et al., 1998)*, but this was before the EBT gafchromic film was developed. *(Butson et al., 2003)* wrote a review article on the use of radiochromic film for medical radiation dosimetry in 2003; since that review article there have been

a number of improvements in radiochromic film design and behaviour when exposed to ionizing radiation. The Gafchromic EBT film type became available in 2004 and has been used for I-125 seed dosimetry in a solid water phantom *(Chiu-Tsao et al., 2008)*. The energy dependence of the EBT film was investigated by *(Chiu-Tsao et al., 2005)* using 6 MV photons, ^{192}Ir, ^{125}I and ^{103}Pd. They concluded that "EBT film response is nearly independent of radiation energy, within the uncertainty of measurement". The film is suitable for radiation dosimetry with a wide energy spectrum, including primary and scattered radiation. *(Butson et al., 2006)* confirmed that the maximum variation in the response of the EBT gafchromic film with energy over the range from 28 keV to 4 MeV was 8 % with an uncertainty of 4 %. The original EBT film had two main absorption peaks at 636 nm and 585 nm after exposure to ionizing radiation *(Butson et al., 2005)*. *(Sutherland and Rogers, 2010)* confirmed that the energy dependence of EBT film varies approximately 10 % below 100 keV.

Gafchromic EBT2 dosimetry film is a self-developing film, which has been formulated to be energy independent from 50 kV into the MeV range *(GAFCHROMIC_EBT2, 2009b)*. The film has been designed to be handled in interior room light, but it is good practice to keep exposed and unexposed film in the dark when not in use. The film can be cut into smaller pieces; however, the pieces should be marked to indicate their orientation with respect to the original sheet. When the film is exposed to radiation a blue polymer is formed. The exposed film appears dark, with a greenish undertone, owing to the presence of a yellow marker dye in the active layer of the film. EBT2 film can be read with a colour scanner, film scanner or digitizer. Care must be taken to position the film reproducibly on the scanner, because the scanner response may not be perfectly flat over the scan field. The film response is also sensitive to the orientation

of the film on the scanner. The response difference is the result of anisotropic light scattering. The active component in EBT2 film is in the form of needle-like particles (approximately 1.2 μm in diameter and 15 – 25 μm in length *(Andres et al., 2010)*) and these particles tend to align with their long axes parallel to the coating direction, thus scattering light differently in orthogonal directions. For this reason the films have to be scanned in the same direction every time. Also, the density of the EBT2 film increases post-exposure and the changes are proportional to log(time after exposure). This means that the films should all be scanned at the same time after exposure when using the films for absolute dosimetry. Doses from 1 cGy – 10 Gy can be measured in the red colour channel, while the green colour channel can be used up to doses of 40 Gy. The blue colour channel response can be used to adjust for small response differences over the area of the film. The film has a high spatial resolution (at least 100 μm) and is water resistant *(GAFCHROMIC_EBT2, 2009a)*. It is important to use the same scanner each time when scanning the exposed films, as different scanners have different sensitivity responses *(Devic et al., 2004)*. *(Devic et al., 2005)* recommend the use of flat-bed document scanners that employ a non-coherent white light emission spectrum as a simple and reliable tool for optical density measurements, but with some uncertainty caveats, which include the overall uncertainty of the dose measurement in the reference field, uncertainty due to the non-uniform thickness of the film's sensitive layer and uncertainties associated with the film scanner. Flatbed scanners exhibit a different response over their lateral scan axis *(Van Battum et al., 2015)*, meaning that the films must be scanned in the same position on the scanner bed and not be moved around.

The absorption peaks in the EBT2 film are also 636 nm and 585 nm, just like the EBT film *(Butson et al., 2009, GAFCHROMIC_EBT2, 2009b)*. Another peak arises at 420 nm due to the yellow marker dye in the active layer.

(Butson et al., 2010) investigated the energy response of the EBT2 radiochromic film and found an improvement in the response of the film with energy, namely 6.5 % from 50 kVp – 10 MV, with an under-response at 50 kVp of 1.5 %. It should be noted that the equivalent photon energies for the X-ray beams were stated as 25.2 keV for the 50 kVp beam, 30 keV for the 75 kVp beam and 36 keV for the 100 kVp beam.

(Arjomandy et al., 2010) found that the energy dependence was "relatively small within measurement uncertainties (1 $\sigma = \pm$ 4.5 %) for all energies and modalities". It was also shown that the EBT2 film evolves over time, potentially changing the optical density of the film *(Devic et al., 2010)*. Scanning orientation *(Desroches et al., 2010, Andres et al., 2010)* and film homogeneity *(Hartmann et al., 2010)* have also been investigated. Film inhomogeneities can potentially lead to ± 6 % uncertainties in dose determination when optical densities are used for dose calibration *(Hartmann et al., 2010)*.

The effective atomic number of EBT2 gafchromic film is Z_{eff} = 6.84 *(Andres et al., 2010)*, which is slightly lower than that of water ($Z_{eff}(H_2O)$ = 7.42) *(Jayachandran, 1971)*.

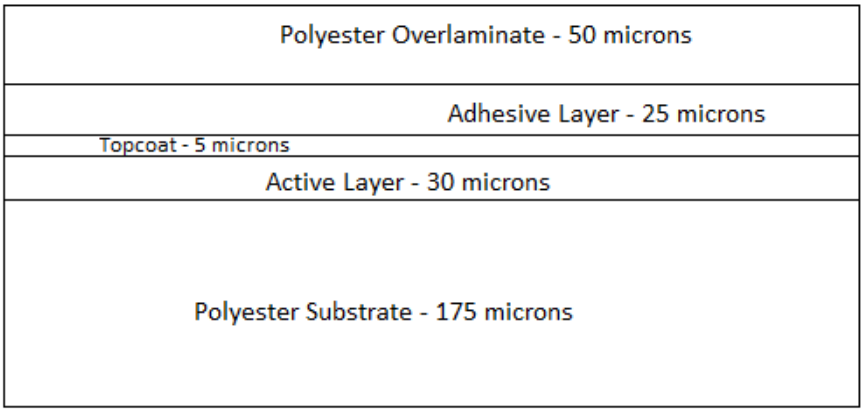

Figure 33: Configuration of the GAFCHROMIC EBT2 Film

Gafchromic EBT2 film was used in this study to determine various seed parameters (anisotropy, radial dose function), as well as measure dose distributions in the "Claws".

2.9.1.2 Gafchromic EBT 3 Film

Gafchromic EBT3 film was introduced in 2012 and immediately described in literature *(Borca et al., 2013).*

The structure of the EBT3 film is shown in Figure 34:

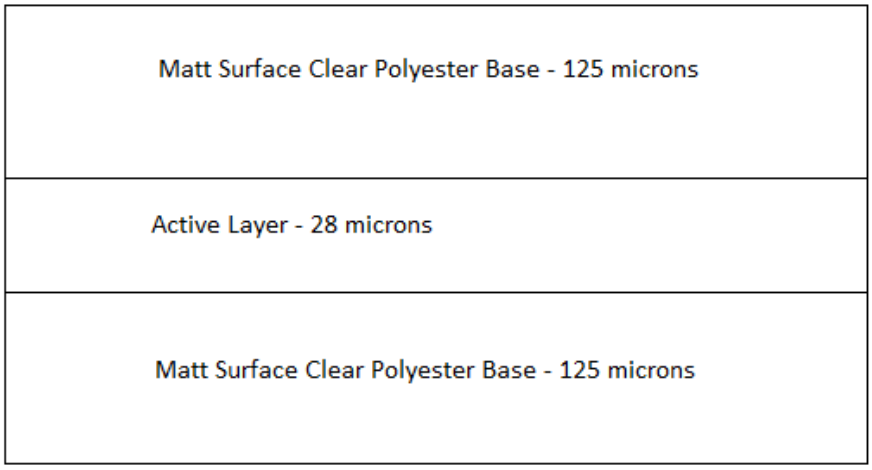

Figure 34: Configuration of the Gafchromic EBT3 Film

The package insert describes the film as near tissue equivalent with a minimal energy-dependence and a high spatial resolution (25 µm). The film comes in 8 inch x 10 inch or 13 inch x 17 inch sheets and also incorporates a yellow marker dye *(GAFCHROMIC_EBT3, 2012).*

Most EBT3 film characteristics are similar to the EBT2 film. The EBT3 film shows a different response between portrait and landscape orientations, similar to the EBT2 film. The film exhibits an energy dependence at low energies of up to 11 %, depending on the absorbed dose, colour channel used and spatial resolution selected on the scanner *(Massillon-JL et al., 2012). (Morrison et al., 2014)* investigated the use of EBT3 film for low-energy seed brachytherapy and found that film calibration should be done with a low-energy source, rather than a 6 MV photon beam.

Gafchromic EBT3 film was used to measure the seed anisotropy and radial dose function, as well as dose distributions in the “Claws”.

2.9.2 Thermoluminescent Dosimetry

Thermoluminescent Dosimeters (TLDs) are inorganic scintillation materials made from materials that exhibit high concentrations of trapping centers within the bandgaps.

Incident radiation interacts with the electrons in the dosimeter and elevates them from the valence band to the conduction band, but they are then captured in various trapping centers. The amount of electrons trapped in these trapping centers is proportional to the dose that was deposited in the TLD material.

For readout, the TLD is placed in a stream of heated nitrogen gas, the temperature is progressively raised and at a temperature determined by the electron trap, the trapped electrons can pick up enough thermal energy to leave the trap and de-excite with the emission of a photon.

A signal can be obtained by converting the light signal into an electrical signal using a photomultiplier tube. The glow-curve describes the amount of photons emitted as a function of temperature. The basic signal related to the exposure is the total number of emitted photons *(Knoll, 2010)*.

TLDs can be re-used after they have been annealed.

The common TLD 100 chip is a LiF chip with a concentration of about 400 ppm of Mg added to serve as the primary trapping centers. Additionally, about 8 ppm of Ti are added to provide “luminescent recombination centers” *(Knoll, 2010)*.

Thermoluminescent dosimetry has been used to describe I-125 sources in literature, for example in *(Patel et al., 2001, Chiu-Tsao et al., 2003, Lymperopoulou et al., 2005, Tailor et al., 2008)*. This has also been done before for the OncoSeed 6711 I-125 seed *(Sloboda and Menon, 2000, Williamson, 1991)*.

The dosimetry of the OncoSeed 6711 was also done in COMS eye plaques using TLDs *(Chiu-Tsao et al., 1993, de La Zerda et al., 1996).* Gold plaque dosimetry has also been done with TLDs *(Luxton et al., 1988, Weaver, 1986).*

LiF dosimeters are recommended for measuring the dose rate around brachytherapy sources by the TG-43U1 report.

In this study Rexon TLD 700 chips were used (Lot # C-7-97-1). The TLDs were supplied as 3 x 3 x 0.9 mm chips. *(Das et al., 1996)* reported that the measured TLD light output per unit dose to TLD was constant as a function of energy for this size chip, but *(Nunn et al., 2008)* suggested an 8 – 13 % increase in TLD-100 signal from 12 keV – 145 keV doses relative to Co-60 photons.

2.9.3 Other Dosimetry

Dosimetry in this work was done using gafchromic film and TLDs. Other dosimetry methods used to describe brachytherapy seeds and dose rate distributions in eye applicators include:

Glass Rod Dosimeters *(Tanaka et al., 2011)*

Plastic scintillators *(Eichmann et al., 2009, Bambynek et al., 1999, Flühs et al., 1996)*

MOSFET dosimeters for prostate cancer *(Buzurovic et al., 2013)*

3-D PRESAGE^{TM} *(Adamovics and Maryanski, 2004)* radiochromic dosimeters (colour forming dye within a polyurethane matrix) *(Poder et al., 2013, Wai et al., 2006)*

Diode *(Knutsen et al., 2001)*

Primary standard laboratories for low-energy brachytherapy sources include the National Institute of Standards and Technology (NIST) – using the Wide-Angle Free-Air Chamber (WAFAC), the Physikalisch-Technische Bundesanstalt (PTB) – using a parallel plate extrapolation chamber with cylindrical geometry and a large volume

extrapolation chamber (Grossvolumen Extrapolationskammer GROVEX), the Variable-Aperture Free-Air Chamber (VAFAC) from the University of Wisconsin, the National Physical Laboratories (NPL) – using a well-type ionization chamber, and the Laboratoire National Henri Becquerel (LNHB) – using a unique torus-shaped free-air chamber *(Mitch and Soares, 2009, Soares et al., 2009, Sander, 2014)*.

While the dosimetry of photon brachytherapy sources is currently still based on air-kerma rate values, efforts are underway to introduce an absorbed dose to water standard for LDR brachytherapy sources *(Soares et al., 2009)*.

2.10 Monte Carlo Methods

(Bielajew, 2016) argues that both basic and applied science depend on "the trinity of measurement, theory and Monte Carlo". This section describes the Monte Carlo component.

Monte Carlo calculations are computational algorithms that rely on repeated random sampling to compute their results. The Monte Carlo method numerically solves a problem that models objects interacting with other objects or the environment, based on their relationships *(Bielajew, 2016)*. It can be described as a formalized and methodical version of trial and error. John von Neumann and Stanislaw Ulam from the Los Alamos National Laboratory are credited with the introduction of Monte Carlo methods *(Ulam, 1952)*.

(Eckhardt, 1987) writes about some unpublished remarks made by Stan Ulam in 1983: "The first thoughts and attempts I made to practice [the Monte Carlo method] were suggested by a question which occurred to me in 1946 as I was convalescing from an illness and playing solitaires. The question was what are the chances that a Canfield solitaire laid out with 52 cards will come out successfully? After spending a lot of time

trying to estimate them by pure combinatorial calculations, I wondered whether a more practical method than “abstract thinking” might not be to lay it out say one hundred times and simply observe and count the number of successful plays. This was already possible to envisage with the beginning of the new era of fast computers, and I immediately thought of problems of neutron diffusion and other questions of mathematical physics, and more generally how to change processes described by certain differential equations into an equivalent form interpretable as a succession of random operations. Later... [in 1946, I] described the idea to John von Neumann and we began to plan actual calculations.”

The Monte Carlo method was described in 1949 as “essentially, a statistical approach to the study of differential equations, or more generally, of integro-differential equations that occur in various branches of the natural sciences” *(Metropolis and Ulam, 1949)*.

John von Neumann saw the relevance of Ulam’s suggestion and in 1947 he outlined a possible statistical approach to solving the problem of neutron diffusion in fissionable material *(Metropolis, 1987)*. It seems that Nicholas Metropolis suggested the name “Monte Carlo” for this type of algorithm, “a suggestion not unrelated to the fact that Stan had an uncle who would borrow money from relatives because he “just had to go to Monte Carlo.”” *(Metropolis, 1987)*

Monte Carlo methods were introduced in radiation therapy in the 1970s *(Andreo, 1991)*. Computational power was limited and the initial use of Monte Carlo methods in radiation therapy was limited. However, over the years this has changed and Monte Carlo techniques are now commonly used to solve complex transport equations analytically *(Rogers, 2006)*. A model is created, which is as similar as possible to the real physical system of interest, and then interactions within that system are created

based on known probabilities of occurrence, with a random sampling of probability density functions (PDFs) *(Amato et al., 2013)*.

A simulation history is defined as the transport of an individual particle and of particles consequently set in motion. The statistical uncertainty of a simulation depends on the number of histories simulated. This is governed by the Central Limit Theorem, which states that the result of a simulation will approach the true result if the number of histories is sufficiently large. However, the uncertainty will never reach 0 %, because some uncertainties will remain, like e.g. uncertainties in the cross section libraries, statistical uncertainty dues to the limited number of histories simulated or uncertainties in the material composition and densities *(Reynaert et al., 2007)*.

The probability that a photon will travel a distance x without any interactions if given by $e^{-\mu \cdot x}$, where μ is the linear attenuation coefficient of that material. The probability of an interaction within an interval dx is given by μ dx. Therefore the interaction probability for an interaction between x and x + dx is given by $\mu \cdot e^{-\mu \cdot x}$ dx. The cumulative probability curve P(x) for the selection of the first interaction site now takes the shape of

$$P(x) = \int_0^x \mu \cdot e^{-\mu \cdot x} dx = 1 - e^{-\mu \cdot x}$$

The travel length d for a random number r in the range [0,1] can now be expressed as

$$r = 1 - e^{-\mu \cdot x} \rightarrow x = -\frac{1}{\mu} \cdot \ln(1 - r) = -\frac{1}{\mu} \cdot \ln r$$

This is true if r is uniformly distributed between [0,1], because then so is (1 – r) and it saves one computing operation in the simulation *(Bielajew, 1994)*.

The photon is then transported to the location of the first interaction, where the type of interaction to be simulated is sampled, based on the interaction cross sections contained in the cross section libraries *(Reynaert et al., 2007)*.

The parameters of the initial photon (energy, position, direction) are placed on top of a stack and are used in the photon transport process. If the photon energy falls below a user-defined cut-off value (1 keV for this work), the photon transport is terminated. If the photon energy is above this cut-off, then the distance to the next interaction is sampled. If the photon leaves the volume of interest the transport is terminated, otherwise the interaction type is sampled and the resultant particles' energies and directions are stored for future processing. When the stack is empty, the history is completed and a new history starts *(Van Eeden, 2014)*.

The following diagram shows the basic photon transport logic *(Bielajew, 1994)*.

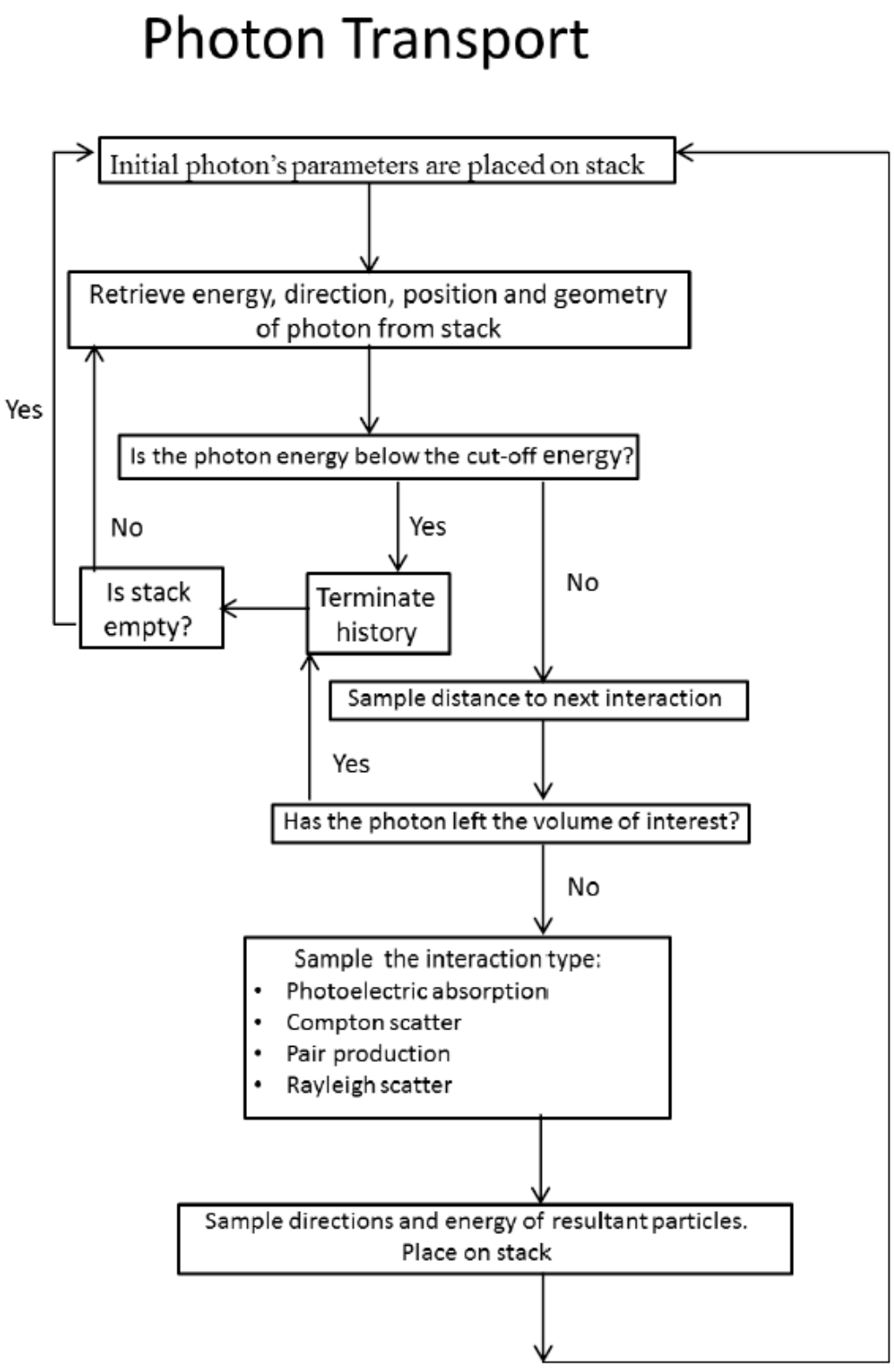

Figure 35: Photon Transport Logic

Monte Carlo simulations have been used extensively in low dose rate brachytherapy *(Williamson, 1987, Williamson, 1988, Williamson, 1991, Dolan et al., 2006, Afsharpour et al., 2008, Bohm et al., 2003, Burns and Raeside, 1983, Chamberland et al., 2016, Howard, 2014, Landry et al., 2010, Landry et al., 2011, Luxton, 1994, Luxton and Jozsef, 1999, Miras et al., 2012, Nuttens and Lucas, 2006, Paixão et al., 2012, Poon et al., 2008, Rivard et al., 2010, Rivard et al., 2011, Rivard, 2009, Taylor and Rogers, 2008a, Taylor, 2006, Taylor et al., 2007, Thomson and Rogers, 2010, Thomson et al., 2008, Williamson, 2000, Zehtabian et al., 2010, Brualla et al., 2013, Burns and Raeside, 1989, Chibani et al., 2005, Melhus and Rivard, 2006)*, to name a few.

Monte Carlo simulations are considered the current state of the art in computational dosimetry *(Beaulieu et al., 2012)*. However, Monte Carlo codes cannot be treated as a "black box" and correct answers are not always easy to obtain *(Garth, 2005)*.

The book "Fundamentals of the Monte Carlo method for neutral and charged particles" *(Bielajew, 2016)* gives an in-depth overview of Monte Carlo fundamentals and is recommended for further studying, as is the book "Monte Carlo Techniques in Radiation Therapy" *(Seco and Verhaegen, 2013)*.

2.10.1 EGSnrc

The EGS (Electron-Gamma-Shower) Monte Carlo package family is a code used for the simulation of coupled transport of photons and electrons in an arbitrary geometry for energies from a few keV up to several hundred GeV *(Kawrakow et al., 2019)*. It is freely available online.

EGS1 was developed in the late 1960s and early 1970s. This was followed by the release of EGS2 in 1975, EGS3 in 1978 in EGS4 in 1985 *(Bielajew, 2004)*.

The EGSnrc code is based on the EGS4 system, but with a number of enhancements and modifications, like e.g. the inclusion of the angular distribution of bremsstrahlung

photons, low-energy photon cross section enhancements, additional incoherent scattering outcomes or new coherent scattering angular sampling *(Kawrakow et al., 2019).*

The PEGS4 code is a stand-alone pre-processing code. It is used to produce cross-section data for EGSnrc user codes based on material composition and densities, as well as energy cutoffs. Data in the existing PEGS4 distribution are based on the collision and radiative stopping powers recommended by the ICRU Report 37 *(Kawrakow et al., 2019).* The US Department of Homeland Security has published a compendium of material composition data for radiation transport modelling, which provides useful data for almost 400 materials *(McConn et al., 2011).*

A number of user codes exist for EGSnrc to simulate the passage of photons or electrons in various geometries *(Rogers et al., 2018).*

These include cylindrical and spherical geometries:

DOSRZnrc is used to analyze the passage of a photon or electron beam in a finite, right cylindrical geometry.

FLURZnrc can be used to calculate the fluence of different particles in cylindrical geometry.

SPRRZnrc calculates Spencer-Attix restricted stopping power ratios.

CAVRZnrc and CAVSPHnrc can be used when cavity ionization chambers are modelled, in cylindrical or spherical geometries respectively.

The BEAMnrc code is a general purpose code to simulate radiotherapy treatment units and uses the EGSnrc Monte Carlo system of radiation transport *(Rogers et al., 2009).*

The original plan was to model the “Claws” using DOSXYZnrc *(Walters et al., 2005),* which is a code used for calculating dose distributions in a rectilinear voxel phantom.

However, when egs_brachy was introduced *(Chamberland et al., 2016)*, it was immediately obvious that this would offer a simpler and more elegant solution.

2.10.2 egs_brachy

Initially, BrachyDose *(Taylor et al., 2007, Thomson et al., 2010)* was introduced to address the need for brachytherapy-specific Monte Carlo codes *(Chamberland et al., 2016)*. BrachyDose is an EGSnrc *(Kawrakow et al., 2019)* user code that uses a multi-geometry package, which was developed by *(Yegin, 2003)*. However, the versatile egs++ class libraries *(Kawrakow, 2005)* prompted the development of egs_brachy, a Monte Carlo code designed specifically for brachytherapy applications and allowing the modelling of complex geometries *(Chamberland et al., 2016)*.

Egs_brachy requires a text-based input file, which defines all the aspects of the simulation.

It includes a library of geometry models for brachytherapy sources, including the OncoSeed 6711 I-125 source. Both electron and photon transport can be modelled using this code, as it is also based on the EGS_nrc code system. The I-125 spectrum used is based on the spectrum published in NCRP Report 58 *(NCRP_58, 1985)*. The egs_brachy library already contains a material data file, which means that simulations can be run in "pegsless" mode if no additional materials are added *(Thomson et al., 2017)*.

The user input file includes data from the library, the input geometry and input source, as well as various Monte Carlo parameters. Volume correction subtracts the partial volume of a seed from a phantom voxel so that the dose is properly determined. Variance reduction methods, often used to speed up Monte Carlo simulations, were

switched off for the simulations in this work and are therefore not discussed. An upper and a lower energy threshold must be specified for photons and electrons.

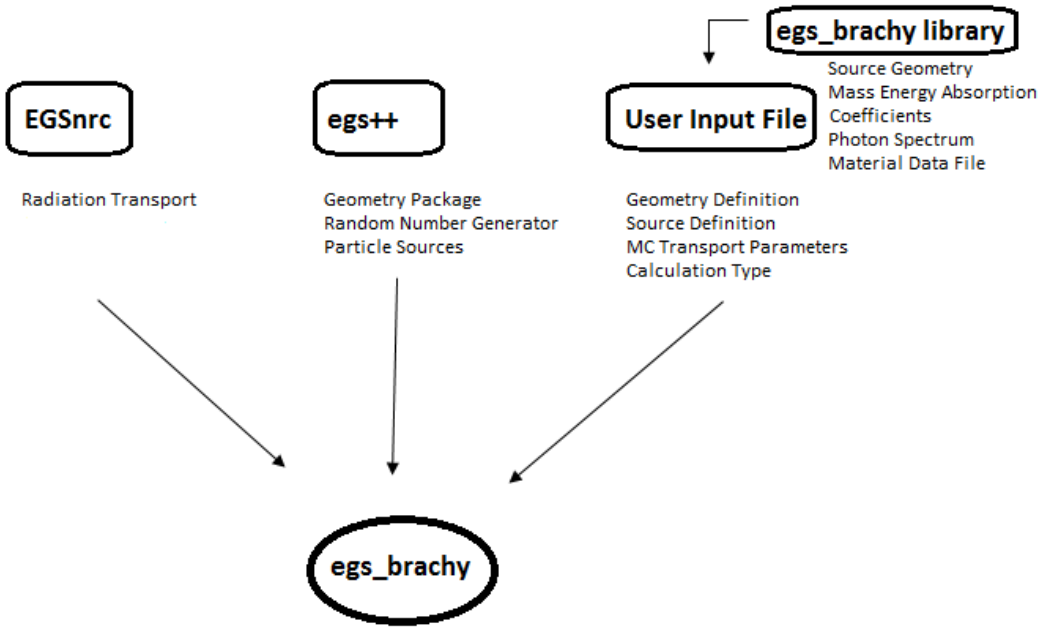

Figure 36: Simplified Schematic Diagram for egs_brachy Input

2.10.3 MCSHOW

MCSHOW is a visualization tool that allows the user to view dose distributions in the phantom geometry. MCSHOW allows the user to define isodose lines, change the normalization value of the isodoses, view dose distributions in the three main planes and zoom into the image. It also allows for region of interest drawing for dose-volume-histogram data for the tumour volume and organs-at-risk. More than one dose distribution can be displayed for comparison purposes. Apart from this, it also contains algorithms for noise reduction on the isodose lines in order to remove sensitive Monte Carlo-induced noise. It thus simplifies tumour volume coverage using smoothed lines. However, caution must be taken to have data that is at least within 2 % variance. Dose smoothing is not a quick-fix to speed up simulation times *(du Plessis, 2019)*.

CHAPTER 3 EQUIPMENT AND METHODS

The first part of the study consists of describing the OncoSeed 6711. This was done by measuring the physical dimensions, the apparent activity / air kerma strength, the spectrum using various detectors, as well as the radial dose function and anisotropy in a solid water phantom using gafchromic film and thermoluminescent dosimetry.

The second part of the study consists of describing the “Claws”. In-phantom dose measurements were done using gafchromic film and thermoluminescent dosimeters. The “Claws” model was formalized in computer-aided-design (CAD) drawings. A PVC model of the “Claws” was manufactured using a milling machine. This model was micro-CT scanned in an attempt to create an input file for the Monte Carlo simulations. The CAD model of the “Claws” could be cut into 100 µm slices, which were eventually used to create the Monte Carlo input file.

Dose distributions in the “Claws” were worked out using two treatment planning systems. Additionally, Monte Carlo simulations to determine the dose distributions in and around the “Claws” were done. The following flowchart gives an overview of measurements done and equipment used. It is meant as a quick reference guide to this chapter and Chapter 4.

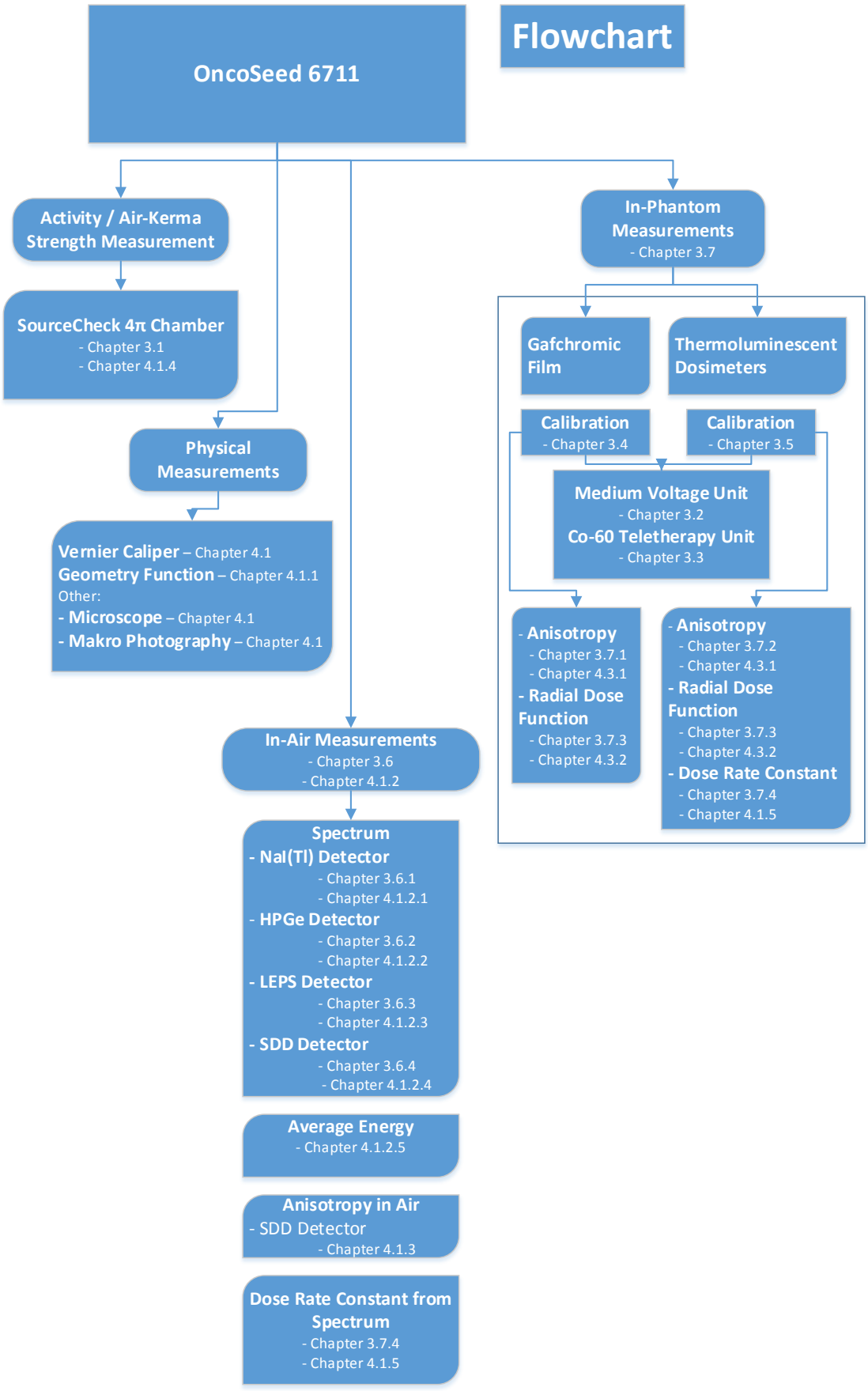

Figure 37: Flowchart for Measurements and Results of the I-125 Seed

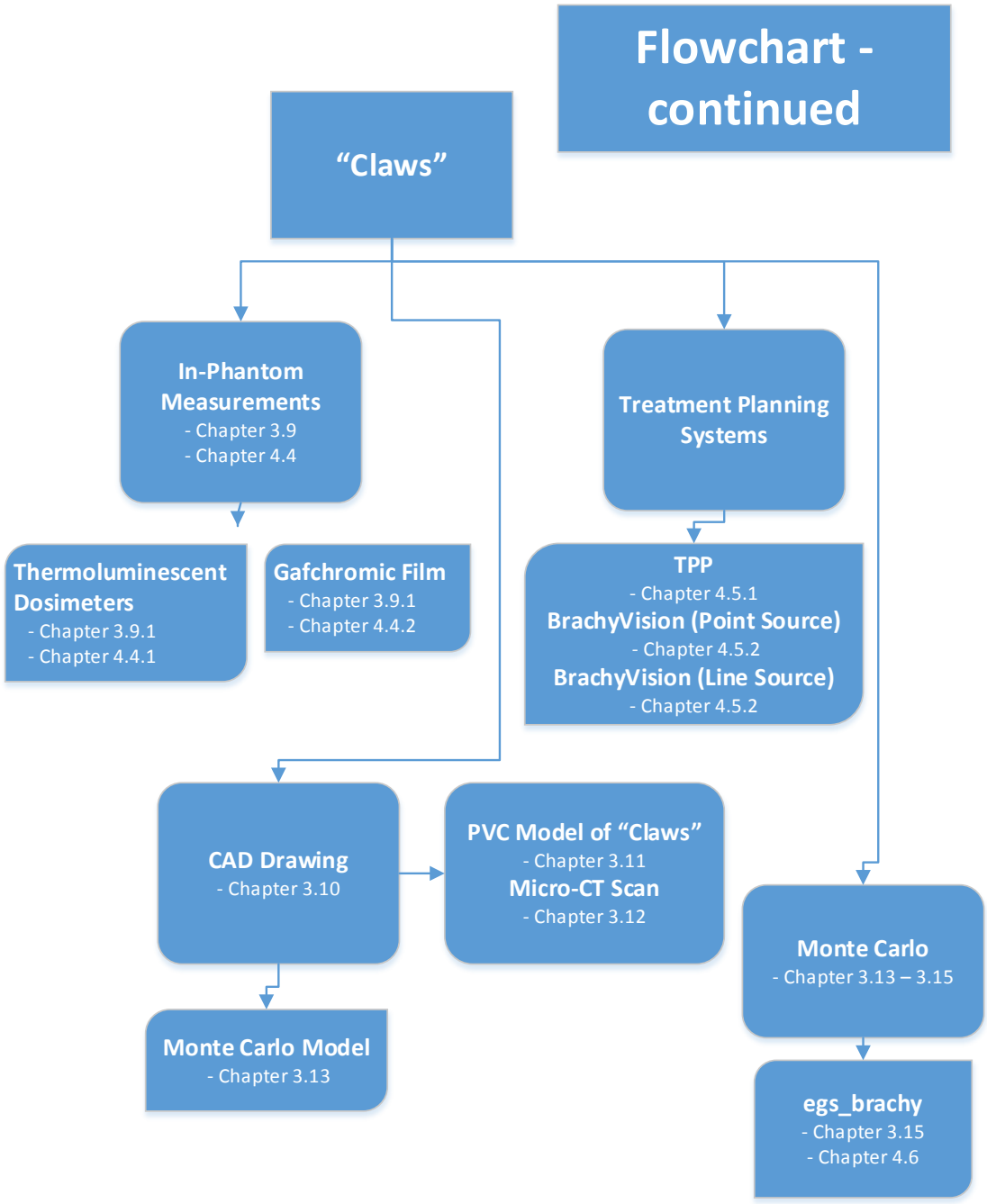

Figure 38: Flowchart for Measurements and Results of the "Claws"

3.1 The PTW Sourcecheck 4π Chamber

The PTW Sourcecheck 4π type 33005 is a well-type ionization chamber and is used to measure the activity or air-kerma strength of brachytherapy sources *(PTW, 2013)*. It has a nominal volume of 116 mm^3 and requires a supply voltage of + 400 V. The detector is a vented detector and requires an air density correction, given by

$$k_{TP} = k_1 \cdot \left(\frac{(T + 273.2) \cdot 1013.25}{293.2 \cdot P} \right)^{k_2}$$

Equation 19: Temperature and Pressure Correction

Where T is the temperature in the sensitive volume [°C]

P is the atmospheric pressure at the measuring site [hPa]

k_1 & k_2 are I-125 specific coefficients and are given by k_1 = 0.998 and k_2 = 0.534.

A custom adapter for single seeds is used for the measurements and the source strength is calculated according to the following formula:

$S = M \cdot N \cdot P_{ion} \cdot k_{TP}$

Equation 20: Source Strength Calculation

Where S is the source strength

M is the measured value

N is the chamber calibration factor (from calibration certificate)

P_{ion} is the inverse of the saturation and equals 1 for a chamber voltage > 300 V

k_{TP} is the air density correction described above

Interval measurements are recommended for low activities. The calibration uncertainty for the OncoSeed 6711 was stated as 3.7 % on the calibration certificate.

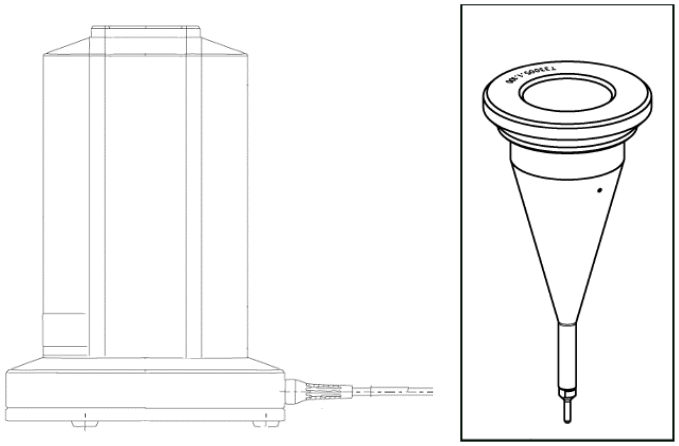

(a) (b)

Figure 39: (a) Diagram of the 4π Chamber (b) Diagram of the I-125 Seed Measurement Insert

3.2 The Medium Voltage Unit

The medium voltage unit at Groote Schuur Hospital was a single focus Philips HT100 unit (superficial therapy tube TÖ 100/8) with a stationary copper anode with a tungsten target. The nominal focal spot size was 4 mm x 4 mm, the anode angle was 45 ° and the beam filtration was a 1.2 mm Beryllium window. Different kV settings could be selected, and an additional filter was then added, depending on the tube voltage. Various applicator sizes were available for patient treatment *(Philips, 1967)*.

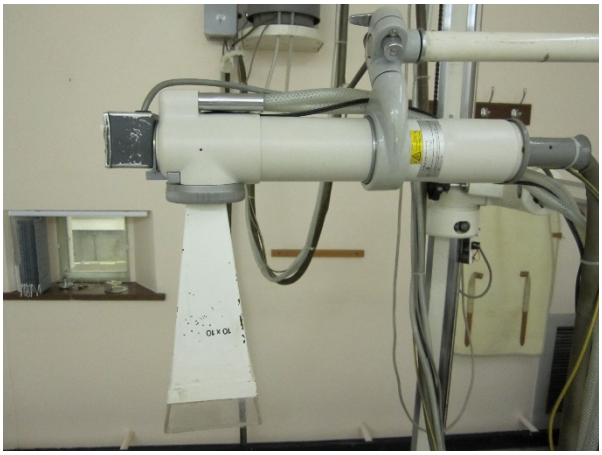

Figure 40: The Medium Voltage Unit at Groote Schuur Hospital

Figure 41: Tube Voltage Selection Options with Filters

This unit was initially used to calibrate gafchromic film and TLDs.

Previous work *(Hering, 1993)* using microdosimetry had shown that the dose normalized single event spectra for the OncoSeed 6711 I-125 seed and the 70 kV beam with 1.25 mm Al filtration were virtually identical.

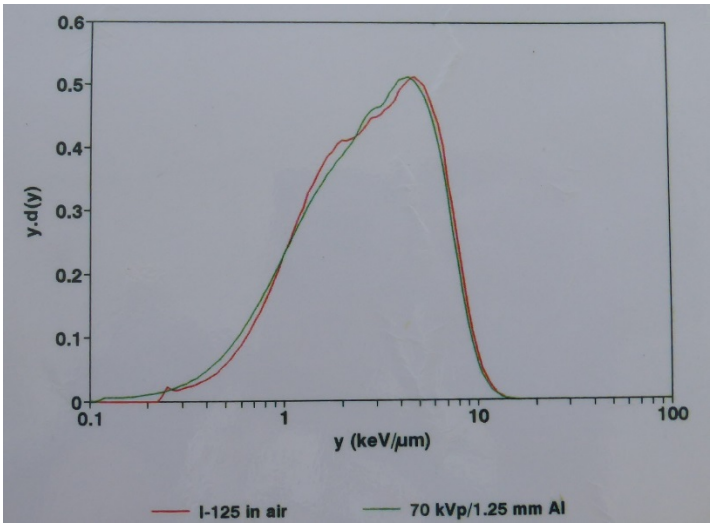

Figure 42: Comparison of Absorbed Dose Distributions in Lineal Energy Measured for the 6711 Seed and an X-Ray Field Generated by an Accelerating Potential of 70 kVp with 1.25 mm Al Filtration

These measurements were done using a tissue equivalent proportional counter with a calibrated dose response to low-energy X-rays.

Unfortunately, this medium voltage unit broke down irreparably during the course of this study.

3.3 The Cobalt Teletherapy Unit

Subsequent calibration of Gafchromic films and TLDs were done on a Theratron 780c Cobalt-60 teletherapy machine. Co-60 decays to Ni-60 with the emission of β-particles and two photons per disintegration of energies 1.17 MeV and 1.33 MeV. The β-particles are absorbed in the source housing, the useful beam is made up of these two γ-rays *(Khan and Gibbons, 2014)*.

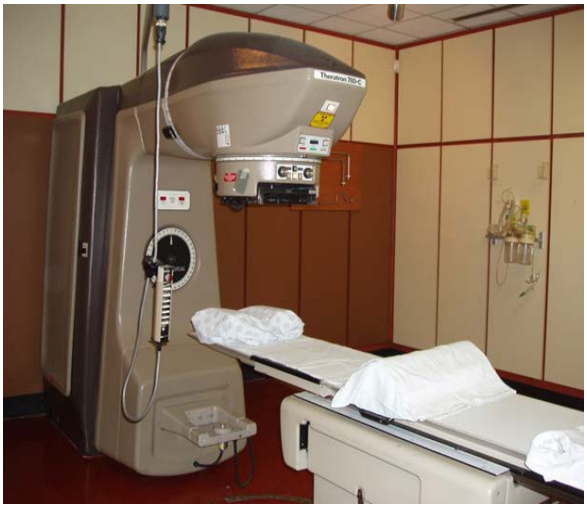

Figure 43: Theratron 780c Co-60 Teletherapy Unit

3.4 Gafchromic Film Calibration

Each set of film data had its own calibration curve. Calibration was done from 0.1 to either 5 Gy or 10 Gy, with at least eight data points per calibration. Some of the EBT2 films were calibrated in the 70 kV X-ray beam when the unit was still functioning. Dosimetry was done on the red colour channel of the image. This channel was extracted from the image using ImageJ Version 1.52a.

As described in the technical brief *(GAFCHROMIC_EBT2, 2009b)*, the density value was given by $\log_{10}$ (65535/scanner value) when using a 48 bit scanning protocol.

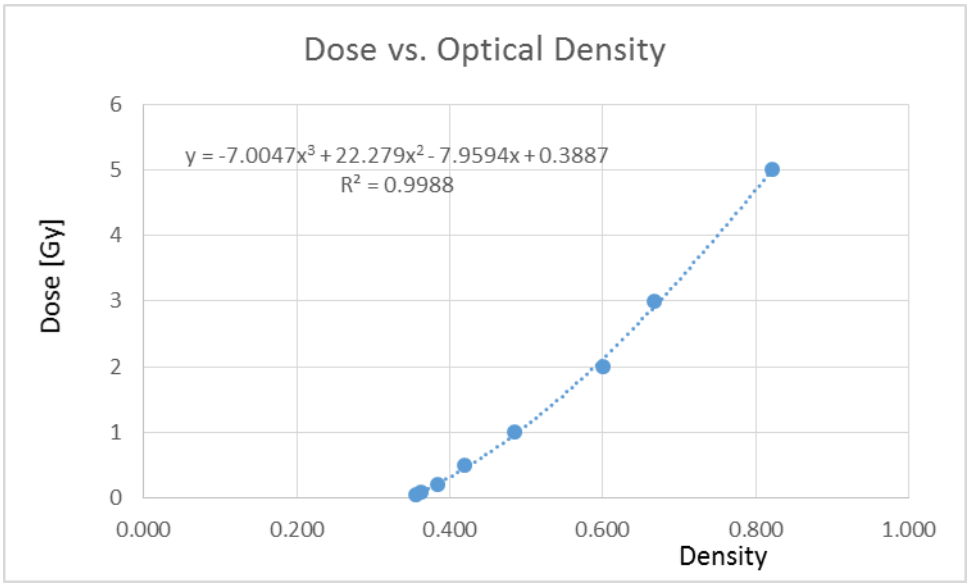

Figure 44: Sample Calibration for an EBT2 Film

A polynomial was fitted to the data. This allowed for the conversion of any obtained grayscale to dose.

For film calibration in the Cobalt-60 teletherapy unit, the film was placed in a 5 cm x 5 cm field at a depth of 5 cm in solid water, with adequate backscatter, and the film was irradiated with doses ranging from 0.05 Gy – 5.00 Gy. In the medium voltage unit film was calibrated in a 70 kV X-ray beam. The output of the unit was checked with a calibrated ionization chamber in terms of air kerma rate (no backscatter), using a 10 cm x 10 cm applicator with a tube current of 10 mA and 1.25 mm added Al filtration. At the measurement point 0.50 Gy was given in 6.33 minutes.

Film was then placed at the same position and irradiated to known doses.

3.5 Thermoluminescent Dosimeter Calibration

TLDs were calibrated in either a 70 kV X-ray beam or a Co-60 teletherapy beam. TLDs were irradiated to a known dose and the light output obtained from the TLD reader (REXON TLD Systems, Inc. UL-320). Each chip had a unique calibration, i.e. no batch calibration was done (see Figure 45 for a sample glow curve). TLD chips were annealed in an oven at 400 °C for 1 hour, followed by 100 °C for 2 hours before cooling back down to room temperature, as per departmental protocol.

In the medium voltage unit the TLDs were calibrated in air with a 10 cm x 10 cm applicator at 70 kV with a tube current of 10 mA and 1.25 mm of added Al filtration. At the point of measurement this meant that 0.50 Gy was given in 6.33 minutes. The tube output was confirmed with a calibrated ionization chamber before every calibration.

In the Cobalt-60 teletherapy unit the TLDs were calibrated in a 10 cm x 10 cm field with a dose of 1.00 Gy given at a depth of 5 cm. The dose rate of the unit was confirmed with a calibrated ionization chamber before calibration of the chips.

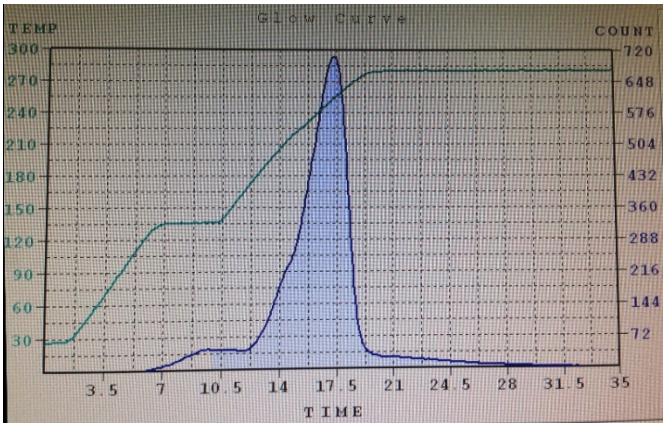

Figure 45: Sample Calibration Glow Curve

In Figure 45, the green line corresponds to the temperature, which rises sharply from room temperature to about 280 °C. The shaded blue region corresponds to the light

output of the exposed TLD chip, which increases dramatically at temperatures above 180 °C.

3.6 Detectors used for Measurements of the I-125 Spectrum

Spectral measurements of the OncoSeed 6711 source were done with a number of different detectors. The spectrum in air was used to determine the average energy of the I-125 seed, as well as its dose rate constant.

3.6.1 NaI(Tl) Scintillation Detector

In 1948, Robert Hofstadter *(Hofstadter, 1948)* demonstrated that crystalline sodium iodide, in which a trace of Thallium had been added, produced a large scintillation output. The NaI(Tl) crystal is commonly used, for example in gamma cameras *(Cherry et al., 2004)*. The crystal is still considered to have excellent light output, but it is hygroscopic and will get damaged if wet *(Knoll, 2010)*. The amount of light emitted by the NaI scintillator after a radiation interaction in the crystal is proportional to the energy deposited in the crystal. A photomultiplier tube (PMT) converts the light input into a measurable current output. The energy resolution is around 40 % at 10 keV, but improves to about 8 % at 140 keV.

Figure 46: The Thin-Window NaI Detector Coupled to a PMT

3.6.2 HPGe Detector

One of the major limitations of scintillation detectors is their poor energy resolution. Semiconductor detectors offer a better energy resolution. The motion of the electron-hole pairs created along the path of the charged particle through the detector give rise to an electronic signal, the strength of which is proportional to the energy deposited in the detectors *(Knoll, 2010)*.

The High-Purity Germanium (HPGe) detector used in this study was a Canberra model GC4520 detector. The detector operates at liquid nitrogen temperatures to prevent valence electrons from gaining sufficient energy to be elevated across the bandgap into the conduction band, which would give rise to an unwanted electric signal.

Figure 47: The HPGe Detector: Model GC4530

The detector has a closed-end co-axial geometry, is 59 mm long and has a diameter of 62.5 mm. The resolution is quoted as 2.0 keV FWHM at 1332 keV and 1.20 keV at 122 keV *(Canberra, 2016)*. The multi-channel analyzer was set to record measurements in 8192 channels at 524 eV/bin.

3.6.3 The Low-Energy Photon Spectrometer

Access was granted to the Low-Energy Photon Spectrometer (LEPS Detector) at the iThemba Laboratory for Accelerator Sciences (iThemba LABS) near Cape Town, South Africa. The LEPS detectors are four electrically segmented planar detectors (10 mm thick, 50 mm diameter), also using high purity Germanium, and are fitted with 300 µm thick Beryllium windows. They are designed to detect photons between 5 – 250 keV. The energy resolution was determined to be 0.8 keV at 40 keV. The multi-channel analyzer was set to bin spectral data into 1000 bins at 100 eV/bin. Similar to the HPGe detector, the LEPS detector also operates at liquid nitrogen temperatures *(Papka, 2013)*.

Figure 48: The LEPS Detector at iThemba LABS

3.6.4 The Silicon Drift Detector

The Amptek Silicon Drift Detector (SDD) is a type of photodiode with a unique electrode structure to improve performance *(R Redus, 2006, Amptek, 2013, Amptek, 2014a)*. A series of drift rings produce a radial field in the detector, guiding the electrons to a small anode. X-rays are incident as shown in the figure below, electrons are produced throughout the active volume and drift to the signal anode. X-rays interacting in the Silicon create an average of one electron/hole pair per 3.62 eV of energy lost in the silicon.

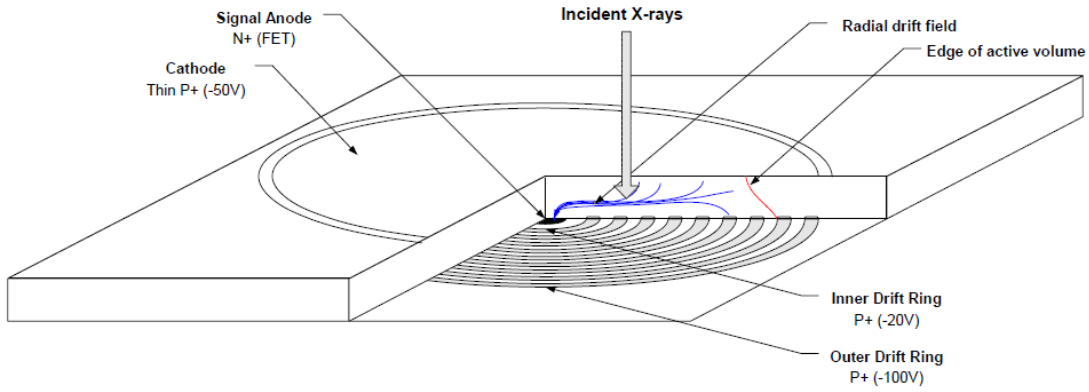

Figure 49: Design of the Amptek Silicon Drift Detector as Shown in the Pamphlet *(Amptek, 2015)*

The X-123 unit includes an X-ray detector and preamplifier, a digital pulse processor and multi-channel analyzer and a power supply in one small box that easily fits into the palm of a hand. The aluminium box size is 7 cm x 10 cm x 2.5 cm.

The detector requires a 5 V DC input and a USB connection to a computer. The X-123 is controlled by the Amptek ADMCA display and acquisition software.

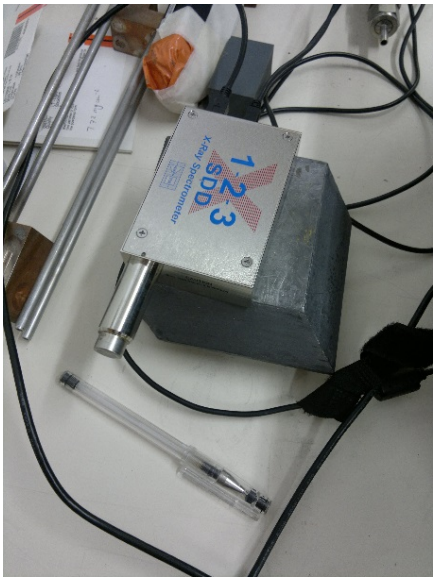

Figure 50: The X-123 Silicon Drift Detector

The SDD has a much lower capacitance than a conventional diode of the same area, reducing electronic noise (i.e. better energy resolution) at short shaping times (i.e. high count rates) *(Amptek, 2014b)*. The energy resolution is quoted by the manufacturer as 145 eV – 260 eV FWHM at 5.9 keV, depending on the detector, peaking time and temperature *(Amptek, 2015)*. The SDD is thermoelectrically cooled and does not operate at liquid nitrogen temperatures.

The entrance Be-window of the detector was specified as 0.5 mil (= 12,5 μm) thick. Over the range of I-125 energies, an efficiency correction needs to be applied to the measured spectra *(Amptek, 2014c)*.

X-ray fluorescence (XRF) is widely used to measure the elemental composition of materials *(Amptek, 2011)*. This detector was able to detect a number of K and/or L shell X-rays from Iodine, Tellurium, Silver and Titanium, the materials present in the OncoSeed 6711.

3.7 Measurements of the OncoSeed 6711 I-125 Seed Dosimetric Parameters

Two solid water phantoms were manufactured and used in the determination of various TG-43 parameters of the OncoSeed 6711.

This was done using both TLD chips and Gafchromic film.

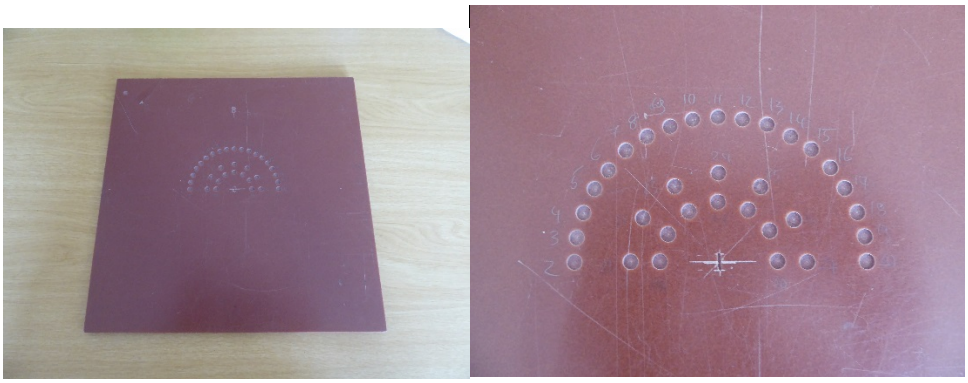

Figure 51: Solid Water Phantom with Slots for TLD Anisotropy Measurements for Different Angles at Distances of 2, 3 and 5 cm

Figure 52: Solid Water Phantom with Slots for TLD Radial Dose Function Measurements

A special Perspex jig was also manufactured for the in-air measurements of the I-125 seed spectrum at different angles and distances. The seed was placed on the rotational axis of the arm. The arm could be positioned at different angles relative to the detector, with lines scribed into the Perspex at 10° intervals. The detector was moved relative to the rotation axis to obtain results at different distances from the seed.

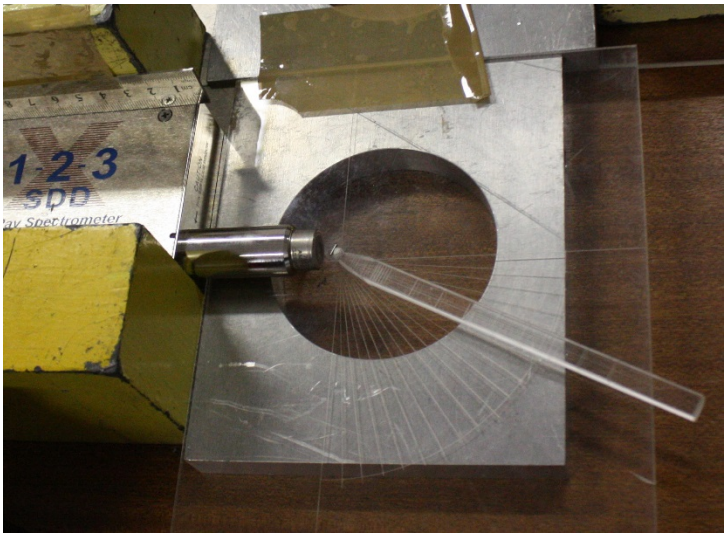

Figure 53: Perspex Jig for In-Air Measurements of the Seed Spectrum

3.7.1 Measurement of the Seed Anisotropy using Film

The OncoSeed 6711 anistropy was measured to a distance of 5 cm in solid water using gafchromic film (EBT2 and EBT3). A small recess was cut into a solid water plate to place a seed.

Film was sandwiched between solid water plates, with at least 10 cm of solid water on either side of the film for adequate scattering.

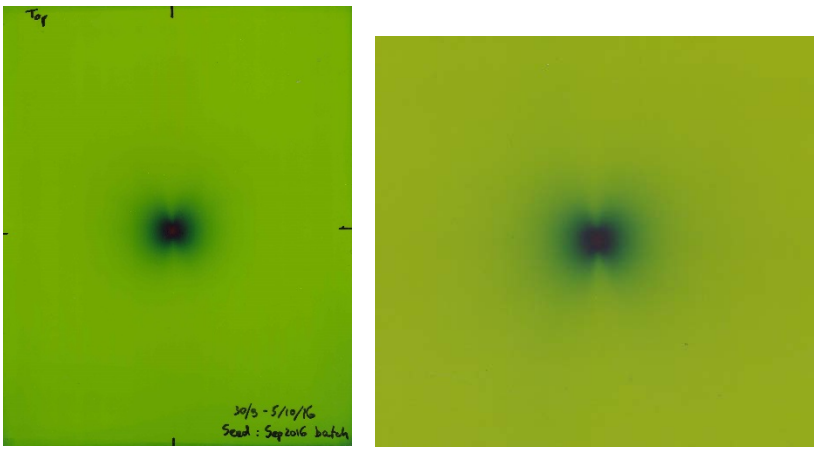

Figure 54: Anisotropy Image in Gafchromic EBT2 Film (Size Reduced for Display Purposes) (left) and EBT3 Film (Cropped for Display Purposes) (right)

The film dimensions were scaled in ImageJ according to known distances. Usually either the 8 inch or 10 inch side of the scanned film was used to set the global scale. The x and y co-ordinates of the center point of the seed were determined. For arbitrary r and θ the x and y co-ordinates are given by:

$x = r \cdot \cos \theta$

$y = r \cdot \sin \theta$

Equation 21: Determination of Co-ordinates

These were either added or subtracted from the center point to obtain co-ordinates for the readings for the anisotropy. A 1 mm x 1 mm region of interest was drawn and moved on the image to obtain the grayscales at each required position on the film.

The relative uncertainties were determined for each data point individually as follows:

The greyscale value in the red colour channel for each data point was determined in ImageJ from the scanned films, together with its standard deviation. The greyscale value was converted to dose using the predetermined calibration curve, as described in Chapter 3.4.

The upper–lower bound method of uncertainty propagation was applied as part of the error analysis *(Deardorff, 2018)*.

Thus, the mean minus the standard deviation and the mean plus the standard deviation of the greyscale value in each region of interest were also converted to dose. Half the difference between the maximum and minimum dose was expressed as a percentage difference from the dose of the mean greyscale value of the region of interest. This gives an uncertainty for each data point. Since the anisotropy includes a ratio of two doses ($\frac{\dot{D}(r,\theta)}{\dot{D}(r,\theta_0)}$), the final uncertainty for each data point was determined as the square root of the sum of squares of the individual uncertainties *(Topping, 1972)*.

3.7.2 Measurement of the Seed Anisotropy using TLDs

The phantom shown in Figure 51 was used to measure the anisotropy with TLDs at distances of 2 cm, 3 cm and 5 cm. Doses were measured at 0°, ± 30°, ± 60° and 90° at distances of 2 cm and 3 cm, and every 10 degrees at a distance of 5 cm.

The chip size was 3 mm x 3 mm x 0.9 mm.

The uncertainty was calculated individually for each data point. The standard deviation for each dose average (based on four data sets) was expressed as a percentage of the mean. The anisotropy includes a ratio of doses ($\frac{\dot{D}(r,\theta)}{\dot{D}(r,\theta_0)}$), therefore the final uncertainty was calculated as the square root of the sum of squares of the data point in question, as well as the one at θ = 90° at that distance *(Topping, 1972)*.

3.7.3 Measurement of the Radial Dose Function

The radial dose function was measured with gafchromic film and TLDs using the solid water phantom shown in Figure 52, once again with adequate scatter material and either side of the film or TLDs.

The radial dose function describes the dose fall-off in the medium along the transverse axis of the source (θ = 90°), taking into account the effects of scatter and absorption.

The radial dose function was measured to 5 cm with film and to 7 cm with TLDs.

The error bars for the film data were determined as follows: 1 mm x 1 mm regions of interest were drawn on the scanned film at distances r = 0.5 cm, 1 cm, 2 cm, 3 cm, 4 cm and 5 cm from the center of the seed. This was done in four directions on the film at angles 90° apart. The value of the red colour channel was used to compute the dose at each position and then the mean and standard deviation of the dose at each distance were determined. The standard deviation was expressed as a percentage of the mean. Since the radial dose function includes the ratio of two doses ($\frac{\dot{D}(r,\theta_0)}{\dot{D}(r_0,\theta_0)}$), the uncertainties

were added as the square root of the sum of squares of the individual uncertainties at the given radius and at r = 1 cm *(Topping, 1972)*.

The uncertainty for the TLD data was determined as follows: Six data sets of TLD readings were combined to determine the radial dose functions. Four data sets overlapped at 2.5 cm and three data sets overlapped at 5 cm to cover the whole range to a distance of 7 cm. Once the data was normalized to a distance of 2.5 cm, the standard deviation of the mean doses at each distance was determined. Once again, the uncertainties were added as the square root of the sum of squares of the individual uncertainties at the given distance and at r = 1 cm *(Topping, 1972)*.

3.7.4 Dose Rate Constant

The dose rate constant is defined as the ratio of the dose rate at the reference position (r = 1 cm and θ = 90°) in water and the air kerma strength S_K.

The units are cGy h^{-1} U^{-1}, which ends up being cm^{-2}.

$$\Lambda = \frac{\dot{D}(r_0,\theta_0)}{S_K} \qquad \text{(Equation 10)}$$

The air kerma strength conversion given in the manufacturer's specifications was used (5.2 mCi ≙ 6.60 μGy·m^2·h^{-1}) and corrected to the date of measurement. TLD doses were measured in the solid water phantom at 1 cm distance when the radial dose function was measured. The measured doses were converted to dose rates, using the equivalent time T_{eq} described in Chapter 2.6. The average of three runs was used to calculate Λ.

Additionally, the method described in *(Chen and Nath, 2001)* was applied to the measured spectrum to obtain a calculated dose rate constant. They derived a formula for calculating the dose rate constant of point sources with known energy spectra as:

$$\Lambda = \frac{\sum_i n_i \cdot E_i \cdot \left(\frac{\mu_{en}(E_i)}{\rho}\right)_{air} \cdot \Lambda(E_i)}{\sum_i n_i \cdot E_i \cdot \left(\frac{\mu_{en}(E_i)}{\rho}\right)_{air}}$$

Equation 22: Formula for Calculating the Dose Rate Constant

with a discrete energy spectrum E_i and n_i denoting the number of photons emitted with energy E_i per nuclear disintegration. $\left(\frac{\mu_{en}(E_i)}{\rho}\right)_{air}$ denotes the mass energy absorption coefficient for that particular energy in air and $\Lambda(E_i)$ is the dose rate constant for a mono-energetic photon source of energy E_i.

The formula *(Chen and Nath, 2001)* show for the dose rate constant for a mono-energetic photon source, $\Lambda(E)$, contains the ratio of the mass energy absorption coefficients of water and air, a term that includes the effect of photon attenuation and the buildup of scattered photons in water. They propose an eighth order polynomial function of log (E) to be used to fit $\Lambda(E)$, given by:

$$\Lambda(E) = \sum_{i=0}^{8} a_i \cdot [\log(E)]^i$$

Equation 23: Polynomial Fit for a Monoenergetic Dose Rate Constant

The coefficients of a_i are given in Table 9:

i	a_i
0	-27.204372
1	100.35773
2	-197.45012
3	238.76679
4	-175.76114
5	78.461086
6	-20.733211
7	2.9835859
8	-0.18021804

Table 9: Coefficients for the Polynomial Fit of Λ(E)

In addition, *(Chen and Nath, 2001)* also propose an eighth order polynomial function of log (E) to fit an equation to the mass-energy absorption coefficient of air, given in Equation 24:

$$\log\left(\frac{\mu_{en}(E)}{\rho}\right)_{air} = \sum_{i=0}^{8} b_i \cdot [\log(E)]^i$$

Equation 24: Proposed Fitting Function to Mass-Energy Absorption Coefficient of Air

The fitting parameters are given in Table 10:

i	b_i
0	759.01395
1	-3216.6698
2	5854.9415
3	-5963.47040
4	3714.66680
5	-1450.42860
6	347.23311
7	-46.67963
8	2.7023655

Table 10: Fitting Parameters for Mass-Energy Absorption Coefficient in Air

The units of energy are keV and the log = $\log_{10}$. The fitting functions are valid between 20 keV and 1 MeV and they explicitly state that all decimals should be used in the fitting procedure.

Measured and calculated dose rate constants are then compared to published data.

3.8 The "Claws"

Each leg of the "Claws" is designed to take up to four I-125 seeds. Standard seed co-ordinates are used for the dose calculation, the nominal positions of the center of each seed are given in the table below:

	Polar Co-Ordinates			Cartesian Co-Ordinates		
	r [cm]	θ [°]	φ [°]	X [cm]	Y [cm]	Z [cm]
Leg 1 Seed 1	1.2	60	-90	0.000	-1.039	0.600
Leg 1 Seed 2	1.2	85	-90	0.000	-1.195	0.105
Leg 1 Seed 3	1.2	110	-90	0.000	-1.128	-0.410
Leg 1 Seed 4	1.2	135	-90	0.000	-0.849	-0.849
Leg 2 Seed 1	1.2	60	0	1.039	0.000	0.600
Leg 2 Seed 2	1.2	85	0	1.195	0.000	0.105
Leg 2 Seed 3	1.2	110	0	1.128	0.000	-0.410
Leg 2 Seed 4	1.2	135	0	0.849	0.000	-0.849
Leg 3 Seed 1	1.2	60	90	0.000	1.039	0.600
Leg 3 Seed 2	1.2	85	90	0.000	1.195	0.105
Leg 3 Seed 3	1.2	110	90	0.000	1.128	-0.410
Leg 3 Seed 4	1.2	135	90	0.000	0.849	-0.849
Leg 4 Seed 1	1.2	60	180	-1.039	0.000	0.600
Leg 4 Seed 2	1.2	85	180	-1.195	0.000	0.105
Leg 4 Seed 3	1.2	110	180	-1.128	0.000	-0.410
Leg 4 Seed 4	1.2	135	180	-0.849	0.000	-0.849

Table 11: Seed Positions in the "Claws"

It should be noted that since the seeds are loaded into the "Claws" manually, the actual seed positions may be subtly different from the ones in the Table 11.

The original "Claws" were planned with nominal seed activities of 3.0 mCi each. For comparison purposes the "Claws" were planned with 3.0 mCi seeds for a treatment time of 1 hour. In practice different seed activities can be loaded or certain seeds can be left out to increase or decrease the dose to certain parts of the eye.

The seed positions from Table 11 were used to calculate the doses using TheraPlan Plus (TPP) Version 3.8 Build 500, the current treatment planning system in use at the hospital, as well as the Varian BrachyVision (version 15.6.05) treatment planning system, which was purchased to replace TPP. Two sets of plans were calculated with BrachyVision, one plan used the OncoSeed 6711 point source model, the other one

the line source model, but both using the TG-43 formalism. The Acuros BV algorithm was not available at the hospital.

3.9 Measurement of the Dose Distribution in the "Claws"

Two solid water phantoms to measure the dose distribution in the "Claws" were manufactured in the hospital workshop. These consisted of two halves of a sphere of 22 mm diameter, which is the inside diameter of the "Claws".

The first one of these phantoms had a small indent down the middle of the phantom on both halves to accommodate TLD chips of 3 x 3 x 0.9 mm dimensions exactly in the middle of the phantom (see Figure 55).

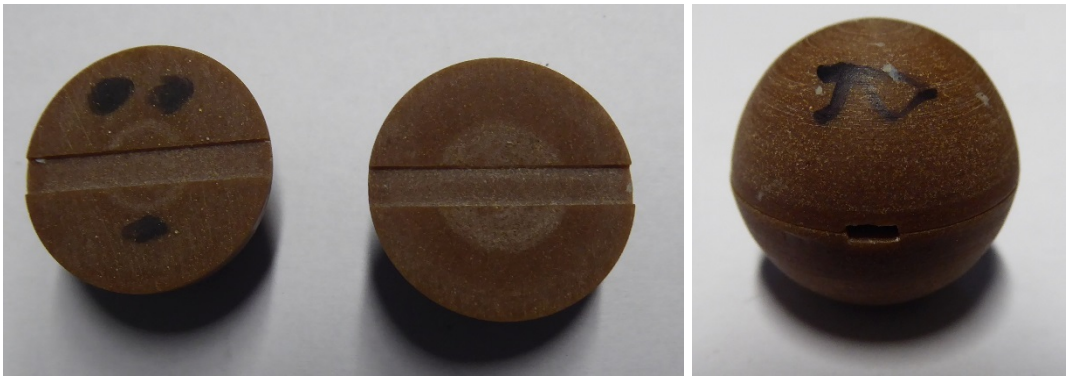

Figure 55: Solid Water Eye Phantom for TLD Measurements in the "Claws"

The second one of these phantoms had no additional modifications and was used for Gafchromic film measurements in the "Claws" (see Figure 56).

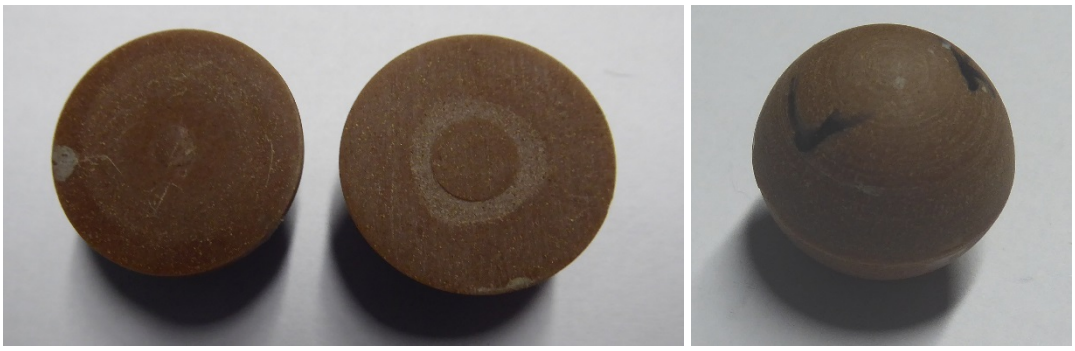

Figure 56: Solid Water Phantom for Gafchromic Film Measurements in the "Claws"

3.9.1 Thermoluminescent Dosimetry (TLD) and Gafchromic Film

TLD chips (Lot C-7-97-1) were used to measure to doses along the central axis of the specially designed solid water phantom, which was placed inside the “Claws” and irradiated.

The “Claws” have an inside diameter of 22 mm; therefore 7 chips could be placed side-by-side in the phantom.

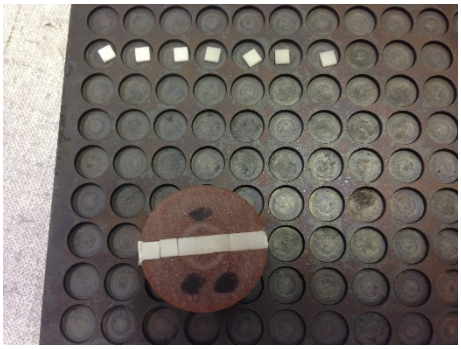

Figure 57: Seven TLDs in the Phantom

Figure 57 shows half of a solid water eye phantom loaded with seven TLDs (bottom of the picture). Additionally, another seven TLDs are ready to be annealed in the TLD annealing tray (as can be seen in the top of the picture).

Because of the inherent symmetry in the “Claws”, measurements were done in three orientations of the phantom, namely with the TLDs positioned from leg to leg (Figure 58), along the central anterior – posterior axis from the cornea of the eye to the retina (Figure 59), and with the TLDs rotated by a 45 ° angle with respect to the legs, which corresponds to the superior-inferior or lateral plane in the patient (Figure 60). Measurements were done with gafchromic film in the same planes.

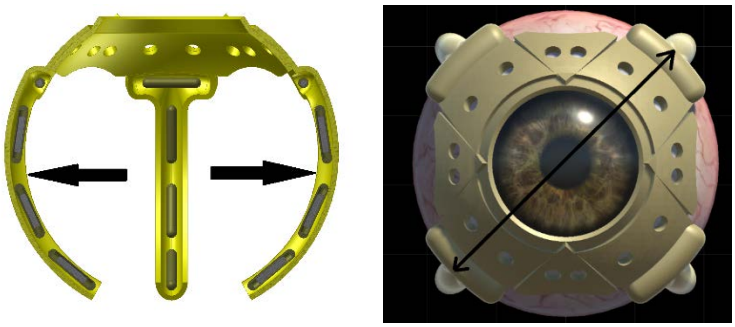

Figure 58: "Leg-to-Leg" Measurement on the Central Plane

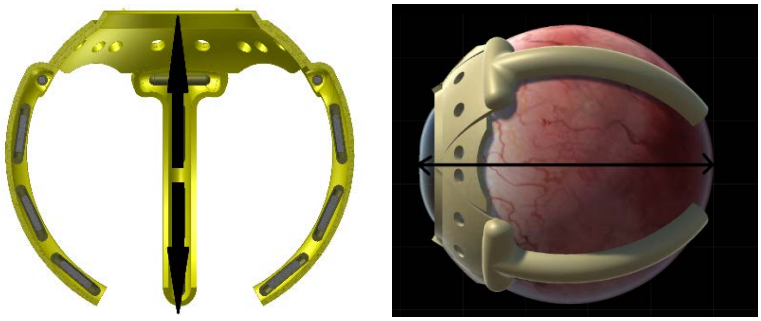

Figure 59: "Anterior-to-Posterior" Measurement

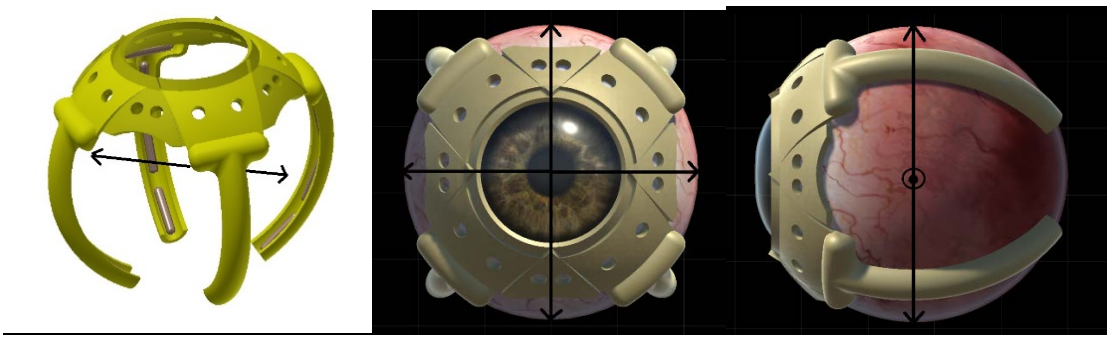

(a) (b) (c)

Figure 60: Sup/Inf or Lateral Measurement (Cylindrical Symmetry)

3.10 The CAD Model of the "Claws"

Computer Aided Design (CAD) drawings allow for easy replication of the design object in various file formats and would be needed for any commercialization of the "Claws". The "Claws" were initially manufactured by a jeweller based on the instructions of the oncologist. No formal drawings existed.

The "Claws" were carefully measured out with a Vernier Caliper and CAD drawings of the "Claws" were put together. The main programme used for this was AutoDesk Inventor 2013 and later 2015. However, during various stages of the project other drawing programmes were also tried and used, e.g. SolidEdge Student Edition (V105) when attempting to cut the "Claws" into slices, Blender 2.78b (for some of the graphics (and rendered by Unity 2018.2.10f1)), or the AutoDesk package (Inventor View, 123D_Make).

The drawings were saved and can be made available in a number of different file formats, either as a whole unit or as parts (four legs and a ring), e.g. .stl (stereolithography), .stp (STandard for the Echange of Product format), .iam (Autodesk Inventor Assembly file format), .ipt (part created with AutoDesk Inventor), .dwg (native CAD format), .igs (Initial Graphics Exchange Specification standard).

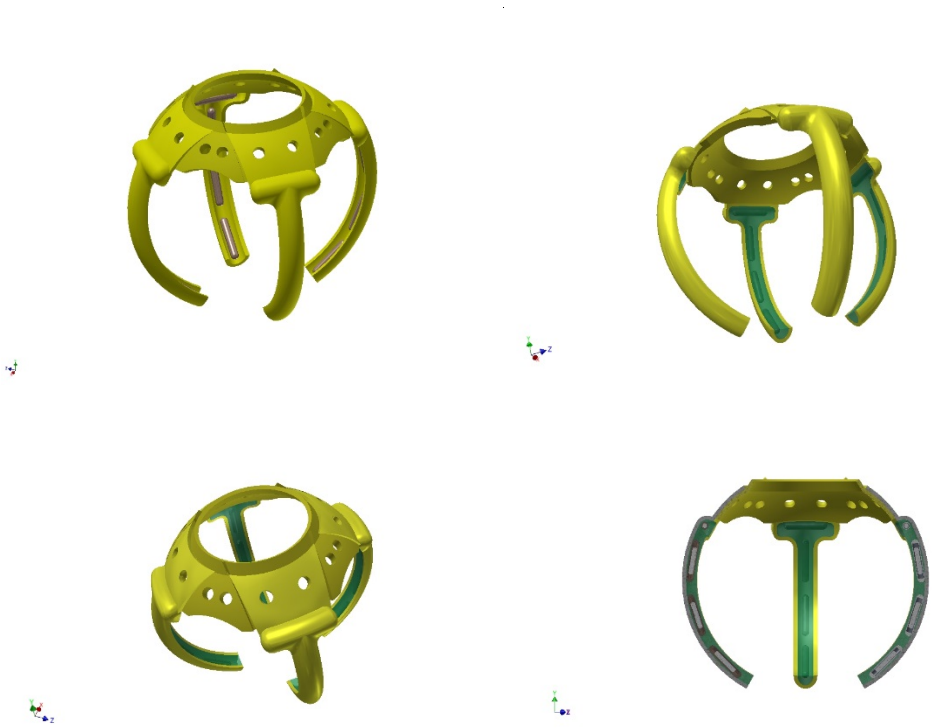

Figure 61: Images of the "Claws" Model

A method was also found to convert the CAD model of the "Claws" into an input file for Monte Carlo simulations, as described in Chapter 3.13.

3.11 Manufacture of PVC "Claws"

A "Claws" model was needed as input for the Monte Carlo simulations. One way of doing this in the egs_nrc code is to input a CT scan. A CT scan of the gold "Claws" would lead to severe artifacts, therefore PVC "Claws" were manufactured.

A model of the "Claws" was manufactured using a Haas VF8 CNC milling machine using PVC as the material. The South African Astronomical Observatory graciously allowed the use of their CNC milling machine for the manufacture of one PVC sample of the "Claws". The milling machine took the completed CAD drawing as input in the .stp format, using the Edgecam software.

This also involved trial and error. The half millimetre thickness of the “Claws” resulted in a very fragile PVC “Claws” that was already damaged during the manufacture and had to be redone.

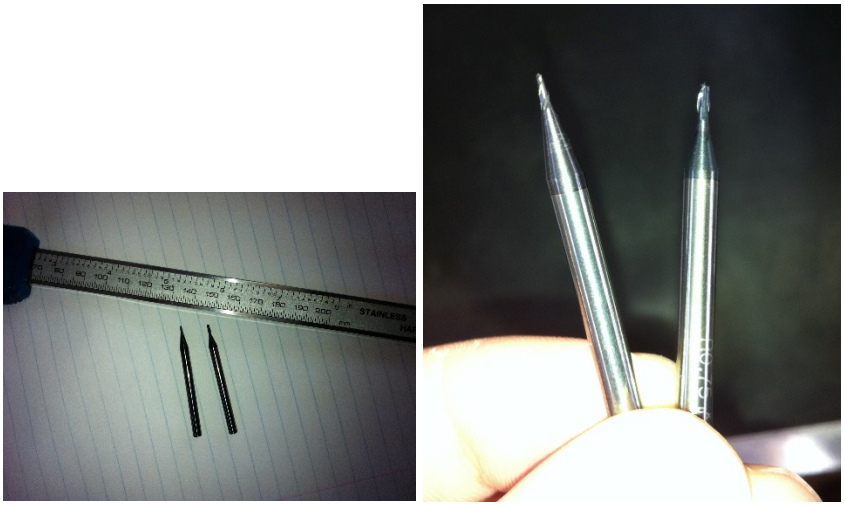

Figure 62: The Ballnose Cutters used during the Manufacture of the PVC “Claws”

The solution that eventually worked involved the milling of half of the ring and the legs of the “Claws”, filling the cast with Woods alloy, a low-melting point alloy, before resuming the milling process on the other side of the model. The alloy stabilized the model and prevented the collapse of the “Claws” during the milling process.

The 2 mm ballnose cutter was used initially during the milling process, the 1 mm ballnose cutter was used to finish off the “Claws”.

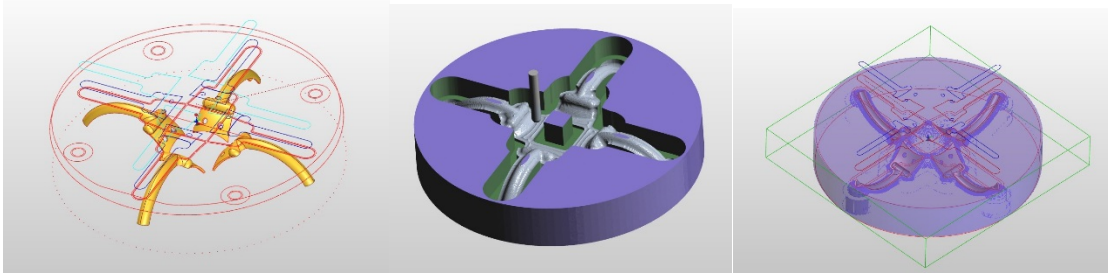

Figure 63: Images showing the Manufacture of the PVC Legs of the “Claws”

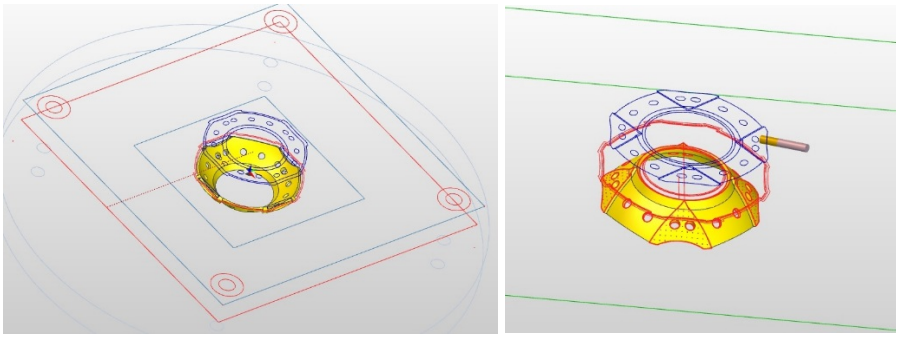

Figure 64: Images Showing the Manufacture of the PVC Ring of the "Claws"

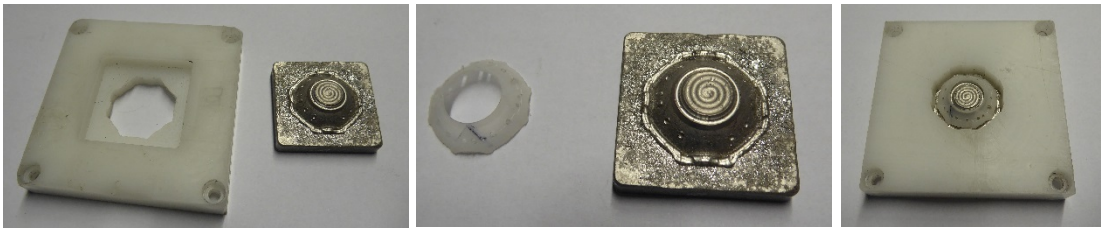

Figure 65: The Original PVC Block, the Woods Metal Insert Added for Stabilization and the Ring

Figure 66: The Woods Metal Insert Used for Stabilization During the Manufacture of the Legs

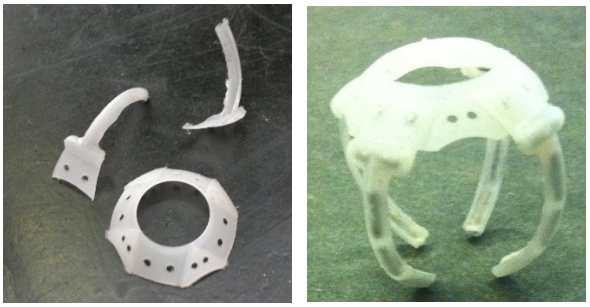

(a) (b)

Figure 67: (a) PVC Legs and Ring (b) PVC "Claws" Glued Together and Loaded with Seeds

Because of the complexity of the manufacturing process, the availability of the CNC milling machine and the cost involved, only a single PVC model was manufactured.

3.12 Attempts at Micro-CT Imaging of the "Claws"

Stellenbosch University has a micro-CT scanner *(du Plessis et al., 2016)* as part of the Central Analytical Facility of the university. The General Electric Vtomex L240 micro-CT scanner is situated in a walk-in cabinet and contains two X-ray tubes, which can be selected depending on the required task. Scanning of the PVC "Claws" was done at various resolutions: 20 µm, 50 µm, 100 µm and 200 µm. The micro-CT scan of the "Claws" was intended to be used as input for the Monte Carlo simulations.

(a) (b)

Figure 68: The micro-CT scanner at Stellenbosch University: (a) the Cabinet (b) the Two X-Ray Tubes inside the Cabinet

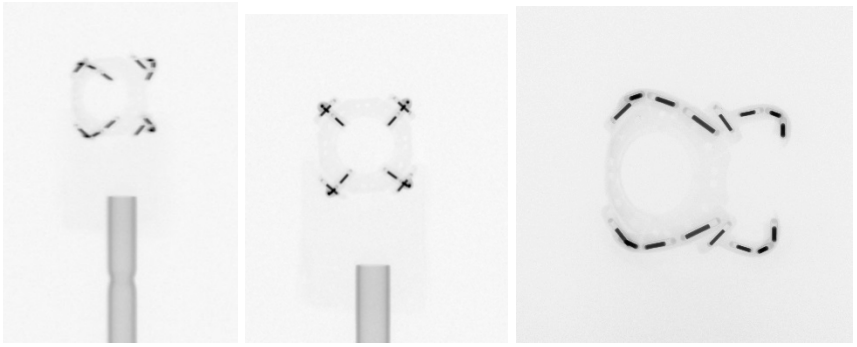

Figure 69: Various Micro-CT Projection Angles

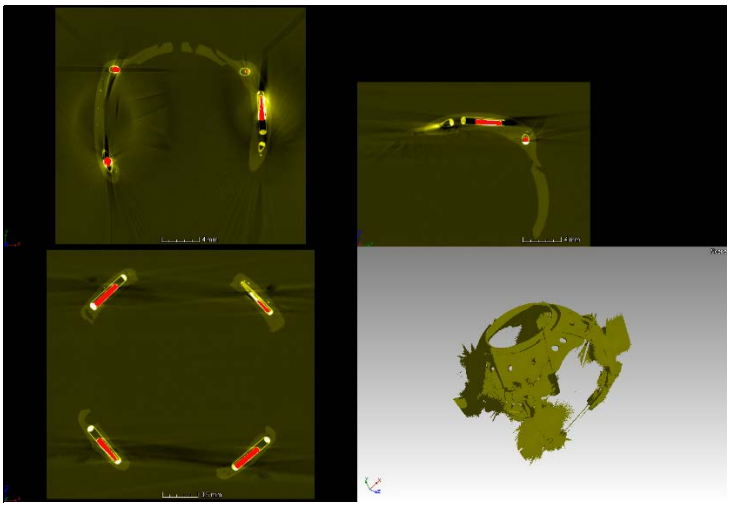

Figure 70: Image Reconstruction at 20 µm Resolution

Unfortunately very severe image artifacts became visible at all resolutions and at all tube potentials, due to the silver rods in the I-125 seeds.

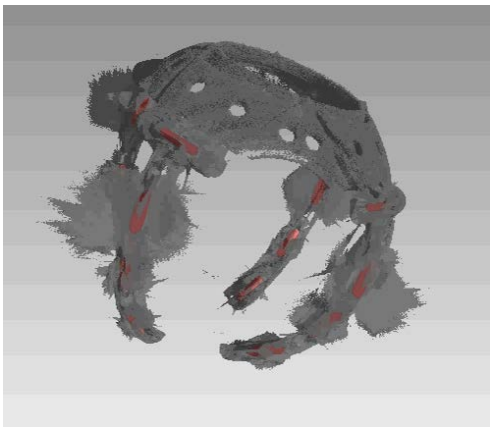

Figure 71: Severe Image Artifacts

Attempts to remove the I-125 seeds from the legs and to replace the seeds with a substitute were only partially successful; the PVC “Claws” with the substitute seeds were somewhat deformed and this meant that another attempt at micro-CT scanning the “Claws” was also unsuccessful.

The image analysis was performed with the software package Volume Graphics VGStudioMax 2.2. Fortunately this software package was able to use the CAD drawing as input and cut the “Claws” into DICOM slices.

This could be done at various resolutions:

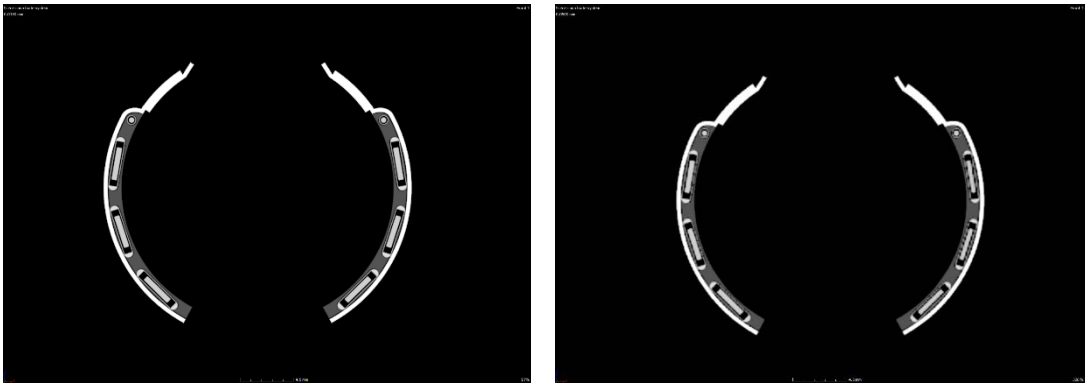

(a) (b)

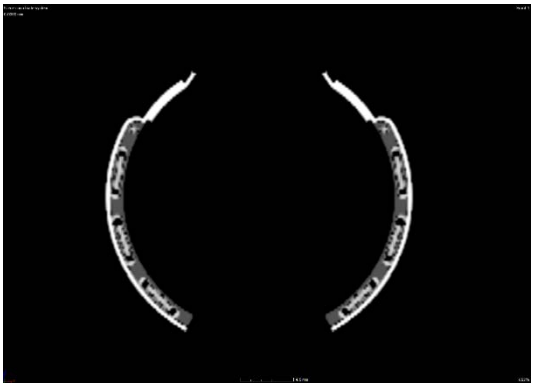

(c)

Figure 72: Sagittal View of the “Claws” at (a) 17 µm (b) 100 µm and (c) 200 µm

It was decided to use the 100 µm slices as input for the Monte Carlo simulations.

For the “Claws’” inner diameter of 22 mm this equates to 220 slices and a total of almost 10.000.000 voxels. Thinner slices meant an even higher number of voxels, thicker slices led to degraded resolution and problems in the creation of the Monte Carlo input phantom file because of the blurring of the edges, as is visible in Figure 72c.

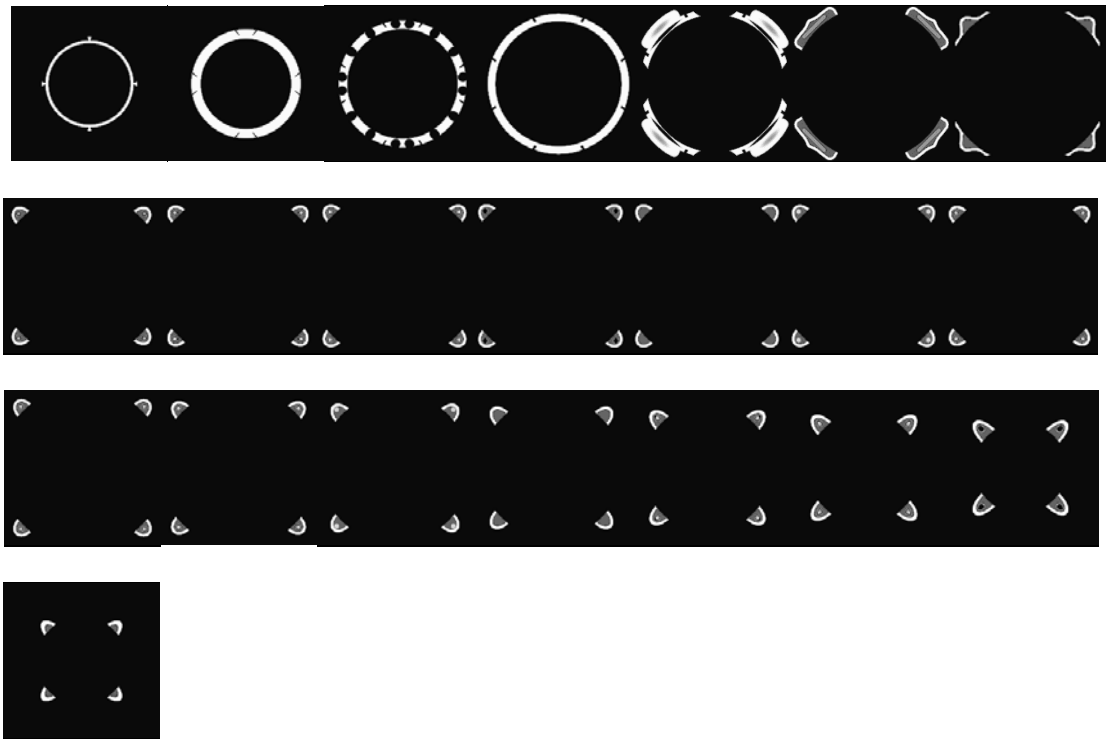

Figure 73: 100 µm Slices of the "Claws" Shown Every 1 mm

3.13 Conversion of the CAD Model to a Phantom File

The CAD model was cut into 0.1 mm slices in the DICOM image format.

The sliced Dicom images of the "Claws", as shown in section in the previous figure (Figure 73), first had to be converted into a readable egsphant file. This was done as a two-step process: first the Dicom images were converted to a *.txt file using Matlab. The following materials of the "Claws" had a greyscale assigned in the Dicom images: the background (water), the gold of the "Claws" and the acrylic, which is used to fill the legs once the seeds are glued into position. The text file now contained the greyscales as text, but with more than one greyscale value in the transition zone from one material to another one, because of partial voluming.

A sharpening filter / ramp filter was applied to the data to sharpen the edges and remove the partial voluming. This was done in IDL by assigning a single greyscale value per material across a range of greyscale values that each material had. The ramp filter was applied in the following way for a 256 greyscale image:

For each voxel
    If that voxel had a greyscale value between 0 and 10 → water
    If that voxel had a greyscale value between 10 and 101 → acrylic
    Else → gold
End For Loop

Initially there were a few other greyscale levels in between, to distinguish between the different materials of the I-125 seed. However, the egs_brachy built-in seed model was used for the simulations.

The correct densities were then assigned to each greyscale.

The final phantom file had dimension of 301 x 301 x 301 voxels for a total of 27.270.901 voxels, with the "Claws" centered in the phantom.

The first and last 25 voxels in the X, Y and Z directions had dimensions of 1.0 mm x 1.0 mm x 1.0 mm. All the other voxels had dimensions of 0.1 mm x 0.1 mm x 0.1 mm.

The final egsphant file had a size of 453.465 kB.

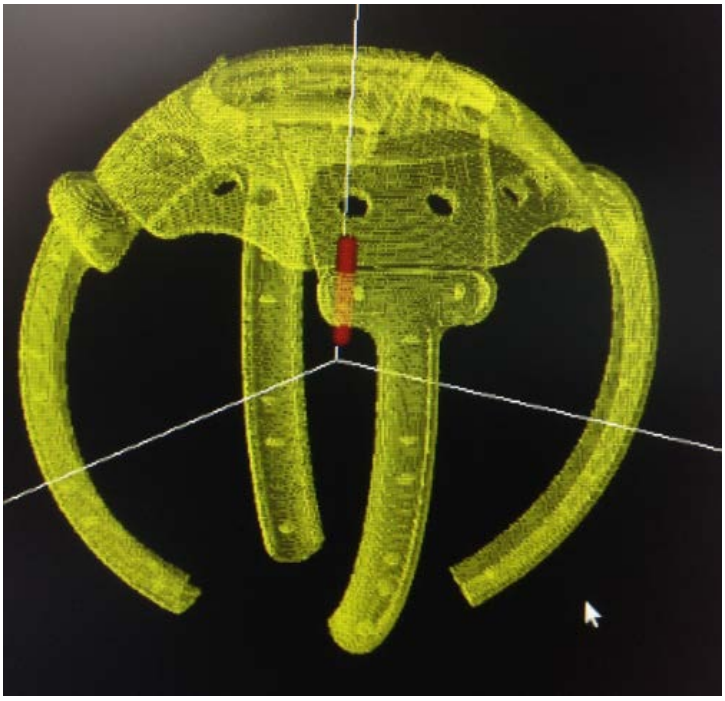

Figure 74: Image of the Monte Carlo "Claws" Model. One seed is included, but not yet in the right position or orientation.

3.14 Description of Monte Carlo Parameters Used (egs_brachy parameters)

Chapter 3.13 describes how the egsphant file was put together.

The “lib/media/material.dat” file included all materials needed for the simulations, therefore all simulations could be run in “pegsless” mode. The file egs_brachy/lib/muen/brachy_xcom_1.5MeV.dat contained the required mass energy absorption coefficients.

The media of importance are:

```
medium = WATER_0.998          (water)
rho = 0.998
elements = H, O
number of atoms = 2, 1

medium = acrylic              (acrylic)
rho = 1.18
elements = H, C, O
number of atoms = 8, 5, 2

medium = Au                   (gold)
rho = 19.32
elements = Au
```

The OncoSeed 6711 is included as a standard seed in egs_brachy *(Chamberland et al., 2016)*. This means that Titanium, Silver, Air and the AgBr/AgI mixture from the radioactive layer of the seed are also included for modelling.

The proposed spectrum (I125_NCRP_line) was used; it is shown in Figure 75. The spectrum includes the Te characteristic X-rays, but excludes the silver X-rays, as these will be produced during the Monte Carlo simulations.

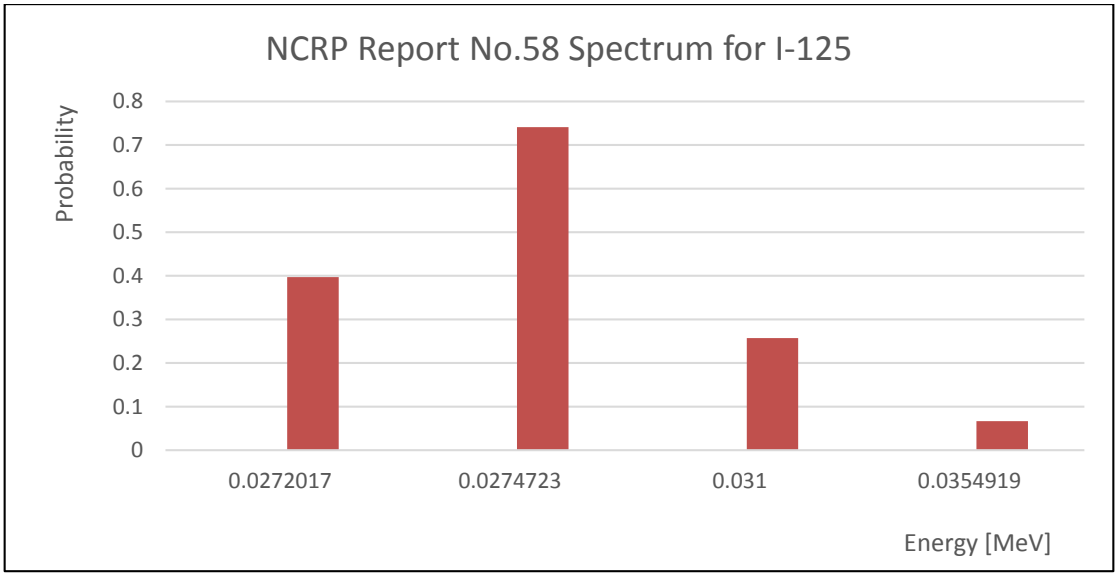

Figure 75: NCRP Report No. 58 Spectrum for I-125

The spectrum shows the $K\alpha_2$ X-rays at 27.202 keV, as well as the $K\alpha_1$ X-rays at 27.472 keV. The $K\beta$ X-rays are averaged to 31 keV. The peak at 35.5 keV corresponds to the photopeak energy of I-125.

The seed co-ordinates and rotation angles of the seeds are user supplied. A large number of "geometry errors" occurred initially, because of overlap of the various geometries of the "Claws" with the seeds. This was a software bug and Marc Chamberland, one of the authors of egs_brachy, proposed creating a wrapper around each seed (with radius = 0.045 cm) when contacted by email. This solved the problem.

The upper and lower energy thresholds for the creation of electrons (AE, UE) and photons (AP, UP) were set at:

AE = 0.512 MeV (i.e. electron rest energy of 511 keV plus 1 keV)

UE = 2.012 MeV

AP = 0.001 MeV (cut-off at 1 keV)

UP = 1.500 MeV

The fluorescent photon cutoff was also set at 1 keV. Rayleigh scattering and electron impact ionization were switched on. The standard NRC bremsstrahlung cross section database was used for the simulations.

Transport parameter and cross section options *	
Photon cross sections	xcom
Pair cross sections	BH
Pair angular sampling	Simple
Triplet production	Off
Bound Compton scattering	Norej
Radiative Compton corrections	Off
Rayleigh scattering	On
Atomic relaxations	eadl
Photoelectron angular sampling	On
Photonuclear attenuation	Off
Brems cross sections	NRC
Brems angular sampling	KM
Spin effects	On
Electron Impact Ionization	ik
Boundary crossing algorithm	EXACT
Electron-step algorithm	EGSnrc
* see description of parameters below	

Table 12: Monte Carlo Transport Parameter and Cross Section Options

No variance reduction was applied. The maximum fractional energy loss per step was set to 0.25 (25 %).

The following option descriptions are taken from *(Rogers et al., 2009)* and *(Kawrakow et al., 2019)*:

Photon cross sections: The “xcom” setting uses the Berger and Hubbell XCOM photon cross section database *(Berger and Hubbell, 1987)*.

Pair cross section refers to paid production cross sections, which are irrelevant for the low energies of I-125. BH refers to Bethe-Heitler pair production cross sections.

Pair angular sampling set to “Simple” turns on the leading term of the angular distribution, which is sufficient for most applications. It is irrelevant for the low energies of I-125, as is triplet production.

Bound Compton scattering should be switched on for low-energy applications. In the setting “Norej” the actual total bound Compton cross section is used.

Radiative Compton corrections were switched off (default).

Rayleigh scattering should be turned on for low energy applications.

Atomic relaxations: Relaxations of vacancies with binding energies above 1 keV are explicitely modeled. Such vacancies can be created in photo-absorption, bound Compton scattering, and electron impact ionization events. All radiative and non-radiative transitions from/to the K, LI, LII and LIII shells are taken into account. Transitions from/to M and N shells are taken into account using “average” M and N shell binding energies.

If photoelectron angular sampling is “on”, Sauter’s formula *(Sauter, 1931)* is used to determine the angle of the photoelectron. If it is “off”, photo-electrons get the direction of the ‘mother’-photon.

Photonuclear attenuation is not relevant for the low energies of I-125 and was switched off.

There are various options for the bremsstrahlung cross-section database: the Bethe-Heitler cross sections are used if “BH” is selected, when “NIST” is selected the NIST bremsstrahlung cross section data base is used, which is the basis for the ICRU radiative stopping powers. If “NRC” is selected, the NIST data includes additional corrections for electron-electron bremsstrahlung. “NRC” was selected for this work.

The bremsstrahlung angular sampling is set to KM (Koch-Motz) *(Koch and Motz, 1959)*, which shows an improvement of handling kinematics at low energies, compared to the “Simple” option.

The spin effects should be switched on for electron elastic scattering and are necessary for good backscattering calculations.

Electron impact ionization: EGSnrc has the ability to simulate the creation of inner shell vacancies by electron impact for all K- and L-shells with binding energies above 1 keV. The setting “ik” makes use of Kawrakow’s theory to derive electron impact ionization cross-sections *(Kawrakow, 2002)*.

The EXACT boundary crossing algorithm means that the algorithm will cross boundaries in a single scattering mode. This is the default selection.

The default EGSnrc electron-step algorithm has been shown to produce artifact free results at the sub 0.1 % level. According to an EGSnrc summary *(Kawrakow and Rogers, 2007)* it is the most accurate electron-step algorithm currently known.

3.15 egs_brachy

After the model was fine-tuned and all the bugs were fixed, the final Monte Carlo run was done on the High Performance Computing Cluster (HPC) at the University of the Free State.

No variance reduction was applied.

64.000.000.000 particle histories were simulated on 32 cores at the HPC. The simulation took 11 days to complete (CPU time = 266.6 hours).

Each core calculated 2.000.000.000 histories, divided into 10 batches each. Each batch had an average uncertainty of ~ 1.50 % (range: 0.94 % - 2.96%), as given by the simulation information output file.

It is somewhat sobering to realize that 64 billion histories corresponds to an actual irradiation time (with 16 x 3 mCi seeds) of just over 36 seconds.

CHAPTER 4 RESULTS

4.1 The OncoSeed 6711 I-125 Seed

For this study, 11 decayed seeds were cut open and magnified under a microscope (Figure 76). The bevelled edge is clearly visible, but not consistent.

(Dolan et al., 2006) observed the beveling angle to be 45 ° ± 10 %.

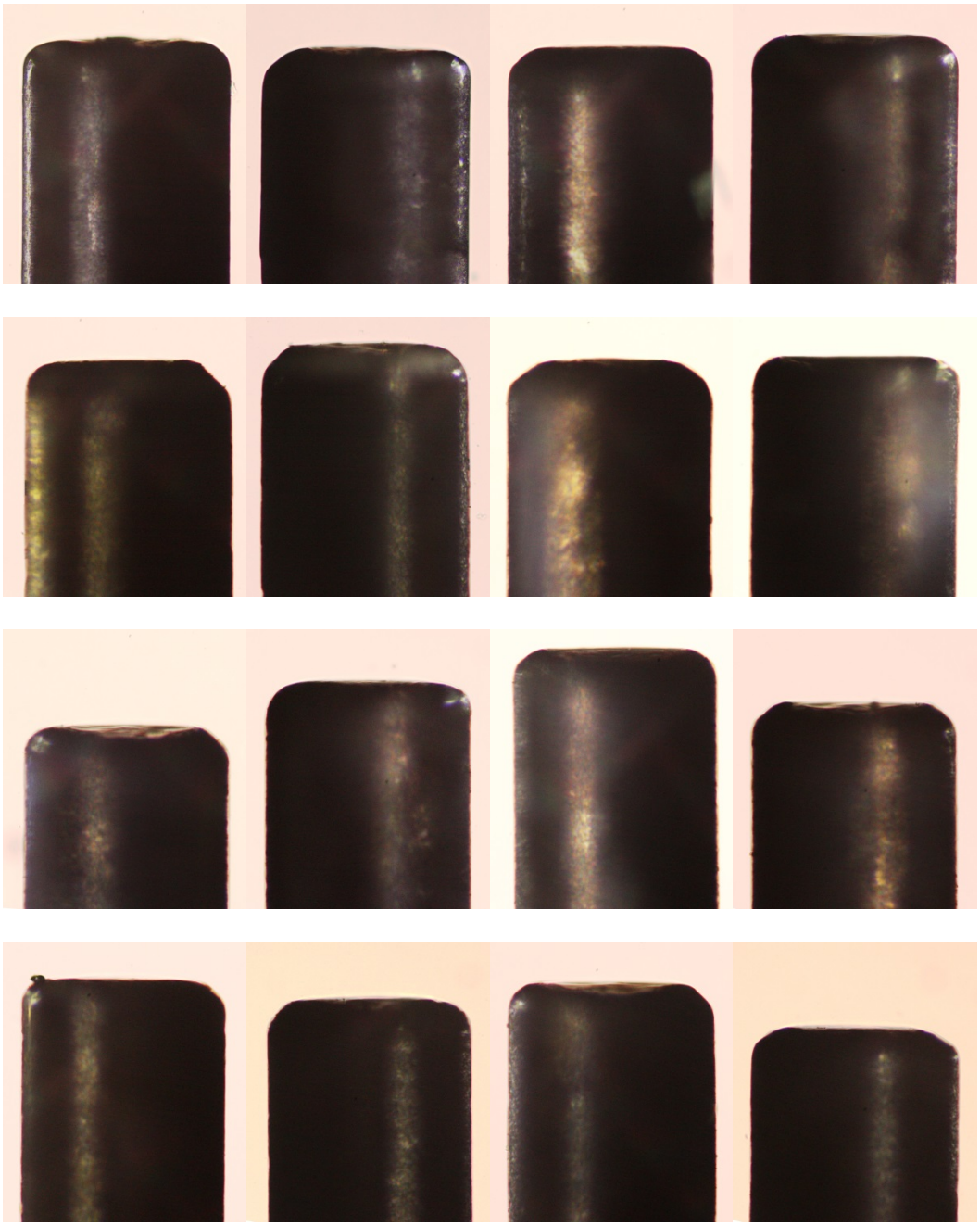

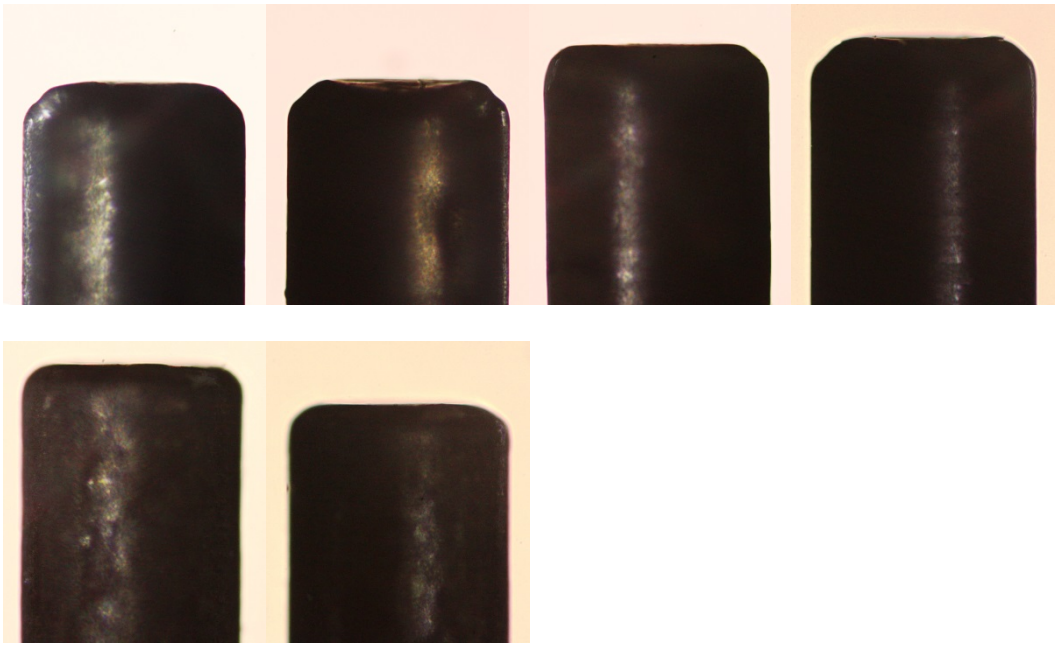

Figure 76: The Ends of 11 Seeds Magnified 100 Times under a Microscope

Macro photography also shows the beveled edge (Figure 77a). It also gives an idea of the slightly grainy consistency of the coating on the seed (Figures 77b, c):

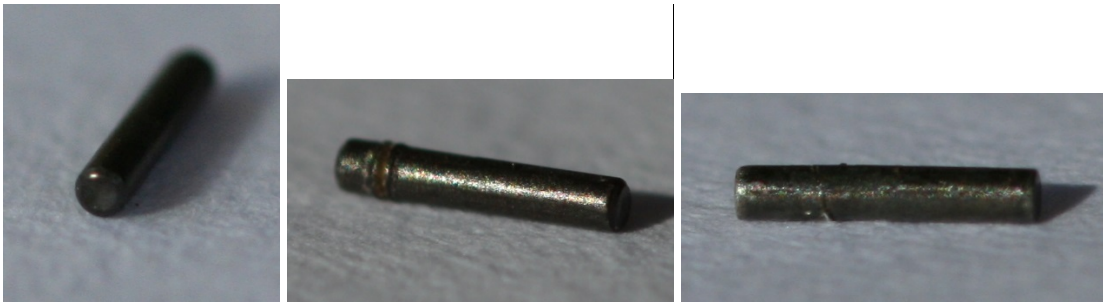

Figure 77 a, b, c: Macro Photographs of the Silver Rod

In Figure 77b damage to the silver rod is visible. This happened when the seed was cut with a scalpel. For interest's sake, a whole seed is also shown in Figure 78.

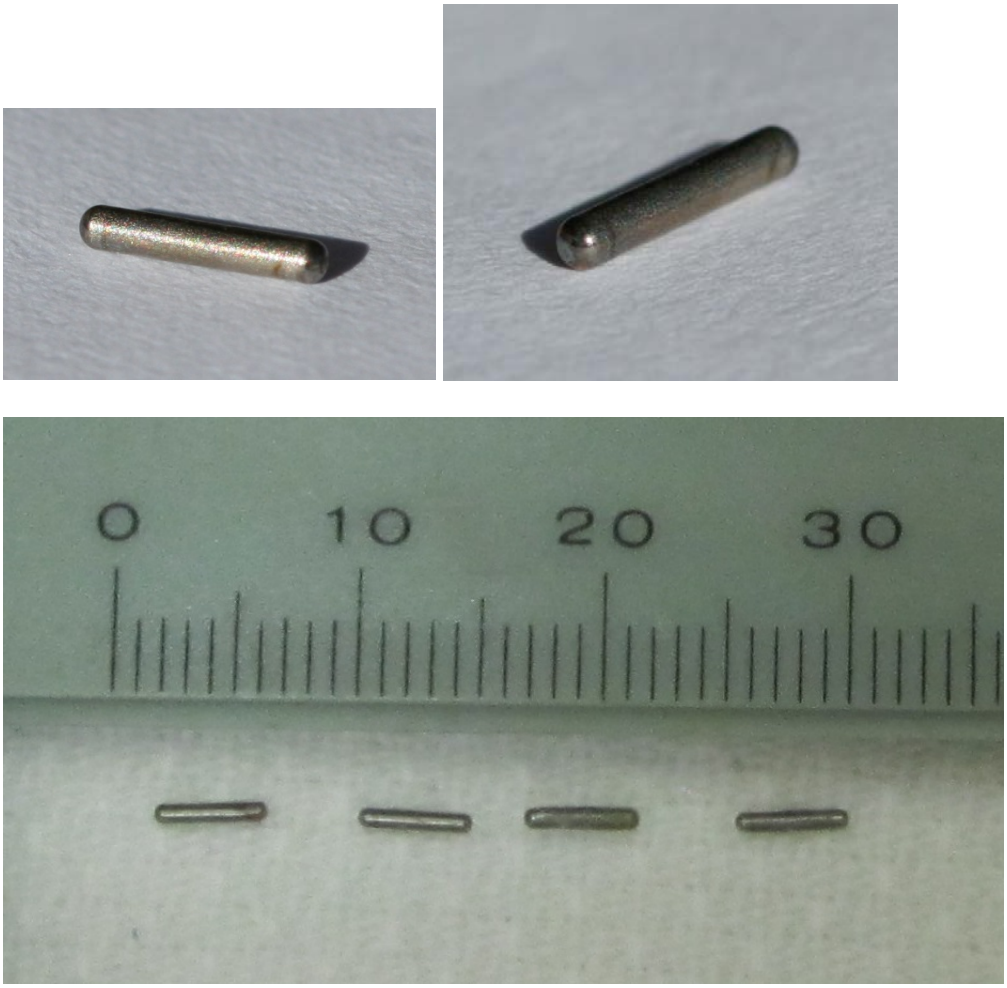

Figure 78: The Titanium Casing

Seed dimensions of 20 seeds were confirmed with a Vernier Caliper accurate to 0.02 mm.

These are given in the Table 13:

Seed	Titanium Casing Length [mm]	Titanium Casing Diameter [mm]	Silver Rod Length [mm]	Silver Rod Diameter [mm]
1	4.62	0.80	2.86	0.52
2	4.64	0.82	2.88	0.50
3	4.58	0.80	2.86	0.50
4	4.62	0.80	2.86	0.54
5	4.64	0.78	2.88	0.50
6	4.68	0.80	2.86	0.52
7	4.62	0.78	2.80	0.48
8	4.54	0.80	2.86	0.54
9	4.52	0.80	2.84	0.50
10	4.56	0.80	2.84	0.56
11	4.60	0.82	2.84	0.50
12	4.70	0.84	2.88	0.52
13	4.66	0.78	2.84	0.50
14	4.64	0.78	2.88	0.52
15	4.72	0.78	2.88	0.50
16	4.66	0.80	2.86	0.48
17	4.64	0.78	2.80	0.54
18	4.60	0.78	2.80	0.50
19	4.52	0.80	2.86	0.50
20	4.52	0.78	2.90	0.50
Average [mm]	4.61 ± 1.28%	0.80 ± 2.09%	2.85 ± 0.99%	0.51 ± 4.11%

Table 13: Measured Seed Dimensions

These dimensions agree with the dimension given in *(Dolan et al., 2006)* to within a standard deviation. A CAD drawing of the seed was made (Figure 79), based on the dimensions of *(Dolan et al., 2006)*:

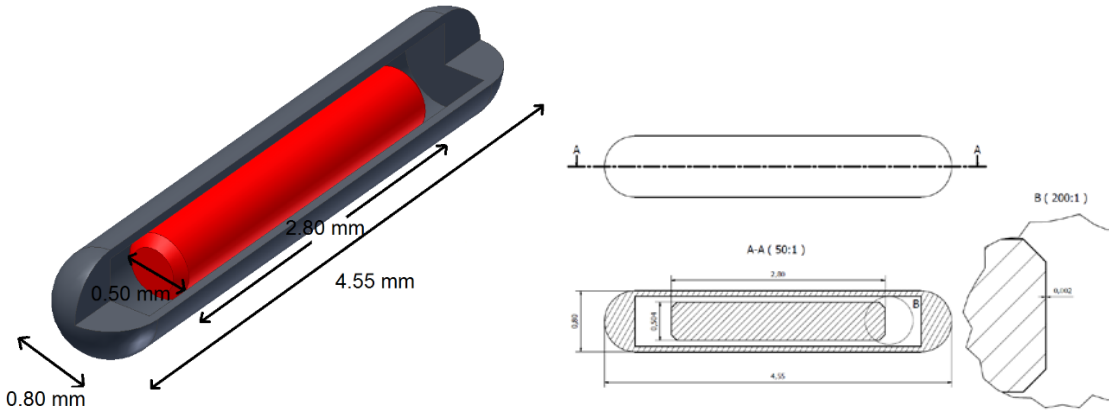

Figure 79: The OncoSeed 6711

Similar to the data from the CLRP TG-43 parameter database, the radioactive coating was assumed to have a thickness of 1.75 μm over the entire surface of the rod.

4.1.1 The Geometry Function for the OncoSeed 6711

The geometry function is simply given by the inverse square correction for the point source approximation, but for the line source approximation is given by Equation 12 in Chapter 2.7.3.

$$G_L(r,\theta) = \begin{cases} \frac{\beta}{L\, r\, sin\theta} & if\ \theta\ \neq 0^{\circ} \\ \left(r^2 - \frac{L^2}{4}\right)^{-1} & if\ \theta = 0^{\circ} \end{cases} \qquad \text{Equation 12}$$

with L, β and r defined in Figure 32 in Chapter 2.7, but also shown below for quick reference:

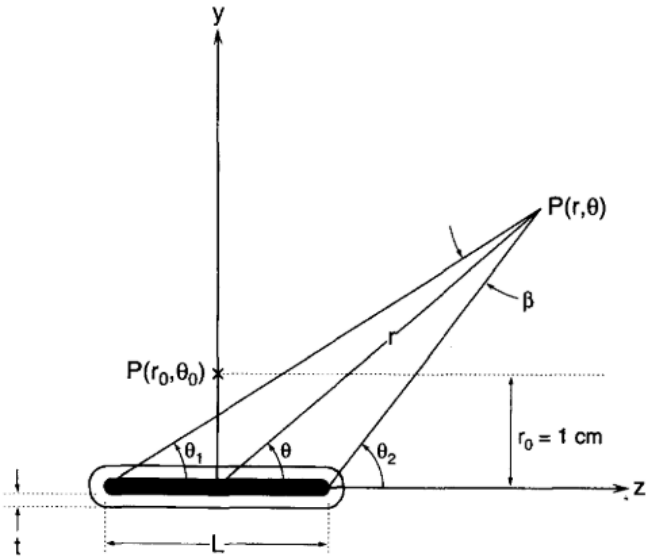

Using simple trigonometry it can be shown that:

$$\theta_1 = \tan^{-1}\left(\frac{r\cdot\sin(\theta)}{r\cdot\cos(\theta)+\frac{L}{2}}\right) \quad \text{and} \quad \theta_2 = \tan^{-1}\left(\frac{r\cdot\sin(\theta)}{r\cdot\cos(\theta)-\frac{L}{2}}\right) \quad \text{with } \beta = \theta_2 - \theta_1$$

Equation 25: Determination of θ_1 and θ_2

(King et al., 2001) goes on to show that β can be expressed as:

$$\beta = sin^{-1}\left(\frac{L \cdot \sin(tan^{-1}\left\{\frac{[r \cdot \sin(\theta)]}{\left[r \cdot \cos(\theta) - \frac{L}{2}\right]}\right\})}{\sqrt{[r \cdot \sin(\theta)]^2 + \left[r \cdot \cos(\theta) + \frac{L}{2}\right]^2}}\right)$$

Equation 26: Determination of β

Using the line source approximation with L = 2.85 mm, the following was calculated:

r↓ \ θ→	0 °	10 °	20 °	30 °	40 °	50 °	60 °	70 °	80 °	90 °
0.5 cm	4.3536	4.3369	4.2900	4.2215	4.1426	4.0642	3.9950	3.9416	3.9081	3.8967
1 cm	1.0207	1.0199	1.0174	1.0136	1.0091	1.0043	0.9999	0.9964	0.9941	0.9933
2 cm	0.2513	0.2512	0.2511	0.2508	0.2506	0.2503	0.2500	0.2498	0.2496	0.2496
3 cm	0.1114	0.1114	0.1113	0.1113	0.1112	0.1112	0.1111	0.1111	0.1110	0.1110
4 cm	0.0626	0.0626	0.0626	0.0626	0.0625	0.0625	0.0625	0.0625	0.0625	0.0625
5 cm	0.0400	0.0400	0.0400	0.0400	0.0400	0.0400	0.0400	0.0400	0.0400	0.0400
6 cm	0.0278	0.0278	0.0278	0.0278	0.0278	0.0278	0.0278	0.0278	0.0278	0.0278
7 cm	0.0204	0.0204	0.0204	0.0204	0.0204	0.0204	0.0204	0.0204	0.0204	0.0204
8 cm	0.0156	0.0156	0.0156	0.0156	0.0156	0.0156	0.0156	0.0156	0.0156	0.0156
9 cm	0.0123	0.0123	0.0123	0.0123	0.0123	0.0123	0.0123	0.0123	0.0123	0.0123
10 cm	0.0100	0.0100	0.0100	0.0100	0.0100	0.0100	0.0100	0.0100	0.0100	0.0100

Table 14: The Geometry Function for the OncoSeed 6711

This data matches data from a nominal 3 mm source to within 1 % at 0.5 cm, 0.23 % at 1 cm and less than 0.06 % from 2 cm onwards.

While θ_1 will always be less than 90°, θ_2 will be greater than 90° for certain angles when θ approaches 90°. This will make cos θ < 0. For these angles 180° will have to be added to θ to make cos θ > 0, as shown in Figure 80.

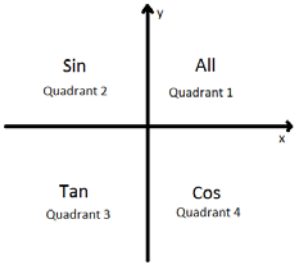

Figure 80: Trigonometry Ratios that are Positive in the Four Quadrants

Table 15 shows the calculated normalized geometry function for a 2.85 mm line source, given by $r^2 \cdot \frac{G(r,\theta)}{G(r_0,\theta_0)}$. In this way the value in the table shows the deviation of a line source versus a point source, with reference distance 1 cm and $\theta_0 = 90°$.

r↓ \ θ→	0 °	10 °	20 °	30 °	40 °	50 °	60 °	70 °	80 °	90 °
0.5 cm	1.0957	1.0915	1.0797	1.0625	1.0426	1.0229	1.0055	0.9920	0.9836	0.9807
1 cm	1.0276	1.0267	1.0242	1.0204	1.0159	1.0111	1.0067	1.0031	1.0008	1.0000
2 cm	1.0119	1.0117	1.0111	1.0101	1.0090	1.0078	1.0067	1.0058	1.0052	1.0050
3 cm	1.0090	1.0089	1.0087	1.0082	1.0078	1.0072	1.0067	1.0063	1.0061	1.0060
4 cm	1.0080	1.0080	1.0078	1.0076	1.0073	1.0070	1.0067	1.0065	1.0064	1.0063
5 cm	1.0076	1.0075	1.0074	1.0073	1.0071	1.0069	1.0067	1.0066	1.0065	1.0065
6 cm	1.0073	1.0073	1.0072	1.0071	1.0070	1.0069	1.0067	1.0066	1.0066	1.0065
7 cm	1.0071	1.0071	1.0071	1.0070	1.0069	1.0068	1.0067	1.0067	1.0066	1.0066
8 cm	1.0071	1.0070	1.0070	1.0069	1.0069	1.0068	1.0067	1.0067	1.0066	1.0066
9 cm	1.0070	1.0070	1.0069	1.0069	1.0068	1.0068	1.0067	1.0067	1.0067	1.0066
10 cm	1.0069	1.0069	1.0069	1.0069	1.0068	1.0068	1.0067	1.0067	1.0067	1.0067

Table 15: The Normalized Geometry Function for the OncoSeed 6711 (Active Length = 2.85 mm)

If the source were a true point source, then all entries in Table 15 would be unity. The largest deviations from unity are seen for small angles and small distances.

This calculated table is in agreement with the data published in TG43 *(Nath et al., 1995)* and the correction provided by *(Rivard, 1999)*, with similar percentage differences as Table 14, because of the use of 2.85 mm vs nominal 3 mm as active seed length. The geometry function is used in the calculation of the radial dose function and the anisotropy of the seed.

4.1.2 Measured Spectra in Air

The spectrum of the OncoSeed 6711 was measured with a number of different detectors in air.

4.1.2.1 NaI(Th) Scintillation Detector

The detector is described in Chapter 3.6.1. The detector was calibrated with Co-57.

The spectrum of the OncoSeed 6711 taken with the NaI(Th) scintillation detector at a distance of 200 mm is shown below:

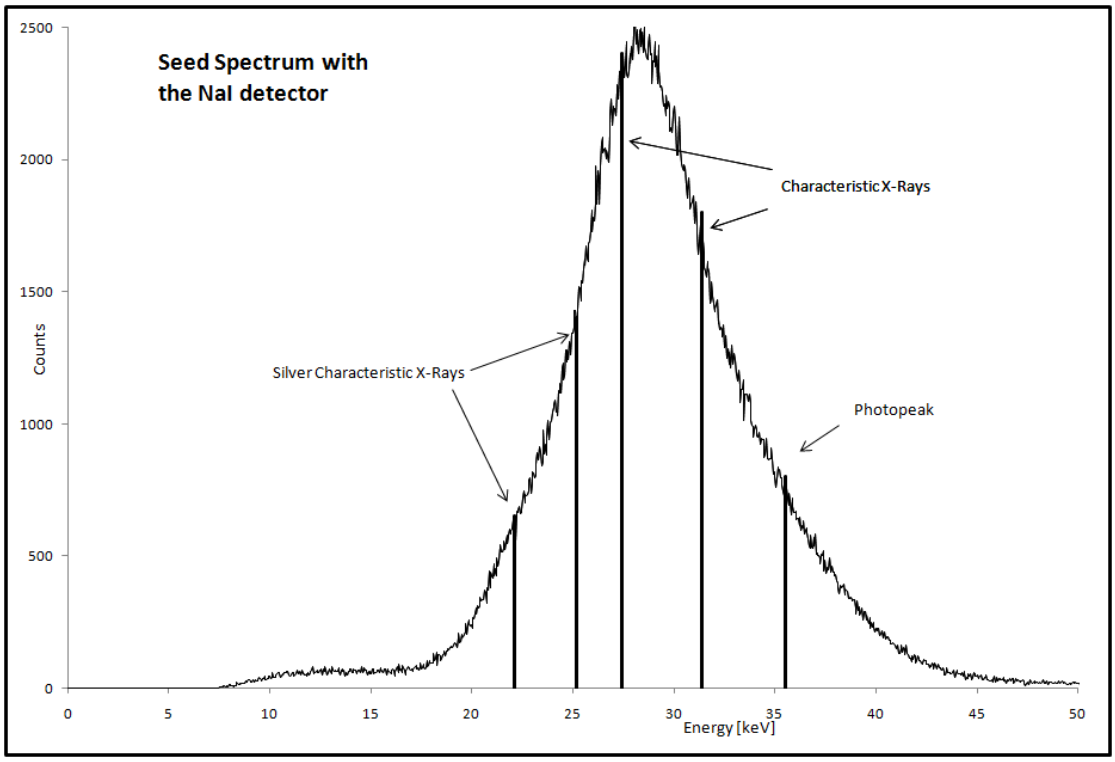

Figure 81: Seed Spectrum Measured with a NaI(Th) Scintillation Detector

It is very obvious that the energy resolution of this scintillation detector cannot distinguish between the different energies that are expected (see Chapter 2.3).

This type of detector can potentially be used for radio-immuno-assay counting of I-125, where the total area under the peak is of interest as a relative measurement.

4.1.2.2 HPGe Detector

The HPGe detector is described in Chapter 3.6.2. The spectrum obtained with the HPGe detector shows more structure than the one measured with NaI(Th).

The 35.5 keV photopeak is clearly visible.

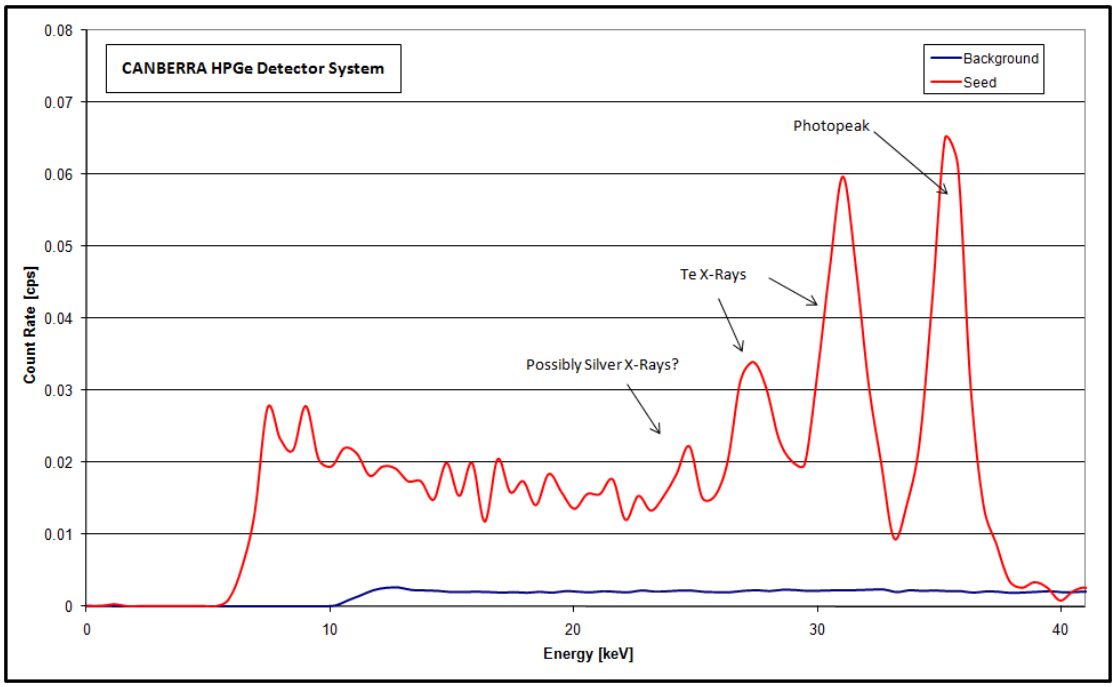

Figure 82: Seed Spectrum Measured with a HPGe Detector

Some tellurium characteristic X-rays are visible, but the detector is operating at its lower energy limit, therefore concealing some structure in the spectrum.

4.1.2.3 The Low-Energy Photon Spectrometer

The Low-Energy Photon Spectrometer (LEPS) is described in Chapter 3.6.3.

The Low-Energy Photon Spectrometer shows an improved energy resolution when compared to the HPGe detector.

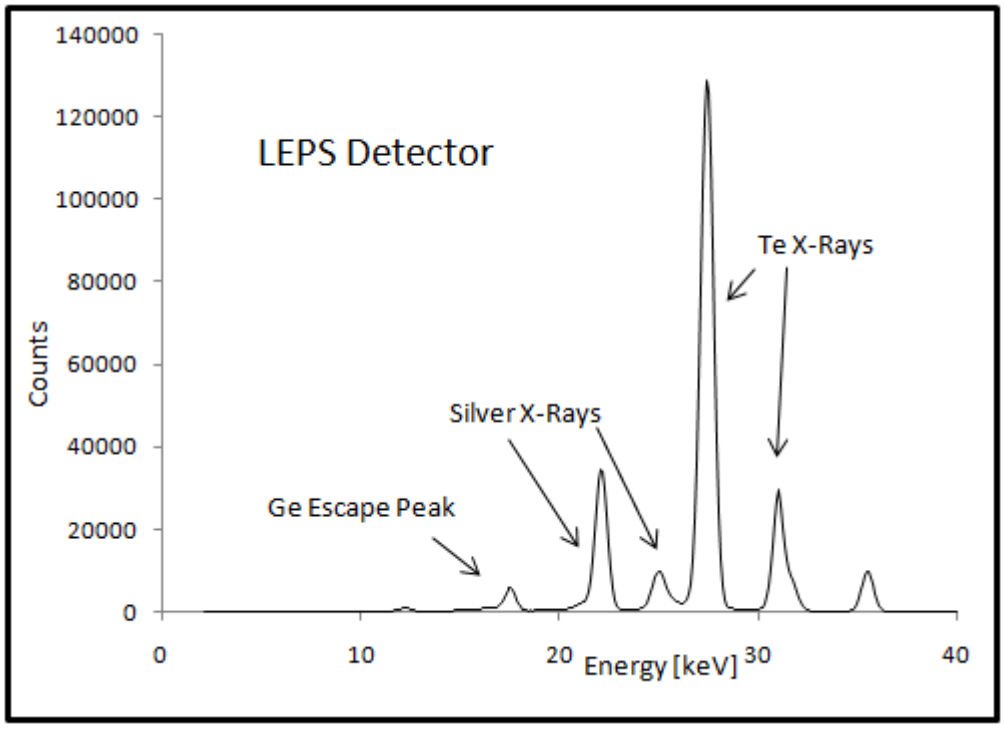

Figure 83: Seed Spectrum Measured with the Low-Energy Photon Spectrometer

The photopeak is clearly visible, as are some tellurium and silver characteristic X-rays. A germanium escape peak is also visible.

4.1.2.4 The Silicon Drift Detector

The Silicon Drift Detector is described in Chapter 3.6.4.

The energy resolution of the silicon drift detector is by far the best of the detectors used in this study, with a number of peaks visible on the measured spectra.

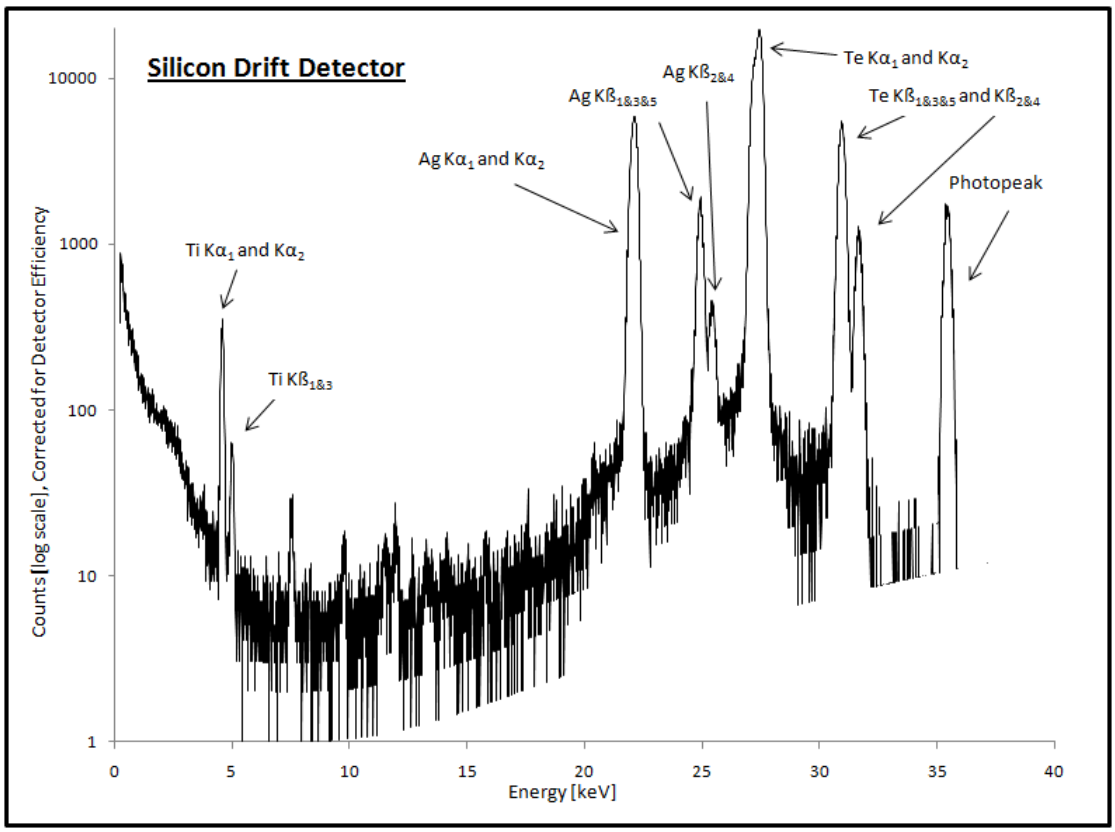

Figure 84: Seed Spectrum Measured with the Silicon Drift Detector

Figure 84 shows the obtained spectrum of the OncoSeed 6711. The spectrum was corrected for detector efficiency. More characteristic X-rays for both tellurium and silver become visible. The low energy characteristic X-rays of titanium also show up very clearly in this spectrum.

If a gold backing is added to the I-125 seed, the L-shell characteristic X-rays of gold also become visible.

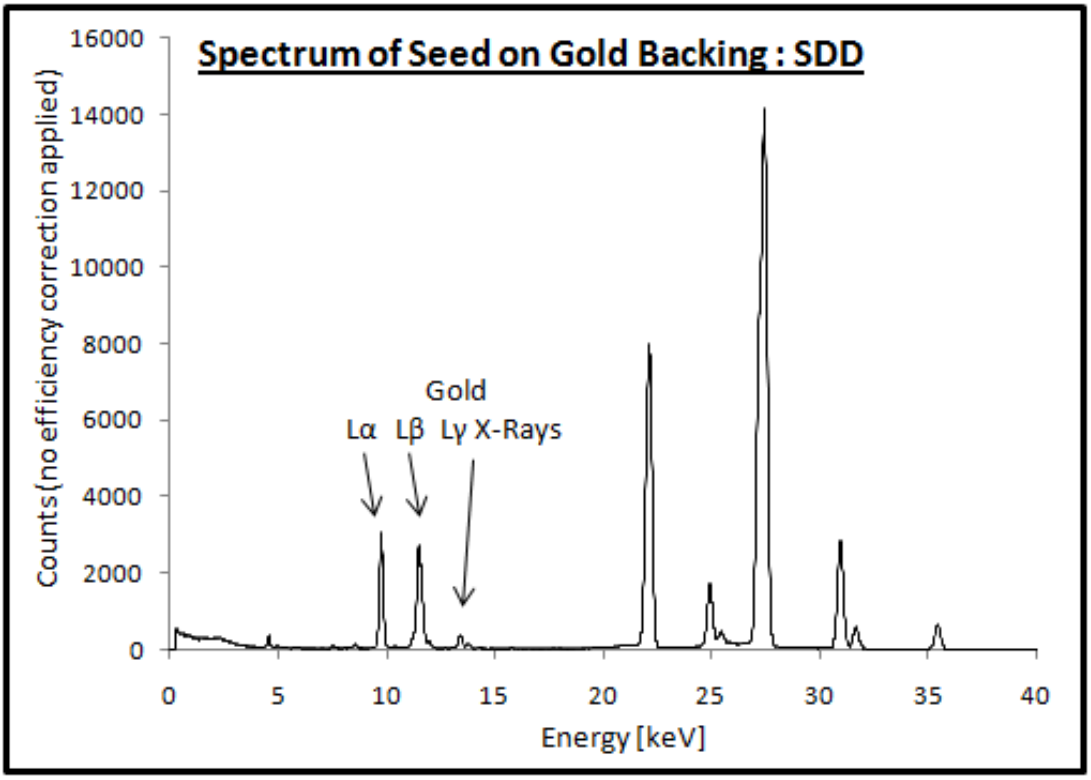

Figure 85: The Gold Backing of the "Claws" Introduces Gold Characteristic X-Rays

The SDD was also used to measure the spectra of the OncoSeed 6711 at different angles and distances. There are obvious spectral differences when the seed is measured at angles of 0° or 90° in air, as shown in Figure 86 (no corrections applied). Both spectra in Figure 86 were measured for the same amount of time and the height of the peaks at 0° are indicative of reduced counts through the ends of the seeds.

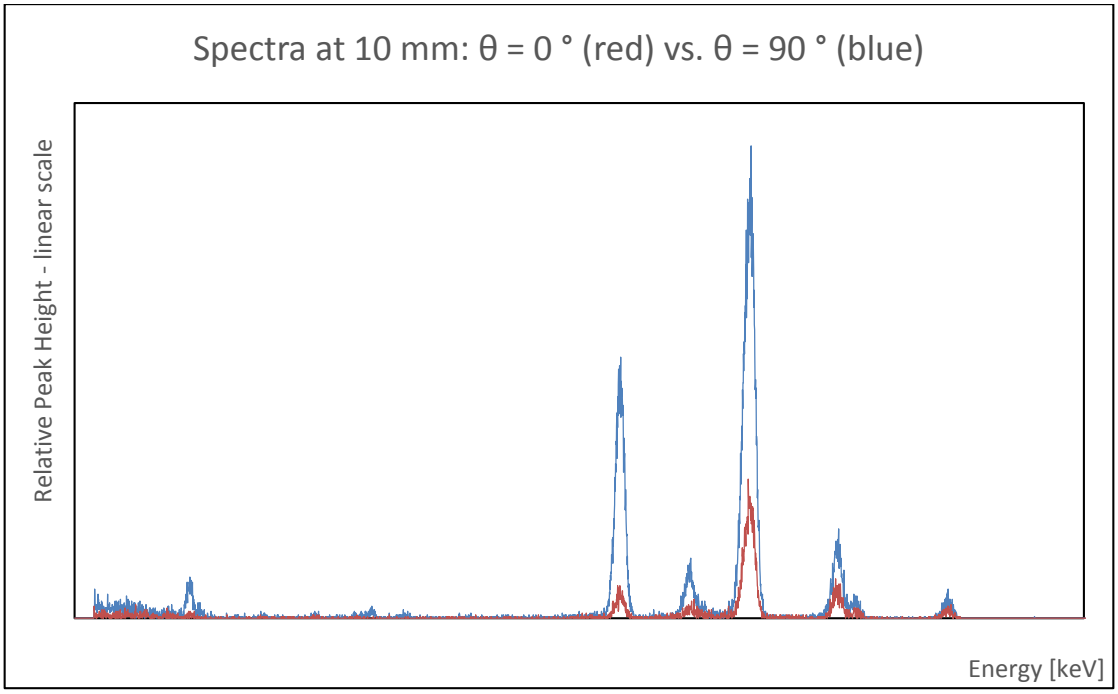

Figure 86: Spectral Changes at 10 mm for θ = 0° (red) vs θ = 90° (blue)

It is very obvious that the red spectrum (0°) shows a spectrum that has been attenuated more. This is because of the seed end-effect / anisotropy.

The spectrum obtained in Figure 84 was used to determine the average energy of the Oncoseed 6711 in Chapter 4.1.2.5, and also to get an estimate of the dose rate constant numerically in Chapter 4.1.5.

4.1.2.5 Determination of the Average Energy of the OncoSeed 6711

(Usher-Moga et al., 2009) used the spectral output to determine the average energy of the OncoSeed 6711 emissions using Equation 27:

$$E_{ave} = \frac{\sum_{i=1}^{n} E_i \cdot \Phi(E_i)}{\sum_{i=1}^{n} \Phi(E_i)}$$

Equation 27: Determination of the Average Energy

where E_i is the energy of the resolved peak i, and $\Phi(E_i)$ is the photon fluence of the same peak.

This was applied to the detector efficiency corrected spectrum of Figure 84, once with the titanium characteristic X-rays included and once without them.

The data is given in Table 16 :

Energy E [keV]	Relative Intensity [%] with Ti in air	Relative Intensity [%] without Ti in air	(Usher-Moga et al., 2009) – *in vacuo*	*(Chen and Nath, 2001)*
4.51 Ti-Kα	0.73	X	X	
4.93 Ti-Kβ	0.13			
22.10 Ag-Kα	12.20	12.30	16.58	15.3
24.93 Ag-Kβ	3.98	4.01	4.11	4.3 (averaged at 25.2 keV)
25.46 Ag-Kβ	0.95	0.96	0.49	
27.20 Te-Kα	23.20	23.41	60.67 (averaged at 27.38 keV)	61.4 (averaged at 27.4 keV)
27.47 Te-Kα	41.04	41.39		
30.98 Te-Kβ	11.51	11.61	12.31	15.3 (averaged at 31.4 keV)
31.70 Te-Kβ	2.68	2.70	2.81	
35.49 γ	3.58	3.62	4.11	3.7
Average Energy	27.24 keV	27.44 keV	27.34 keV	27.40 keV

Table 16: Relative Intensity of Emissions

The obtained values of 27.24 keV (including the titanium characteristic X-rays) or 27.44 keV (excluding the titanium characteristic X-rays) are in good agreement with published data.

Measured spectra in air can potentially be used as input for Monte Carlo calculations, e.g. this seed spectrum can be used as in input spectrum for use in DOSXYZnrc. It already includes all the characteristic X-rays that are formed when the I-125 decays in the OncoSeed 6711 and can be made available as a .txt file.

4.1.3 Anisotropy in Air

The anisotropy was measured in air using the silicon drift detector. The spectra of three different seeds were measured at different angles (0 - 90°) and different distances (5 – 30 mm) from the detector. Figure 86 shows that the spectrum varies with relative seed angle because of the end-effect. A region of interest (ROI) ranging from 21.07 – 36.85 keV was set on the multi-channel analyzer (i.e. including all significant peaks, but excluding the low-energy titanium characteristic X-rays below 5 keV) and the seed spectra were measured. Counts over the ROI were compared for the same counting time at different distances and angles from the seed. The dead time of the detector at 6 kHz was 0.24 % and at 15.5 kHz it was 1.15 %. Low-activity seeds were used to keep the dead time low. Spectra were counted for 30 s each, giving count uncertainties of less than 1 % over the region of interest. Results of three seeds were averaged.

The anisotropy is defined in water and takes into account the attenuation and scatter inside the medium as well. It should be pointed out that these measurements were done in air; therefore differences are expected when comparing the anisotropy in air to that in water.

These differences will become visible at smaller angles (i.e. where the end-effect is more pronounced) and larger radii, since anisotropy data is normalized to 1 at $\theta = 90°$ at each radius r and larger radii mean that there is more scatter and attenuation than for smaller radii.

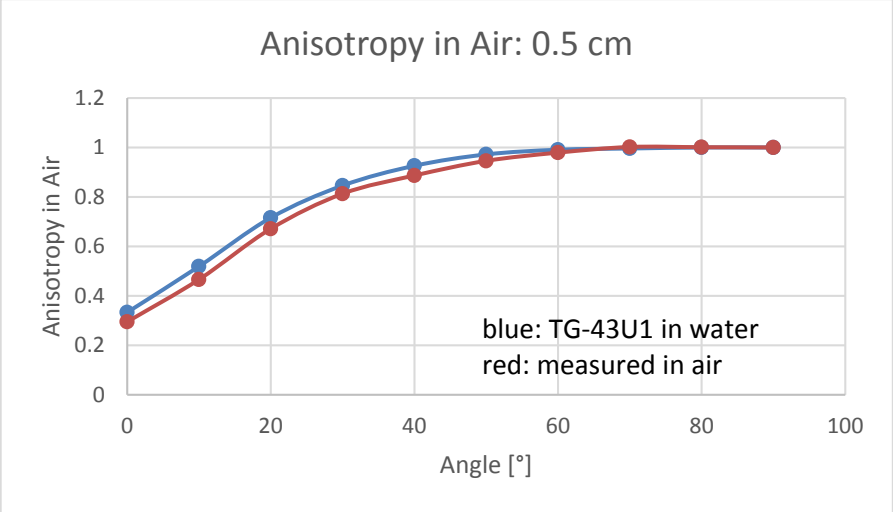

Figure 87: Anisotropy in Air at r = 0.5 cm

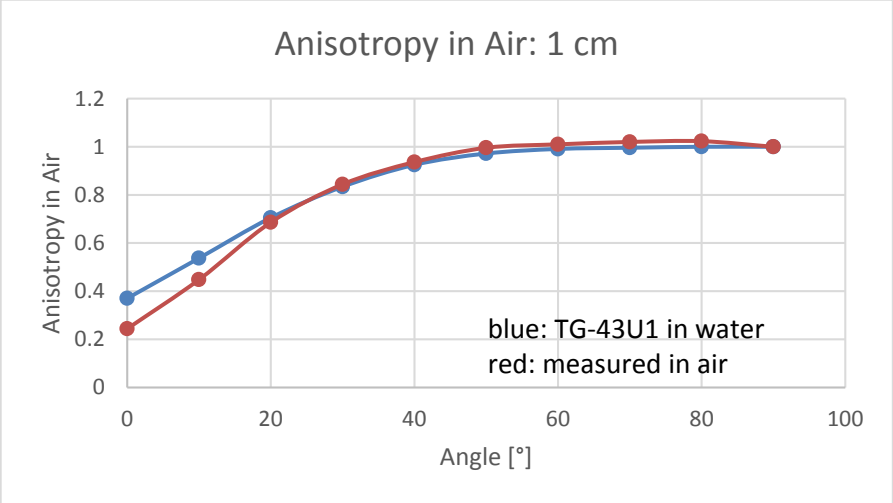

Figure 88: Anisotropy in Air at r = 1 cm

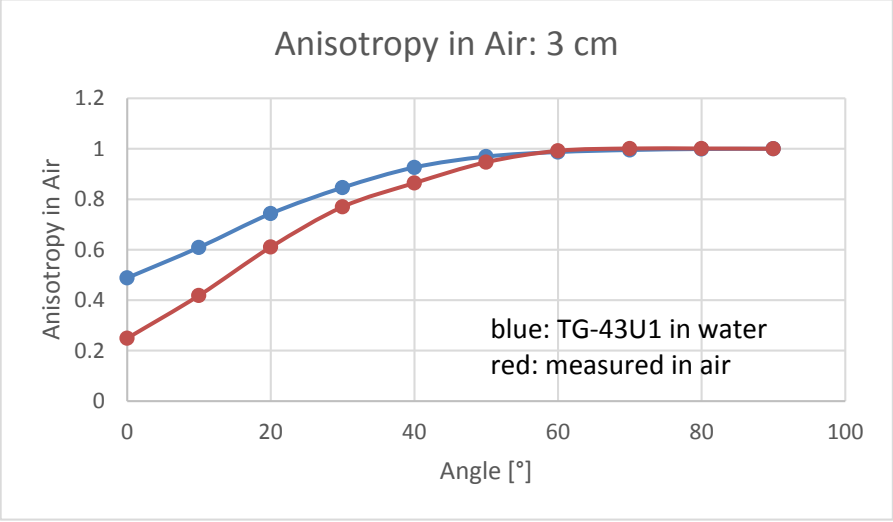

Figure 89: Anisotropy in Air at r = 3 cm

4.1.4 Apparent Activity Measurements with the Sourcecheck 4π Chamber

The chamber is described in Chapter 3.1.

Measurements were made in terms of apparent activity to be consistent with the implant protocol in use at the hospital; however, calibration factors for both apparent activity and air kerma strength were supplied.

An apparent activity of 5.20 mCi corresponds to air kerma strength of 6.60 μGym^2h^{-1}.

Seven batches of 25 seeds were measured. Seeds were counted for 10 s each and the collected charge was converted to a current. Temperature and pressure corrections were applied to the data, as shown in Chapter 3.1. The average apparent activity for each batch was compared to the stated decay corrected apparent activity. The source strength of the radiation source is given by the product of the measured value, the chamber calibration factor (given by $5.095 \cdot 10^8$ $Ci \cdot A^{-1}$) and an air density correction factor.

Seed Batch	1	2	3	4	5	6	7
Average Measured Apparent Activity [mCi]	4.92	2.99	1.96	0.93	0.62	0.34	0.20
Standard Deviation [%]	2.17	2.32	2.39	2.73	1.67	5.96	3.05
Stated Decay Corrected Activity [mCi]	4.91	3.01	2.00	0.96	0.59	0.33	0.20
% Difference	0.20	-0.52	-2.00	-3.31	5.40	2.35	-2.49
Range [mCi]	4.60 – 5.02	2.84 – 3.07	1.89 – 2.06	0.89 – 0.97	0.60 – 0.64	0.31 – 0.38	0.19 – 0.21
Measured / Stated Ratio	1.002	0.995	0.980	0.967	1.054	1.023	0.975
Average Ratio over 7 Batches	0.999 ± 0.031						

Table 17: Measurement Results

The variability in the readings for a single seed was also investigated. This was done by measuring five individual seeds from batch 1 twenty times each.

	Average of 20 Measurements
Seed A	4.85 Ci ± 0.14 %
Seed B	4.94 Ci ± 0.11 %
Seed C	4.89 Ci ± 0.14 %
Seed D	4.97 Ci ± 0.15 %
Seed E	5.01 Ci ± 0.13 %

Table 18: Measurement Results

A total of 175 seeds were measured from 7 batches of seeds. The ratio of measured to stated apparent activities ranged from 0.967 – 1.054, with an average over all batches of 0.999 ± 0.031. This confirms the measurement accuracy of the 4π chamber.

Five individual seeds from batch 1 were measured 20 times each. The precision (stated as the ratio of the standard deviation and the mean, expressed as a percentage) ranged from 0.11 – 0.15 %, which confirms the measurement precision of the chamber.

Uncertainties for lower activity seeds (0.2 – 1.0 mCi) were larger than for higher activity seeds (1.0 – 5.0 mCi), which is consistent with a larger uncertainty in the electrometer reading for the very small currents (< 1 pA) that low activity seeds produce.

4.1.5 Dose Rate Constant

The dose rate constant is defined as the ratio of the dose rate at the reference position (r = 1 cm and θ = 90°) in water and the air kerma strength S_K.

The units are cGy h^{-1} U^{-1}, which ends up being cm^{-2}.

$$\Lambda = \frac{\dot{D}(r_0,\theta_0)}{S_K} \qquad \text{(Equation 10)}$$

The air kerma strength conversion given in the manufacturer's specifications was used (5.2 mCi ≙ 6.60 μGy·m^2·h^{-1}) and corrected to the date of measurement.

TLD doses were measured in the solid water phantom at 1 cm distance when the radial dose function was measured. The measured doses were converted to dose rates, using the equivalent time T_{eq} described in Chapter 2.6. The average of three runs was used

and Λ was calculated to be $\underline{\Lambda = 0.96 \pm 0.20}$ cGy h^{-1} U^{-1} in solid water. Unfortunately the uncertainty in the measurement is quite large, but due to the non-availability of the 6711 seed during the latter part of this study these measurements could not be repeated any more. This large uncertainty may be in part due to the size of the TLDs used (3 mm x 3 mm x 0.9 mm), which is quite substantial at the measurement distance of 1 cm.

Additionally, the method described in *(Chen and Nath, 2001)* was applied to the detector efficiency corrected spectrum of Figure 84 to obtain a calculated dose rate constant.

Applying Equations 22 – 24 to the data from the measured spectrum in Figure 84, which is also shown in Table 16, a dose rate constant for the OncoSeed 6711 of

$\underline{\Lambda = 0.978}$ cGy h^{-1} U^{-1} is obtained.

Both obtained values for the dose rate constant are in good agreement with published values for Λ in water, as shown in the following table:

Author	Method	Dose Rate Constant [cGy h^{-1} U^{-1}]
(Taylor and Rogers, 2008a)	Monte Carlo	0.942 ± 0.003
(Rivard et al., 2004)	Consensus Value in TG43-U1	0.965
(Kennedy et al., 2010)	TLD in PMMA	0.921 ± 0.055
(Kennedy et al., 2010)	Monte Carlo (MCNP) WAFAC Geometry	0.921 ± 0.0037
(Kennedy et al., 2010)	MCNP with pointlike detector	0.939 ± 0.0037
(Rivard, 2009)	MCNP WAFAC	0.904 ± 0.021
(Rivard, 2009)	MCNP with pointlike detector	0.929 ± 0.021
(Chiu-Tsao et al., 1990)	TLD	0.853
(Nath et al., 1990)	TLD	0.85 ± 0.03
(Weaver et al., 1989)	TLD	0.83
(Sahoo et al., 2009)	Monte Carlo EGSnrc	0.931 ± 0.004
(Sahoo et al., 2009)	TLD	0.971 ± 0.061
(Dolan et al., 2006)	Monte Carlo (ptran)	0.942 ± 1.76 %
(Dolan et al., 2006)	TLD	0.971 ± 6.1 %
(Nath and Chen, 2007)	HPGe Spectroscopy	0.960 ± 0.037
(Melhus and Rivard, 2008)	Monte Carlo	0.924 ± 2.6 %
(Williamson, 2000)	Monte Carlo (MCPT)	0.964
(Williamson, 2000)	MCPT WAFAC	0.925
(Chen and Nath, 2001)	Analytic / Calculated	0.971
This work	TLD in Solid Water	0.96
This work	Analytic / Calculated	0.978

Table 19: Dose Rate Constants for the OncoSeed 6711

4.2 Differences in Gafchromic Film with Time and Scanner

Early dosimetric testing with gafchromic film led to a number of inconsistencies, which were investigated. These included different film optical densities when different scanners were used, differences in optical density between portrait and landscape mode scanning for the same film, as well as film response over time and variation of optical density with position on the scanning surface. The findings are briefly described here:

Different scanners exhibit potentially very different greyscale values for the red colour channel for the same film. Initial tests were done on EBT2 film calibrated in the 70 kV X-ray beam using a Canon MP600 and an Epson Stylus CS4300 scanner. Their response was markedly different (see Figure 90 below), making it very obvious that the same scanner should be used for film readout all the time.

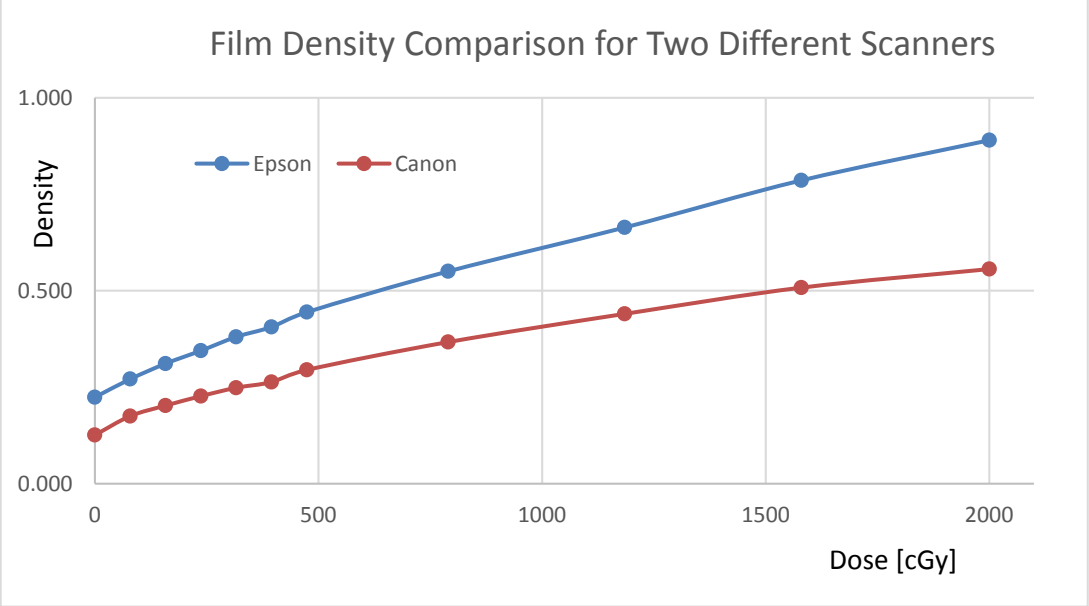

Figure 90: Film Density Comparison for Two Different Scanners

Scanning the film in portrait mode reduced the greyscale value by an average of 9.0 % when compared to the landscape mode.

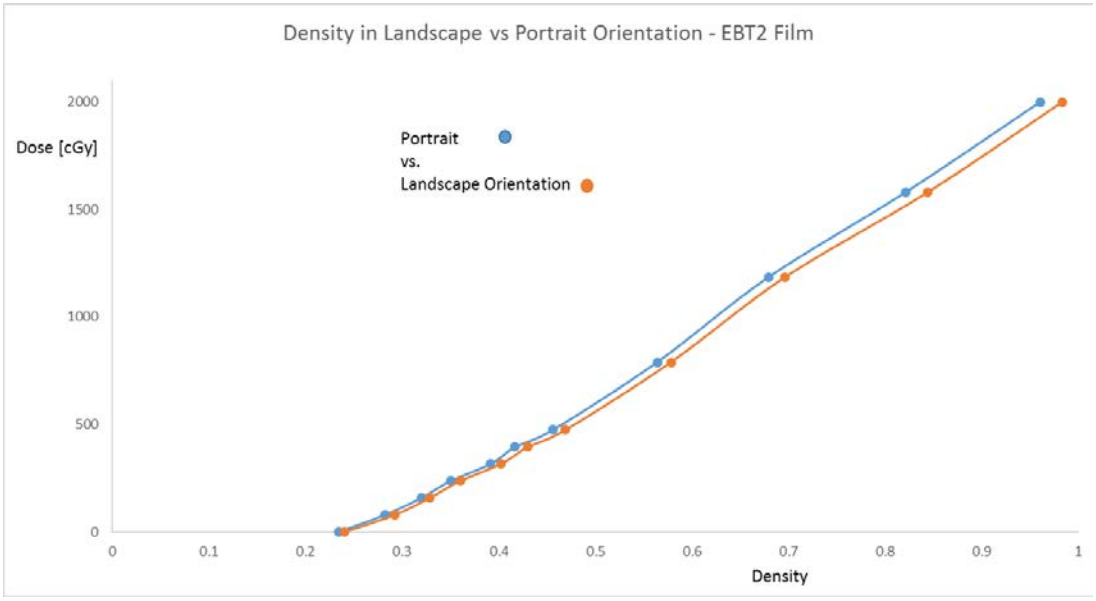

Figure 91: Optical Density vs. Dose when Scanning in Landscape vs Portrait Orientation

As described in the literature review, the EBT2 film does show some post-irradiation darkening.

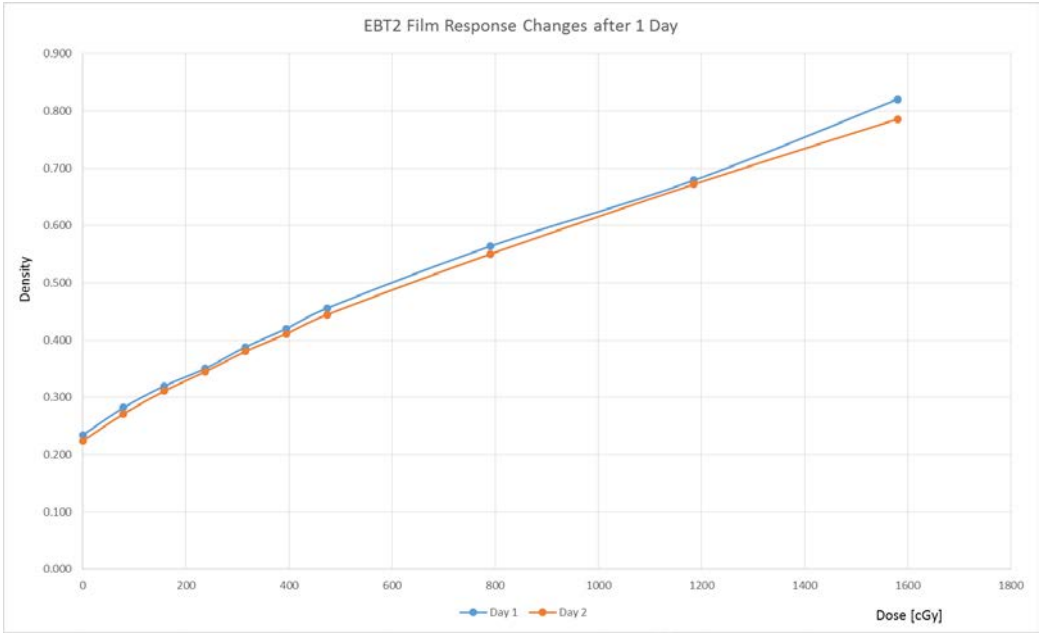

Figure 92: EBT2 Film Response Changes after 1 Day

A piece of irradiated gafchromic film was also scanned on the Canon MP600 scanner at 11 different time points over 166 hours post-irradiation. It seems like the most significant contributor to relative response was if the scanner had been warmed up or not, with relative responses over time varying by about ± 1 % relative to the scan at 1 hour post irradiation.

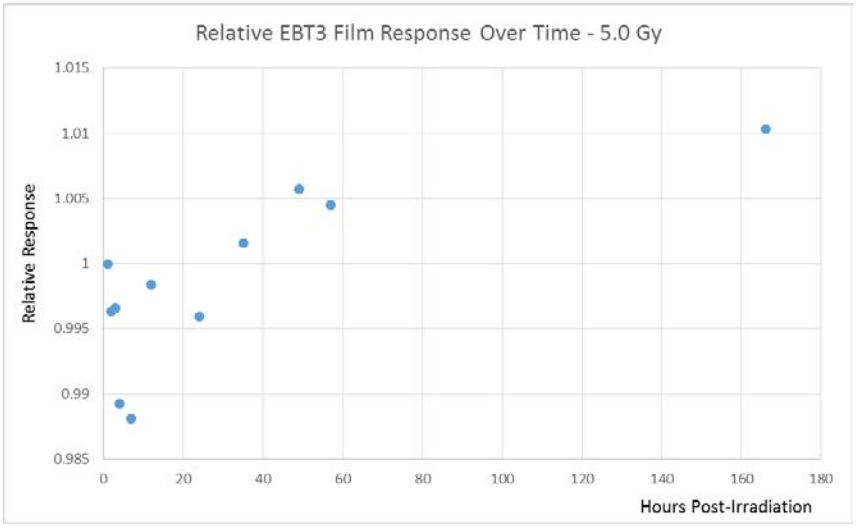

Figure 93: Relative Gafchromic Film Response Over Time

The gafchromic films were eventually scanned with a flatbed MICROTEK ScanMaker 9800XL (TMA 1600) scanner in 48 bit colour mode at 50 points per inch resolution. No image corrections were applied during scanning, consistent with the recommended protocol. The red channel was extracted using ImageJ Version 1.52a *(Rasband, 1997-2018, Schneider et al., 2012, Abràmoff et al., 2004)*. Regions of Interest were drawn to obtain the greyscale values of the red colour channel.

To obtain an indication of variation of scanner response over the area of the scanner, the same piece of film was scanned at the top of scanner window in the middle of the window, and at increments of 5 cm up to 20 cm (Table 20). It can be seen that the relative response of the film varies between 0.991 and 1.026 over the length of the scanner.

Distance from Top of Scanner Window [cm]	Red Channel Greyscale Value	Relative Response to Top of Scanner Window
0	20465	1.000
5	20290	0.991
10	20581	1.006
15	20996	1.026
20	20976	1.025
Standard Deviation:	314	1.52 %

Table 20: Scanner Response

This makes it abundantly clear that the film should be scanned on the same scanner, at the same position, under the same conditions and at the same time post-irradiation as the calibration film was scanned, to reduce any uncertainties.

Gafchromic film was used to determine seed anisotropy and radial dose function, as well as dose distributions in solid water inside the “Claws”.

4.3 Measured Anisotropy and Radial Dose Function in Solid Water

The anisotropy and radial dose function were measured in specially designed solid water phantoms, as described in Chapter 3.7.

4.3.1 Anisotropy

The anisotropy measured with film is shown first. One should bear in mind that a 1 mm x 1 mm region of interest, as was used for the film dosimetry, has a substantial dose gradient across it at small distances of 0.5 cm or 1 cm. This results in a relatively large standard deviation (around 10 % at 1 cm, around 25 % at 0.5 cm), as can be seen in the results.

The results are shown oin Figures 94 - 98:

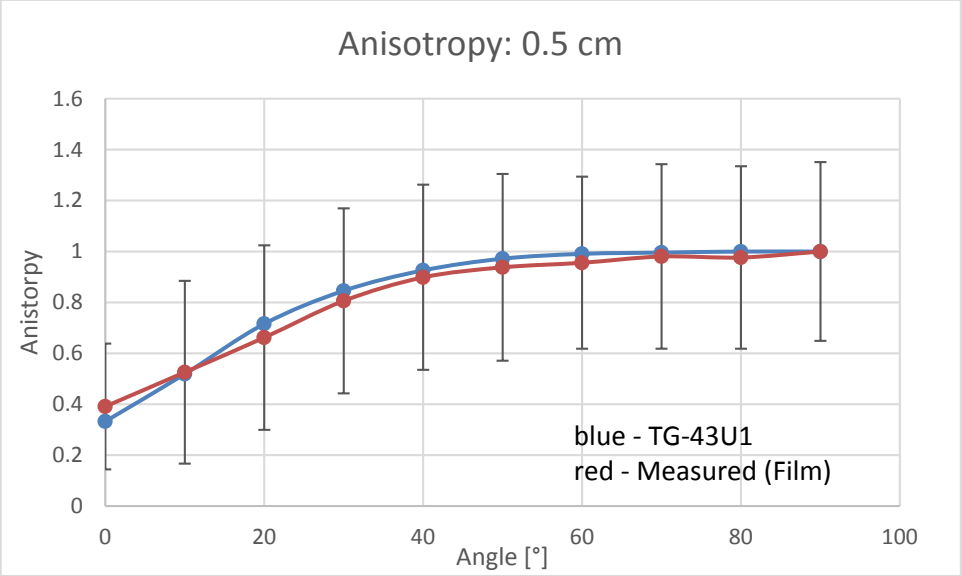

Figure 94: Anisotropy at 0.5 cm

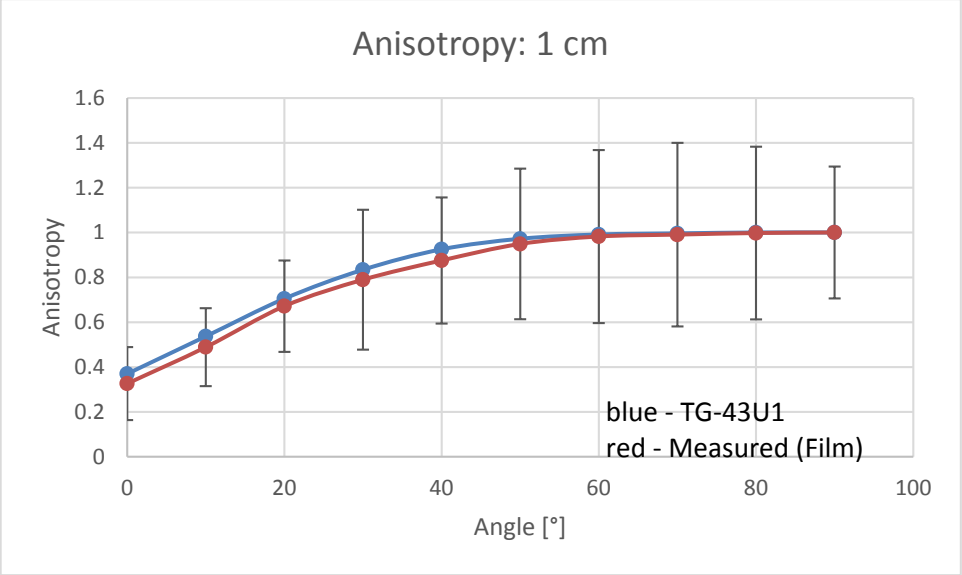

Figure 95: Anisotropy at 1 cm

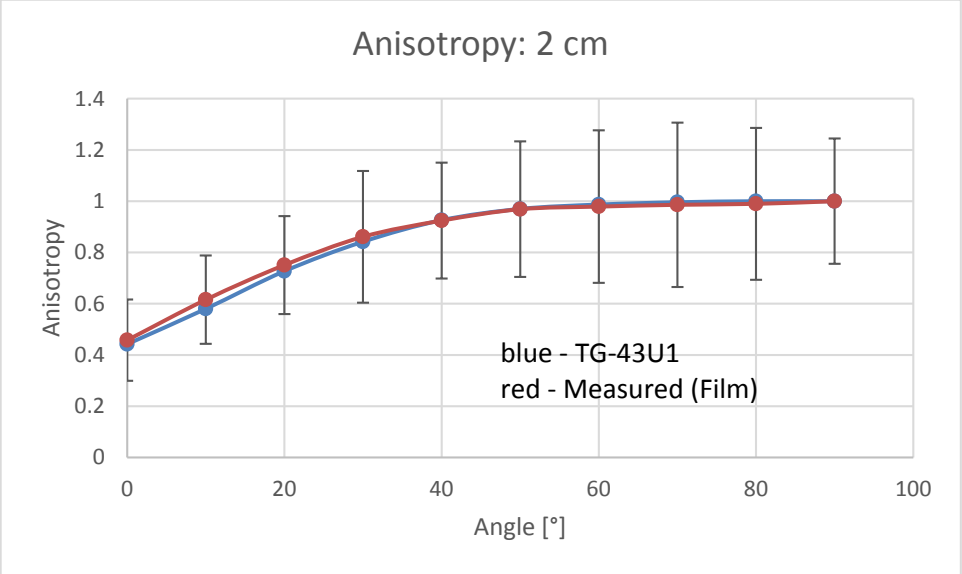

Figure 96: Anisotropy at 2 cm

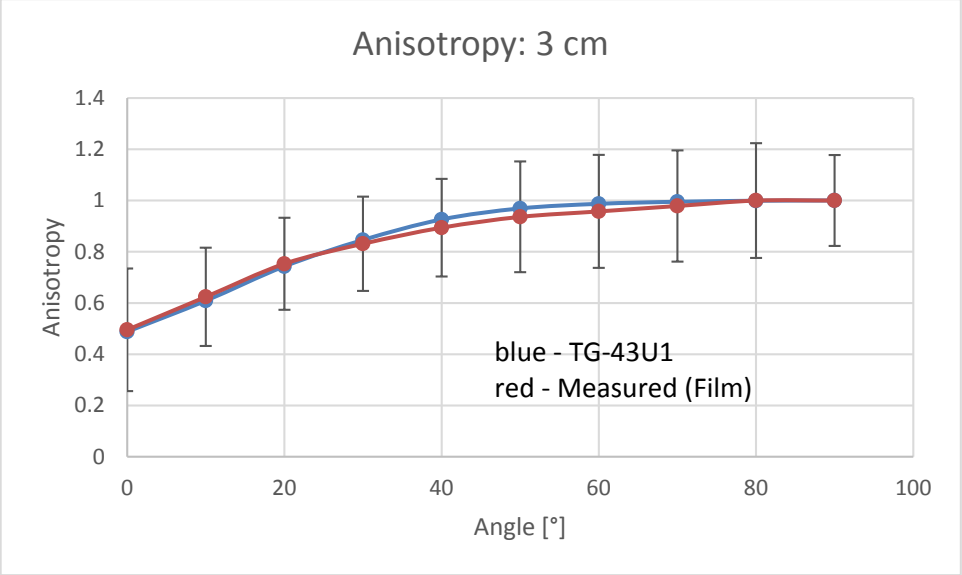

Figure 97: Anisotropy at 3 cm

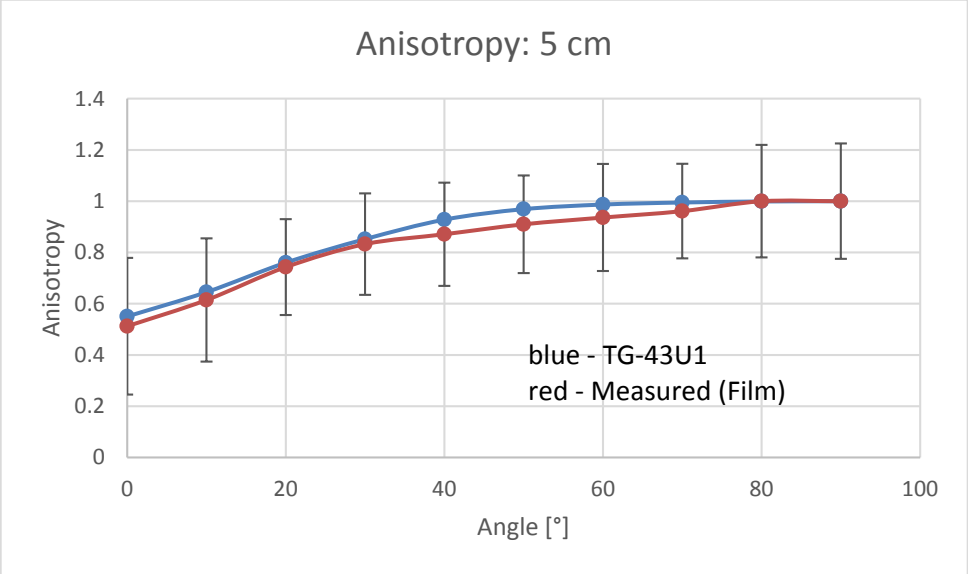

Figure 98: Anisotropy at 5 cm

The TLD-measured results are shown below in Figure 99 - 101. The measured data is shown together with the data from TG-43U1, as well as the data from the Carleton Laboratory for Radiotherapy Physics (CLRP) database of TG-43 brachytherapy dosimetry parameters (https://physics.carleton.ca/clrp/seed_database).

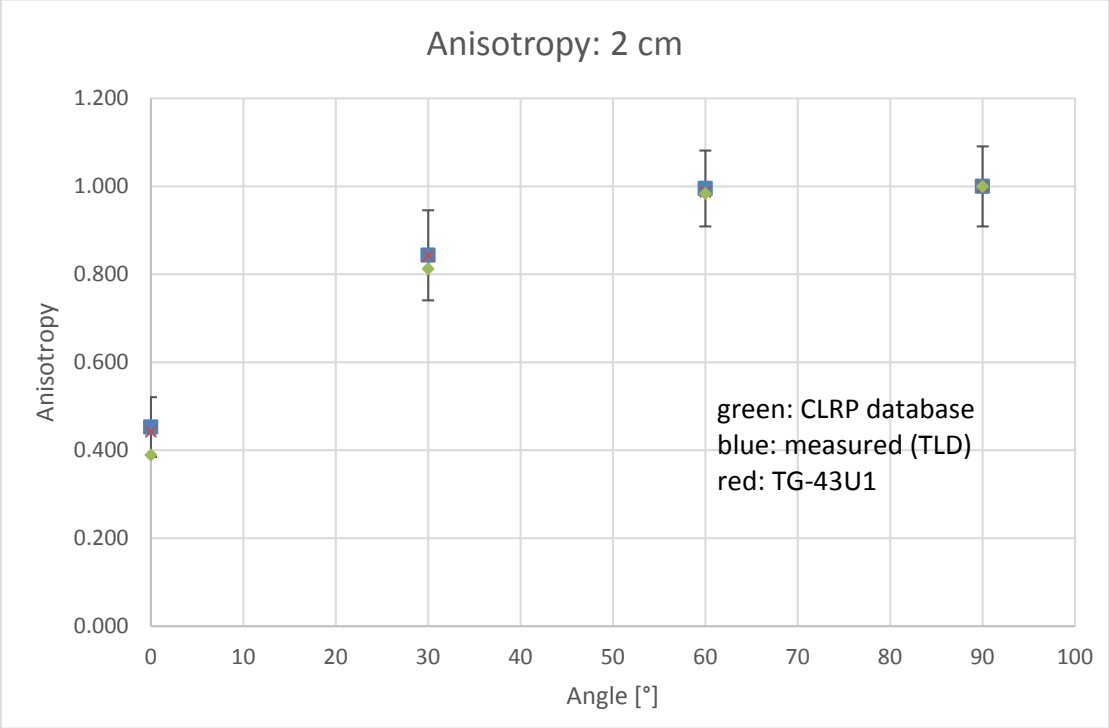

Figure 99: Anisotropy Measured with TLDs at 2 cm

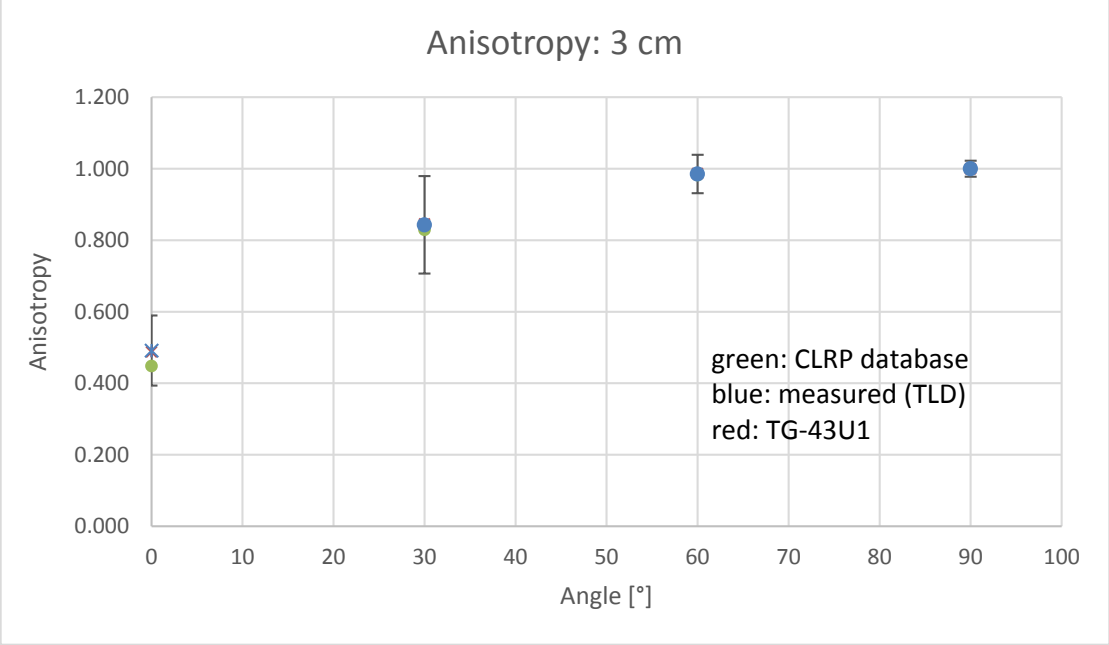

Figure 100: Anisotropy Measured with TLDs at 3 cm

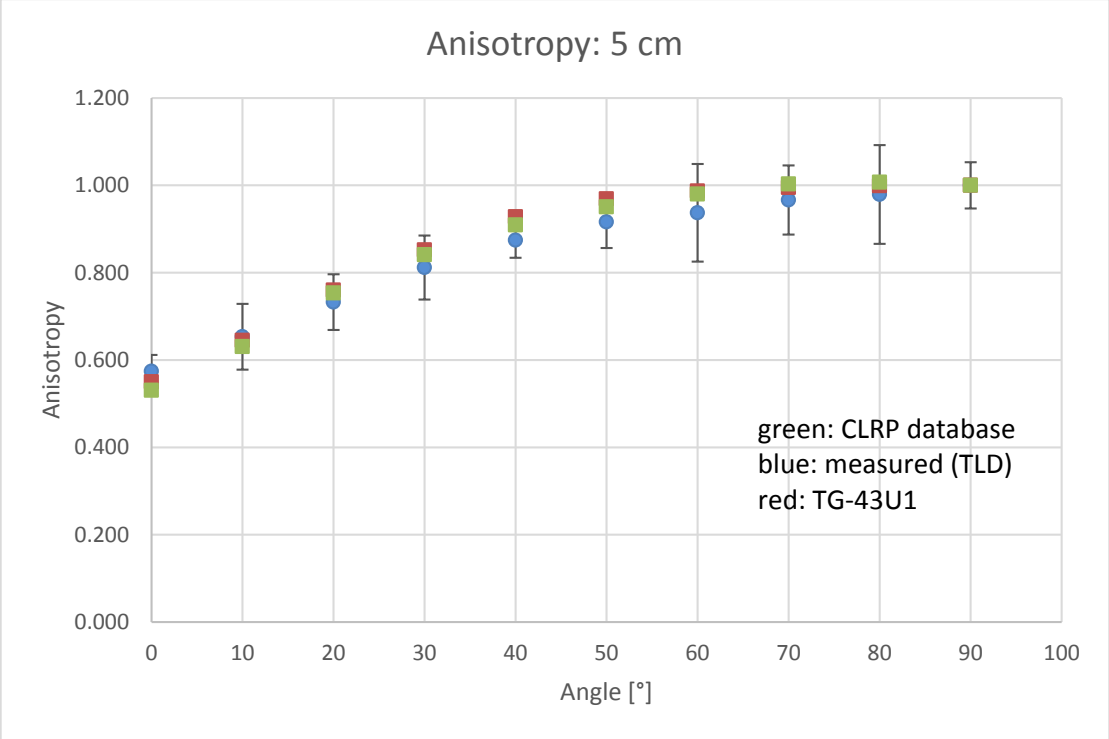

Figure 101: Anisotropy Measured with TLDs at 5 cm

It can be seen that there is good agreement between measured data and published data. The uncertainty for the anisotropy measured with film is larger than for the anisotropy determined with TLDs.

4.3.2 Radial Dose Function

The combined film / TLD results are shown in Figure 102.

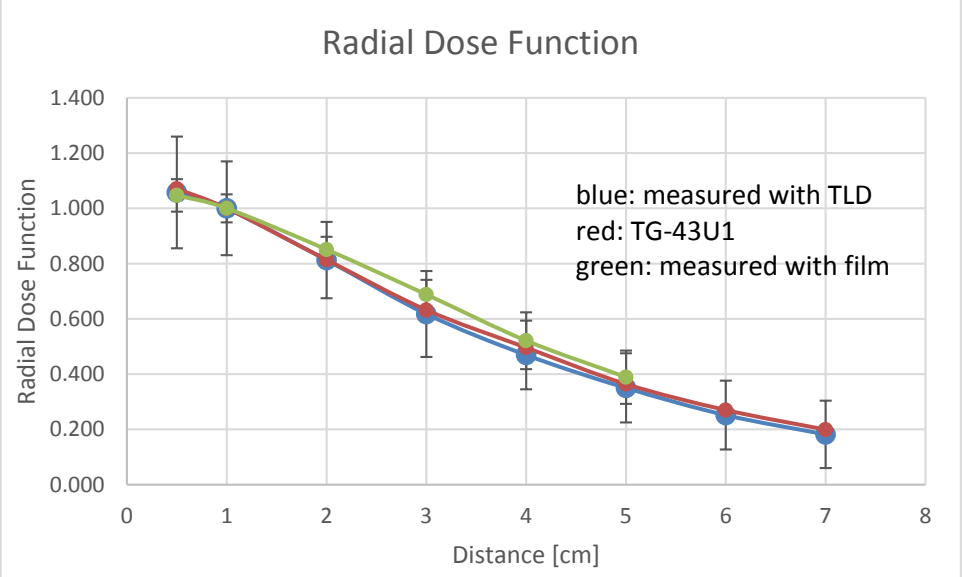

Figure 102: Radial Dose Function Measured with Film (green) and TLDs (blue)

Measured and published data match quite well to within one standard deviation.

4.4 Measured Doses in the "Claws"

Doses and dose distributions were measured in the "Claws" using gafchromic film, as well as TLDs. Comparison to planned and Monte Carlo simulated doses follow later in the chapter.

4.4.1 TLD Measurements

It was found that the TLD measured dose at the center was 81.5 ± 1.4 % of the planned dose from TheraPlan Plus. One of the main reasons for this discrepancy is a historical one: when the change was made from "activity" to "apparent activity" in the dosimetry, a factor of 0.897 was introduced. However, the clinicians at Groote Schuur Hospital did not want to have any dosimetric changes to their plans, therefore the apparent activities of all seeds that are received at the hospital are divided by 0.897, making all plans "hot" by 11.5 %. Another reason for this discrepancy is that measurements were done in solid water and not liquid water. *(Williamson, 1991)* published a conversion factor of 1.043 for the Solid Water to water conversion of dose for the 6711 source, while *(Meigooni et al., 2006)* calculated a 4 % difference for an I-125 seed with a silver marker. The combination of these two factors brings the measured and calculated values much closer together.

Doses were normalized to 100 % at the center of the "Claws" for display and comparison purposes. Dose profiles were drawn through the measurement planes.

The error bars correspond to the standard deviation of the averaged and normalized readings at the measurement points.

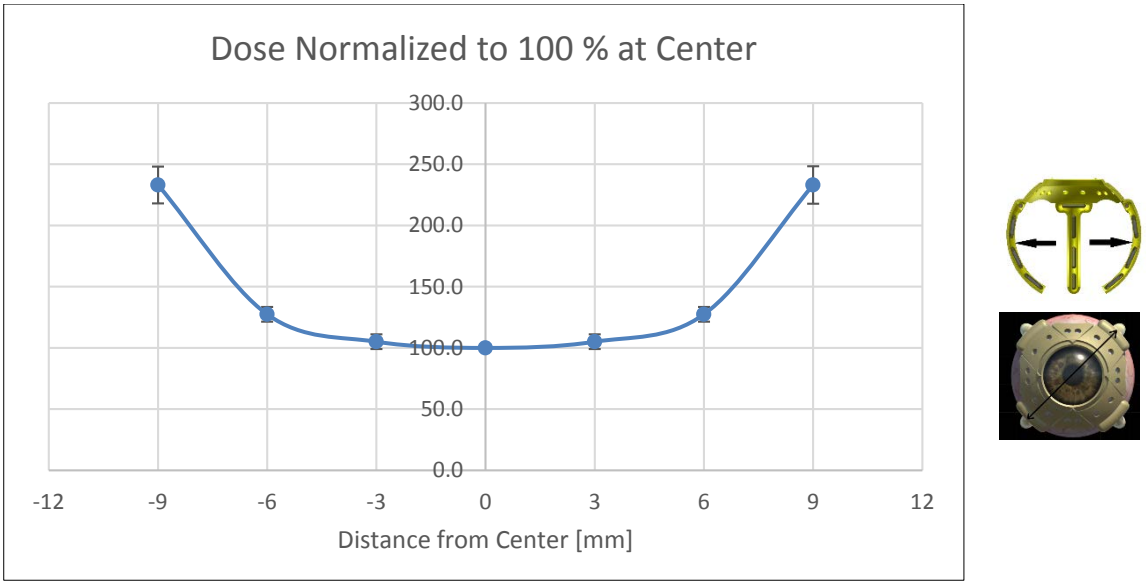

Figure 103: "Leg-to-Leg" Measured Doses on the Central Plane

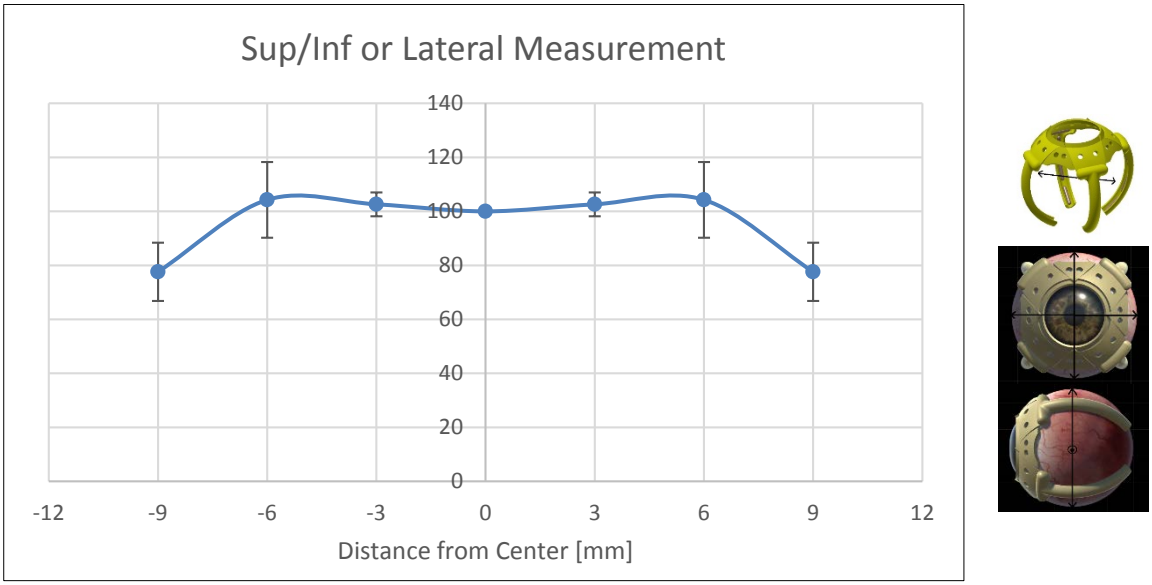

Figure 104: Sup/Inf or Lateral Measurement on the Central Plane

Each measurement point corresponds to the center of a TLD chip at that position. Relative doses are interpolated between data points.

4.4.2 Gafchromic Film Measurements

Film measurements were also done in the “Claws” along various orientations.

Figure 105 (left) shows an inverted red channel image after exposure in the “Claws”. This is an image of the film placed into the “Claws” with the film sandwiched from leg-to-leg (Figure 105 – right), the higher doses near the seeds are clearly visible on the image. Films were cut with a “handle” for labelling and to keep track of film orientation. It was not practical to suture the legs into position in the measurement set-up, they were kept in position using a re-useable putty adhesive.

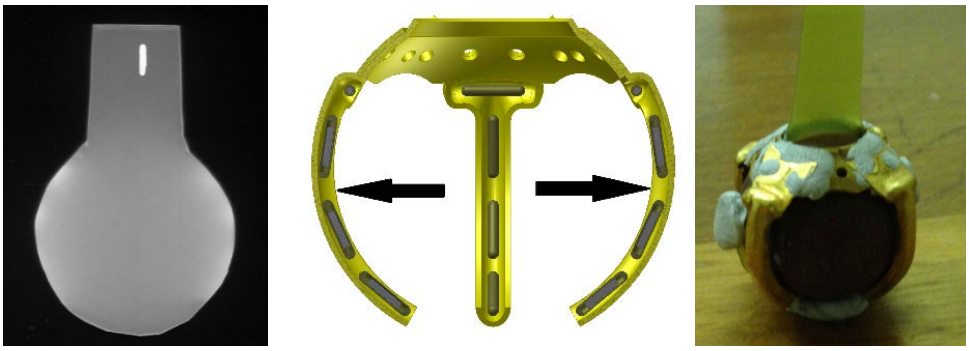

Figure 105: Inverted Red Channel Image and Measuring Plane of the Film

Dose points were added on the films during the image analysis at the same positions as the TLD measurement positions, as shown in Figure 107. Data was normalized to 100 % at the center of the eye. Error bars represent the standard deviation of the average of the readings at the respective dose points.

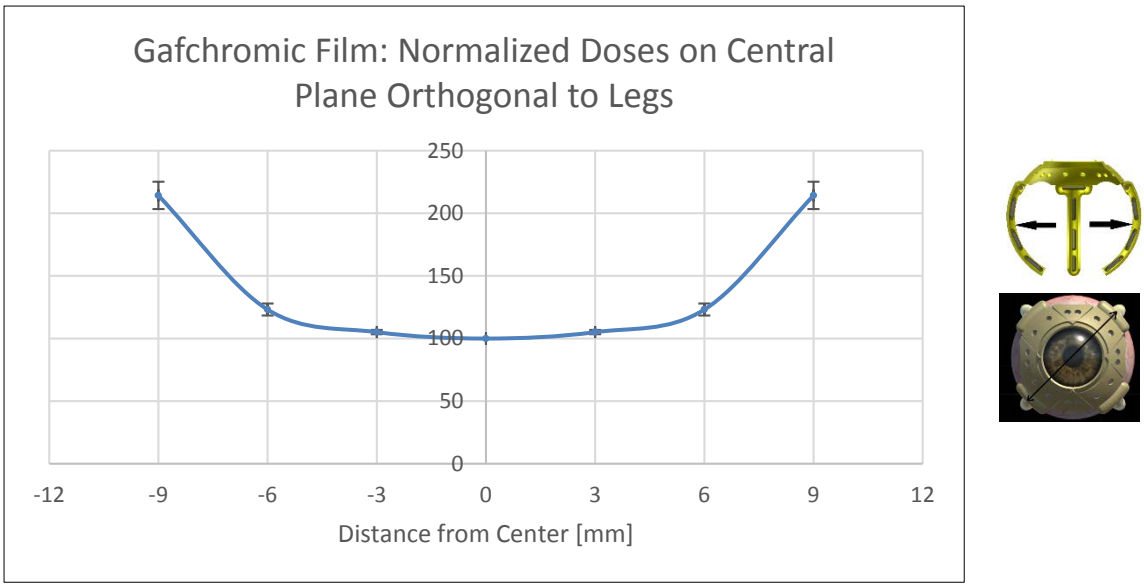

Figure 106: Measurements from Leg-to-Leg on Central Plane

Figure 106 is averaged from five data sets.

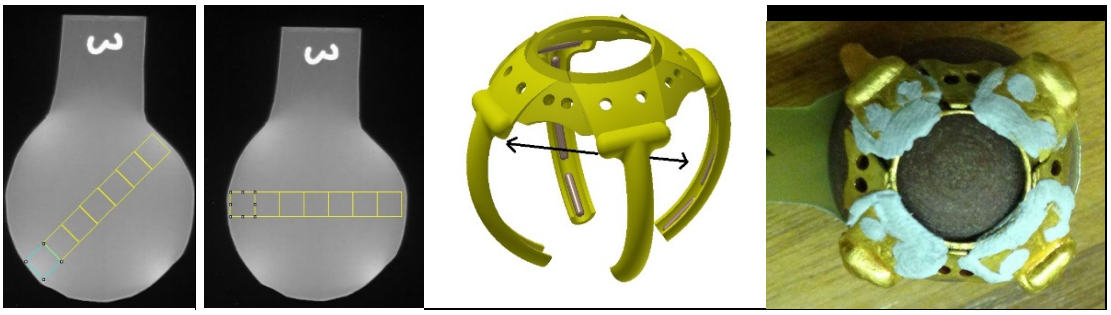

Figure 107: Inverted Red Channel Image on the Central Plane of the "Claws"

Figure 107 shows another inverted red channel image on the central plane of the "Claws". The position of the legs is clearly visible at angles of ±45 ° and ±135°, where the film appears brighter. The yellow regions of interest correspond to the positions and sizes of the TLDs for comparison purposes.

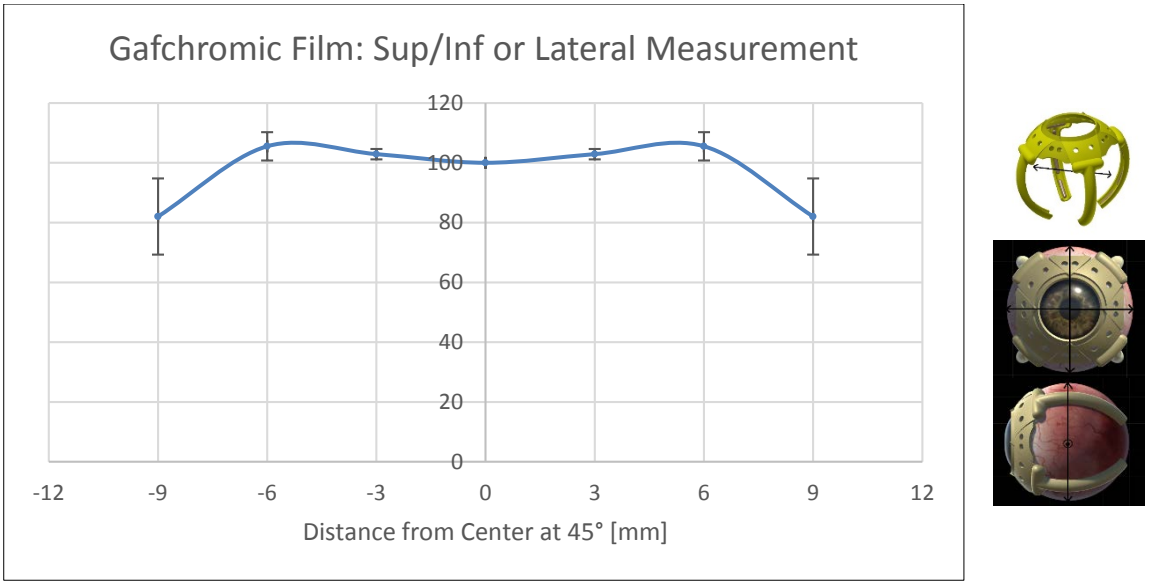

Figure 108: Measured Sup/Inf or Lateral Doses on Central Plane

Relative doses from the lens to the posterior of the eye are shown in Figure 109.

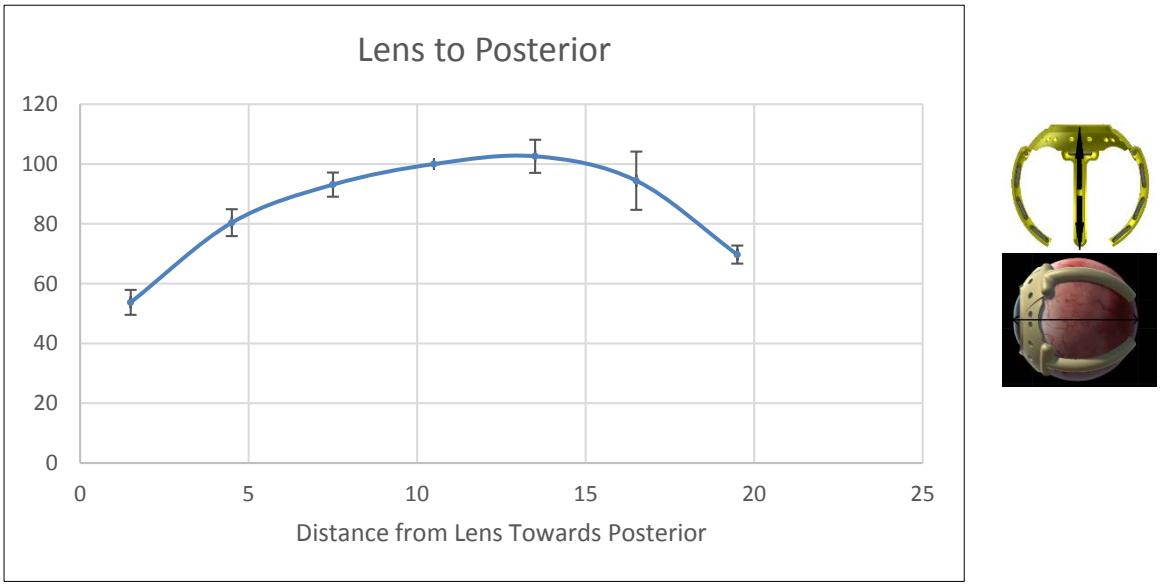

Figure 109: Measured Doses from Lens towards the Posterior of the Eye at 3 mm Intervals

4.5 Planned Doses in the "Claws"

The "Claws" were planned with 3.0 mCi seeds for a treatment time of 1 hour for both TPP and BrachyVision planning systems.

Points of interest were drawn into each plan at the TLD measurement positions in the phantom for comparison purposes. Comparison to measured and Monte Carlo simulated doses follow later in the chapter.

4.5.1 TheraPlan Plus

The following plan images show the dose distribution as calculated by TheraPlan Plus Version 3.8 Build 500 (TPP). The blue isodose-rate line corresponds to 40 cGy/h, the green one to 50 cGy/h and the red one to 60 cGy/h. The calculation grid size was 0.05 cm in all three dimensions, which is the grid size used for clinical cases at the hospital. The colours of the seeds correspond to whether they are in the viewing plane (red), behind the viewing plane (blue) or in front of the viewing plane (green). If the seeds fall on top of each other in any projection, the displayed colour depends on which seeds were added first to the plan.

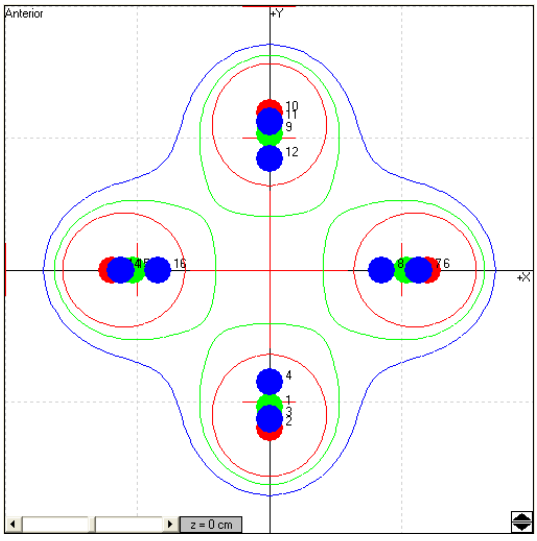

Figure 110: Dose Distribution (Anterior View) on the Central Plane at z = 0.

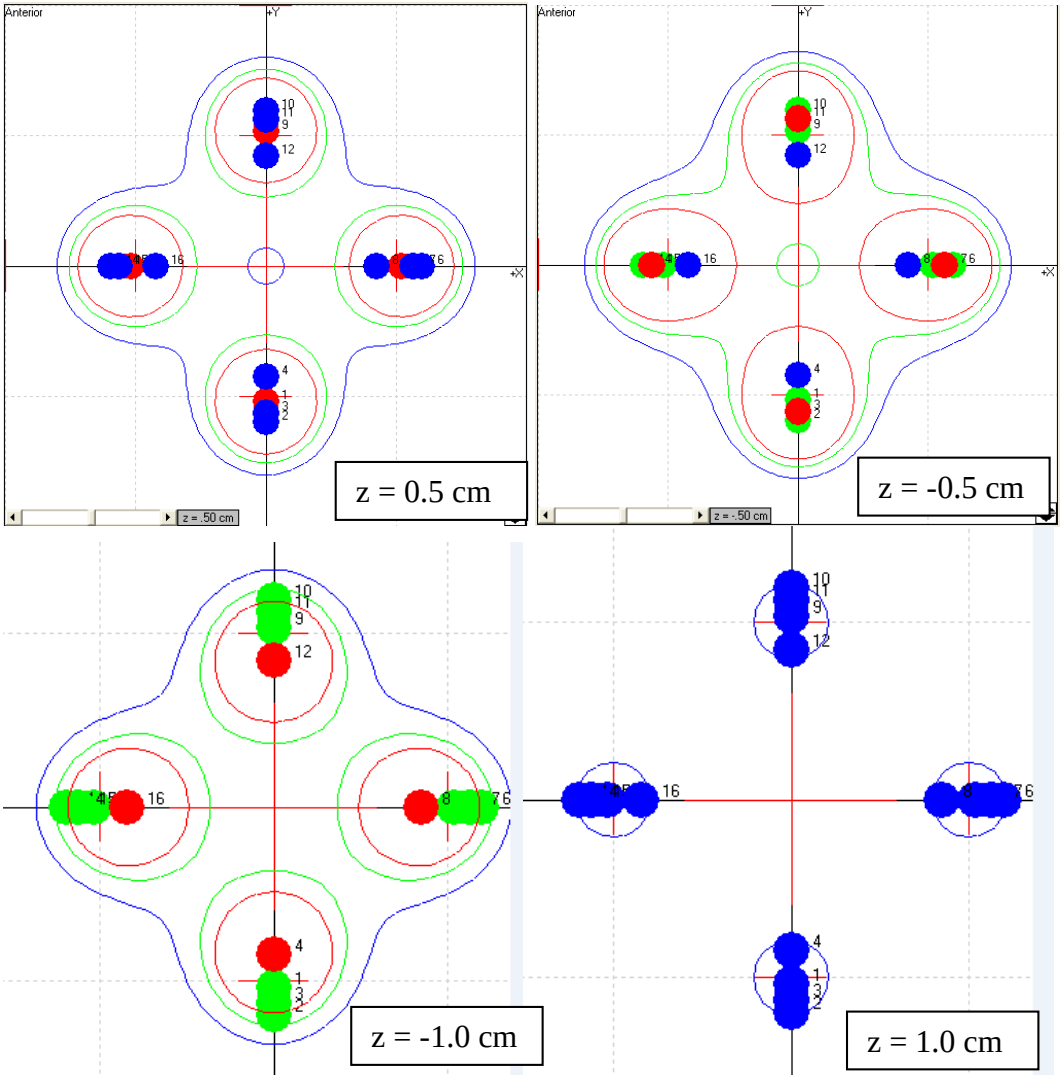

Figure 111: Dose Distribution (Anterior Views) at z = 0.5 cm, -0.5 cm, 1 cm, -1 cm (Clockwise from Top Left)

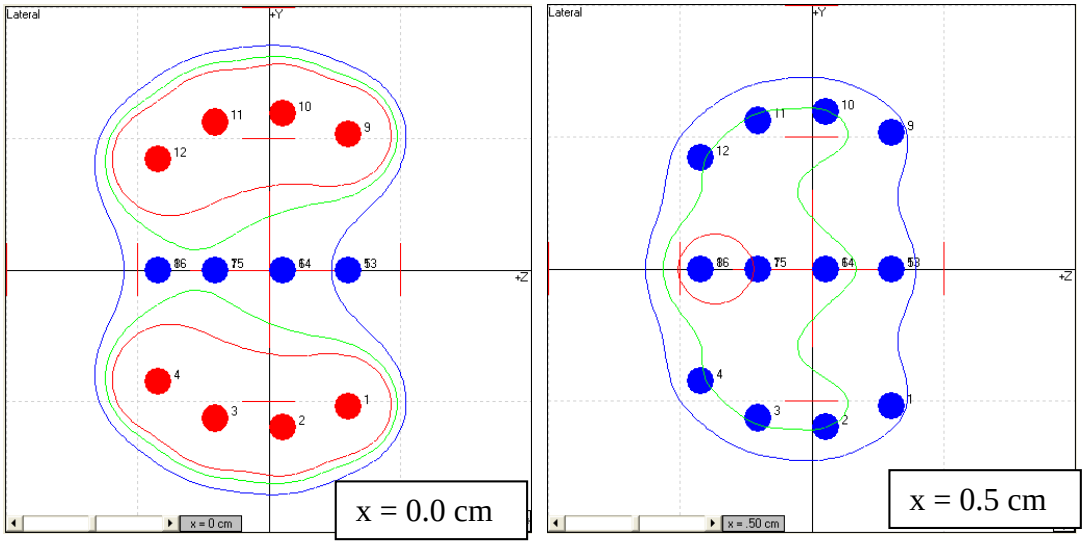

Figure 112: Dose Distribution (Lateral View) on the x = 0 cm and x = 0.5 cm Planes

In Figure 112 the lens is on the right side of the image (+Z direction), while the optic nerve is on the left side of the image (-Z direction). The transverse image also looks like Figure 112 because of the inherent symmetry in the “Claws”.

The dose distribution at x = -0.5 cm is identical to the one at x = 0.5 cm and is therefore not shown.

Theraplan Plus calculated the dose to the center to be 0.459 Gy with 3 mCi seeds in-situ for one hour. The dose at the posterior end of the “Claws” (0, 0, -1.1) was calculated as 0.400 Gy and the dose at the optic nerve (0.201, 0.201, -1.063) was 0.430 Gy.

For display and comparison purposes of the dose points, the dose at the center was normalized to 100 %. Dose points were placed at the TLD measurement positions. Results are shown in the next three figures.

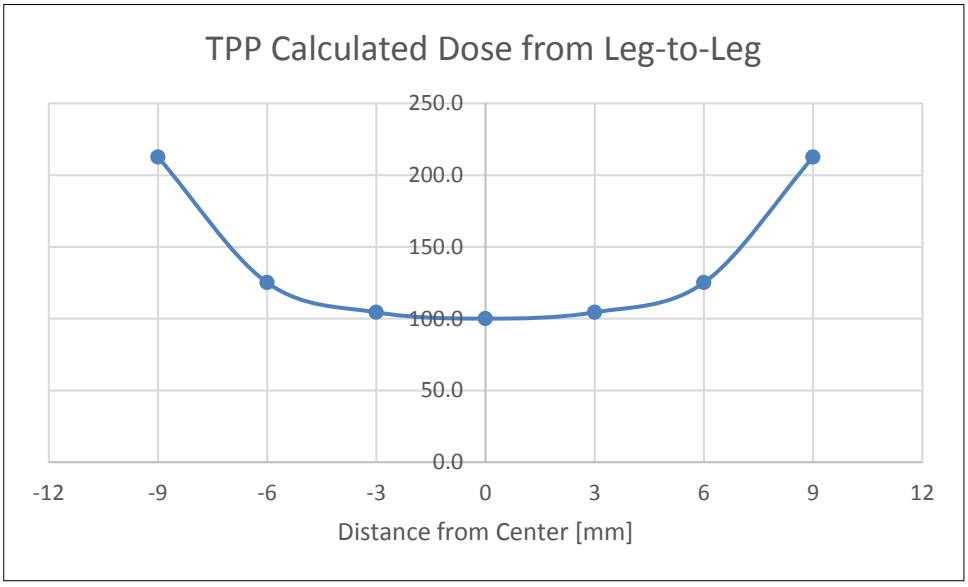

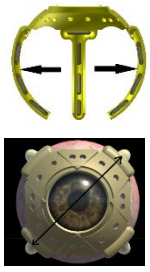

Figure 113: Calculated Dose from Leg-to-Leg on the Central Plane

It can clearly be seen that the dose directly next to each leg is highest, with the center receiving a substantially lower dose.

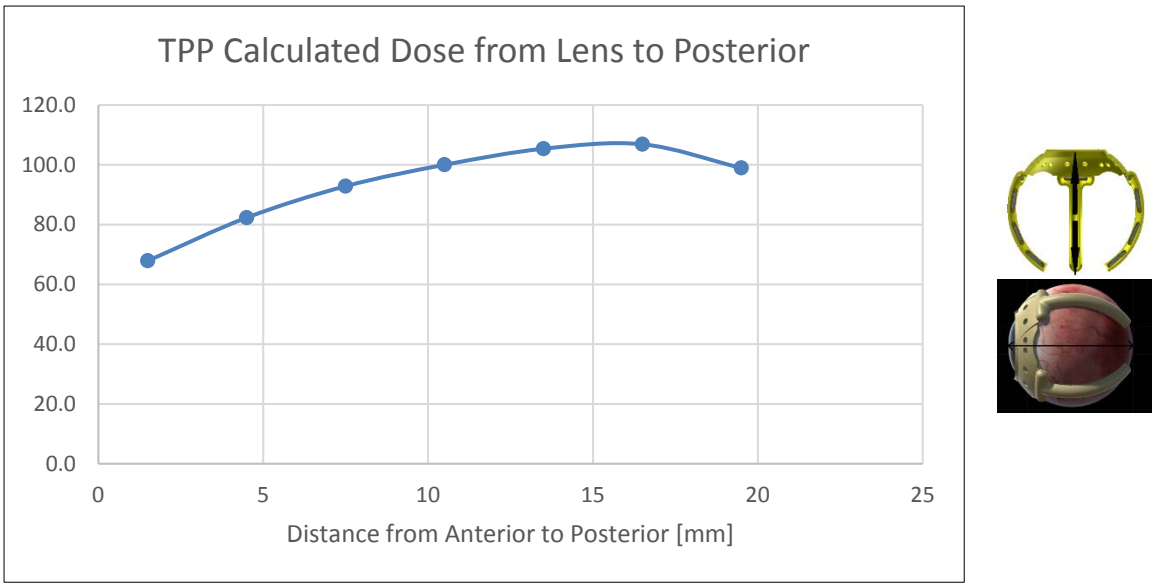

Figure 114: Calculated Dose from Lens to Posterior, Normalized to 100 % at the Center

Doses near the lens are lower than at the posterior of the eye.

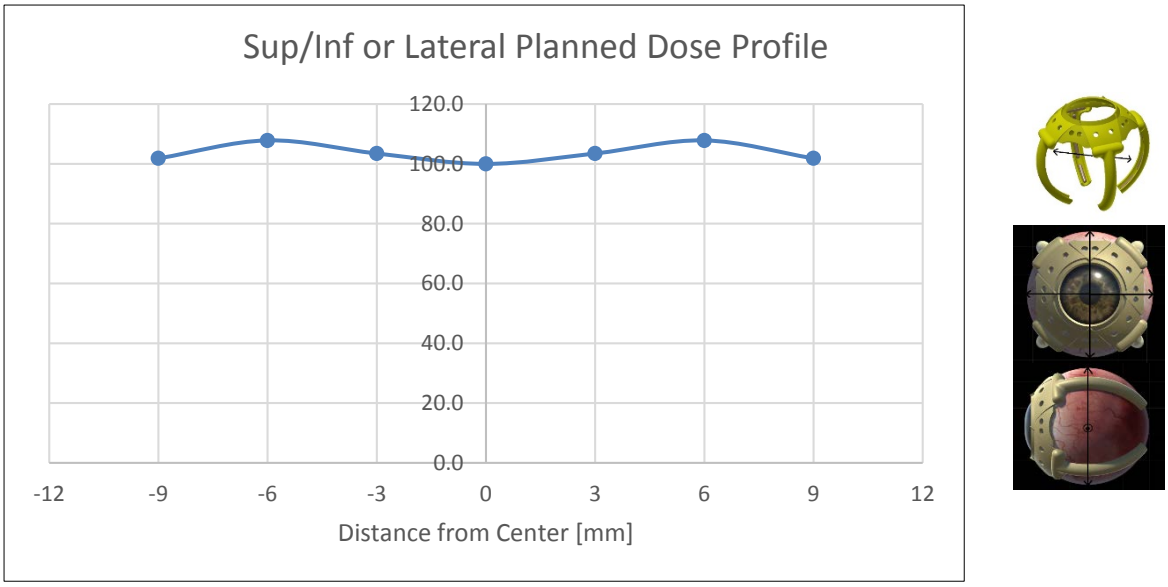

Figure 115: Dose on Central Plane

Planned doses on the sup/inf or lateral profile show very little variation, in contrast to the measured doses.

4.5.2 BrachyVision

For plans calculated with BrachyVision the 0.4 Gy, 0.5 Gy and 0.6 Gy isodoses are displayed. The calculation grid size used was 1.0 mm in the x and y directions and 1.25 mm in the z direction, which was the default grid size.

Figures 116 – 120 refer to the point source dose calculations. Data comparison to measured, other planned and Monte Carlo data follows later in the chapter.

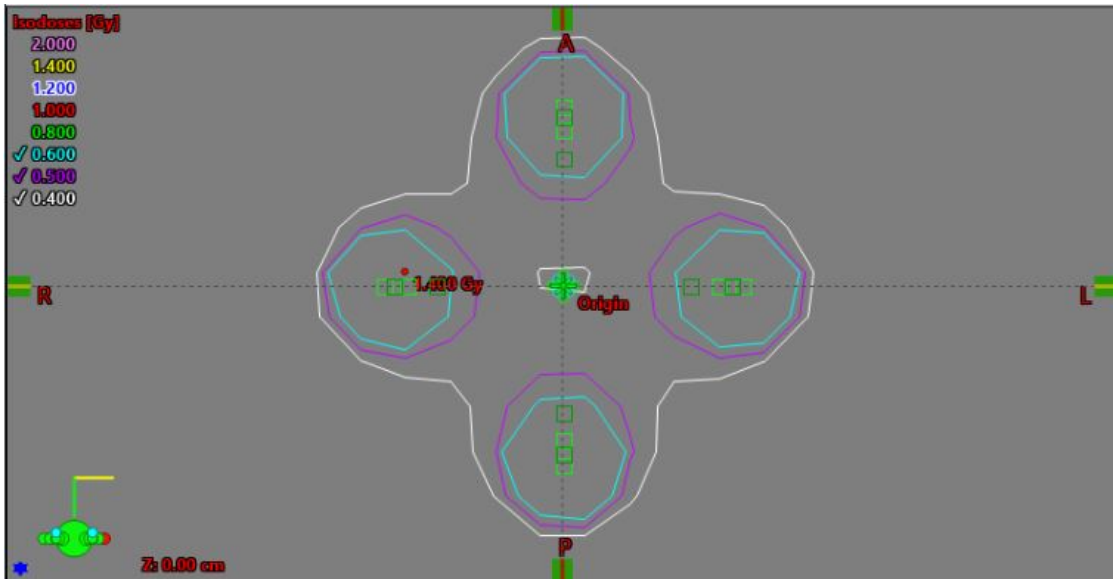

Figure 116: Anterior View: Dose Calculated with Point Source Model of 6711 Seed

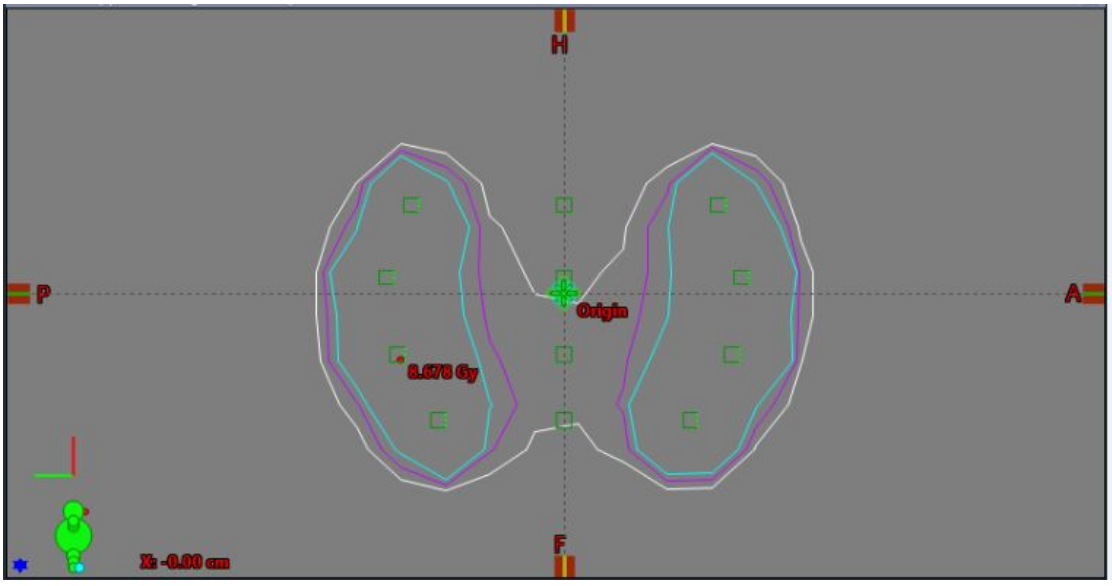

Figure 117: Transverse View: Dose Calculated with Point Source Model of 6711 Seed

The central dose was calculated to be 0.394 Gy. Once again, this was normalized to 100 %. Dose points were placed at the at the TLD measurement positions. The calculated dose at the "Post" point (0, 0, -1.1) was 0.375 Gy and the dose at the "Nerve" point (0.201, 0.201, -1.063) was 0.407 Gy.

Results for the point source calculation are shown in the next three figures.

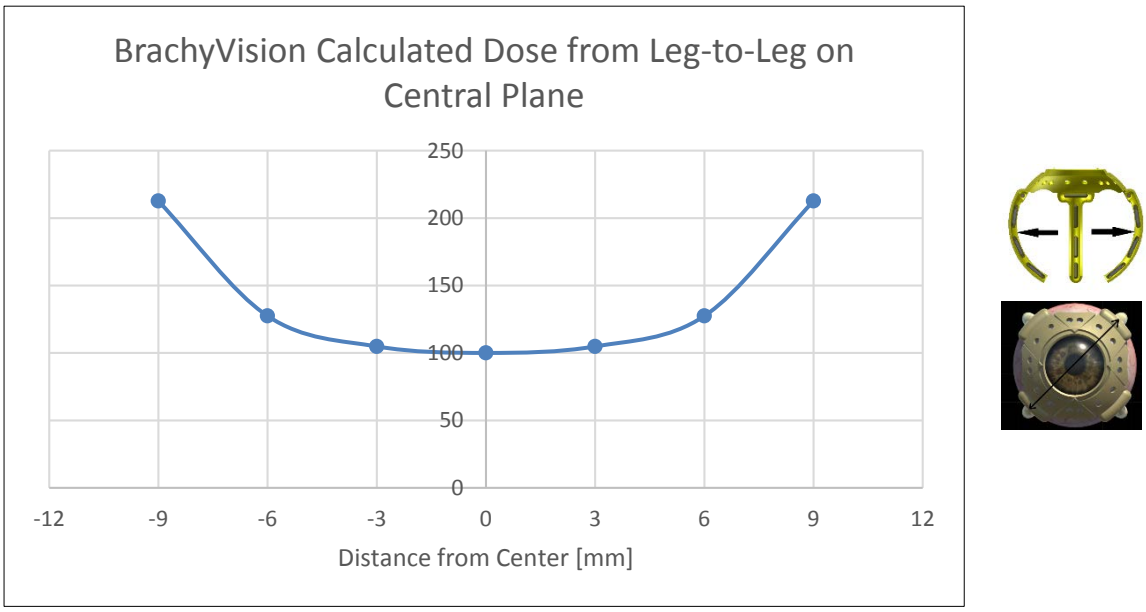

Figure 118: Calculated Dose from Leg-to-Leg on the Central Plane

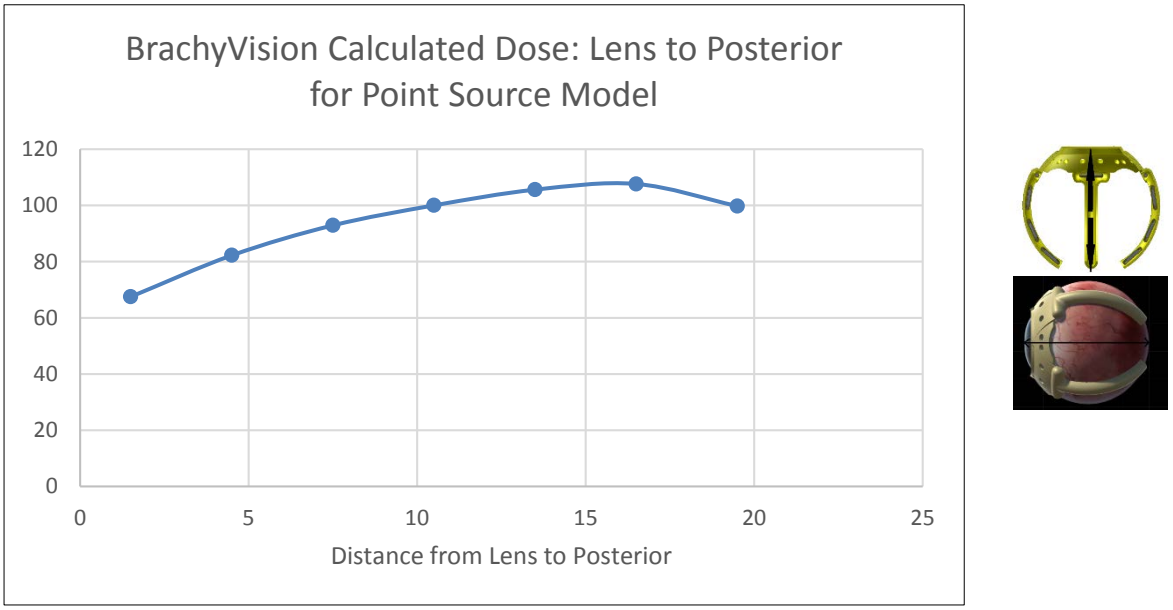

Figure 119: Calculated Dose from Lens to Posterior

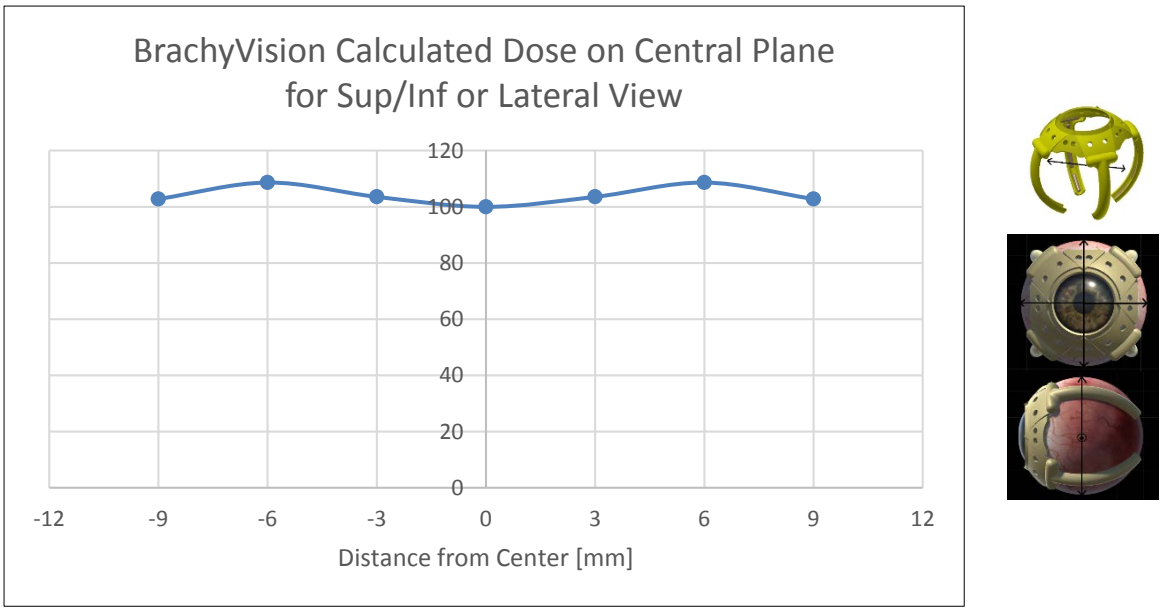

Figure 120: Dose Profile on Central Plane for Sup/Inf or Lateral View

A very similar pattern is observed for the point source calculations of BrachyVision as for TheraPlan Plus. For the leg-to-leg profiles, the dose distribution shows a dip near the center and is higher closer to the legs, as expected. The sup/inf or lateral dose profile is fairly flat, and the dose near the lens is lower than at the posterior of the “Claws”. The calculated dose at the center is only 85.8 % of the dose calculated by TheraPlan Plus. Once again, the largest contributor to this difference is the 0.897 factor in the conversion of apparent activity that is used (incorrectly) at Groote Schuur Hospital and described in Chapter 4.4.1.

The TG-43 line source model of the 6711 seed was also used for BrachyVision dose calculations. The line source model requires two sets of co-ordinates, one for each end of the seed. Line sources are displayed as little cylinders in the treatment planning system. The same calculation grid size as for the point sources was used, and the same dose points were calculated.

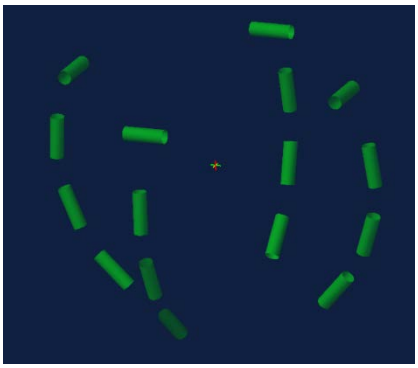

Figure 121: Display of the Line Sources in the BrachyVision Treatment Planning System

The seeds are visualized very nicely in BrachyVision, but the gold shielding of the "Claws" cannot be taken into account.

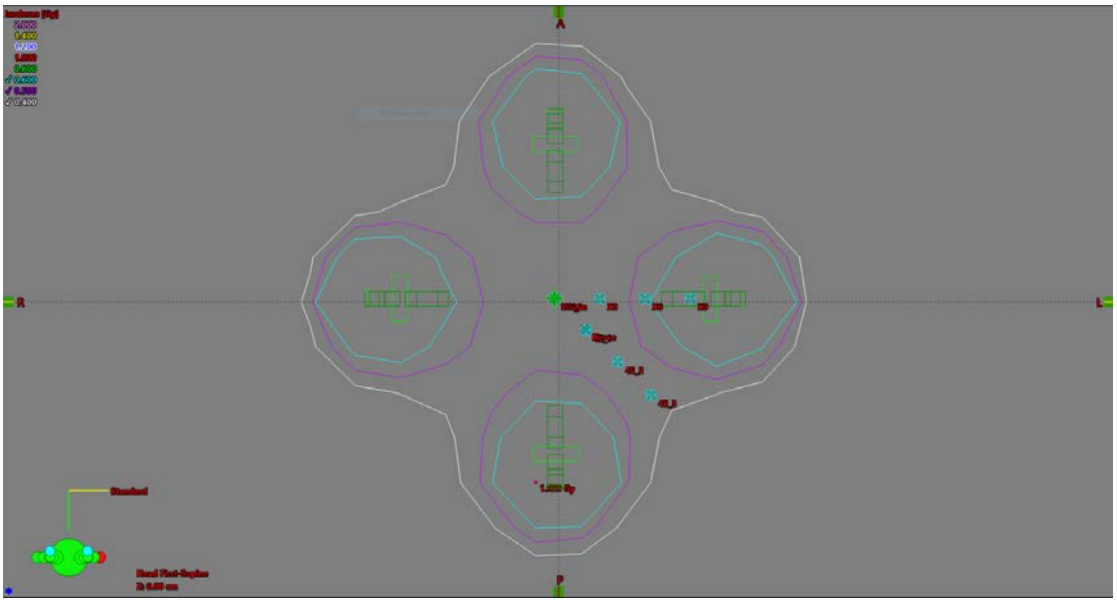

Figure 122: Anterior View: Dose Calculated with Line Source Model of 6711 Seed

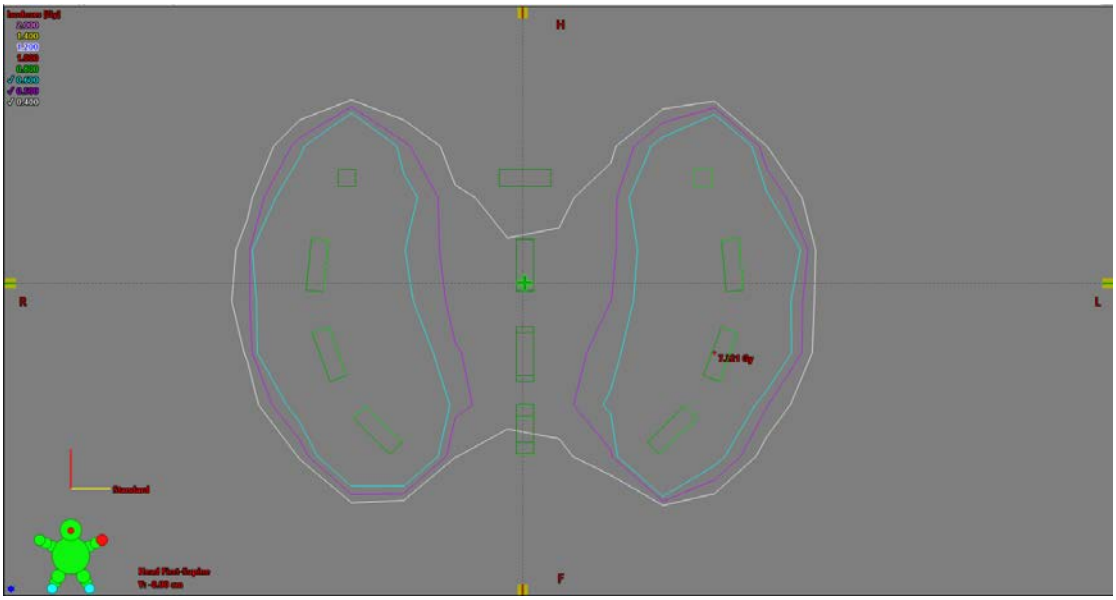

Figure 123: Transverse View: Dose Calculated with Line Source Model of 6711 Seed

The dose at the center (0, 0, 0) was calculated to be 0.425 Gy, the dose at the optic nerve (0.201, 0.201, -1.063) was 0.370 Gy and at the posterior of the eye (0, 0, -1.1) it was 0.333 Gy.

Once again, doses were normalized to the central dose and are displayed as profiles in the next three figures:

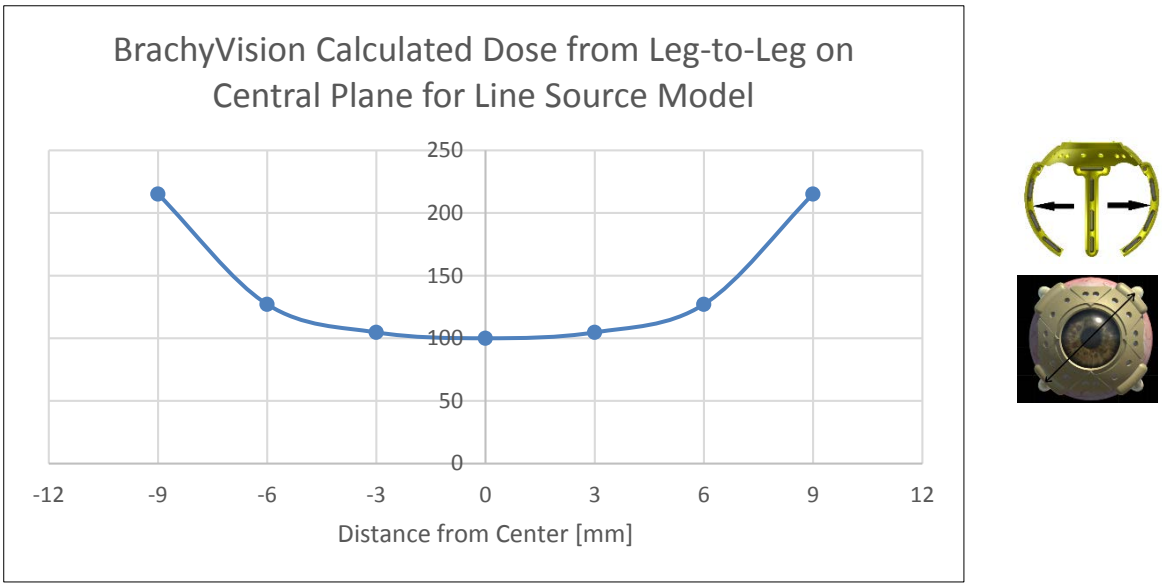

Figure 124: Calculated Dose from Leg-to-Leg on the Central Plane

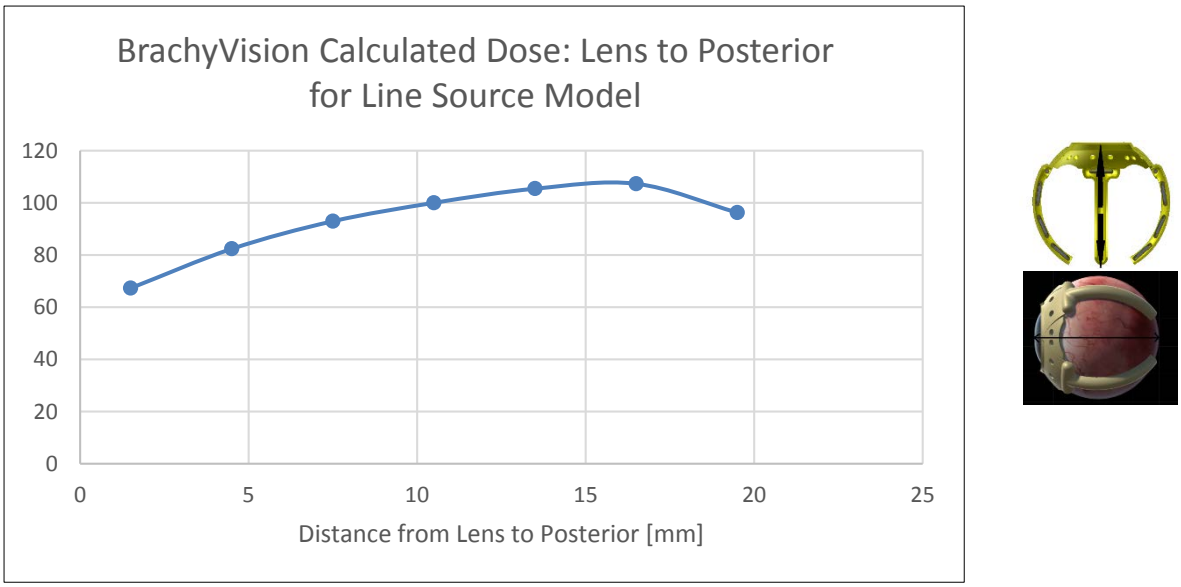

Figure 125: Calculated Dose from Lens to Posterior

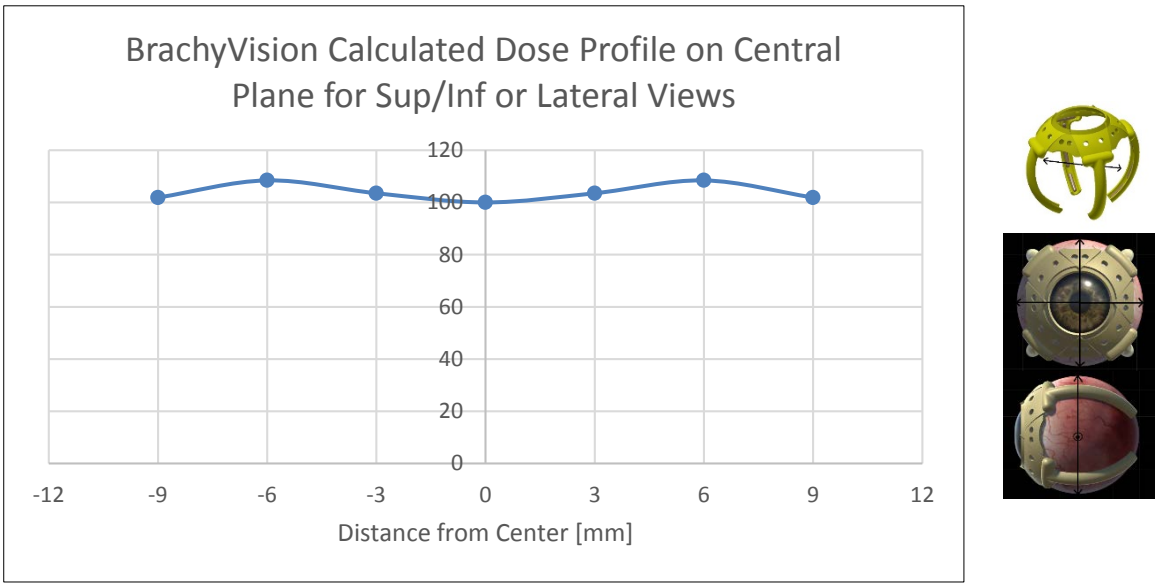

Figure 126: Dose on Central Plane for Sup/Inf or Lateral Views

The central dose for the line source model of BrachyVision (0.425 Gy) is lower than the TPP dose at that point (0.459 Gy) by 7.4 %. Once again, this difference can mostly be explained away by that 0.897 factor that is used at Groote Schuur Hospital.

4.6 Monte Carlo Dose Distributions

MCSHOW was used to display obtained dose distributions. The software is somewhat limited in its display normalization options, but an attempt was made to get the equivalent of the 40 (blue), 50 (green) and 60 cGy/hour (red) isodoserate lines.

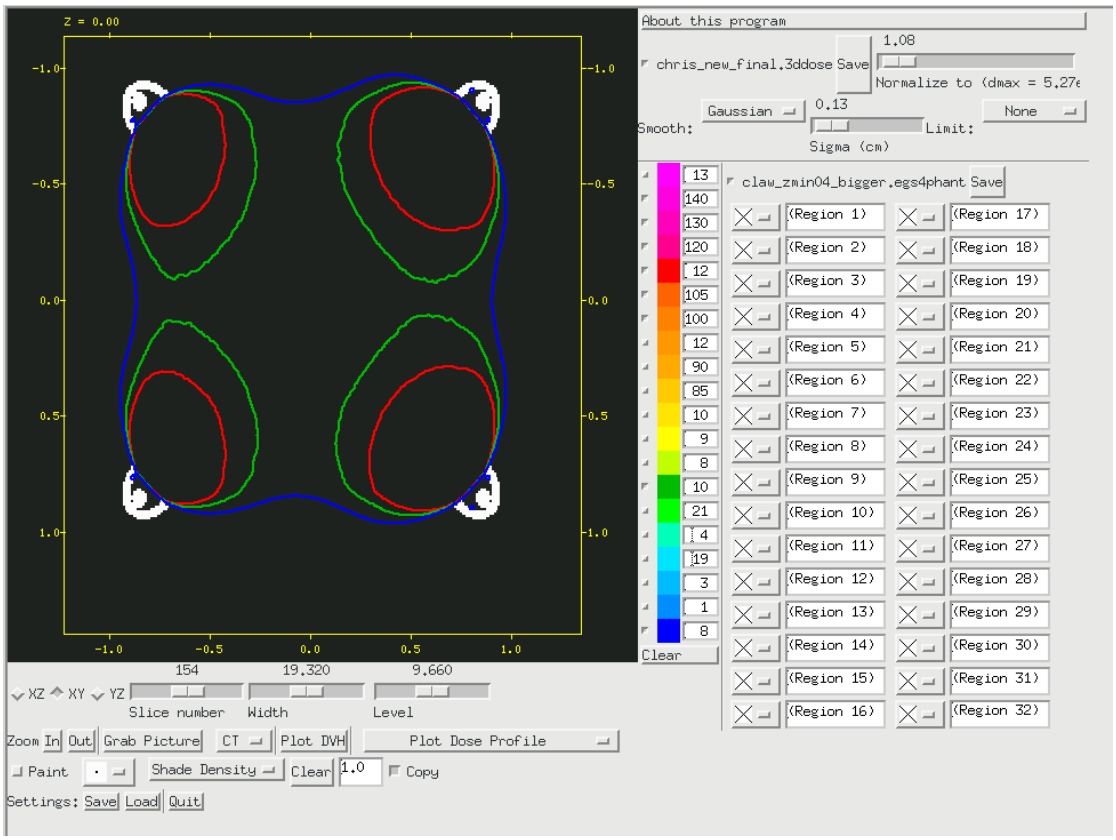

Figure 127: Anterior View on the Central Plane (z=0)

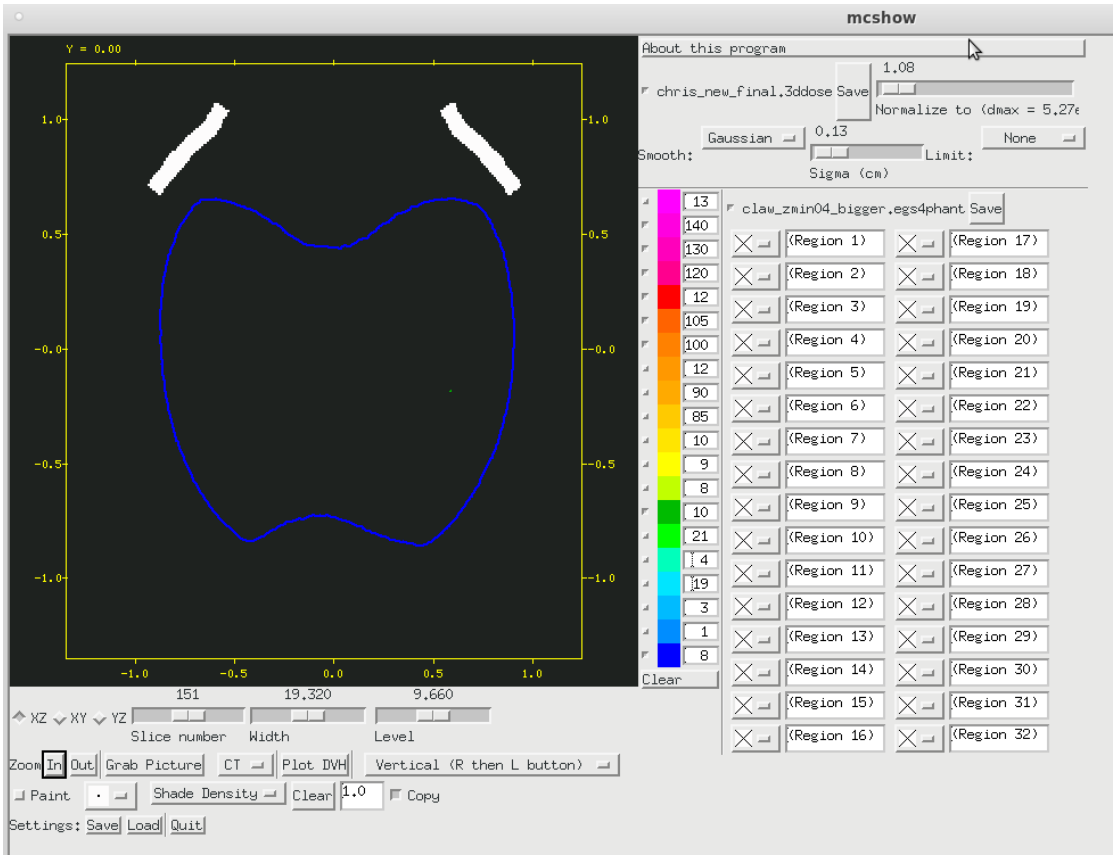

Figure 128: Lateral View

It should be noted that in Figure 128 the same isodose lines are activated as in Figure 127. However, the Monte Carlo phantom has a 45 ° rotation compared to the lateral views from TPP and BrachyVision. In this view the 50 cGy/hr and 60 cGy/hr isodose lines are not visible. Therefore some code was written in IDL to rotate the dose file by 45 ° and to then display these isodose lines (Figure 129). Since only the dose file was rotated, the “Claws” and seeds are not visible, therefore the approximate seed positions were added manually in one leg in Figure 129. The isodose lines are as before (40 cGy/hr – blue, 50 cGy/hr – green, 60 cGy/hr – red).

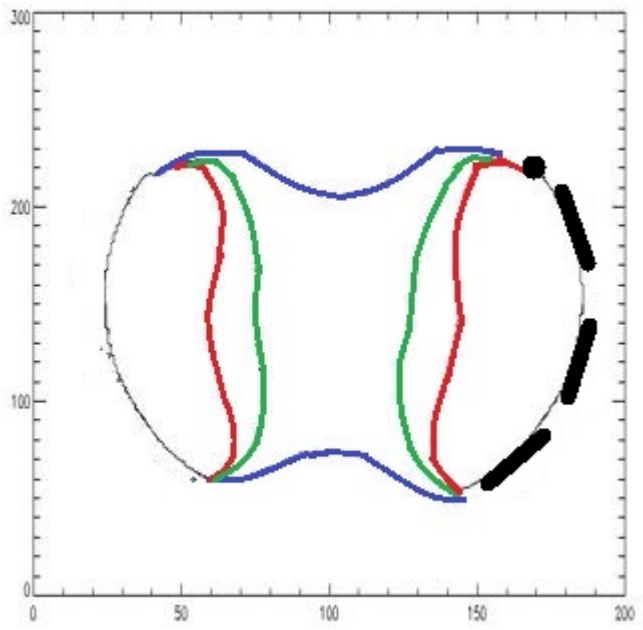

Figure 129: “Leg-to-Leg” Doses – Monte Carlo Simulated Results

As before, dose points were selected for comparison purposes with measured and calculated data. Data was normalized to 100 % at the center of the “Claws”.

The same profiles were drawn as for the measured and planned “Claws” dose distributions, based on point dose data in the Monte Carlo dose file.

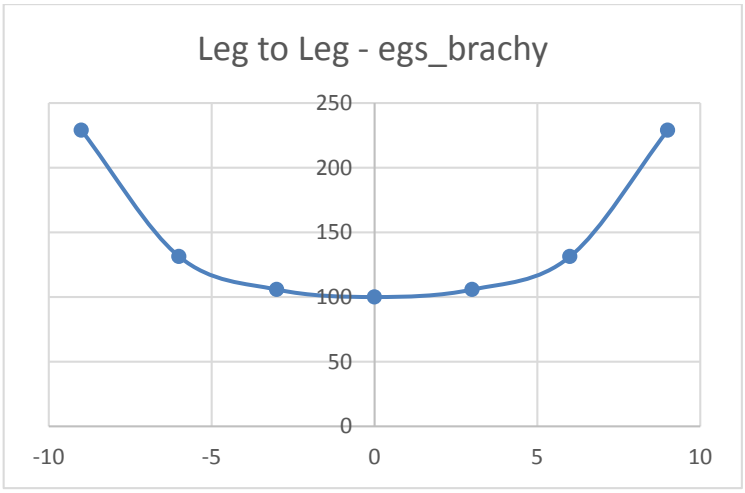

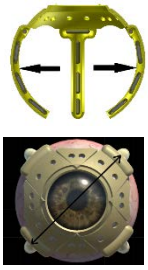

Figure 130: Egs_brachy Calculated Profile from Leg-to-Leg

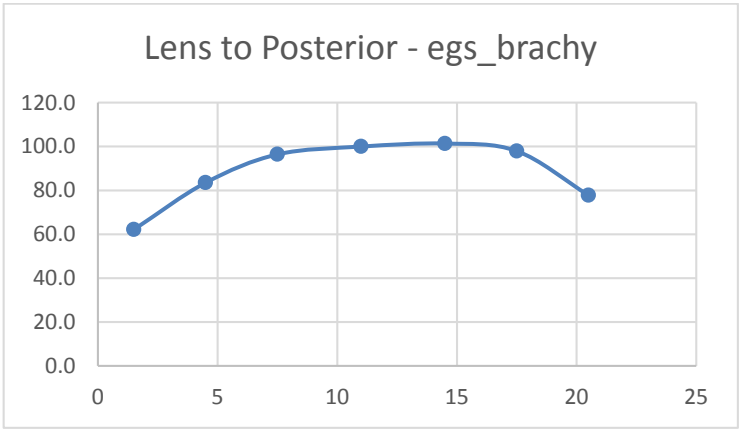

Figure 131: Egs_brachy Calculated Profile from Lens to Posterior

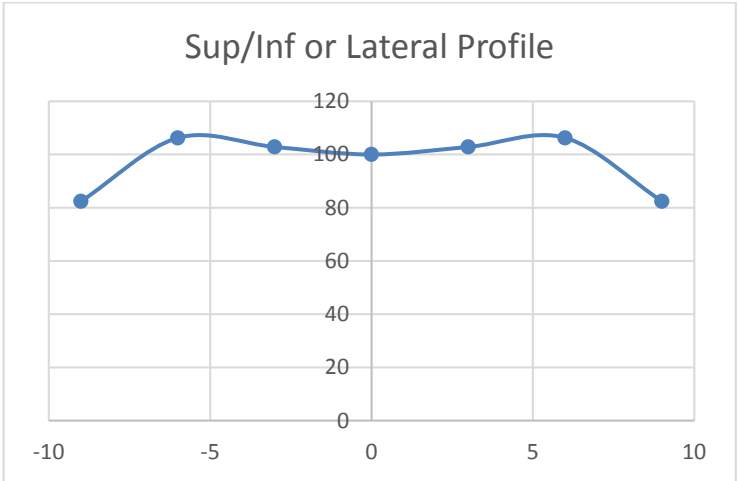

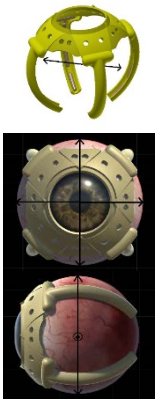

Figure 132: Egs_brachy Calculated Profile for Sup/Inf or Lateral Views

Additionally, the Monte Carlo simulation of the “Claws” now allows the visualization of isodose lines outside of the eye, with the gold shielding of the applicator taken into account. For Figures 133 and 134 the MCSHOW normalization is the same as Figures 127 and 128.

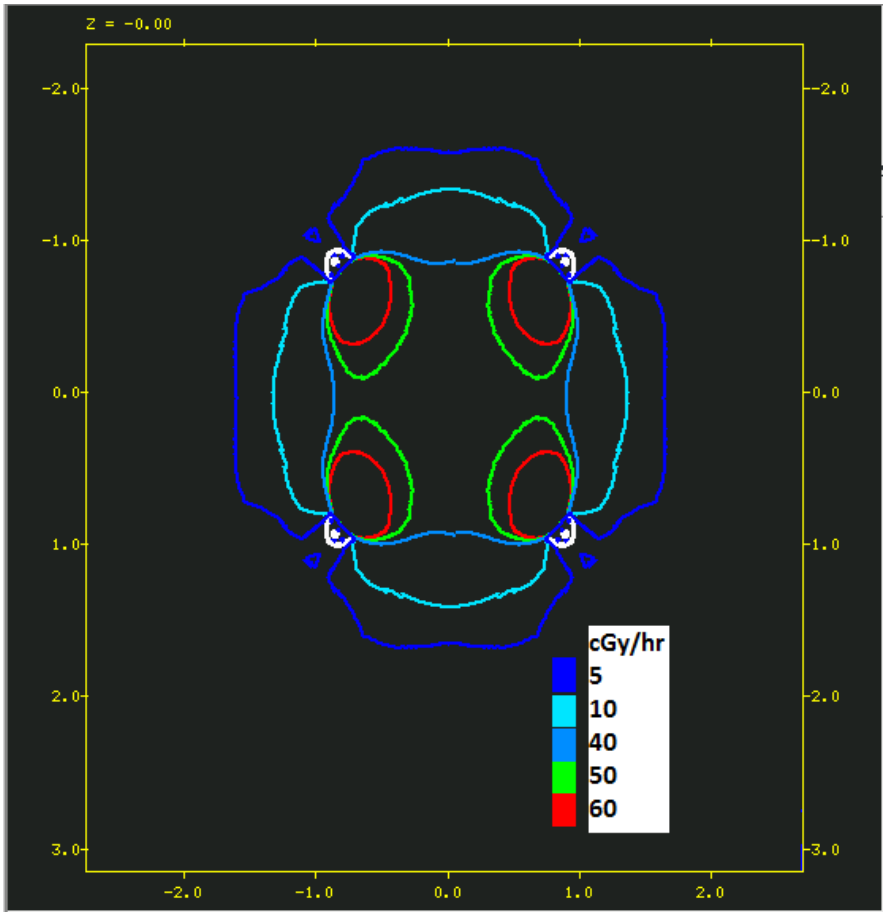

Figure 133: Anterior View on the z = 0 Plane

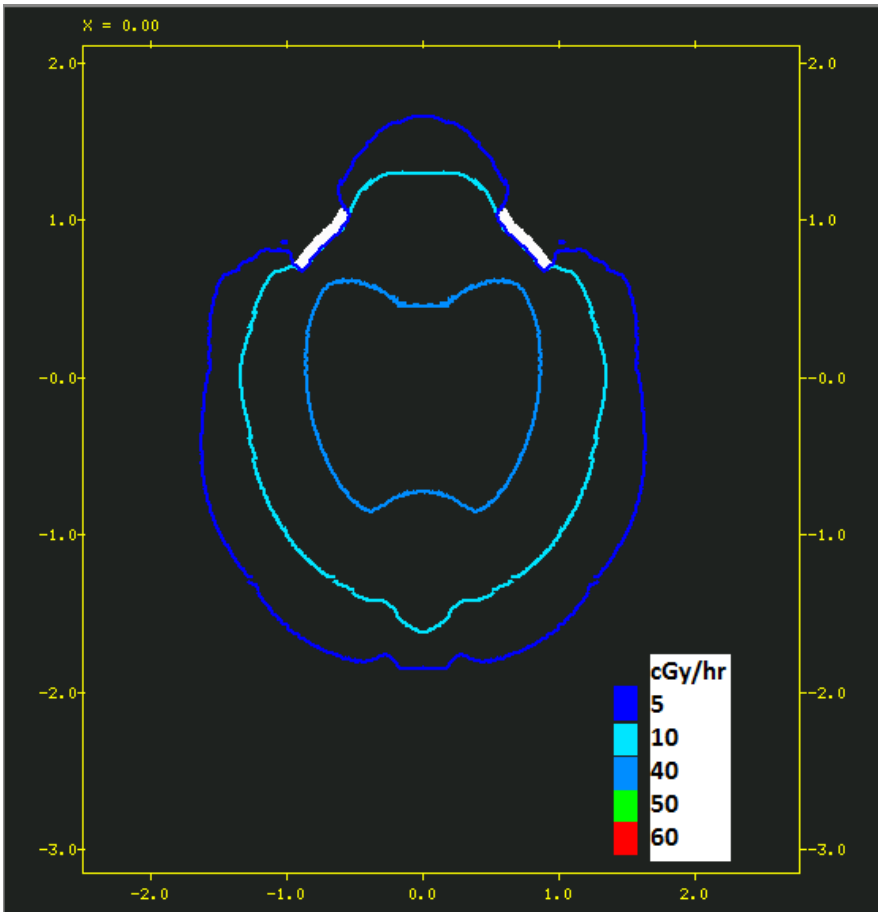

Figure 134: Lateral View on the X = 0 Plane

4.7 Comparison of Dose Profiles in the "Claws"

The dose profiles measured with gafchromic film and TLDs were compared to the planned data (TPP, BrachyVision – Point Source, BrachyVision – Line Source), as well as the Monte Carlo simulated data, as described in Chapters 4.4, 4.5 and 4.6 respectively.

In this section all the measured data is displayed in a single figure per profile.

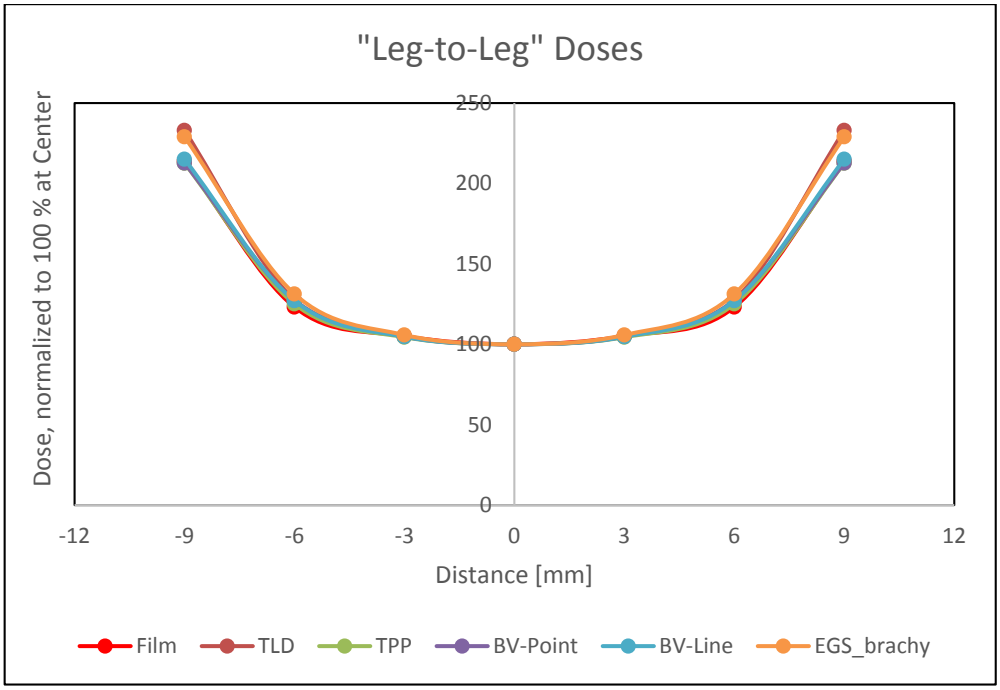

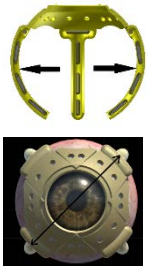

Figure 135: Comparison of "Leg-to-Leg" Profiles

Measured data between the legs on the central plane is a good match throughout. There is a slight mismatch near the seeds closest to the legs, with the biggest difference being between TLD data (233.0 %) and the BrachyVision Point Source data (212.7 %), a maximum difference of 8.7 %.

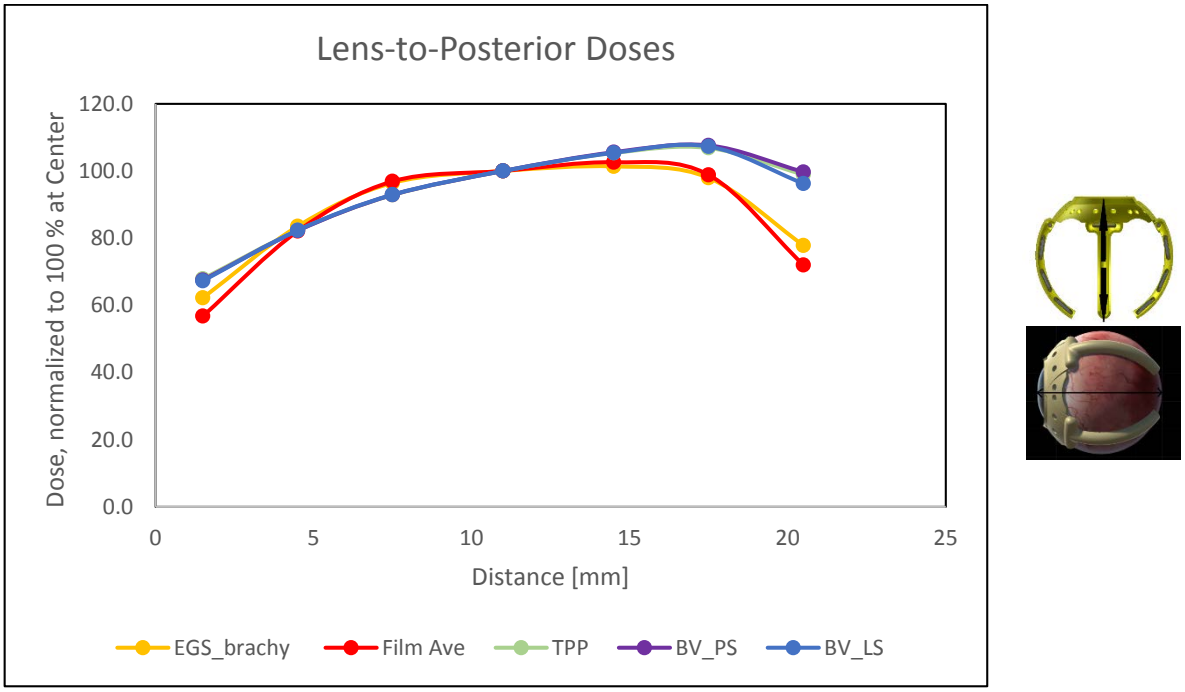

Figure 136: Comparison of Lens-to-Posterior Doses

All the treatment planning systems show different results to the measured and Monte Carlo data near the lens and posterior of the applicator, but all the treatment planning systems match each other very well.

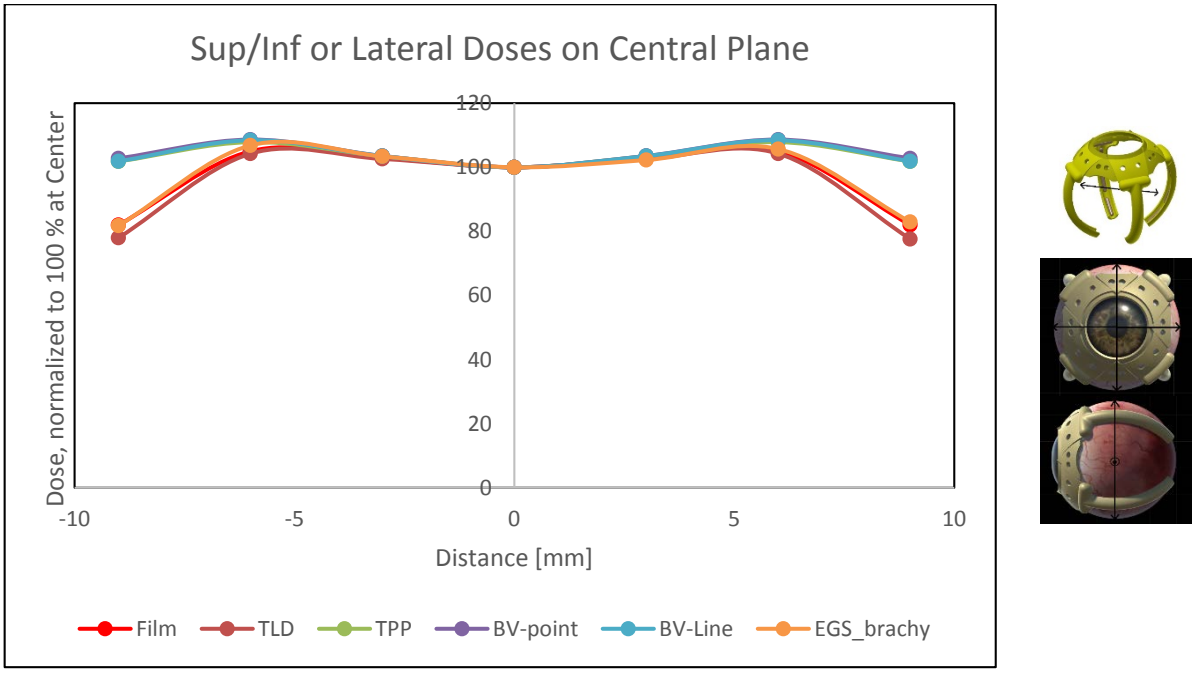

Figure 137: Sup/Inf or Lateral Profile Comparison

Figure 137 represents one of the most interesting results of this thesis.

The three treatment planning systems (TPP, BrachyVision – Point Source, BrachyVision – Line Source) match each other almost perfectly and indicate an almost flat dose response hovering near the central prescription dose, but never less than the prescription dose.

However, the TLD and film measured data match the egs_brachy simulated data, but do not match the planned data near the periphery of the eye.

Differences of up to 20 % are seen at distances of ± 9 mm from the center of the eye.

Figure 138 is a cross-section of the "Claws", with the seeds in the legs of the applicator. It can be seen that the seeds are recessed in the legs, and that there is a geometric occlusion of regions near the periphery of the eye, leading to a significant dose reduction.

The treatment planning systems cannot take the gold shielding into account and therefore calculate significantly higher doses in those regions. However, both measurements and Monte Carlo simulations clearly show a dose reduction, which may have potential clinical implications in that any tumour may potentially be underdosed, if it is located near the periphery of the eye.

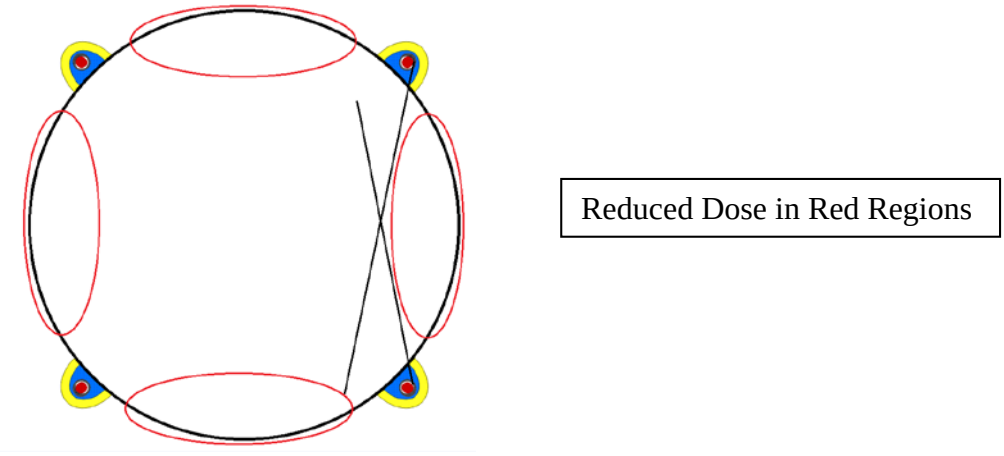

Figure 138: Cross-Section Through the "Claws", Showing the Recessed Seeds in the Legs

4.8 Doses to Critical Structures

4.8.1 Nerve

When the “Claws” are planned, usually the dose at the posterior of the eye (0, 0, -1.1) and the optic nerve (0.201, 0.201, -1.063) are also calculated. These are given in the Table 21 below, normalized to 100 % at the center of the eye.

	TPP	BrachyVision (Point Source	BrachyVision (Line Source)	Egs_brachy
Post	87.1 %	95.2 %	78.4 %	58.0 %
Nerve	93.7 %	103.3 %	87.1 %	64.8 %

Table 21: Comparison of Relative Doses

The original “Claws” Monte Carlo phantom only included 0.1 mm x 0.1 mm x 0.1 mm voxels.

The phantom was extended from the original phantom by 25 1 mm x 1 mm x 1 mm voxels in each direction to get to the final 301 x 301 x 301 voxel cube. This was done particularly to allow the determination of the dose to the bony orbit.

4.8.2 Bony Orbit

The eye socket is quite a complex structure, consisting of seven bones around the eye, namely the frontal bone, the lacrimal bone, the ethmoid bone, the zygomatic bone, the maxillary bone, the palatine bone and the sphenoid bone *(Marieb, 2001)*. The superior margin is made up of the frontal bone and sphenoid, the inferior margin is made up of the maxillary bone, the palatine and the zygomatic bone, the medial margin is made up of the lacrimal, ethmoid and maxillary bones and the lateral margin consists of the zygomatic and sphenoid bones.

The indicator of the dose to the bony orbit is taken as the dose at a distance of 0.5 cm outside of the eye, on the central axis of the sup/inf and lateral axes *(Hering, 2019)*. Relative dose data was obtained from the Monte Carlo dose file.

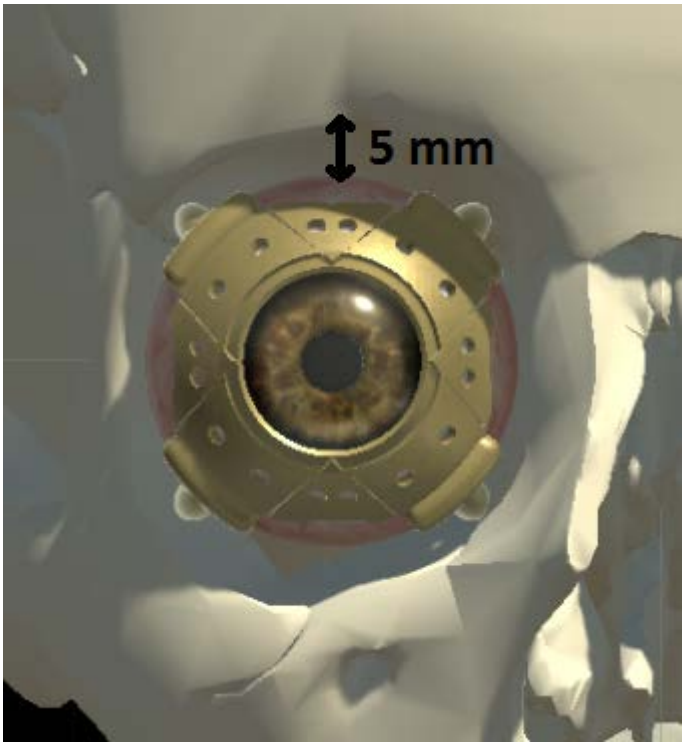

Figure 139: Dose Point for the Bony Orbit Dose

The relative dose to the bony orbit is 11.3 % of the dose to the center of the eye.

4.8.3 Lens of the Eye

Figure 140, taken from *(Damato, 2000)*, indicates a distance of about 6 mm from the center of the eye to the lens for an adult eye of 24 mm diameter.

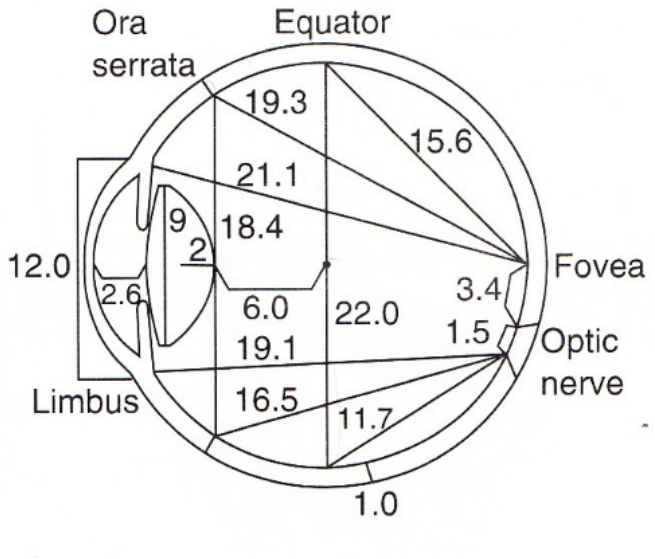

Figure 140: Chart for Estimating Lengths in Millimetres in an Emmetropic (Normal) Eye

This is in good agreement with Figure 141 (adapted from *(Stannard et al., 2001)*), which shows a simplified diagram that was used at Groote Schuur Hospital to show the approximate lens position in the eye for a 22 mm eyeball of a child.

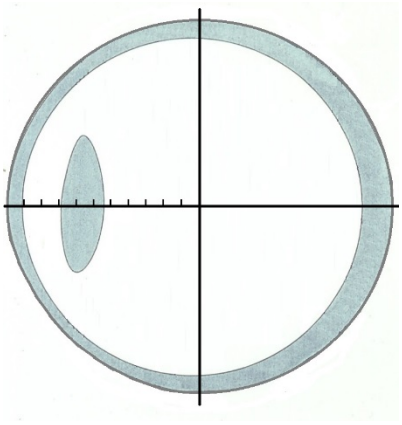

Figure 141: Simplified Diagram of an Eye Used at Groote Schuur Hospital

Dose data was obtained in millimeter intervals from the Monte Carlo dose file on the anterior/posterior central axis. Data was normalized to a dose of 100 % at the center of the eye.

The results are shown in Table 22.

Distance from Center of the Eye	Relative Dose [%]
Center of the Eye	100.0
1.0 mm	99.1
2.0 mm	98.1
3.0 mm	95.9
4.0 mm	93.1
5.0 mm	89.0
5.5 mm (Lens edge near center of eye)	86.3
6.0 mm	83.5
7.0 mm	77.4
8.0 mm (Lens edge near cornea)	72.0
9.0 mm	60.2
10.0 mm	48.5
11.0 mm	38.2

Table 22: Lens Dose in the "Claws"

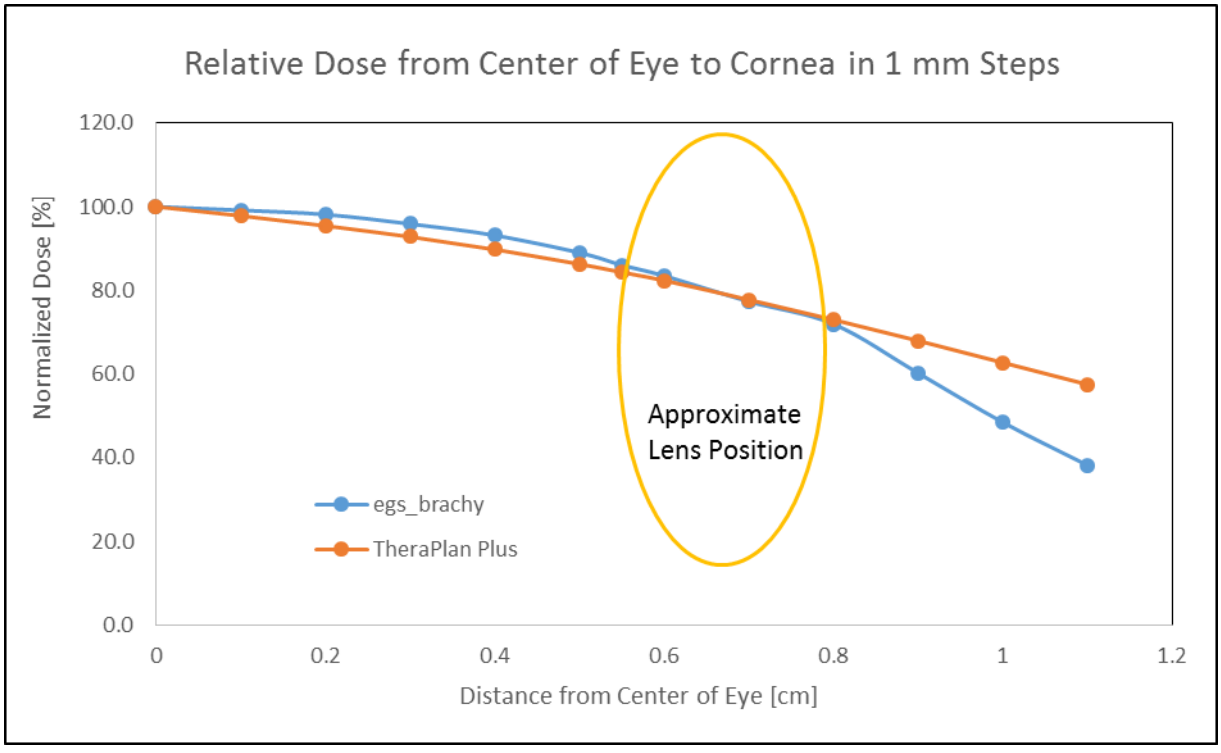

Figure 142: Dose Gradient from Center of Eye to Cornea towards the Cornea on Central Axis

It can be seen that there is a dose gradient across the lens of the eye. The lens dose on the central axis varies from 72.0 % - 86.1 % of the central dose according to the Monte Carlo calculations, while it varies from 73.0 % - 84.3 % for the TheraPlan Plus planned doses.

4.9 Qualitative Comparison of TPP Planned Dose Distribution and egs_brachy Results

For the images in Figures 143 & 144 an attempt was made to match the isodose-rate lines from the Monte Carlo simulations to the TPP calculated ones. Calculated dose distributions were superimposed on an X-ray of the “Claws” in-situ. This was done by removing the background of the isodose distribution image, adding the remainder (i.e. the isodose-rate lines) as a layer to the X-ray image in the image manipulation programme GIMP (Version 2.10.10), and scaling that layer to best match the outline of the “Claws” with the outline of the “Claws” in the X-ray image. Once this was done, the two layers were merged and the image saved.

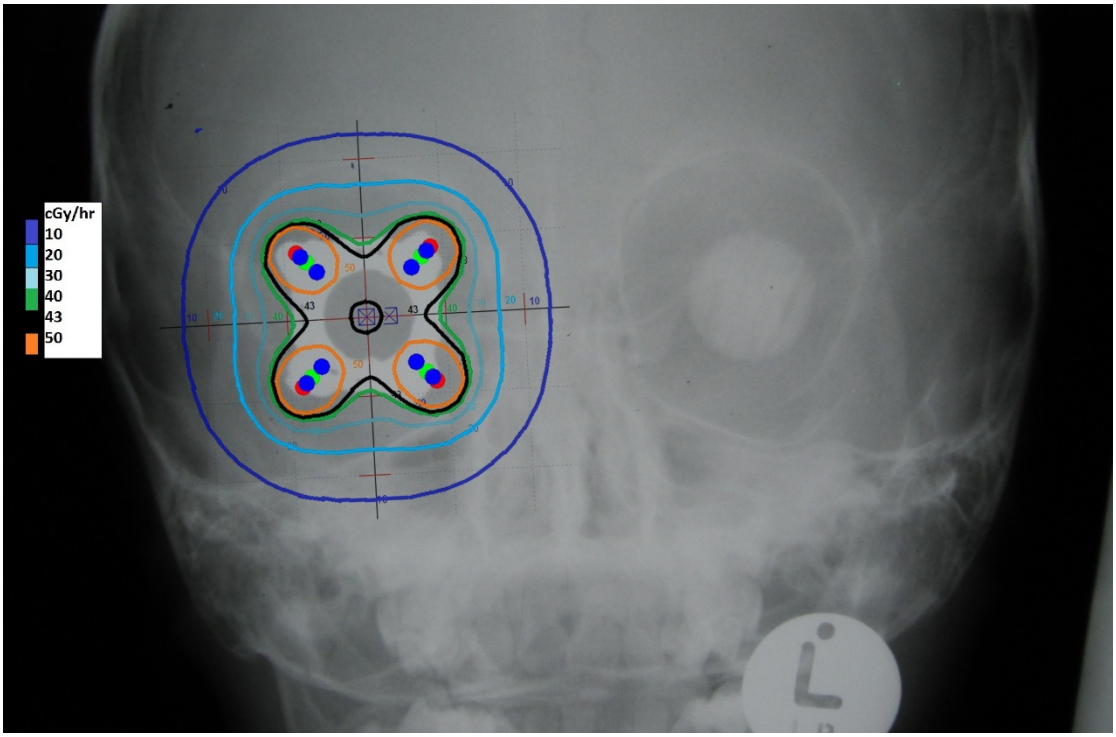

Figure 143: TPP Planned Dose Distribution

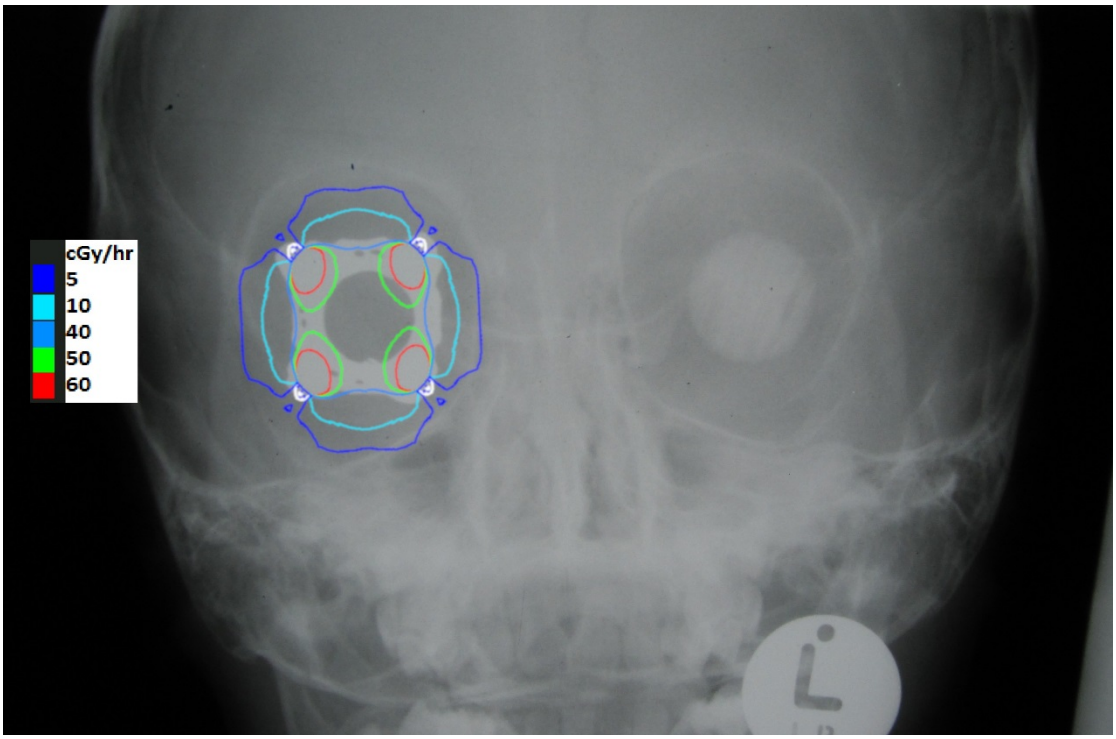

Figure 144: Egs_brachy Calculated Dose Distribution

It can clearly be seen that the Monte Carlo simulated dose distribution conforms much better to the eye, with much less dose reaching the bony orbit than would be expected

from the TPP plan. This is a clear indication that the gold shielding is very effective in sparing the bony orbit. A Monte Carlo dose atlas of the “Claws” dose distribution in and around the eye is superior to the dose distribution calculated by the treatment planning systems, because the gold shielding is clearly taken into account by the Monte Carlo simulations. Now that the “Claws” model is also formalized, it would be possible to manufacture “Claws” reproducibly for use elsewhere on a bigger scale.

CHAPTER 5 DISCUSSION AND CONCLUSION

This thesis described the OncoSeed 6711 I-125 seed in terms of the TG-43 protocol and measured spectra in air.

The thesis also described the “Claws”, a unique gold applicator loaded with I-125 seeds, that is used for whole-eye radiotherapy in the treatment of retinoblastoma.

5.1 The OncoSeed 6711 I-125 Seed

The OncoSeed 6711 I-125 seed has been widely described in literature.

For this study, different detectors were used for spectral measurements in air. The NaI(Tl) detector had the worst energy resolution of all the detectors used; the HPGe detector showed a substantial increase in spectral structure, with more improvement evident when the Low-Energy Photon Spectrometer (LEPS) detector was used. The most suitable detector for the I-125 seed proved to be the silicon drift detector (SDD), which showed a lot of fine detail, including the characteristic X-rays of the titanium casing of the seed. A special jig was constructed for the measurement of the spectra in air at different distances and angles. The spectrum obtained with the SDD was used to determine the average energy of the OncoSeed 6711 spectrum (27.44 keV), as well as a calculated dose rate constant (Λ = 0.978 cGy h^{-1} U^{-1}), both of which are in good agreement with published data. The spectrum could potentially be used as input when using the dosxyz_nrc module of the egs_nrc Monte Carlo code.

Apparent activity / air kerma measurements using the PTW SourceCheck 4π chamber proved that the chamber is an accurate and precise measuring device for I-125 seeds.

Additionally, the geometry function for the OncoSeed 6711 was calculated, based on measured seed data.

The dose rate constant was determined to be $\Lambda = 0.96 \pm 0.20$ cGy h^{-1} U^{-1} in solid water, which is in good agreement with published data.

The anisotropy and radial dose functions of the OncoSeed 6711 seed were determined with gafchromic film and thermoluminescent dosimeters (TLDs) in specially designed and manufactured solid water phantoms.

Calibration of film and TLDs was initially done on a 70 kV X-ray unit with an unusual anode angle of 45 ° and 1.25 mm added filtration. Later on a Co-60 teletherapy unit was used. Film dosimetry was done on the red colour channel after a suitable calibration curve was determined. It was clearly shown that there is a scanner dependence on the greyscale value of the red colour channel, that there is post-irradiation darkening of the film and that there is a difference between portrait and landscape scanning of the film (around 9 % difference in greyscale). It was also shown that a ± 1 % difference in signal can be expected if the scanner is not warmed up before use, and that a maximum difference in greyscale of 3.8 % can be expected for the scanner used in this study, depending on the position of the film on the scanning surface.

Measured anisotropy and radial dose function data matched published data very well. The uncertainty estimation for the film was done based on the standard deviation of the greyscale within a 1 mm x 1 mm region of interest at each measurement position on the film. High dose gradients are evident through a larger standard deviation. The greyscales of the mean ± the standard deviation were converted to maximum and minimum doses using the relevant calibration curve. The upper-lower bound method of uncertainty propagation was used to determine a percentage uncertainty for each reading. Since both the anisotropy and radial dose function include a ratio of doses (or

dose-rates), the final uncertainty was calculated as the square root of the sum of squares of the individual uncertainties.

For the TLD measurements the uncertainty was obtained from the standard deviation from four sets of measurements.

The two hypothesis formulated in Chapter 1.3 for the Oncoseed 6711 were:

Hypothesis 1: Measured I-125 spectra will vary depending on the detector. A detector with a better energy resolution will show more detail.

Hypothesis 2: Measured dosimetric and physical characteristics of the I-125 seeds match published data

Hypothesis 1 was found to be true: the silicone drift detector has the best energy resolution and showed the most detail in the spectrum, allowing the calculation of the average energy, as well as the dose rate constant of the I-125 seed.

Hypothesis 2 was also found to be true. The measured physical dimensions matched the published data to within one standard deviation. Measured anisotropy, radial dose function and dose rate constant also matched published data well.

5.2 The "Claws"

The original "Claws" were manufactured by a jeweller, based on the clinician's description. The "Claws" were formalized in this study. Each component was carefully measured out with a Vernier caliper and a CAD drawing was put together, describing each component exactly. These drawings are available in a range of different formats.

A PVC model of the "Claws" was manufactured using a CNC milling machine. The PVC model was micro-CT scanned at the Central Analytical Facility of Stellenbosch

University. The PVC model was loaded with decayed I-125 seeds and the silver in the seeds led to severe CT artefacts, which made the scan unusable as input for egs_brachy. The CAD drawing of the scan was cut into different slice thicknesses, eventually the 100 μm slices were used to create the Monte Carlo phantom file.

Two solid water phantoms were manufactured for dose distribution measurements in the "Claws" – one for film measurements and one for TLD measurements.

Dose distributions in the "Claws" were calculated with the TheraPlan Plus (Version 3.8 Build 500) treatment planning system, which is still in use at Groote Schuur Hospital for low dose-rate brachytherapy calculations. Additionally, dose distributions were calculated with BrachyVision Version 15.6.05, once using the point source approximation and once using a line-source approximation.

It was found that the TPP treatment planning system overestimates the dose to the center of the eye by 14.2 % when compared to the BrachyVision point source model and by 7.4 % when using the line source model of BrachyVision. TLD measured doses at the center were 81.5 ± 1.4 % of the planned dose from TheraPlan Plus.

Two significant factors contribute to these differences: when the change was made from "activity" to "apparent activity" in the dosimetry, a factor of 0.897 was introduced. However, the clinicians did not want to have any dosimetric changes to their plans, therefore all apparent activities at Groote Schuur Hospital are divided by 0.897, making all plans "hot" by 11.5 %. Another reason for this discrepancy is that measurements were done in solid water and not liquid water, which leads to an additional 4.3 % difference.

An input phantom file for egs_brachy was created, consisting of a 301 x 301 x 301 voxel cube. The first 25 voxels in each direction had dimensions of 1 mm on each side, all other voxel dimensions were 0.1 mm on each side. After some bug fixing a large

simulation of 64.000.000.000 histories was run on 32 cores of the high performance computing cluster at the University of the Free State. The simulation took a little over 11 days to complete, but yielded some interesting results, particularly when looking at the various profiles.

“Leg-to-Leg” profiles (Figure 135) showed good correlation between measured, calculated and Monte Carlo simulated dose distributions.

The profiles down the center of the eye from the cornea to the posterior of the eye (Figure 136) showed reasonable agreement, but with some differences near the lens and posterior of the “Claws”.

The profiles along a Sup/Inf or Lateral cut, identical because of the cylindrical symmetry of the “Claws”, showed substantial differences of up to 20 % between calculated data vs. measured and simulated data (Figure 137). The reason for this is the partial occlusion of the I-125 seeds, because they are recessed in the legs of the “Claws”. Neither TPP nor BrachyVision have the ability to include the gold shielding in their brachytherapy dose calculation. This substantial dose difference was not known and may have clinical implications, with potential underdosing of cancerous tissue near the periphery of the eye.

The Monte Carlo simulations allowed an estimation of the dose to critical structures outside of the eye for the first time.

The optic nerve dose was determined to be only 64.8 % of the central dose, compared to a previous TPP estimate of 93.7 %.

The relative dose to the lens of the eye was also determined using Monte Carlo simulations and ranged from 72.0 % - 86.1 % of the central eye dose on the central axis.

There is very little dose that “spills” out of the eyeball into the bony orbit, as is evident by a low dose of 11.3 % at a distance of 5 mm on the lateral and sup/inf sides of the eye. The TPP planned dose at that point is 54.7 %.
For TPP calculations the dose crossing the patient midway lies around 25 % and is thus a much higher estimate.

The two hypothesis formulated in Chapter 1.3 for the “Claws” were:
Hypothesis 3: Dose distributions inside the eye will be similar for measured data, planned data and Monte Carlo simulated data.
Hypothesis 4: Simulated doses to critical organs will be less than planned doses, because of the gold shielding of the applicator.

Hypothesis 3 was rejected, because the observed results show large discrepancies of up to 20 % in certain regions of the eye. It was shown that the seeds are partially shielded by the gold of the legs, leading to an underdose near the periphery of the eye.
Hypothesis 4 was shown to be true. Gold shields the low-energy radiation from the I-125 seeds very effectively, leading to marked dose reductions to the bony orbit and the optic nerve when comparing Monte Carlo simulated with planned data.

5.3 Future Work

A discussion with the ophthalmic oncologist is needed to decide whether the “Claws” design needs some changes to reduce the gold shielding to the periphery of the eye. Shallower legs will reduce the partial shielding of the sides of the eye, which could potentially improve the clinical outcome of patients. However, this is a clinical decision that should be made by an oncologist.

A methodology was developed to allow the creation of a Monte Carlo phantom file from a CAD drawing. This process could potentially be streamlined to allow for Monte Carlo simulations of other plaques and implants used at Groote Schuur Hospital. It remains to be seen whether this is a feasible option, since every other plaque is custom-made for a patient.

Egs_brachy has been found to be an excellent tool for modelling the “Claws” and has proved to be quite versatile. A graphic user interface may be useful for some users of the code. It may also be useful to create a “CAD to egs_phant” conversion tool, but this was outside of the scope of this work.

It can be concluded that the “Claws” applicator was extensively described and characterized in this work. The Curie Institute in Paris requested a prototype at one point and a group in Essen, Germany, requested the CAD drawings to manufacture their own “Claws”. The “Claws” offer a good way of doing whole-eye radiotherapy when it is clinically indicated. It should be noted that this process is very specialized and requires input from multiple disciplines, including oncology, ophthalmology, medical physics and a mould room. Additionally, the use of newer chemotherapy drugs, like e.g. intra-arterial administration of Melphalan, delivered into the eye under fluoroscopic guidance, offer feasible alternatives, but also require a highly specialized team of clinicians and expensive imaging capabilities to deliver the therapy.

CHAPTER 6 REFERENCES

AALBERS, A., DE BRABANDERE, M., KOEDOODER, C., MOERLAND, M., RIJNDERS, A., SCHAEKEN, B., THISSEN, B., VAN'T RIET, A. & VYNCKIER, S. 2012. Dosimetry and quality control of brachytherapy with low-energ y photon sources (125I). *Report 20 of the Netherlands Commission on Radiation Dosimetry*.

ABBOUD, F., HOLLOWS, M., SCALLIET, P. & VYNCKIER, S. 2010. Experimental and theoretical dosimetry of a new polymer encapsulated iodine-125 source—SmartSeed: Dosimetric impact of fluorescence x rays. *Medical Physics,* 37**,** 2054-2062.

ABRÀMOFF, M. D., MAGALHÃES, P. J. & RAM, S. J. 2004. Image processing with ImageJ. *Biophotonics International* 11**,** 36-42.

ABRATT, R.E. 2006: https://www.news.uct.ac.za/article/-2006-02-27-obituary-gordon-rossall-hamilton-sealy

ACAR, H., CHIU-TSAO, S. T., ÖZBAY, İ., KEMIKLER, G. & TUNCER, S. 2013. Evaluation of material heterogeneity dosimetric effects using radiochromic film for COMS eye plaques loaded with 125I seeds (model I25. S16). *Medical Physics,* 40.

ADAMOVICS, J. & MARYANSKI, M. 2004. A new approach to radiochromic three-dimensional dosimetry-polyurethane. *Journal of Physics: Conference Series*. IOP Publishing, Vol 3, Issue 1.

AFSHARPOUR, H., D'AMOURS, M., COTÉ, B., CARRIER, J. F., VERHAEGEN, F. & BEAULIEU, L. 2008. A Monte Carlo study on the effect of seed design on the interseed attenuation in permanent prostate implants. *Medical Physics,* 35**,** 3671-3681.

ALBERT, D., DIENER-WEST, M., ROBINSON, N., GROSSNIKLAUS, H., GREEN, W., VINE, A., WILLIS, J., FRUEH, B., KURTZ, R. & ELNER, S. 1998. Histopathologic characteristics of uveal melanomas in eyes enucleated from the collaborative ocular melanoma study COMS Report No. 6. *American Journal of Ophthalmology*, 125**,** 745-766.

AMATO, E., LIZIO, D. & BALDARI, S. 2013. Applications of the Monte Carlo Method in Medical Physics. *Medical Physics.* Nova Science Publishers, Inc. Editor: M Balcerzyk

AMPTEK 2011. X-Ray Fluorescence (XRF).

AMPTEK 2013. X-123 Complete X-Ray Spectrometer.

AMPTEK 2014a. AN-AMP-005: A COMPARISON OF SILICON DRIFT (SDD) AND SI-PIN DETECTORS.

AMPTEK 2014b. Application Note: AN-SDD-001 RevB0 - Amptek Silicon Drift Diode (SDD) at High Count Rates.

AMPTEK 2014c. DETECTOR EFFICIENCY FAQ.

AMPTEK 2015. Application Note AN-SDD-003: Amptek Silicon Drift Detectors.

ANAGNOSTOPOULOS, G., BALTAS, D., KARAISKOS, P., SANDILOS, P., PAPAGIANNIS, P. & SAKELLIOU, L. 2002. Thermoluminescent dosimetry of the selectSeed 125I interstitial brachytherapy seed. *Medical Physics,* 29**,** 709-716.

ANDREO, P. 1991. Monte Carlo Techniques in Medical Radiation Physics. *Physics in Medicine & Biology,* 36**,** 861.

ANDRES, C., DEL CASTILLO, A., TORTOSA, R., ALONSO, D. & BARQUERO, R. 2010. A comprehensive study of the Gafchromic EBT2 radiochromic film. A comparison with EBT. *Medical Physics,* 37**,** 6271-6278.

ARJOMANDY, B., TAILOR, R., ANAND, A., SAHOO, N., GILLIN, M., PRADO, K. & VICIC, M. J. M. P. 2010. Energy dependence and dose response of Gafchromic EBT2 film over a wide range of photon, electron, and proton beam energies. *Medical Physics* 37**,** 1942-1947.

ASTRAHAN, M. A. 2005. Improved treatment planning for COMS eye plaques. *International Journal of Radiation Oncology* Biology* Physics,* 61**,** 1227-1242.

ASTRAHAN, M. A. 2019. *RE: Personal Communication.*

ASTRAHAN, M. A., LUXTON, G., JOZSEF, G., KAMPP, T. D., LIGGETT, P. E., SAPOZINK, M. D. & PETROVICH, Z. 1990a. An interactive treatment planning system for ophthalmic plaque radiotherapy. *International Journal of Radiation Oncology* Biology* Physics,* 18**,** 679-687.

ASTRAHAN, M. A., LUXTON, G., JOZSEF, G., LIGGETT, P. E. & PETROVICH, Z. 1990b. Optimization of 125I ophthalmic plaque brachytherapy. *Medical Physics,* 17**,** 1053-1057.

ASTRAHAN, M. A., LUXTON, G., PU, Q. & PETROVICH, Z. 1997. Conformal episcleral plaque therapy. *International Journal of Radiation Oncology* Biology* Physics,* 39**,** 505-519.

ASTRAHAN, M. A., SZECHTER, A. & FINGER, P. T. 2005. Design and dosimetric considerations of a modified COMS plaque: the reusable “seed-guide” insert. *Medical Physics,* 32**,** 2706-2716.

ATTIX, F. H. 1986. *Introduction to Radiological Physics and Radiation Dosimetry,* John Wiley & Sons.

BAMBYNEK, M., FLÜHS, D., HEINTZ, M., KOLANOSKI, H., WEGENER, D. & QUAST, U. 1999. Fluorescence 125I eye applicator. *Medical Physics,* 26**,** 2476-2481.

BEARDEN, J. A. 1967. X-ray wavelengths. *Reviews of Modern Physics,* 39**,** 78.

BEARDEN, J. A. & BURR, A. 1967. Reevaluation of X-ray atomic energy levels. *Reviews of Modern Physics,* 39**,** 125.

BEAULIEU, L., CARLSSON TEDGREN, Å., CARRIER, J. F., DAVIS, S. D., MOURTADA, F., RIVARD, M. J., THOMSON, R. M., VERHAEGEN, F., WAREING, T. A. & WILLIAMSON, J. F. 2012. Report of the Task Group 186 on model-based dose calculation methods in brachytherapy beyond the TG-43 formalism: Current status and recommendations for clinical implementation. *Medical Physics,* 39**,** 6208-6236.

BERGER, M. J. & HUBBELL, J. 1987. XCOM: Photon cross sections on a personal computer. National Bureau of Standards, Washington, DC (USA). Center for Radiation Research

BERGER, M. J., HUBBELL, J.H., SELTZER, S.M., CHANG, J., COURSEY, J.S., SUKUMAR, R., ZUCKER, D.S AND OLSEN, K. 1998. *XCOM: Photon Cross Sections Database* [Online]. Available: https://www.nist.gov/pml/xcom-photon-cross-sections-database [Accessed 5 Oct 2019].

BERGER, M. J. & SELTZER, S. M. 1982. Stopping Powers and Ranges of Electrons and Positions. NATIONAL STANDARD REFERENCE DATA SYSTEM.

BIELAJEW, A. 2004. History, Overview and Recent Improvement of EGS4. Stanford Linear Accelerator Center (SLAC), Menlo Park, CA.

BIELAJEW, A. F. 2016. Fundamentals of the Monte Carlo method for neutral and charged particle transport. *Lecture Notes*.

BIELAJEW, A. F. J. I. F. N. M. S., NATIONAL RESEARCH COUNCIL OF CANADA 1994. *Lecture notes: Photon Monte Carlo Simulation*.

BINDER, C., CRILLY, R., BROWN, S., SKALET, A. & HUNG, A. 2016. Plaque Size and Dose in I-125 Eye Plaque Brachytherapy. *International Journal of Radiation Oncology* Biology* Physics,* 96**,** E596.

BOHM, T. D., DELUCA JR, P. M. & DEWERD, L. A. 2003. Brachytherapy dosimetry of 125I and 103Pd sources using an updated cross section library for the MCNP Monte Carlo transport code. *Medical Physics,* 30**,** 701-711.

BORCA, V. C., PASQUINO, M., RUSSO, G., GROSSO, P., CANTE, D., SCIACERO, P., GIRELLI, G., PORTA, M. R. L. & TOFANI, S. 2013. Dosimetric characterization and use of GAFCHROMIC EBT3 film for IMRT dose verification. *Journal of Applied Clinical Medical Physics,* 14**,** 158-171.

BRADY, L. W., SHIELDS, J. A., AUGSBURGER, J. J. & DAY, J. L. 1982. Malignant intraocular tumors. *Cancer,* 49**,** 578-585.

BRENNER, D. J., LEU, C.-S., BEATTY, J. F., SHEFER, R. E. 1999. Clinical relative biological effectiveness of low-energy x-rays emitted by miniature x-ray devices. *Physics in Medicine and Biology,* 44**,** 323.

BRUALLA, L., SEMPAU, J., ZARAGOZA, F., WITTIG, A. & SAUERWEIN, W. 2013. Accurate estimation of dose distributions inside an eye irradiated with 106 Ru plaques. *Strahlentherapie und Onkologie,* 189**,** 68-73.

BUCHGEISTER, M., GRISANTI, S., SÜSSKIND, D., BAMBERG, M. & PAULSEN, F. 2007. A new fixation aid for the radiotherapy of eye tumors. *Medical Physics,* 34**,** 4649-4653.

BUG, M., SCHNEIDER, T. 2017. EP-1475: RBE estimation of different Brachytherapy sources based on micro-and nanodosimetry. *Radiotherapy & Oncology* 123**,** S788.

BURNS, G. & RAESIDE, D. 1989. The accuracy of single-seed dose superposition for I-125 implants. *Medical Physics,* 16**,** 627-631.

BURNS, G. S. & RAESIDE, D. E. 1983. Monte Carlo estimates of specific absorbed fractions for an I-125 point source in water. *Medical Physics,* 10**,** 197-198.

BUSHBERG, J. T., SEIBERT, J. A., LEIDHOLDT JR, E. M., BOONE, J. M. & GOLDSCHMIDT JR, 2003. The essential physics of medical imaging. Lippincott Williams & Wilkins

BUTLER, W. M., BICE, W. S., DEWERD, L. A., HEVEZI, J. M., HUQ, M. S., IBBOTT, G. S., PALTA, J. R., RIVARD, M. J., SEUNTJENS, J. P. & THOMADSEN, B. R. 2008. Third-party brachytherapy source calibrations and physicist responsibilities: Report of the AAPM Low Energy Brachytherapy Source Calibration Working Group. *Medical Physics,* 35**,** 3860-3865.

BUTSON, M. J., CHEUNG, T. & PETER, K. 2006. Weak energy dependence of EBT gafchromic film dose response in the 50kVp–10MVp X-ray range. *Applied Radiation and Isotopes,* 64**,** 60-62.

BUTSON, M. J., CHEUNG, T., YU, P. K., ALNAWAF, H. 2009. Dose and absorption spectra response of EBT2 Gafchromic film to high energy x-rays. *Australasian Physical & Engineering Sciences in Medicine* Volume 32**,** 196-202.

BUTSON, M. J., CHEUNG, T., YU, P. K. N. 2005. Absorption spectra variations of EBT radiochromic film from radiation exposure. *Physics in Medicine and Biology* 50**,** N135-N140.

BUTSON, M. J., PETER, K., CHEUNG, T. & ALNAWAF, H. 2010. Energy response of the new EBT2 radiochromic film to x-ray radiation. *Radiation Measurements* 45**,** 836-839.

BUTSON, M. J., PETER, K., CHEUNG, T. & METCALFE, P. 2003. Radiochromic film for medical radiation dosimetry. *Materials Science and Engineering: Reports, R*41**,** 61-120.

BUZUROVIC, I., SHOWALTER, T. N., STUDENSKI, M. T., DEN, R. B., DICKER, A. P., CAO, J., XIAO, Y., YU, Y. & HARRISON, A. 2013. Commissioning and implementation of an implantable dosimeter for radiation therapy. *Journal of Applied Clinical Medical Physics,* 14**,** 234-252.

BYRNE, S. F., MARSH, M. J., BOLDT, H. C., GREEN, R. L., JOHNSON, R. N. & WILSON, D. J. 2002. Consistency of observations from echograms made centrally in the Collaborative Ocular Melanoma Study COMS Report No. 13. *Ophthalmic Epidemiology,* 9**,** 11-27.

CANBERRA 2016. Standard Electrode Coaxial Ge Detectors.

CASSADY, J. R. & ABRAMSON, D. H. 1993. Retinoblastoma: Genetics, diagnosis, treatment and consequences. *International Journal of Radiation Oncology* Biology* Physics,* 27**,** 116.

CASSOUX, N., LUMBROSO, L., LEVY-GABRIEL, C., AERTS, I., DOZ, F. & DESJARDINS, L. 2017. Retinoblastoma: Update on current management. *Asia-Pacific Journal of Ophthalmology (Philadelphia, Pa.),* 6**,** 290-295.

CHAMBERLAIN, W. E. & NEWELL, R. 1928. The Epilation and the Erythema Dose: A comparison of filtered and unfiltered roentgen ray. *Radiology* 10**,** 280-283.

CHAMBERLAND, M. J., TAYLOR, R. E., ROGERS, D., THOMSON, R. M. 2016. egs_brachy: a versatile and fast Monte Carlo code for brachytherapy. *Physics in Medicine & Biology* 61**,** 8214.

CHAN, G. H. & PRESTWICH, W. V. 2002. Dosimetric properties of the new 125I BrachySeed™ model LS-1 source. *Medical Physics,* 29**,** 190-200.

CHANTADA, G. L. 2011. Retinoblastoma: lessons and challenges from developing countries. Ellsworth Lecture 2011. *Ophthalmic Genetics,* 32**,** 196-203.

CHEN, Z., BONGIORNI, P. & NATH, R. 2012. Experimental characterization of the dosimetric properties of a newly designed I-Seed model AgX100 125I interstitial brachytherapy source. *Brachytherapy,* 11**,** 476-482.

CHEN, Z. & NATH, R. 2001. Dose rate constant and energy spectrum of interstitial brachytherapy sources. *Medical Physics,* 28**,** 86-96.

CHERRY, S. R., SORENSON, J. & PHELPS, M. E. 2004. Physics in nuclear medicine. Elsevier

CHIBANI, O., WILLIAMSON, J. F. & TODOR, D. 2005. Dosimetric effects of seed anisotropy and interseed attenuation for Pd103 and I125 prostate implants. *Medical Physics,* 32**,** 2557-2566.

CHIU-TSAO, S.-T., ASTRAHAN, M. A., FINGER, P. T., FOLLOWILL, D. S., MEIGOONI, A. S., MELHUS, C. S., MOURTADA, F., NAPOLITANO, M. E., NATH, R. & RIVARD, M. J. 2012. Dosimetry of 125I and 103Pd COMS eye plaques for intraocular tumors: Report of Task Group 129 by the AAPM and ABS. *Medical Physics,* 39**,** 6161-6184.

CHIU-TSAO, S. T., ANDERSON, L. L., O'BRIEN, K. & SANNA, R. 1990. Dose rate determination for 125I seeds. *Medical Physics,* 17**,** 815-825.
CHIU-TSAO, S. T., ANDERSON, L. L., O'BRIEN, K., STABILE, L. & LIU, J. C. 1993. Dosimetry for 125I seed (model 6711) in eye plaques. *Medical Physics,* 20**,** 383-389.
CHIU-TSAO, S. T., DUCKWORTH, T. L., HSIUNG, C. Y., LI, Z., WILLIAMSON, J., PATEL, N. S. & HARRISON, L. B. 2003. Thermoluminescent dosimetry of the SourceTech Medical model STM1251 125I seed. *Medical Physics,* 30**,** 1732-1735.
CHIU-TSAO, S. T., HO, Y., SHANKAR, R., WANG, L. & HARRISON, L. B. 2005. Energy dependence of response of new high sensitivity radiochromic films for megavoltage and kilovoltage radiation energies. *Medical Physics,* 32**,** 3350-3354.
CHIU-TSAO, S. T., MEDICH, D. & MUNRO, J. 2008. The use of new GAFCHROMIC® EBT film for I125 seed dosimetry in Solid Water® phantom. *Medical Physics,* 35**,** 3787-3799.
COMPTON, A. H. 1923. A quantum theory of the scattering of X-rays by light elements. *Physical Review,* 21**,** 483.
COMS, G. 1993. Design and methods of a clinical trial for a rare condition: the Collaborative Ocular Melanoma Study: COMS report No. 3.
COMS, G. 1997. Factors predictive of growth and treatment of small melanoma. COMS report No. 5. *Archives of Ophthalmology,* 115**,** 1573-1544.
COMS, G. 2004. Ten-year follow-up of fellow eyes of patients enrolled in Collaborative Ocular Melanoma Study randomized trials: COMS report no. 22. *Ophthalmology,* 111**,** 966-976.
CURRY, T. S., DOWDEY, J. E. & MURRY, R. C. 1990. *Christensen's physics of diagnostic radiology*, Lippincott Williams & Wilkins.
DAMATO, B. 2000. *Ocular tumours: diagnosis and treatment,* Butterworth-Heinemann Oxford.
DAS, R., LI, Z., PERERA, H., WILLIAMSON, J. 1996. Accuracy of Monte Carlo photon transport simulation in characterizing brachytherapy dosimeter energy-response artefacts. *Physics in Medicine and Biology* 41**,** 995.
DE LA ZERDA, A., CHIU-TSAO, S. T., LIN, J., BOULAY, L. L., KANNA, I., KIM, J. H. & TSAO, H. S. 1996. 125I eye plaque dose distribution including penumbra characteristics. *Medical Physics,* 23**,** 407-418.
DE SUTTER, E., HAVERS, W., HOPPING, W., ZELLER, G. & ALBERTI, W. 1987a. The prognosis of retinoblastoma in terms of survival. A computer assisted study. Part II. *Ophthalmic Paediatrics and Genetics,* 8**,** 85-88.
DE SUTTER, E., HAVERS, W., HÖPPING, W., ZELLER, G. & ALBERTI, W. 1987b. The prognosis of retinoblastoma in terms of globe saving treatment. A computer assisted study. Part I. *Ophthalmic Paediatrics and Genetics,* 8**,** 77-84.
DEARDORFF, D. 2018. Measurement & Uncertainty Analysis Guide. Available: https://physics.unc.edu/files/2018/07/Measurement-and-Uncertainty-Techniques.pdf.
DESROCHES, J., BOUCHARD, H. & LACROIX, F. 2010. Potential errors in optical density measurements due to scanning side in EBT and EBT2 Gafchromic film dosimetry. *Medical Physics* 37**,** 1565-1570.
DEVIC, S. 2011. Radiochromic film dosimetry: past, present, and future. *Physica Medica,* 27**,** 122-134.

DEVIC, S., ALDELAIJAN, S., MOHAMMED, H., TOMIC, N., LIANG, L. H., DEBLOIS, F. & SEUNTJENS, J. 2010. Absorption spectra time evolution of EBT-2 model GAFCHROMIC™ film. *Medical Physics* 37**,** 2207-2214.

DEVIC, S., SEUNTJENS, J., HEGYI, G., PODGORSAK, E. B., SOARES, C. G., KIROV, A. S., ALI, I., WILLIAMSON, J. F. & ELIZONDO, A. 2004. Dosimetric properties of improved GafChromic films for seven different digitizers. *Medical Physics,* 31**,** 2392-2401.

DEVIC, S., SEUNTJENS, J., SHAM, E., PODGORSAK, E. B., SCHMIDTLEIN, C. R., KIROV, A. S. & SOARES, C. G. 2005. Precise radiochromic film dosimetry using a flat-bed document scanner. *Medical Physics,* 32**,** 2245-2253.

DEWERD, L. A., IBBOTT, G. S., MEIGOONI, A. S., MITCH, M. G., RIVARD, M. J., STUMP, K. E., THOMADSEN, B. R. & VENSELAAR, J. L. M. 2011. A dosimetric uncertainty analysis for photon-emitting brachytherapy sources: Report of AAPM Task Group No. 138 and GEC-ESTRO. *Medical Physics,* 38**,** 782-801.

DIENER-WEST, M., EARLE, J., FINE, S., HAWKINS, B., MOY, C., REYNOLDS, S., SCHACHAT, A. & STRAATSMA, B. 2001a. The COMS randomized trial of iodine 125 brachytherapy for choroidal melanoma, II: characteristics of patients enrolled and not enrolled. COMS Report No. 17. *Archives of Ophthalmology (Chicago, Ill.: 1960),* 119**,** 951-965.

DIENER-WEST, M., HAWKINS, B. S., MOY, C. S. & EARLE, J. D. 2001b. Sociodemographic and clinical predictors of participation in two randomized trials: findings from the Collaborative Ocular Melanoma Study COMS report no. 7. *Controlled Clinical Trials,* 22**,** 526-537.

DOLAN, J., LI, Z. & WILLIAMSON, J. F. 2006. Monte Carlo and experimental dosimetry of an I125 brachytherapy seed. *Medical Physics,* 33**,** 4675-4684.

DU PLESSIS, A., LE ROUX, S. G., GUELPA, A. 2016. The CT Scanner Facility at Stellenbosch University: an open access X-ray computed tomography laboratory. *Nuclear Instruments and Methods in Physics Research B* 384**,** 42-49.

DU PLESSIS, F. 2019. *Personal Communication.*

DUGGAN, D. & JOHNSON, B. 2001. Dosimetry of the I-Plant Model 3500 iodine-125 brachytherapy source. *Medical Physics,* 28**,** 661-670.

DUGGAN, D. M. 2004. Improved radial dose function estimation using current version MCNP Monte-Carlo simulation: Model 6711 and ISC3500 125I brachytherapy sources. *Applied Radiation and Isotopes,* 61**,** 1443-1450.

EARLE, J., KLINE, R. W. & ROBERTSON, D. M. 1987. Selection of iodine 125 for the collaborative ocular melanoma study. *Archives of Ophthalmology,* 105**,** 763-764.

ECKHARDT, R. 1987. Stan ulam, john von neumann, and the monte carlo method. *Los Alamos Science* 15**,** 30.

EICHMANN, M., FLÜHS, D. & SPAAN, B. 2009. Development of a high precision dosimetry system for the measurement of surface dose rate distribution for eye applicators. *Medical Physics,* 36**,** 4634-4643.

ELLSWORTH, R. 1969. The practical management of retinoblastoma. *Transactions of the American Ophthalmological Society,* 67**,** 462.

EMERY, R. S. & SZECHTER, A. 1998. Seed localization in eye plaque brachytherapy. *Medical Physics,* 25**,** 1491-1492.

FINGER, P. T., BERSON, A., NG, T. & SZECHTER, A. 2002. Palladium-103 plaque radiotherapy for choroidal melanoma: an 11-year study. *International Journal of Radiation Oncology * Biology * Physics* 54**,** 1438-1445.
FINGER, P. T., LU, D., BUFFA, A., DEBLASIO, D. & BOSWORTH, J. L. 1993. Palladium-103 versus iodine-125 for ophthalmic plaque radiotherapy. *International Journal of Radiation Oncology* Biology* Physics* 27**,** 849-854.
FINGER, P. T. 2007. Finger's "slotted" eye plaque for radiation therapy: treatment of juxtapapillary and circumpapillary intraocular tumours. *British Journal of Opthalmology* 91**,** 891-894.
FINGER, P. T. 2009. Radiation therapy for orbital tumors: concepts, current use, and ophthalmic radiation side effects. *Survey of Ophthalmology* 54**,** 545-568.
FLÜHS, D., HEINTZ, M., INDENKÄMPEN, F., WIECZOREK, C., KOLANOSKI, H. & QUAST, U. 1996. Direct reading measurement of absorbed dose with plastic scintillators—the general concept and applications to ophthalmic plaque dosimetry. *Medical Physics,* 23**,** 427-434.
FURHANG, E. E. & ANDERSON, L. L. 1999. Functional fitting of interstitial brachytherapy dosimetry data recommended by the AAPM Radiation Therapy Committee Task Group 43. *Medical Physics* 26**,** 153-160.
FURHANG, E. E. & WALLACE, R. E. 2000. Fitting and benchmarking of dosimetry data for new brachytherapy sources. *Medical Physics* 27**,** 2302-2306.
GAFCHROMIC_EBT2 2009a. GAFCHROMIC® EBT2 Dosimetry Film - Product Specification.
GAFCHROMIC_EBT2 2009b. GAFCHROMIC® EBT2 SELF-DEVELOPING FILM FOR RADIOTHERAPY DOSIMETRY.
GAFCHROMIC_EBT3 2012. GAFCHROMIC™ DOSIMETRY MEDIA, TYPE EBT-3.
GARTH, J. C. 2005. Electron/photon transport and its applications. *The Monte Carlo Method: Versatility Unbounded in a Dynamic Computing World, Chattanooga, Tennessee*
GEARHEART, D. M., DROGIN, A., SOWARDS, K., MEIGOONI, A. S. & IBBOTT, G. S. 2000. Dosimetric characteristics of a new 125I brachytherapy source. *Medical Physics,* 27**,** 2278-2285.
GRABOWSKI, E. F. & ABRAMSON, D. H. 1987. Intraocular and extraocular retinoblastoma. *Hematology/Oncology Clinics,* 1**,** 721-735.
GRANERO, D., PÉREZ-CALATAYUD, J., BALLESTER, F., CASAL, E. & DE FRUTOS, J. 2004. Dosimetric study of the 15mm ROPES eye plaque. *Medical Physics,* 31**,** 3330-3336.
GROSSNIKLAUS, H. E., ALBERT, D. M., GREEN, W. R., CONWAY, B. P. & HOVLAND, K. R. 1997. Clear cell differentiation in choroidal melanoma: COMS report No. 8. *Archives of Ophthalmology,* 115**,** 894-898.
HARTMANN, B., MARTIŠÍKOVÁ, M. & JÄKEL, O. 2010. Homogeneity of Gafchromic® EBT2 film. *Medical Physics* 37**,** 1753-1756.
HAWKINS, B. S. & MELIA, M. 1997. Mortality in patients with small choroidal melanoma: COMS Report No. 4. *Archives of Ophthalmology,* 115**,** 886-893.
HEDTJÄRN, H., CARLSSON, G. A. & WILLIAMSON, J. F. 2000. Monte Carlo-aided dosimetry of the symmetra model I25. S06 125I, interstitial brachytherapy seed. *Medical Physics,* 27**,** 1076-1085.
HEINTZ, B. H., WALLACE, R. E. & HEVEZI, J. M. 2001. Comparison of I-125 sources used for permanent interstitial implants. *Medical Physics,* 28**,** 671-682.
HERING, E. 2019. *Personal Communication.*

HERING, E., LE ROUX, P. & SEALY, R. 1978. A comparison of the biological effect of iodine 125 and tantalum 182 gamma rays using vicia faba roots. *The British Journal of Radiology* 51**,** 392-393.
HERING, E., SEALY, G., DOWMAN, P., BLEKKENHORST, G. 1987. OER and RBE for 125I and 192Ir at low dose rateon mammalian cells. *Radiotherapy & Oncology* 10**,** 247-252.
HERING, E., SEALY, R., KORRUBEL, J. & HILL, J. 1989. An iodine-125 applicator designed for irradiating blood vessels growing into the cornea of the eye. *The British Journal of Radiology* 62**,** 266-268.
HERING, E., SEALY, R., LE ROUX, P. & CLEMINSHAW, H. 1977. The use of screened low energy radiation sources for moulds. *The British Journal of Radiology* 50**,** 357-359.
HERING, E. BINNS, P. 1993. Microdosimetry for I-125 Seeds Used for Brachytherapy. Poster presented at SAAPMB Congress, Groote Schuur Hospital.
HERING, E. 1980. A comparison of the biological effect of 125I and 192Ir gamma rays on the roots of Vicia faba using a specially designed applicator. *The British Journal of Radiology* 53**,** 255-258.
HILL, J., SEALY, R., SHACKLETON, D., STANNARD, C., KORRUBEL, J., HERING, E. & LOXTON, C. 1992. Improved iodine-125 plaque design in the treatment of choroidal malignant melanoma. *British Journal of Ophthalmology,* 76**,** 91-94.
HOFSTADTER, R. 1948. Alkali halide scintillation counters. *Physical Review* 74**,** 100-101.
HOWARD, L. K. 2014. Monte Carlo optimisation of detector packaging for real time urethral dosimetry during low dose rate brachytherapy. University of Wollongong Thesis Collection
HUANG, D. Y. C., SCHELL, M. C., WEAVER, K. A. & LING, C. C. 1990. Dose distribution of 125I sources in different tissues. *Medical Physics,* 17**,** 826-832.
IBBOTT, G. S., MEIGOONI, A. S. & GEARHEART, D. M. 2002. Monte Carlo determination of dose rate constant. *Medical Physics,* 29**,** 1637-1638.
IBBOTT, G. S. & NATH, R. 2001. Dose-rate constant for Imagyn 125I brachytherapy source. *Medical Physics,* 28**,** 705-705.
JAYACHANDRAN, C. 1971. Calculated effective atomic number and kerma values for tissue-equivalent and dosimetry materials. *Physics in Medicine & Biology,* 16**,** 617.
JOHN, D., EARLE, M., FINE, S. L., HAWKINS, B. S., STRAATSMA, M. & OCULAR, C. 2001. The COMS randomized trial of iodine 125 brachytherapy for choroidal melanoma, III: initial mortality findings. *Archives of Ophthalmology,* 119**,** 969-982.
KARAISKOS, P., PAPAGIANNIS, P., SAKELLIOU, L., ANAGNOSTOPOULOS, G. & BALTAS, D. 2001. Monte Carlo dosimetry of the selectSeed 125I interstitial brachytherapy seed. *Medical Physics,* 28**,** 1753-1760.
KARAISKOS, P., SAKELLIOU, L., SANDILOS, P. & VLACHAS, L. 2000. Limitations of the point and line source approximations for the determination of geometry factors around brachytherapy sources. *Medical Physics,* 27**,** 124-128.
KAWRAKOW, I. 2002, Electron impact ionization cross sections for EGSnrc. MEDICAL PHYSICS(Conference). American Institute of Physics 1230-1230.

KAWRAKOW, I. 2005. EGSnrc C++ class library Technical Report PIRS–898, National Research Council of Canada, Ottawa, Canada.
KAWRAKOW, I., MAINEGRA-HING, E., ROGERS, D. W. O., TESSIER, F. & WALTERS, B. 2019. The EGSnrc code system: Monte Carlo simulation of electron and photon transport, NRCC Report PIRS-701. *National Research Council of Canada*.
KAWRAKOW, I. & ROGERS, D. W. O. 2007. EGSnrc Summary. *http://resource.npl.co.uk/docs/science_technology/ionising%20radiation/clubs_groups/monte_carlo/2007/workshop/kawrakow_egsnrc_overview.pdf*.
KENNEDY, R. M., DAVIS, S. D., MICKA, J. A. & DEWERD, L. A. 2010. Experimental and Monte Carlo determination of the TG-43 dosimetric parameters for the model 9011 THINSeed™ brachytherapy source. *Medical Physics,* 37**,** 1681-1688.
KHAN, F. M. & GIBBONS, J. P. 2014. *Khan's the physics of radiation therapy*, Lippincott Williams & Wilkins.
KIM, J. & HILARIS, B. 1975. Iodine 125 source in interstitial tumor therapy: Clinical and biologic considerations. *American Journal of Roentgenology* 123**,** 163-169.
KING, R. P., ANDERSON, R. S. & MILLS, M. D. 2001. Geometry function of a linear brachytherapy source. *Journal of Applied Clinical Medical Physics* 2**,** 69-72.
KIROV, A. S. & WILLIAMSON, J. F. 2001. Monte Carlo-aided dosimetry of the Source Tech Medical Model STM1251 I-125 interstitial brachytherapy source. *Medical Physics,* 28**,** 764-772.
KLEVENHAGEN, S. 1985. Physics of electron beam therapy.
KNOLL, G. F. 2010. *Radiation detection and measurement*, John Wiley & Sons.
KNUTSEN, S., HAFSLUND, R., MONGE, O. R., VALEN, H., MUREN, L. P., REKSTAD, B. L., KROHN, J. & DAHL, O. 2001. Dosimetric verification of a dedicated 3D treatment planning system for episcleral plaque therapy. *International Journal of Radiation Oncology* Biology* Physics,* 51**,** 1159-1166.
KOCH, H. & MOTZ, J. 1959. Bremsstrahlung cross-section formulas and related data. *Reviews of Modern Physics* 31**,** 920.
KRINTZ, A. L., HANSON, W. F., IBBOTT, G. S. & FOLLOWILL, D. S. 2003. A reanalysis of the collaborative ocular melanoma study medium tumor trial eye plaque dosimetry. *International Journal of Radiation Oncology* Biology* Physics,* 56**,** 889-898.
KUBO, H. 1985a. Comparison of two independent exposure measurement techniques for clinical I-125 seeds. *Medical Physics,* 12**,** 221-224.
KUBO, H. 1985b. Exposure contribution from Ti K x rays produced in the titanium capsule of the clinical I-125 seed. *Medical Physics,* 12**,** 215-220.
KUTCHER, G. J., COIA, L., GILLIN, M., HANSON, W. F., LEIBEL, S., MORTON, R. J., PALTA, J. R., PURDY, J. A., REINSTEIN, L. E. & SVENSSON, G. K. 1994. Comprehensive QA for radiation oncology: report of AAPM radiation therapy committee task group 40. *Medical Physics,* 21**,** 581-618.
LANDRY, G., RENIERS, B., MURRER, L., LUTGENS, L., BLOEMEN-VAN GURP, E., PIGNOL, J.-P., KELLER, B., BEAULIEU, L. & VERHAEGEN, F. 2010. Sensitivity of low energy brachytherapy Monte Carlo dose calculations to uncertainties in human tissue composition. *Medical Physics,* 37**,** 5188-5198.

LANDRY, G., RENIERS, B., PIGNOL, J.-P., BEAULIEU, L. & VERHAEGEN, F. 2011. The difference of scoring dose to water or tissues in Monte Carlo dose calculations for low energy brachytherapy photon sources. *Medical Physics,* 38**,** 1526-1533.

LAWSON, A. & DAVIDSON, J. M. 1910. Radium therapy in eye disease. *The British Medical Journal,* 2**,** 1491.

LI, Z. 2002. Monte Carlo calculations of dosimetry parameters of the Urocor Prostaseed 125I source. *Medical Physics,* 29**,** 1029-1034.

LI, Z., FAN, J. & PALTA, J. R. 2000. Experimental measurements of dosimetric parameters on the transverse axis of a new 125I source. *Medical Physics,* 27**,** 1275-1280.

LI, Z. & WILLIAMSON, J. 2002. Measured transverse-axis dosimetric parameters of the model STM1251 I125 interstitial source. *Journal of Applied Clinical Medical Physics,* 3**,** 212-217.

LING, C. C., LI, W. X. & ANDERSON, L. L. 1995. The relative biological effectiveness of I-125 and Pd-103. *Internatioal Journal of Radiation Oncology * Biology * Physics* 32**,** 373-378.

LING, C. C., SCHELL, M. C., YORKE, E. D., PALOS, B. B. & KUBIATOWICZ, D. O. 1985. Two-dimensional dose distribution of 125I seeds. *Medical Physics,* 12**,** 652-655.

LOMMATZSCH, P. & VOLLMAR, R. 1966. Ein neuer Weg zur konservativen Therapie intraokularer Tumoren mit Betastrahlen (106Ru/106Rh) unter Erhaltung der Sehfähigkeit. *Klinisches Monatsblatt Augenheilkunde,* 148**,** 682-699.

LUXTON, G. 1994. Comparison of radiation dosimetry in water and in solid phantom materials for I-125 and Pd-103 brachytherapy sources: EGS4 Monte Carlo study. *Medical Physics,* 21**,** 631-641.

LUXTON, G., ASTRAHAN, M. A., FINDLEY, D. O. & PETROVICH, Z. 1990. Measurement of dose rate from exposure-calibrated 125I seeds. *International Journal of Radiation Oncology• Biology• Physics,* 18**,** 1199-1207.

LUXTON, G., ASTRAHAN, M. A., LIGGETT, P. E., NEBLETT, D. L., COHEN, D. M. & PETROVICH, Z. 1988. Dosimetric calculations and measurements of gold plaque ophthalmic irradiators using iridium-192 and iodine-125 seeds. *International Journal of Radiation Oncology* Biology* Physics,* 15**,** 167-176.

LUXTON, G. & JOZSEF, G. 1999. Radial dose distribution, dose to water and dose rate constant for monoenergetic photon point sources from 10 keV to 2 MeV: EGS4 Monte Carlo model calculation. *Medical Physics,* 26**,** 2531-2538.

LYMPEROPOULOU, G., PAPAGIANNIS, P., SAKELLIOU, L., KARAISKOS, P., SANDILOS, P., PRZYKUTTA, A. & BALTAS, D. 2005. Monte Carlo and thermoluminescence dosimetry of the new IsoSeed® model I25.S17 I125 interstitial brachytherapy seed. *Medical Physics,* 32**,** 3313-3317.

MANBY, A. R. 1905. Radium bromide in the treatment of rodent ulcer. *The British Medical Journal,* 2**,** 8.

MARCHESE, M. J., HALL, E. J. & HILARIS, B. S. 1984. Encapsulated iodine-125 in radiation oncology. I. Study of the relative biological effectiveness (RBE) using low dose rate irradiation of mammalian cell cultures. *American Journal of Clinical Oncology* 7**,** 607-611.

MAREE, G. J. 2019. *Personal Communication*

MARGO, C. E. 2004. The collaborative ocular melanoma study: an overview. *Cancer Control,* 11**,** 304-309.

MARIEB, E. N. 2001. Human Anatomy & Physiology - 5th Edition. 32**,** 28.
MARMIER, P. & SHELDON, E. 1969. PHYSICS OF NUCLEI AND PARTICLES. VOLUME I.
MASSILLON-JL, G., CHIU-TSAO, S.-T., DOMINGO-MUÑOZ, I. & CHAN, M. F. 2012. Energy dependence of the new Gafchromic EBT3 film: dose response curves for 50 kV, 6 and 15 MV X-ray beams. *International Journal of Medical Physics, Clinical Engineering and Radiation Oncology,* 1**,** 60.
MCCONN, R. J., GESH, C. J., PAGH, R. T., RUCKER, R. A. & WILLIAMS III, R. 2011. Compendium of material composition data for radiation transport modeling. Pacific Northwest National Laboratory (PNNL), Richland, WA (US).
MEIGOONI, A., DINI, S. A., SOWARDS, K., HAYES, J. L. & AL-OTOOM, A. 2002a. Experimental determination of the TG-43 dosimetric characteristics of EchoSeed™ model 6733 125I brachytherapy source. *Medical Physics,* 29**,** 939-942.
MEIGOONI, A. S., AWAN, S. B., THOMPSON, N. S. & DINI, S. A. 2006. Updated Solid Water™ to water conversion factors for I125 and Pd103 brachytherapy sources. *Medical Physics,* 33**,** 3988-3992.
MEIGOONI, A. S., GEARHEART, D. M. & SOWARDS, K. 2000. Experimental determination of dosimetric characteristics of Best® brachytherapy source. *Medical Physics,* 27**,** 2168-2173.
MEIGOONI, A. S., HAYES, J. L., ZHANG, H. & SOWARDS, K. 2002b. Experimental and theoretical determination of dosimetric characteristics of IsoAid ADVANTAGE™ 125I brachytherapy source. *Medical Physics,* 29**,** 2152-2158.
MEIGOONI, A. S., YOE-SEIN, M. M., AL-OTOOM, A. Y. & SOWARDS, K. T. 2002c. Determination of the dosimetric characteristics of InterSource125 iodine brachytherapy source. *Applied Radiation and Isotopes,* 56**,** 589-599.
MEIGOONI, A. S., ZHANG, H., PERRY, C., DINI, S. A., KOONA, R. A. 2003. Theoretical and experimental determination of dosimetric characteristics for brachyseed™ Pd-103, model Pd-1, source. *Applied Radiation and Isotopes* 58**,** 533-541.
MELHUS, C. S. & RIVARD, M. J. 2006. Approaches to calculating AAPM TG-43 brachytherapy dosimetry parameters for Cs137, I125, Ir192, Pd103, and Yb169 sources. *Medical Physics,* 33**,** 1729-1737.
MELHUS, C. S. & RIVARD, M. J. J. M. P. 2008. COMS eye plaque brachytherapy dosimetry simulations for Pd-103, I-125 and Cs-131. *Medical Physics,* 35**,** 3364-3371.
MELIA, B., ABRAMSON, D., ALBERT, D., BOLDT, H., EARLE, J., HANSON, W., MONTAGUE, P., MOY, C., SCHACHAT, A. & SIMPSON, E. 2001. Collaborative ocular melanoma study (COMS) randomized trial of I-125 brachytherapy for medium choroidal melanoma. I. Visual acuity after 3 years COMS report no. 16. *Ophthalmology,* 108**,** 348-366.
METROPOLIS, N. & ULAM, S. 1949. The monte carlo method. *Journal of the American Statistical Association* 44**,** 335-341.
METROPOLIS, N. 1987. The beginning of the Monte Carlo method. *Los Alamos Science* 15**,** 125-130.
MEYER, W. H. & GLASSER, O. 1926. Erythema doses in absolute units. *Radiology* 6**,** 320-328.

MIRAS, H., TERRÓN, J. A. & LALLENA, A. M. 2012. Monte Carlo simulation of COMS ophthalmic applicators loaded with Bebig I25. S16 seeds and comparison with planning system predictions. *Physica Medica,* 20**,** 1- 9.
MITCH, M. G., DEWERD, L. A., MINNITI, R. & WILLIAMSON, J. F. 2009. Treatment of uncertainties in radiation dosimetry. *Clinical Dosimetry Measurements in Radiotherapy, Medical Physics Monograph***,** 724-757.
MITCH, M. G. & SOARES, C. G. 2009. Primary standards for brachytherapy sources. *Clinical Dosimetry for Radiotherapy: AAPM Summer School***,** 549-565.
MOLL, A. C., KUIK, D. J., BOUTER, L. M., DEN OTTER, W., BEZEMER, P. D., KOTEN, J. W., IMHOF, S. M., KUYT, B. P. & TAN, K. E. 1997. Incidence and survival of retinoblastoma in The Netherlands: a register based study 1862–1995. *British Journal of Ophthalmology,* 81**,** 559-562.
MOORE, R. F. 1930. Choroidal sarcoma treated by the intraocular insertion of radon seeds. *The British Journal of Ophthalmology,* 14**,** 145.
MOORE, R. F., STALLARD, H. & MILNER, J. 1931. Retinal gliomata treated by radon seeds. *The British Journal of Ophthalmology,* 15**,** 673.
MORRISON, H., MENON, G. & SLOBODA, R. S. 2014. Radiochromic film calibration for low-energy seed brachytherapy dose measurement. *Medical Physics* 41.
MOSS, D. C. 2000. Improved analytical fit to the TG-43 radial dose function, g (r). *Medical Physics,* 27**,** 659-661.
MOULD, R. F. 1993. *A century of X-rays and radioactivity in medicine: with emphasis on photographic records of the early years*, CRC Press.
MOURTADA, F., MIKELL, J. & IBBOTT, G. 2012. Monte Carlo calculations of AAPM Task Group Report No. 43 dosimetry parameters for the 125I I-Seed AgX100 source model. *Brachytherapy,* 11**,** 237-244.
MOUTSATSOS, A., PANTELIS, E., PAPAGIANNIS, P. & BALTAS, D. 2014. Experimental determination of the Task Group-43 dosimetric parameters of the new I25. S17plus 125I brachytherapy source. *Brachytherapy* 13**,** 618-626.
MOY, C. S., ALBERT, D. M., DIENER-WEST, M., MCCAFFREY, L. D., SCULLY, R. E., WILLSON, J. K. & GROUP, C. O. M. S. 2001. Cause-specific mortality coding: methods in the collaborative ocular melanoma study COMS report No. 14. *Controlled Clinical Trials,* 22**,** 248-262.
MOY, S. C. & MELIA, B. M. 1999. Quality of Life assessment in the Collaborative Ocular Melanoma Study: Design and Methods COMS-QOLS Report No. 1. *Ophthalmic Epidemiology,* 6**,** 5-17.
MURPHREE, A. L. 2005. Intraocular retinoblastoma: the case for a new group classification. *Ophthalmology Clinics of North America,* 18**,** 41-53, viii.
MUSTAK, H. 2019. *Personal Communication*
NAG, S., WANG, D., WU, H., BAUER, C. J., CHAMBERS, R. B. & DAVIDORF, F. H. 2003. Custom-made “Nag” eye plaques for 125I brachytherapy. *International Journal of Radiation Oncology* Biology* Physics* 56**,** 1373-1380.
NATH, R., ANDERSON, L. L., LUXTON, G., WEAVER, K. A., WILLIAMSON, J. F. & MEIGOONI, A. S. 1995. Dosimetry of interstitial brachytherapy sources: Recommendations of the AAPM Radiation Therapy Committee Task Group No. 43. *Medical Physics,* 22**,** 209-234.
NATH, R., ANDERSON, L. L., MELI, J. A., OLCH, A. J., STITT, J. A. & WILLIAMSON, J. F. 1997. Code of practice for brachytherapy physics:

Report of the AAPM Radiation Therapy Committee Task Group No. 56. *Medical Physics,* 24**,** 1557-1598.
NATH, R., BONGIORNI, P., CHEN, Z., GRAGNANO, J. & ROCKWELL, S. 2005. Relative biological effectiveness of 103Pd and 125I photons for continuous low-dose-rate irradiation of Chinese hamster cells. *Radiation Research* 163**,** 501-509.
NATH, R. & CHEN, Z. J. 2007. Silver fluorescent x-ray yield and its influence on the dose rate constant for nine low-energy brachytherapy source models. *Medical Physics,* 34**,** 3785-3793.
NATH, R., MEIGOONI, A. S. & MELI, J. A. 1990. Dosimetry on transverse axes of 125I and 192Ir interstitial brachytherapy sources. *Medical Physics,* 17**,** 1032-1040.
NATH, R. & YUE, N. 2000. Dose distribution along the transverse axis of a new 125I source for interstitial brachytherapy. *Medical Physics,* 27**,** 2536-2540.
NATH, R. & YUE, N. 2001. Dosimetric characterization of a newly designed encapsulated interstitial brachytherapy source of iodine-125—model LS-1 BrachyseedTM. *Applied Radiation and Isotopes,* 55**,** 813-821.
NATH, R. & YUE, N. 2002. Dosimetric characterization of an encapsulated interstitial brachytherapy source of 125I on a tungsten substrate. *Brachytherapy,* 1**,** 102-109.
NCRP_58 1985. *Handbook of radioactivity measurements procedures*, National Council on Radiation Protection and Measurements (NCRP).
NIKJOO, H. & LINDBORG, L. 2010. RBE of low energy electrons and photons. *Physics in Medicine & Biology,* 55**,** R65.
NIROOMAND-RAD, A., BLACKWELL, C. R., COURSEY, B. M., GALL, K. P., GALVIN, J. M., MCLAUGHLIN, W. L., MEIGOONI, A. S., NATH, R., RODGERS, J. E. & SOARES, C. G. 1998. Radiochromic film dosimetry: recommendations of AAPM radiation therapy committee task group 55. *Medical Physics,* 25**,** 2093-2115.
NUNN, A. A., DAVIS, S. D., MICKA, J. A. & DEWERD, L. A. 2008. LiF:Mg,Ti TLD response as a function of photon energy for moderately filtered x-ray spectra in the range of 20–250 kVp relative to C60o. *Medical Physics,* 35**,** 1859-1869.
NUTTENS, V. & LUCAS, S. 2006. AAPM TG-43U1 formalism adaptation and Monte Carlo dosimetry simulations of multiple-radionuclide brachytherapy sources. *Medical Physics,* 33**,** 1101-1107.
ONCOSEED 2005. Instructions for the Use of Iodine-125 Seeds for Medical Brachytherapy Treatments - Product Code: IMC6711. Product Pamphlet
PAIXÃO, L., FACURE, A., SANTOS, A. M. M., SANTOS, A. M. & GRYNBERG, S. E. 2012. Monte Carlo study of a new I-125 brachytherapy prototype seed with a ceramic radionuclide carrier and radiographic marker. *Journal of Applied Clinical Medical Physics,* 13**,** 74-82.
PANTELIS, E., BALTAS, D., GEORGIOU, E., KARAISKOS, P., LYMPEROPOULOU, G., PAPAGIANNIS, P., SAKELLIOU, L., SEIMENIS, I. & STILLIARIS, E. 2006. Dose characterization of the new Bebig IsoSeed® I25. S17 using polymer gel and MRI. *Nuclear Instruments and Methods in Physics Research Section A: Accelerators, Spectrometers, Detectors and Associated Equipment,* 569**,** 529-532.

PAPAGIANNIS, P., SAKELLIOU, L., ANAGNOSTOPOULOS, G. & BALTAS, D. 2006. On the dose rate constant of the selectSeed interstitial brachytherapy seed. *Medical Physics,* 33**,** 1522-1523.
PAPKA, P. 2013. *Personal communication.*
PATEL, N. S., CHIU-TSAO, S.-T., WILLIAMSON, J. F., FAN, P., DUCKWORTH, T., SHASHA, D. & HARRISON, L. B. 2001. Thermoluminescent dosimetry of the Symmetra™ 125I model I25.S06 interstitial brachytherapy seed. *Medical Physics,* 28**,** 1761-1769.
PHILIPS 1967. Operating Instructions "HT 100".
PIRCHIO, R., GALIANO, E., SARAVÍ, M., BANCHIK, D. & MUÑOZ, C. 2007. On the physical, spectral, and dosimetric characteristics of a new I125 brachytherapy source. *Medical Physics,* 34**,** 2801-2806.
PODER, J., ANNABELL, N., GESO, M., ALQATHAMI, M. & CORDE, S. ROPES eye plaque dosimetry: commissioning and verification of an ophthalmic brachytherapy treatment planning system. Journal of Physics: Conference Series, 2013. IOP Publishing, 012102.
POON, E., LE, Y., WILLIAMSON, J. F. & VERHAEGEN, F. BrachyGUI: an adjunct to an accelerated Monte Carlo photon transport code for patient-specific brachytherapy dose calculations and analysis. Journal of Physics: Conference Series, 2008. IOP Publishing, 012018.
POPESCU, C., WISE, J., SOWARDS, K., MEIGOONI, A. & IBBOTT, G. 2000. Dosimetric characteristics of the Pharma Seed™ model BT-125-I source. *Medical Physics,* 27**,** 2174-2181.
PRATT, C. B., FONTANESI, J., LU, X., PARHAM, D. M., ELFERVIG, J. & MEYER, D. 1997. Proposal for a new staging scheme for intraocular and extraocular retinoblastoma based on an analysis of 103 globes. *The Oncologist,* 2**,** 1-5.
PTW 2013. User Manual: Sourcecheck 4pi Well-Type Ionization Chamber Type 33005.
R REDUS, A. H., J PANTAZIS, T PANTAZIS, D SPERRY 2006. Design and performance of the X-123 compact X-ray and gamma-ray spectroscopy system. *Symposium on Room Temperature Detectors, IEEE Nuclear Science Symposium.*
RABUS, H. 2019. Nanodosimetry-on the tracks of biological radiation effectiveness arXiv.org.
RASBAND, W. S. 1997-2018. *ImageJ* [Online]. U. S. National Institutes of Health, Bethesda, Maryland, USA. Available: https://imagej.nih.gov/ij/ [Accessed 5 Oct 2019].
REESE, A. & ELLSWORTH, R. 1963. The evaluation and current concept of retinoblastoma therapy. *Transactions-American Academy of Ophthalmology and Otolaryngology. American Academy of Ophthalmology and Otolaryngology,* 67**,** 164.
REESE, A. B., MERRIAM, G. R. & MARTIN, H. E. 1949. Treatment of Bilateral Retinoblastoma by Irradiation and Surgery*: Report on 15-Year Results. *American Journal of Ophthalmology,* 32**,** 175-190.
RENIERS, B., VYNCKIER, S. & SCALLIET, P. 2001. Dosimetric study of the new InterSource125 iodine seed. *Medical Physics,* 28**,** 2285-2288.
REYNAERT, N., VAN DER MARCK, S., SCHAART, D., VAN DER ZEE, W., VAN VLIET-VROEGINDEWEIJ, C., TOMSEJ, M., JANSEN, J., HEIJMEN,

B., COGHE, M., DE WAGTER, C. 2007. Monte Carlo treatment planning for photon and electron beams. *Radiation Physics and Chemistry* 76**,** 643-686.
RICHARDS, A. G. 1955. The Production of Erythema of the Skin by Exposure to X-ray Radiation. *Journal of Dental Research* 34**,** 100-103.
RIVARD, M. J. 2001. Monte Carlo calculations of AAPM Task Group Report No. 43 dosimetry parameters for the MED3631-A/M 125I source. *Medical Physics,* 28**,** 629-637.
RIVARD, M. J. 2002. Comprehensive Monte Carlo calculations of AAPM Task Group Report No. 43 dosimetry parameters for the model 3500 I-Plant 125I brachytherapy source. *Applied Radiation and Isotopes,* 57**,** 381-389.
RIVARD, M. J., BALLESTER, F., BUTLER, W. M., DEWERD, L. A., IBBOTT, G. S., MEIGOONI, A. S., MELHUS, C. S., MITCH, M. G., NATH, R. & PAPAGIANNIS, P. 2017. Supplement 2 for the 2004 update of the AAPM Task Group No. 43 Report: joint recommendations by the AAPM and GEC-ESTRO. *Medical Physics* 44**,** e297-e338.
RIVARD, M. J., BUTLER, W. M., DEWERD, L. A., HUQ, M. S., IBBOTT, G. S., MEIGOONI, A. S., MELHUS, C. S., MITCH, M. G., NATH, R. & WILLIAMSON, J. F. 2007. Supplement to the 2004 update of the AAPM Task Group No. 43 Report. *Medical Physics,* 34**,** 2187-2205.
RIVARD, M. J., CHIU-TSAO, S. T., FINGER, P. T., MEIGOONI, A. S., MELHUS, C. S., MOURTADA, F., NAPOLITANO, M. E., ROGERS, D., THOMSON, R. M. & NATH, R. 2011. Comparison of dose calculation methods for brachytherapy of intraocular tumors. *Medical Physics,* 38**,** 306-316.
RIVARD, M. J., COURSEY, B. M., DEWERD, L. A., HANSON, W. F., HUQ, M. S., IBBOTT, G. S., MITCH, M. G., NATH, R. & WILLIAMSON, J. F. 2004. Update of AAPM Task Group No. 43 Report: A revised AAPM protocol for brachytherapy dose calculations. *Medical Physics,* 31**,** 633-674.
RIVARD, M. J., GRANERO, D., PEREZ-CALATAYUD, J. & BALLESTER, F. 2010. Influence of photon energy spectra from brachytherapy sources on Monte Carlo simulations of kerma and dose rates in water and air. *Medical Physics,* 37**,** 869-876.
RIVARD, M. J. 1999. Comment on "Dosimetry of interstitial brachytherapy sources: Recommendations of the AAPM Radiation Therapy Committee Task Group 43"[Med. Phys. 22, 209–234 (1995)]. *Medical Physics* 26**,** 2514-2514.
RIVARD, M. J. 2009. Monte Carlo radiation dose simulations and dosimetric comparison of the model 6711 and 9011 brachytherapy sources. *Medical Physics* 36**,** 486-491.
ROBERTSON, K. 2014. *Personal Communication via Wright-Millners.*
ROGERS, D. 2006. Fifty years of Monte Carlo simulations for medical physics. *Physics in Medicine & Biology,* 51**,** R287.
ROGERS, D., KAWRAKOW, I., SEUNTJENS, J., WALTERS, B. & MAINEGRA-HING, E. 2018. NRC User Codes for EGSnrc.
ROGERS, D., WALTERS, B. & KAWRAKOW, I. J. N. R. P. 2009. BEAMnrc users manual. 509**,** 12.
ROSENGREN, B., MONGE, O. & FLAGE, T. 1989. Proposal of a New Pretreatment Clinicaltnm Classification of Retin Oblastoma. *Acta Oncologica,* 28**,** 547-548.
SAHOO, S., SELVAM, T. P. 2009. An EGSnrc investigation of the air-kerma strength, dose rate constant, and radial dose function of 125 I brachytherapy sources. *Radiological Physics and Technology* 2**,** 198-204.

SANDER, T. 2014. Air kerma and absorbed dose standards for reference dosimetry in brachytherapy. *The British Journal of Radiology,* 87**,** 20140176.
SAUTER, F. 1931. Über den atomaren Photoeffekt in der K-Schale nach der relativistischen Wellenmechanik Diracs. *Annalen der Physik,* 403**,** 454-488.
SCALLIET, P. & WAMBERSIE, A. 1987. Which RBE for iodine 125 in clinical applications? *Radiotherapy and Oncology,* 9**,** 221-230.
SCHNEIDER, C. A., RASBAND, W. S. & ELICEIRI, K. W. 2012. NIH Image to ImageJ: 25 years of image analysis. *Nature Methods* 9**,** 671.
SEALY, R., BURET, E., CLEMINSHAW, H., STANNARD, C., HERING, E., SHACKLETON, D., KORRUBEL, J., LE ROUX, P., SEVEL, D. & VAN OLDENBORGH, M. 1980. Progress in the use of iodine therapy for tumours of the eye. *The British Journal of Radiology* 53**,** 1052-1060.
SEALY, R., LE ROUX, L., RAPLEY, F., HERING, E., SHACKLETON, D. & SEVEL, D. 1976. The treatment of ophthalmic tumours with low-energy sources. *The British Journal of Radiology,* 49**,** 551-554.
SEALY, R., LE ROUX, P. & VAN DER MERWE, E. 1964. Two intra-oral implants. *South African Medical Journal* 38.
SEALY, R., STANNARD, C., SHACKLETON, D. 1987. Improved cosmesis in retinoblastoma patients treated with iodine-125 orbital irradiation. *Ophthalmic Paediatrics & Genetics* 8**,** 95-99.
SEALY, R. 1977. Some aspects of radiotherapy of tumours of the eye. *Transactions of the Colleges of Medicine of South Africa* 21**,** 3-23.
SECO, J. & VERHAEGEN, F. 2013. *Monte Carlo techniques in radiation therapy*, CRC press.
SEVEL, D., SEALY, R. & LAWTON, E. 1973a. Retinoblastoma at Groote Schuur Hospital *Transactions of the Ophthalmological Societies of the United Kingdom* 1952-1972. 93**,** 23.
SEVEL, D. & SEALY, R. 1969. Pterygia and carcinoma of the conjunctiva. *Transactions of the Ophthalmological Societies of the United Kingdom* 88**,** 567-578.
SEVEL, M., SEALY, R., LAWTON, E. & MB, B. 1973b. The early symptomatology of retinoblastoma. *South African Medical Journal,* 47**,** 1143-1144.
SIMPSON, E. R., GALLIE, B., LAPERRIERRE, N., BEIKI-ARDAKANI, A., KIVELÄ, T., RAIVIO, V., HEIKKONEN, J., DESJARDINS, L., DENDALE, R. & MAZAL, A. 2014. The American Brachytherapy Society consensus guidelines for plaque brachytherapy of uveal melanoma and retinoblastoma. *Brachytherapy,* 13**,** 1-14.
SINGH, A. D., PELAYES, D. E., SEREGARD, S. & MACKLIS, R. 2013. *Ophthalmic Radiation Therapy*, Karger Medical and Scientific Publishers.
SINGH, G. & DANIELS, A. B. Disparities in retinoblastoma presentation, treatment, and outcomes in developed and less-developed countries. *Seminars in Ophthalmology*, 2016. Taylor & Francis, 310-316.
SLOBODA, R. S. & MENON, G. V. 2000. Experimental determination of the anisotropy function and anisotropy factor for model 6711 I-125 seeds. *Medical Physics,* 27**,** 1789-1799.
SOARES, C. G. 2006. Radiochromic film dosimetry. *Radiation Measurements,* 41**,** S100-S116.
SOARES, C. G., DOUYSSET, G. & MITCH, M. G. 2009. Primary standards and dosimetry protocols for brachytherapy sources. *Metrologia,* 46**,** S80.

SOLBERG, T. D., DEMARCO, J. J., HUGO, G. & WALLACE, R. E. 2002. Dosimetric parameters of three new solid core I-125 brachytherapy sources. *Journal of Applied Clinical Medical Physics,* 3**,** 119-134.
SOWARDS, K. T. & MEIGOONI, A. S. 2002a. A Monte Carlo evaluation of the dosimetric characteristics of the Best® Model 2301 125I brachytherapy source. *Applied Radiation and Isotopes,* 57**,** 327-333.
SOWARDS, K. T. & MEIGOONI, A. S. 2002b. A Monte Carlo evaluation of the dosimetric characteristics of the EchoSeed™ Model 6733 125I brachytherapy source. *Brachytherapy,* 1**,** 227-232.
STALLARD, H. 1966. Radiotherapy for malignant melanoma of the choroid. *The British Journal of Ophthalmology,* 50**,** 147.
STALLARD, H. B. 1948. Radiotherapy of malignant intra-ocular neoplasms. *The British Journal of Ophthalmology,* 32**,** 618.
STANNARD, C., LIPPER, S., SEALY, R. & SEVEL, D. 1979. Retinoblastoma: correlation of invasion of the optic nerve and choroid with prognosis and metastases. *British Journal of Ophthalmology* 63**,** 560-570.
STANNARD, C., MAREE, G., MUNRO, R., LECUONA, K. & SAUERWEIN, W. 2011. Iodine-125 orbital brachytherapy with a prosthetic implant in situ. *Strahlentherapie und Onkologie,* 187**,** 322.
STANNARD, C., MAREE, G., TOVEY, S., HUNTER, A. & WETTER, J. 2014. Iodine-125 brachytherapy in the management of squamous cell carcinoma of the oral cavity and oropharynx. *Brachytherapy,* 13**,** 405-412.
STANNARD, C., SAUERWEIN, W., MAREE, G. & LECUONA, K. 2013. Radiotherapy for ocular tumours. *Eye,* 27**,** 119-127.
STANNARD, C., SEALY, R., HERING, E., KORRUBEL, J., HILL, J., BARRON, A. & KNOWLES, R. 2001. Localized whole eye radiotherapy for retinoblastoma using a 125 I applicator,"claws". *International Journal of Radiation Oncology* Biology* Physics,* 51**,** 399-409.
STANNARD, C., SEALY, R., SHACKLETON, D., HILL, J., KORRUBEL, J. 1987. The use of iodine-125 plaques in the treatment of retinoblastoma. *Ophthalmic Paediatric & Genetics* 8**,** 89-93.
STANNARD, C. E., HERING, E., HOUGH, J., KNOWLES, R., MUNRO, R. & HILLE, J. 2004. Post-operative treatment of malignant salivary gland tumours of the palate with iodine-125 brachytherapy. *Radiotherapy and Oncology,* 73**,** 307-311.
STANNARD, C. E., SEALY, G. R. H., HERING, E. R., PEREIRA, S. B., KNOWLES, R. & HILL, J. C. 2000. Malignant melanoma of the eyelid and palpebral conjunctiva treated with iodine-125 brachytherapy. *Ophthalmology,* 107**,** 951-958.
STANTON, R. & STINSON, D. 1996. *Applied Physics for Radiation Oncology,* Medical Physics Publishing Corporation.
SUTHERLAND, J. & ROGERS, D. 2010. Monte Carlo calculated absorbed-dose energy dependence of EBT and EBT2 film. *Medical Physics,* 37**,** 1110-1116.
TAILOR, R., TOLANI, N. & IBBOTT, G. S. 2008. Thermoluminescence dosimetry measurements of brachytherapy sources in liquid water. *Medical Physics,* 35**,** 4063-4069.
TANAKA, K., TATEOKA, K., ASANUMA, O., KAMO, K. I., BENGUA, G., SATO, K., UEDA, T., TAKEDA, H., TAKAGI, M. & HAREYAMA, M. 2011. A dosimetry study of the Oncoseed 6711 using glass rod dosimeters and

EGS5 Monte Carlo code in a geometry lacking radiation equilibrium scatter conditions. *Medical Physics,* 38**,** 3069-3076.
TAYLOR, R. & ROGERS, D. 2008a. An EGSnrc Monte Carlo-calculated database of TG-43 parameters. *Medical Physics,* 35**,** 4228-4241.
TAYLOR, R. & ROGERS, D. 2008b. More accurate fitting of I125 and Pd103 radial dose functions. *Medical Physics,* 35**,** 4242-4250.
TAYLOR, R. E. 2006. *Monte Carlo calculations for brachytherapy,* Carleton University.
TAYLOR, R. E. P., YEGIN, G. & ROGERS, D. W. O. 2007. Benchmarking BrachyDose: Voxel based EGSnrc Monte Carlo calculations of TG-43 dosimetry parameters. *Medical Physics,* 34**,** 445-457.
THOMSON, R., YEGIN, G., TAYLOR, R., SUTHERLAND, J. & ROGERS, D. 2010. Sci—sat am (2): Brachy—05: fast monte carlo dose calculations for brachytherapy with brachydose. *Medical Physics* 37**,** 3910-3911.
THOMSON, R. M. & ROGERS, D. W. O. 2010. Monte Carlo dosimetry for I125 and P103d eye plaque brachytherapy with various seed models. *Medical Physics,* 37**,** 368-376.
THOMSON, R. M., TAYLOR, R. E., CHAMBERLAND, M. J. & ROGERS, D. 2017. User manual for egs_brachy.
THOMSON, R. M., TAYLOR, R. E. P. & ROGERS, D. W. O. 2008. Monte Carlo dosimetry for I125 and Pd103 eye plaque brachytherapy. *Medical Physics,* 35**,** 5530-5543.
TOPPING, J. 1972. *Errors of Observation and their Treatment (Science Paperbacks),* Chapman and Hall, UK.
TOVEY, S., STANNARD, C., MAREE, G., HISCOCK, R., THOMSON, C., PANIERI, E. & GOLDBERG, P. 2017. Perianal synovial sarcoma treated postoperatively with Iodine-125 brachytherapy: Technical details. *Brachytherapy,* 16**,** 565-571.
ULAM, S. Random processes and transformations. Proceedings of the International Congress on Mathematics, 1952. Citeseer, 264-275.
USHER-MOGA, J., BEACH, S. M. & DEWERD, L. A. 2009. Spectroscopic output of I125 and Pd103 low dose rate brachytherapy sources. *Medical Physics,* 36**,** 270-278.
VAN BATTUM, L., HUIZENGA, H., VERDAASDONK, R., HEUKELOM, S. 2015. How flatbed scanners upset accurate film dosimetry. *Physics in Medicine and Biology* 61**,** 625.
VAN EEDEN, D. 2014. *Development of a particle source model for a synergy linear accelerator to be used in Monte Carlo radiation dose calculations for cancer therapy.* Thesis - University of the Free State.
WAI, P., KRSTAJIĆ, N., ADAMOVICS, J., ISMAIL, A. & DORAN, S. Dosimetry of the Amersham 6711 OncoseedTM using PRESAGETM and optical CT. Journal of Physics: Conference Series, 2006. IOP Publishing, 235.
WALLACE, R. E. 2000. Empirical dosimetric characterization of model I125-SL 125Iodine brachytherapy source in phantom. *Medical Physics,* 27**,** 2796-2802.
WALLACE, R. E. 2002. Model 3500 125I brachytherapy source dosimetric characterization. *Applied Radiation and Isotopes,* 56**,** 581-587.
WALLACE, R. E. & FAN, J. J. 1998. Evaluation of a new brachytherapy iodine-125 source by AAPM TG43 formalism. *Medical Physics,* 25**,** 2190-2196.
WALLACE, R. E. & FAN, J. J. 1999. Report on the dosimetry of a new design 125Iodine brachytherapy source. *Medical Physics,* 26**,** 1925-1931.

WALTERS, B., KAWRAKOW, I. & ROGERS, D.W.O. 2005. DOSXYZnrc users manual. NRC Report Pirs 794.
WANG, R. & SLOBODA, R. S. 2002. Monte Carlo dose parameters of the BrachySeed model LS-1 125I brachytherapy source. *Applied Radiation and Isotopes,* 56**,** 805-813.
WEAVER, K. 1998. Anisotropy functions for 125I and 103Pd sources. *Medical Physics,* 25**,** 2271-2278.
WEAVER, K. A. 1986. The dosimetry of 125I seed eye plaques. *Medical Physics,* 13**,** 78-83.
WEAVER, K. A., SMITH, V., HUANG, D., BARNETT, C., SCHELL, M. C. & LING, C. 1989. Dose parameters of 125I and 192Ir seed sources. *Medical Physics,* 16**,** 636-643.
WELLS, C. G., BRADFORD, R. H., FISH, G. E., STRAATSMA, B. R. & HAWKINS, B. S. 1996. Choroidal melanomas in American Indians. *Archives of Ophthalmology,* 114**,** 1017-1018.
WILLIAMSON, J. F. 1988. Monte Carlo evaluation of specific dose constants in water for 125I seeds. *Medical Physics,* 15**,** 686-694.
WILLIAMSON, J. F. 1991. Comparison of measured and calculated dose rates in water near I-125 and Ir-192 seeds. *Medical Physics,* 18**,** 776-786.
WILLIAMSON, J. F. 2002. Dosimetric characteristics of the DRAXIMAGE model LS-1 I-125 interstitial brachytherapy source design: A Monte Carlo investigation. *Medical Physics,* 29**,** 509-521.
WILLIAMSON, J. F., COURSEY, B. M., DEWERD, L. A., HANSON, W. F., NATH, R., RIVARD, M. J. & IBBOTT, G. 1999. On the use of apparent activity (Aapp) for treatment planning of 125I and 103Pd interstitial brachytherapy sources: recommendations of the American Association of Physicists in Medicine radiation therapy committee subcommittee on low-energy brachytherapy source dosimetry. *Medical Physics,* 26**,** 2529.
WILLIAMSON, J. F. & QUINTERO, F. J. 1988. Theoretical evaluation of dose distributions in water about models 6711 and 6702 125I seeds. *Medical Physics,* 15**,** 891-897.
WILLIAMSON, J. F. 1987. Monte Carlo evaluation of kerma at a point for photon transport problems. *Medical Physics* 14**,** 567-576.
WILLIAMSON, J. F. 2000. Monte Carlo modeling of the transverse-axis dose distribution of the Model 200 interstitial brachytherapy source. *Medical Physics* 27**,** 643-654.
WILLSON, J. K., ALBERT, D. M., DIENER-WEST, M., MCCAFFREY, L., MOY, C. S. & SCULLY, R. E. 2001. Assessment of metastatic disease status at death in 435 patients with large choroidal melanoma in the collaborative ocular melanoma study (coms) coms report no. 15. *Archives of Ophthalmology,* 119**,** 670-676.
WUU, C. & ZAIDER, M. 1998. A calculation of the relative biological effectiveness of 125I and 103Pd brachytherapy sources using the concept of proximity function. *Medical Physics,* 25**,** 2186-2189.
YEGIN, G. 2003. A new approach to geometry modeling for Monte Carlo particle transport: An application to the EGS code system. *Nuclear Instruments and Methods in Physics Research Section B: Beam Interactions with Materials and Atoms,* 211**,** 331-338.
YU, C.-L., TUCKER, M. A., ABRAMSON, D. H., FURUKAWA, K., SEDDON, J. M., STOVALL, M., FRAUMENI JR, J. F. & KLEINERMAN, R. A. 2009.

Cause-specific mortality in long-term survivors of retinoblastoma. *Journal of the National Cancer Institute,* 101**,** 581-591.
ZEHTABIAN, M., FAGHIHI, R. & SINA, S. 2010. Comparison of dosimetry parameters of two commercially available Iodine brachytherapy seeds using Monte Carlo calculations. *Iranian Journal of Radiation Research* 7, 217-222
ZEITZ, L., KIM, S. H., KIM, J. H. & DETKO, J. F. 1977. Determination of relative biological effectiveness (RBE) of soft X rays. *Radiation Research* 70**,** 552-563.